

ZOOMING INTO  $\gamma$ -RAY LOUD GALACTIC NUCLEI:  
BROADBAND EMISSION AND STRUCTURE DYNAMICS  
OF THE BLAZAR PKS 1502+106 AND THE NARROW-LINE  
SEYFERT 1 1H 0323+342

INAUGURAL-DISSERTATION

zur  
Erlangung des Doktorgrades  
der Mathematisch-Naturwissenschaftlichen Fakultät  
der Universität zu Köln



vorgelegt von

**Vasileios (Vassilis) Karamanavis**

aus  
Thessaloniki, Griechenland

Köln 2015

Berichtersteller:

Prof. Dr. J. Anton Zensus  
Prof. Dr. Andreas Eckart

Tag der letzten mündlichen Prüfung: 6. Mai 2015

Dedicated to all those I've left behind,  
while chasing my dreams.



## ABSTRACT

---

Blazars are accretion-powered systems representing the most extreme flavor of active galactic nuclei (AGN). This thesis focuses on the study of blazar PKS 1502+106 during a prominent broadband outburst using ultra-high resolution imaging and a broadband single-dish study. The former is accomplished through very-long-baseline interferometry (VLBI) down to short millimeter (mm) wavelengths, while the latter uses densely-sampled radio light curves at a wide frequency range. The same combination allows the detailed study of the galaxy 1H 0323+342. This is a prominent member of the narrow-line Seyfert 1 (NLS1) class of AGN, recently discovered to emit  $\gamma$  rays.

General aspects of AGN along with an introduction to their discovery, phenomenology, and their constituent parts are discussed in Chapter 1. Here, specific aspects of blazars and concepts used in later chapters are also introduced.

Chapter 2 introduces the technique of VLBI from a theoretical standpoint, while in Chapter 3 the practical aspects of VLBI calibration and imaging at mm wavelengths are discussed.

The phenomenology and physical characteristics of PKS 1502+106 through a cm- to mm-VLBI study are presented in Chapter 4. The data set features Global Millimeter VLBI Array (GMVA) observations at 7 mm (43 GHz) and 3 mm (86 GHz) along with complementary observations at 2 cm (15 GHz) from the MOJAVE program. We also combine the analysis with F-GAMMA program data at frequencies matching the VLBI monitoring and with the *Fermi*/LAT  $\gamma$ -ray light curve. From the rich data set we deduce its kinematical and spectral characteristics which allow the inference of physical parameters of the ultra-relativistic jet of PKS 1502+106. For the jet features identified across observing frequencies we deduce Doppler factors in the range  $\sim 10$ – $50$  at different positions within the flow. Magnetic field strengths and brightness temperatures along the jet are also deduced. The position-dependent differences in viewing angle and Lorentz factors, indicate a jet bending towards the observer that also accelerates. The kinematical model and radio flux density decomposition into distinct jet components in conjunction with the  $\gamma$ -ray data indicate that the broadband flare, seen first at  $\gamma$ -rays and its delayed counterparts at radio wavelengths, can be attributed to one traveling jet feature (C<sub>3</sub>). Finally, the emission site of the  $\gamma$ -ray emission is constrained to  $\leq 10$ – $15$  pc from the jet base.

The outburst of PKS 1502+106 seen through the dense, single-dish, F-GAMMA data set between 2.64–345 GHz is discussed in Chapter 5. By employing three different time series analysis techniques relevant light curve parameters, such as the flare amplitude, flare time scales, and time delays of maxima are extracted. Those exhibit dependencies on observing frequency that are well-described by power laws. The frequency-dependent light curve parameters are compared with the expectations of analytical simulations (see Chapter 5 for references) under the shock-in-jet scenario with which a good agreement is found. From the frequency-dependent time lags, equipartition magnetic field strengths are calculated and in combination with the VLBI findings from Chapter 4, the MeV/GeV emitting region is localized at the edge or slightly further from the bulk of the broad-line region (BLR) material of PKS 1502+106 with important consequences on the origin of photons available for inverse Compton up-scattering.

In Chapter 6 the powerful combination of previous findings based on the F-GAMMA monitoring with VLBI images at 15 GHz allows the determination of the viewing angle towards the NLS1 galaxy 1H 0323+342. This is found to be  $\theta = 12$ – $13^\circ$ .

A summary and concluding remarks arising from the thesis at hand are presented in Chapter 7.

## ZUSAMMENFASSUNG

---

Blazare sind akkretionsgetriebene Systeme und stellen die extremste Kategorie aktiver galaktischer Kerne (AGN) dar. Der Schwerpunkt dieser Arbeit liegt auf der Untersuchung des Blazars PKS 1502+106 während eines markanten Breitband-Helligkeitsausbruchs. Mit Hilfe ultra-hochauflösender Bildverarbeitung und breitbandiger Einzelteleskop-Beobachtungen wurde die Quelle analysiert. Erstere wird durch Very Long Baseline Interferometry (VLBI) bei Wellenlängen im mm-Bereich bewerkstelligt, für letztere werden Radiolichtkurven mit dichtem Sampling in einem breiten Frequenzbereich verwendet. Diese Kombination ermöglicht darüber hinaus die Untersuchung der Galaxie 1H 0323+342. Diese ist ein bedeutendes Mitglied der Narrow-Line Seyfert 1 (NLS1) Klasse der AGN, von denen seit kurzem bekannt ist, dass sie  $\gamma$ -Strahlen emittieren.

Allgemeine Aspekte der AGN, einschließlich ihrer Entdeckung, Phänomenologie und ihrer Bestandteile, werden in Kapitel 1 behandelt. Hier werden auch spezifische Aspekte der Blazare, sowie in späteren Kapiteln verwendete Begriffe, eingeführt.

In Kapitel 2 erfolgt eine Einführung in die VLBI-Methode aus theoretischer Sicht, während in Kapitel 3 die praktischen Aspekte der VLBI-Kalibration und -Bildverarbeitung bei mm-Wellenlängen erörtert werden.

Die Phänomenologie und physikalischen Merkmale von PKS 1502+106 werden anhand von VLBI-Beobachtungen im cm- bis mm-Bereich in Kapitel 4 vorgestellt. Der Datensatz beinhaltet Beobachtungen mit dem Global Millimeter VLBI Array (GMVA) bei 7 mm (43 GHz) und 3 mm (86 GHz), zusammen mit ergänzenden Beobachtungen bei 2 cm (15 GHz) aus dem MOJAVE-Programm. Wir kombinieren die Analyse außerdem mit Daten des F-GAMMA-Programms bei Frequenzen, die denen der VLBI-Messungen entsprechen, sowie mit der Fermi/LAT  $\gamma$ -Strahlungs-Lichtkurve. Mithilfe dieses reichhaltigen Datensatzes ermitteln wir die kinematischen und spektralen Eigenschaften, die Rückschlüsse auf physikalische Parameter des ultrarelativistischen Jets von PKS 1502+106 erlauben. Für die Merkmale des Jets, die im beobachteten Frequenzbereich ermittelt wurden, erhalten wir Dopplereffektoren im Bereich  $\sim 10$ –50 an verschiedenen Positionen entlang der Ausbreitungsrichtung. Magnetische Feldstärken und Helligkeitstemperaturen entlang des Jets werden ebenfalls bestimmt. Die positionsabhängige Änderung des Sichtwinkels sowie des Lorentz-Faktors deuten auf einen sich in Richtung des Beobachters krümmenden Jet hin, der sich noch dazu beschleunigt. Das kinematische Modell und die Zerlegung der Radioflussdichte in verschiedene Jet-Komponenten in Verbindung mit den Gammadaten weisen auf eine breitbandige Eruption hin, welche zuerst im Gammabereich, zeitlich verzögert anschließend im Radiowellenbereich, gesehen wurde. Dies entspricht einem bewegten Jet-Knoten ( $C_3$ ) zugeordnet werden kann. Letztendlich kann der Emissionsbereich der Gammastrahlung bis auf 10–15 pc von der Jetbasis festgelegt werden.

Der Ausbruch von PKS 1502+106, welcher mittels Einzelteleskop-, F-GAMMA-Daten im Bereich zwischen 2.64–345 GHz beobachtet wurde, wird in Kapitel 5 besprochen. Mittels drei unterschiedlicher Methoden zur Zeitreihenanalyse werden die relevanten Lichtkurvenparameter, wie Flareamplitude, Zeitskala des Flares sowie zeitliche Verzögerungen der Maxima, ermittelt. Diese zeigen durch ein Potenzgesetz beschreibbare Abhängigkeiten von der Beobachtungsfrequenz. Die frequenzabhängigen Lichtkurvenparameter werden mit den Erwartungen aus analytischen Simulationen (für Referenzen siehe Kapitel 5) im Rahmen des Schock-in-Jet-Szenarios verglichen, mit welchem gute Übereinstimmung gefunden werden. Ausgehend von den frequenzabhängigen Zeitverzögerungen werden Equipartitions Magnetfeldstärken berechnet und mit den VLBI Ergebnissen aus Kapitel 4 kombiniert. Dadurch wird die MeV/GeV Emissionsregion

am Rand oder leicht entfernt vom Großteil des Materials der broad line region (BLR) von PKS 1502+106 bestimmt, was wichtige Konsequenzen für den Ursprung der Photonen in Bezug auf inverse Comptonstreuung ergibt.

Die Kombination von früheren Entdeckungen basierend auf der F-GAMMA Überwachung zusammen mit VLBI Bildern bei 15 GHz ermöglicht die Bestimmung des Betrachtungswinkels in Richtung der NLS1 Galaxie 1H 0323+342. Jener wird mit  $\theta = 12\text{--}13^\circ$  bestimmt.

Eine Zusammenfassung, sowie abschließende Schlussfolgerungen zur vorliegenden Dissertation werden in Kapitel 7 vorgelegt.



## ΠΕΡΙΛΗΨΗ

---

Τα μπλέιζαρς, τροφοδοτούμενα από την προσαύξηση μάζας σε μελανές οπές, αποτελούν την πιο ακραία έκφανση των ενεργών γαλαξιακών πυρήνων (AGN). Η παρούσα διατριβή εστιάζει στη μελέτη του μπλέιζαρ PKS 1502+106 κατά τη διάρκεια μίας ενεργειακής έκλαμψης ακτίνων  $\gamma$ , αξιοποιώντας δύο προσεγγίσεις: (i) απεικόνιση υψηλής διακριτικής ικανότητας και (ii) συστηματικές παρατηρήσεις σε πολλαπλές συχνότητες του ραδιοφωνικού φάσματος. Στην πρώτη γίνεται χρήση συμβολομετρίας πολύ μεγάλων αποστάσεων (VLBI) σε μήκη κύματος εκατοστών και χιλιοστών του μέτρου. Στη δεύτερη, αξιοποιούνται δεδομένα μεμονωμένων τηλεσκοπίων και καμπύλες φωτός με υψηλό ρυθμό δειγματοληψίας. Ο ίδιος συνδυασμός τεχνικών επιτρέπει την λεπτομερή μελέτη του ενεργού γαλαξία 1H 0323+342. Ο τελευταίος αποτελεί μέλος της κατηγορίας των γαλαξιών narrow-line Seyfert 1 (NLS1) που πρόσφατα ανακαλύφθηκε ότι εκπέμπουν ακτινοβολία  $\gamma$ .

Μία γενική εισαγωγή σχετικά με τους πυρήνες ενεργών γαλαξιών, την ανακάλυψή τους, την φαινομενολογία αλλά και τα συστατικά στοιχεία τους δίνονται στο Κεφάλαιο 1. Παράλληλα, παρουσιάζονται και συζητούνται έννοιες σχετικές με τα μπλέιζαρς.

Στο Κεφάλαιο 2, εισάγεται η τεχνική της συμβολομετρίας πολύ μεγάλων αποστάσεων από θεωρητική σκοπιά, ενώ στο επόμενο κεφάλαιο συζητούνται πρακτικές απόψεις της τεχνικής αυτής σχετικές με την επεξεργασία των δεδομένων και την παραγωγή εικόνων. Δίνεται έμφαση στο VLBI στη περιοχή των χιλιοστομετρικών μηκών κύματος.

Φαινομενολογικά και φυσικά χαρακτηριστικά του μπλέιζαρ PKS 1502+106, μέσω της τεχνικής VLBI σε μήκη κύματος από εκατοστά μέχρι χιλιοστά, παρουσιάζονται στο Κεφάλαιο 4. Τα δεδομένα προέρχονται από τη συστοιχία τηλεσκοπίων Global Millimeter VLBI Array (GMVA) και αποτελούνται από παρατηρήσεις στα 7 mm (43 GHz) και 3 mm (86 GHz). Επιπλέον δεδομένα στα 2 cm (15 GHz) προέρχονται από το πρόγραμμα MOJAVE. Η συμβολομετρική ανάλυση συνδυάζεται με δεδομένα από το πρόγραμμα F-GAMMA στις προαναφερθείσες συχνότητες και παρατηρήσεις ακτίνων  $\gamma$  από το διαστημικό τηλεσκόπιο *Fermi*. Από την συλλογή αυτή των δεδομένων συνάγονται οι κινηματικές και φασματικές ιδιότητες της πηγής που επιτρέπουν την ποσοτικοποίηση των φυσικών χαρακτηριστικών της σχετικιστικής ροής (τζετ) του PKS 1502+106. Για στοιχεία της ροής (VLBI components), ταυτοποιημένα μεταξύ συχνοτήτων, υπολογίζονται παράγοντες ενίσχυσης Ντόπλερ μεταξύ 10 και 50 σε διαφορετικές θέσεις του τζετ. Υπολογίζονται επίσης η ένταση του μαγνητικού πεδίου και η θερμοκρασία λαμπρότητας κατά μήκος της σχετικιστικής ροής. Οι διαφορές σε γωνία θέασης και παράγοντα Λόρεντς που εξαρτώνται από τη θέση (εντός της ροής) οδηγούν στο συμπέρασμα ότι η ροή όχι μόνο κάμπτεται προς τον παρατηρητή αλλά επιπλέον παρουσιάζει εσωτερική επιτάχυνση. Το κινηματικό μοντέλο και η κατανομή της ραδιοφωνικής πυκνότητας ροής (flux density) μεταξύ στοιχείων του τζετ σε συνάρτηση με τα δεδομένα στις ακτίνες  $\gamma$ , καταδεικνύουν ότι η έκλαμψη (ορατή πρώτα στις υψηλές ενέργειες και με καθυστέρηση σε ραδιοφωνικά μήκη κύματος) συνδέεται με ένα κινούμενο στοιχείο της ροής (C3). Τέλος, η περιοχή εκπομπής ακτινοβολίας  $\gamma$  περιορίζεται σε μία απόσταση μικρότερη των 10–15 pc από τη βάση του τζετ.

Η έκλαμψη του PKS 1502+106, όπως παρατηρείται από τα δεδομένα μεμονωμένων τηλεσκοπίων και υψηλού ρυθμού δειγματοληψίας του προγράμματος F-GAMMA, σχολιάζεται στο Κεφάλαιο 5. Χρησιμοποιώντας τρεις διαφορετικές μεθόδους ανάλυσης χρονοσειρών εξάγονται χαρακτηριστικές ποσότητες των καμπυλών φωτός, όπως το εύρος της μεταβολής, η διάρκεια της και η χρονική διαφορά μεταξύ των μεγίστων τιμών (σε διαφορετικά μήκη κύματος). Η εξάρτηση των παραπάνω ποσοτήτων από την συχνότητα παρατήρησης ακολουθεί νόμους δύναμης (power laws). Οι ίδιες εξαρτήσεις βρίσκονται σε καλή συμφωνία με την αναμενόμενη συμπεριφορά από μοντέλα που υιοθετούν την διάδοση διαταραχών (κρουστικών μετώπων, shocks) εντός του τζετ. Η εξαρτώμενη από τη συχνότητα χρονική καθυστέρηση μεταξύ των μεγίστων στις καμπύλες φωτός, επιτρέπει μια τομογραφία του μαγνητικού πεδίου κατά μήκος του τζετ. Η σύγκριση με τα ευρήματα της ανάλυσης VLBI οδηγεί στο συμπέρασμα ότι η ακτινοβολία ακτίνων  $\gamma$  προέρχεται από μία περιοχή στα όρια ή πέρα από την περιοχή διευρυμένων φασματικών γραμμών (BLR) του PKS 1502+106. Το συμπέρασμα αυτό έχει σημαντικές συνέπειες για την προέλευση του πεδίου φωτονίων που μπορούν να αποτελέσουν στόχο για αντίστροφη σκέδαση Κόμπτον προς υψηλές ενέργειες.

Στο Κεφάλαιο 6 ο ίδιος συνδυασμός τεχνικών επιτρέπει τον περιορισμό της γωνίας θέασης του γαλαξία 1H 0323+342 στο εύρος  $12-13^\circ$ .

Τα ευρήματα αυτής της διατριβής και οι τελικές παρατηρήσεις παρουσιάζονται στο Κεφάλαιο 7.

## ACKNOWLEDGMENTS

---

Over the course of these three wonderful years, some people have contributed the most towards completion of the present work. First, my deep appreciation and special thanks go to Dr. Lars Fuhrmann for his constant support and our insightful scientific exchanges. Like with any PhD adviser, there have been hard and great times. The latter, though, have been by far more! I enjoyed a lot our collaboration and I have learned a lot from him through our stimulating discussions.

I am grateful to Prof. Dr. J. Anton Zensus, head of the VLBI group at the MPIfR. To him I express my deep appreciation and gratitude for his trust and support throughout this effort. His support has come in many levels and in many different forms; without it, this thesis would have never existed.

I also feel obligated to Prof. Dr. Andreas Eckart for agreeing to review my thesis and to Prof. Dr. Carsten Münker for chairing the examination committee. They have both dedicated their valuable time and I appreciate their support.

Special thanks I owe to Dr. Emmanouil (Manolis) Angelakis. He was there to support me and exchange scientific (and other) ideas throughout these three years. We have spent a lot of time with him discussing about science and numerous other things! I deeply thank him for also making the adaptation here a lot easier.

Dr. Thomas P. Krichbaum has helped me a lot with the difficulties that VLBI brings along. He has been there to listen to my problems and propose solutions.

Special thanks and deep appreciation go to Prof. Dr. Eduardo Ros. He has been helpful with all my VLBI and non-VLBI related problems. I really enjoyed all our discussions, formal and informal. Him, along with Dr. Andrei Lobanov and Dr. Tuomas Savolainen have shown me a lot about how things actually work.

I deeply thank Dr. Richard Porcas for sharing his knowledge and experience in the field with all the students. I enjoy his critical comments on just about anything. Many—even five-minute—conversations with him, made me change almost whole chapters of this thesis!

I acknowledge the help of Dr. Stefanie Komossa. She has always been available for discussion and sharing her expertise.

Special thanks go to my friends John Antoniadis and Ioannis Nestoras. If only we were spending more time all together! Also Ioannis Myserlis with whom we started together this amazing journey.

Warm thanks go to Sebastian Kiehlmann. He has been inspiring in many ways. Thanks also to Christoph Rauch! With both we have been sharing an office for quite some time and we have also been sharing our thoughts about science and much more. Jeff Hodgson and Florent Mertens could not be forgotten, neither them nor the days (and nights) we spent dissecting AGN jets. Dr. Bindu Rani, Dr. Shoko Koyama, Dhanya G. Nair, and Laura Vega Garcia have always been offering a helping hand. I thank them all!

In these three years I have met a lot of amazing people through the IMPRS in Bonn and Cologne. It was a very fun experience and they all helped me in their own unique way!

During the long observing runs at Effelsberg and IRAM Pico Veleta, the telescope staff offered their help many times. I would like to thank them all: Jörg Barthel, Thomas Georgi, Alexander Hochgürtel, Marcus Keseberg, Ralf Kisky, Klaus Schlich, Willy Schmitz, Norbert Tacke, Peter Vogt, and Thomas Wedel at Effelsberg. Manuel Ruiz, Víctor Puela, Ignacio Ruiz, and Joaquín Santiago at Pico Veleta.

Dr. Simone Pott, Beate Naunheim, Barbara Menten, Tuyet-Le Tran, and Karin Gotzmann made a lot of things much easier during this period. I appreciate all their help.

I also thank Gerrit Schellenberger and Philip Schmidt for helping me translate (in no time!) the thesis' abstract into German and Dr. Silke Britzen for its final editing.

I wholeheartedly thank Bia Boccardi for all her help and support.

Last but not least, Prof. Dr. John H. Seiradakis will always have a special place in my heart and mind. He has always been the reference point of our scientific quests.

Bonn, 15 March 2015

## CONTENTS

---

1	A GALAXY AND ITS JET	1
1.1	Introduction	1
1.2	The discovery of active galaxies	1
1.3	Discoveries at radio wavelengths	2
1.4	The first quasars	3
1.5	Unification of active galaxies	3
1.6	Building blocks of AGN	4
1.6.1	The supermassive black hole	4
1.6.2	Accretion disk	4
1.6.3	Broad-line region	6
1.6.4	Molecular torus	7
1.6.5	Narrow-line region	7
1.6.6	The relativistic jet	7
1.7	Observational properties of astrophysical jets from black holes	7
1.7.1	Relativistic beaming	9
1.7.2	Apparent luminosity	9
1.7.3	Eddington luminosity and limiting mass-accretion rate	11
1.7.4	Brightness temperature	11
1.7.5	Superluminal motion	12
1.8	Blazar properties	13
1.9	Radiation mechanisms	14
1.9.1	Synchrotron radiation	14
1.9.2	Inverse Compton scattering	17
1.10	Formation and stability of relativistic flows	18
1.10.1	Formation of jets	18
1.10.2	Stability of relativistic jets	19
1.11	Open questions	21
1.12	Outline and impact of the present work	21
2	INTERFEROMETRY AND VLBI	23
2.1	Introduction	23
2.2	Correlated noise and the visibility function	25
2.2.1	The correlator input: voltages and noise	25
2.2.2	The correlator output	26
2.2.3	The uv-plane: Sampling the visibilities, coverage and the dirty beam	29
2.3	Visibility phase self-calibration	31
2.4	Visibility amplitude self-calibration	35
2.5	Applications of VLBI to blazars	36
2.5.1	Frequency-dependent core position	37
3	PRACTICAL MILLIMETER-VLBI CALIBRATION AND IMAGING	39
3.1	Millimeter-VLBI observations and the GMVA	39
3.2	Practical millimeter-VLBI data reduction and the rationale behind it	40
3.2.1	<i>A priori</i> calibration in AIPS	40

3.2.2	Manual phase calibration and fringe fitting . . . . .	41
3.2.3	Amplitude calibration . . . . .	42
3.2.4	Imaging and model fitting with DIFMAP . . . . .	45
4	MULTI-FREQUENCY VLBI STUDY OF THE BLAZAR PKS 1502+106 . . . . .	49
4.1	Introduction . . . . .	49
4.2	Observations and complementary data . . . . .	50
4.2.1	High frequency 43 GHz and 86 GHz GMVA data . . . . .	50
4.2.2	15 GHz MOJAVE survey data . . . . .	51
4.2.3	Single-dish 15, 43 and 86 GHz F-GAMMA data . . . . .	51
4.2.4	Fermi/LAT $\gamma$ -ray data . . . . .	52
4.3	PKS 1502+106 jet phenomenology . . . . .	54
4.3.1	Parsec-scale jet morphology . . . . .	54
4.3.2	VLBI kinematics at 15, 43 and 86 GHz . . . . .	54
4.3.3	Radio flux density decomposition . . . . .	64
4.3.4	Spectra of individual knots . . . . .	64
4.4	Inferred physical parameters . . . . .	66
4.4.1	Doppler and Lorentz factor estimates . . . . .	68
4.4.2	The viewing angle towards PKS 1502+106 . . . . .	70
4.4.3	Opening angle of the jet . . . . .	70
4.4.4	Radial brightness temperature distribution . . . . .	72
4.4.5	Magnetic field estimates . . . . .	73
4.5	Discussion . . . . .	75
4.5.1	The $\gamma$ -ray/radio flare . . . . .	75
4.5.2	Distance estimates to the central engine . . . . .	76
4.5.3	Intrinsic jet properties . . . . .	78
4.5.4	Particle versus magnetic field dominated jet . . . . .	80
4.6	Chapter summary and concluding remarks . . . . .	81
5	THE BROADBAND OUTBURST OF PKS 1502+106: WHAT CAN IT TELL US? . . . . .	85
5.1	Introduction . . . . .	85
5.2	Radio observations and the F-GAMMA program . . . . .	86
5.2.1	Effelsberg 100-m telescope data analysis . . . . .	86
5.2.2	IRAM 30-m telescope data analysis . . . . .	89
5.2.3	APEX 12-m data . . . . .	91
5.3	Fermi-GST $\gamma$ -ray observations . . . . .	91
5.4	Light curve time series analysis . . . . .	94
5.4.1	Decomposition into exponential flares . . . . .	94
5.4.2	Gaussian process regression . . . . .	98
5.4.3	The discrete cross-correlation function (DCCF) . . . . .	102
5.5	Frequency-dependent time lags . . . . .	107
5.6	Time-lag core shifts and opacity structure of PKS 1502+106 . . . . .	111
5.6.1	Localizing the $\gamma$ -ray emission region . . . . .	115
5.6.2	Equipartition magnetic field . . . . .	116
5.7	Comparison with shock-in-jet model simulations . . . . .	117
5.7.1	The shock-in-jet scenario and flare evolution . . . . .	117
5.7.2	Analytical model simulations . . . . .	119
5.7.3	Results . . . . .	120

5.8	Chapter summary and concluding remarks . . . . .	123
6	THE VIEWING ANGLE TOWARDS THE RLNLS1 GALAXY 1H 0323+342	127
6.1	Introduction . . . . .	127
6.1.1	Radio-loud NLS1 galaxies . . . . .	127
6.1.2	Radio- and $\gamma$ -ray-loud NLS1 galaxies . . . . .	128
6.2	Why are NLS1 galaxies interesting after all? . . . . .	131
6.3	The source: 1H 0323+342 (a.k.a. J0324+3410) . . . . .	131
6.4	VLBI observations and data reduction . . . . .	132
6.5	Parsec-scale jet morphology . . . . .	133
6.6	Radio flux density decomposition . . . . .	134
6.7	Source kinematics . . . . .	134
6.8	Jet-to-counter-jet ratio . . . . .	139
6.8.1	A first lower limit for the Doppler factor . . . . .	142
6.9	The viewing angle towards 1H0323+342 . . . . .	143
6.9.1	Viewing angle using only VLBI data . . . . .	143
6.9.2	A powerful combination of VLBI and single-dish data . . . . .	145
6.10	Discussion . . . . .	145
7	CONCLUDING REMARKS AND OUTLOOK	151
	APPENDICES	155
A	PKS 1502+106: INDIVIDUAL VLBI COMPONENT LIGHT CURVES AT 15, 43, AND 86 GHz	157
B	PKS 1502+106 MODELFIT RESULTS	159
C	1H 0323+342 MODELFIT RESULTS	165
	BIBLIOGRAPHY	167

## LIST OF FIGURES

Figure 1.1	Classification of AGN depending on their radio-loudness. . . .	5
Figure 1.2	AGN unification by orientation. Image credit: NASA/Aurore Simonnet, Sonoma State University. . . . .	6
Figure 1.3	The building blocks of an active galactic nucleus. Shown in colors are: (black) the supermassive black hole at the center; (from purple to white) the accretion disk; (red) clouds of the broad-line region (BLR); (light gray and cut in darker shade) the obscuring molecular torus surrounding the system; (light blue) clouds of the narrow-line region (NLR); (bright yellow) the relativistic jet. The sketch is not to scale. For details refer to Section 1.6. . . . .	8
Figure 1.4	Dependence of the Doppler boosting factor on viewing angle for the given range of intrinsic speeds, $\beta$ , between 0.1 and 0.9999. Inset: Note the de-boosting ( $\delta < 1$ ) that occurs for large viewing angles, even close to the plane of the sky, and for high flow speeds. . . . .	10
Figure 1.5	Dependence of the observed apparent velocity, $\beta_{app}$ , on view- ing angle for the same range of intrinsic velocities as in Fig. 1.4 only here expressed as the equivalent Lorentz factor. . . . .	10
Figure 1.6	Geometry of superluminal motion. . . . .	13
Figure 1.7	Broadband SED of the blazar 3C 66A during a multi-wavelength observing campaign. The fit corresponds to an EC+SSC model (see text). Data contributed from different programs and instru- ments are shown. Image from <a href="#">Abdo et al. [2011]</a> . . . . .	14
Figure 1.8	Typical synchrotron self-absorption spectrum. Here $S_{max} = 3$ Jy, $\nu_{max} = 3$ GHz are the turnover flux density and turnover fre- quency, respectively. The optically thick and thin spectral in- dices are shown on the plot and have typical values of 5/2 and −0.7, respectively. . . . .	16
Figure 1.9	Superposition of six SSA spectra, able to produce flat spectral characteristics across a broad frequency band. Here all SSA components are characterized by optically thick and thin parts with indices of 2.5 and −0.7, respectively. The resulting—from superposition—spectrum is shown in black. . . . .	17
Figure 1.10	Realization of a global 3-dimensional GRMHD simulation. A relativistic jet emerges from an initial configuration featuring a spinning SMBH, an accretion disk and a large-scale, poloidal magnetic field. Images from <a href="#">McKinney et al. [2012]</a> . . . . .	20
Figure 2.1	Power response of a receiving element to a point source as a function of angular offset from the peak, $P(\theta)$ . For a uniform circular aperture $P(\theta) = (J_1(x)/x)^2$ also known as the Airy pat- tern, where $J_1$ is the first order Bessel function. The half-power beam width (HPBW) is at $\sim 1.02 \lambda/D$ and the instrument's reso- lution is defined by the first null at $\sim 1.22 \lambda/D$ . . . . .	25



Figure 2.2	Schematic diagram of the two-element, very-long-baseline interferometer. The plane waveform reaches the antennas with a delay $c\tau_g$ which needs to be compensated in order to coherently (or in-phase) combine the signal of each element with one another. Image from <a href="#">Wiesemeyer and Nothnagel [2014]</a> . . . . .	26
Figure 2.3	Fringe intensity of two unresolved sources and of their sum. While for the unresolved ones the intensity reaches zero, the same does not happen for the resolved one. . . . .	28
Figure 2.4	Four hypothetical baseline configurations (with their projected length shown as a red line) and their respective on-sky fringe pattern dictated by their projected length. Here, cosinusoidal fringe patterns are shown. The color code denotes their response with values between 0 (black) and 1 (bright yellow). . .	32
Figure 2.5	Example uv-coverage of a Giant Metrewave Radio Telescope (GMRT) observation. Figures courtesy of Hans-Rainer Klöckner (MPIfR). . . . .	33
Figure 2.6	Closure relations geometry. . . . .	35
Figure 3.1	The effect of manual phase calibration on the data. Here, cross-power spectra of three VLBA baselines are shown. Those between FD-PT, LA-PT, and OV-PT for 3C 454.3. Data on the left are before the application of manual phase calibration, while on the right, after it. Note the slopes in phases (upper panels) that are gone after application of manual phase calibration. Original image courtesy of Dhanya G. Nair (MPIfR). . . . .	42
Figure 3.2	Flow chart of the <i>a priori</i> visibility data calibration procedure. . .	43
Figure 3.3	System temperature and other noise contributions, with the amount of correlated noise being the important observable of VLBI. . . . .	45
Figure 3.4	The Global Millimeter-VLBI Array (GMVA). Original image: T. P. Krichbaum (MPIfR). . . . .	47
Figure 3.5	The Very Long Baseline Array (VLBA). Image courtesy of NRAO, AUI and Earth image courtesy of the SeaWiFS Project NASA, GSFC and ORBIMAGE. . . . .	47
Figure 4.1	Uniform weighted, untapered MODELFIT images of the blazar PKS 1502+106, at 15 GHz. Contour levels correspond to $-0.15\%$ , $0.15\%$ , $0.3\%$ , $0.6\%$ , $1.2\%$ , $2.4\%$ , $4.8\%$ , $9.6\%$ , and $19.2\%$ of the highest peak flux density of $2.79$ Jy/beam (epoch 2009.23) as a common reference. The restoring beam has FWHM of $1.04$ mas $\times$ $0.45$ mas at a position angle of $-6.4^\circ$ . Unmarked components indicate non-robust features. Time progresses from top to bottom and from left to right. . . . .	55
Figure 4.1	continued. . . . .	56
Figure 4.1	continued. . . . .	57
Figure 4.2	Uniform weighted, untapered MODELFIT images of the blazar PKS 1502+106, at 43 GHz. Contour levels correspond to $-0.1\%$ , $0.1\%$ , $0.2\%$ , $0.4\%$ , $0.8\%$ , $1.6\%$ , $3.2\%$ , $6.4\%$ , and $12.8\%$ of the peak flux density of $3.47$ Jy/beam (epoch 2009.35) as a common reference. The restoring beam is shown at the bottom left of each image, with FWHM $0.61$ mas $\times$ $0.19$ mas at a position angle of $-19.9^\circ$ . Unmarked components indicate non-robustly cross-identified features. Time progresses from top to bottom and from left to right. . . . .	58

Figure 4.3	Uniform weighted, tapered MODELFIT images of the blazar PKS 1502+106, at 86 GHz. Contour levels correspond to $-0.15\%$ , $0.15\%$ , $0.3\%$ , $0.6\%$ , $1.2\%$ , $2.4\%$ , $4.8\%$ , $9.6\%$ and $19.2\%$ of the peak flux density of $2.23 \text{ Jy/beam}$ (epoch 2009.35) as a common reference. The restoring beam is shown at the bottom left of each image. Unmarked components indicate non-robustly cross-identified features. Time progresses from top to bottom and from left to right. . . . .	59
Figure 4.4	X and Y coordinates (relative RA and DEC with respect to the core) of all robustly identified components at the frequencies of 15, 43, and 86 GHz. . . . .	60
Figure 4.5	Temporal evolution of component radial separation from the core at—from top to bottom—15, 43 and 86 GHz. While the long-term kinematical behavior of PKS 1502+106 is visible at the lowest frequency, 43 and 86 GHz observations allow for a high resolution view towards the inner jet of PKS 1502+106. Components C1 and C2 being identifiable across all frequencies can be seen using the same color code. . . . .	62
Figure 4.6	Apparent speed profile of superluminal components as a function of radial separation from the core. . . . .	63
Figure 4.7	Light curves of PKS 1502+106. From top to bottom are shown: the <i>Fermi</i> /LAT $\gamma$ -ray light curve at $E > 100 \text{ MeV}$ ; F-GAMMA single-dish radio light curve at 15 GHz with the core and component light curves from the VLBI flux density decomposition; same as before but at 43 GHz and (lower panel) at 86 GHz. Note the VLBI knot C3, only visible at the two highest frequencies, at its decaying flux density phase. The gray shaded area delineates the full duration of the flare $\sim 650$ days. The red shaded area marks the estimated ejection interval of knot C3 with the red solid line designating its $t_{ej}$ . . . . .	65
Figure 4.8	Three-point spectra of knots C1, C2, the VLBI core and their temporal evolution. For C3 spectra are only available at 43 GHz and 86 GHz since it is blended at 15 GHz. Black lines represent the time-averaged spectra of components and their slopes are reported in Table 4.7. For component C1 the fitted SSA model spectra are also shown. The red curve is a SSA fit during its highest state, while the black corresponds to the mean SSA spectrum. . . . .	67
Figure 4.9	Deconvolved FWHM of all resolved jet components with respect to radial separation from the core at all available frequencies. The black solid line represents the best linear fit to the data. . . . .	71
Figure 4.10	Brightness temperature, $T_b$ , distribution with respect to radial separation from the core at all observing frequencies. Filled symbols represent $T_b$ measurements, while open symbols represent lower limits. . . . .	74

Figure 4.11	Doppler factor as a function of apparent speed for given viewing angle, $\delta = f(\beta_{\text{app}} \theta)$ , and given intrinsic speed $\beta$ , $\delta = f(\beta_{\text{app}} \beta)$ . Loci represent these two functions for a range of $\theta$ and $\beta$ . The values of intrinsic speeds plotted are $\beta = 0.9, 0.95, 0.98, 0.99, 0.995, 0.998, 0.999, 0.9995, \text{ and } 0.9999$ shown as solid lines. For the viewing angle the values are $\theta = 0.5^\circ, 1^\circ, 1.5^\circ, 2^\circ, 2.5^\circ, 3^\circ, 4^\circ, 5^\circ, 6^\circ, 8^\circ, 10^\circ, 15^\circ, \text{ and } 30^\circ$ shown as dashed lines. Note the two different jet regions, in terms of physical characteristics, where components C1 and C3 are traveling. Shaded areas represent the observables from our VLBI monitoring, namely the Doppler factor and the apparent velocity for each of the two knots. . . . .	80
Figure 5.1	Example of a real-life PV sub-scan. Image courtesy of I. Nestoras (MPIfR). . . . .	91
Figure 5.2	Facilities used by the F-GAMMA blazar monitoring program. .	92
Figure 5.3	Multi-wavelength light curves at radio frequencies from the F-GAMMA program and the $\gamma$ -ray light curve from <i>Fermi</i> . From top to bottom data are shown from: the Effelsberg 100-m at 2.64 GHz, 4.85 GHz, 8.35 GHz, 10.45 GHz, 14.60 GHz, 23.05 GHz, 32.00 GHz, and 43.00 GHz; the IRAM 30-m at 86.24 GHz and 142.33 GHz; APEX 12-m at 345.00 GHz. The bottom panel features the monthly-binned light curve from <i>Fermi</i> /LAT at $E > 100$ MeV. See also Table 5.1. . . . .	93
Figure 5.4	Light curve at 15.00 GHz from the OVRO 40 m blazar monitoring program [Richards et al., 2011]. See Section 5.1 for details. .	94
Figure 5.5	Light curve at a central frequency of 226.50 GHz from the high-frequency SMA calibrator list archive [see e.g. Gurwell et al., 2007]. See Section 5.1 for details. . . . .	94
Figure 5.6	Flare decomposition into exponential rise and decay parts. Here from top to bottom and left to right, frequencies in the range 2.64–32.00 GHz are shown. The reference date is MJD 54300. . .	96
Figure 5.7	Flare decomposition into exponential rise and decay parts. Here from top to bottom and left to right, frequencies in the range 43.00–226.5 GHz are shown. The reference date is MJD 54300. .	97
Figure 5.8	Gaussian process prior and posterior distributions. Shaded area is delineating a range of 2 standard deviations above and below the mean. For the purposes of this illustration the length scale hyperparameter was set to $\ell = 0.8$ (see text for discussion). . . . .	99
Figure 5.9	Gaussian process regression curves for the radio light curves in the range 2.64–15.00 GHz. Data points are shown in red, the prediction curve in dark blue and the 95% confidence interval is the lighter blue shaded area. . . . .	103
Figure 5.10	Gaussian process regression curves for the radio light curves in the range 23.05–226.50 GHz. Data points are shown in red, the prediction curve in dark blue and the 95% confidence interval is the lighter blue shaded area. . . . .	104
Figure 5.11	DCCF of PKS 1502+106 between light curves at 86.24 GHz and $\gamma$ rays. Lines represent significance levels above correlation by chance, at 99% (dotted line) and 90% (dashed line) levels. Image adopted from Fuhrmann et al. [2014] . . . . .	106

Figure 5.12	DCCFs for the light curves in the frequency range 2.64–10.45 with respect to the 15.00 GHz OVRO light curve. Also shown is the best-fit Gaussian function, the peak of which corresponds to the time lag. . . . .	108
Figure 5.13	DCCFs for the light curves in the frequency range 14.60–43.00 with respect to the 15.00 GHz OVRO light curve. Also shown is the best-fit Gaussian function, the peak of which corresponds to the time lag. . . . .	109
Figure 5.14	DCCFs for the light curves in the frequency range 86.24–226.50 with respect to the 15.00 GHz OVRO light curve. Also shown is the best-fit Gaussian function, the peak of which corresponds to the time lag. . . . .	110
Figure 5.15	Frequency-dependent time lags with respect to the 142.33 GHz data obtained through the three methods employed here. Open squares denote the values obtained from the DCCF analysis, red circles those from the Gaussian process regression and gray triangles the time lags from the exponential flare decomposition. The trend of decreasing time lag as observing frequency increases is evident with the use of all methods. Solid lines of the same color represent the best fit curves of the form $\alpha\nu^{-1/k_r}$ and indices $k_r$ are shown on the plot for each method. . . . .	113
Figure 5.16	Illustration of the frequency-dependent core position effect seen in VLBI images obtained at different frequency bands. Each frequency is "sensitive" to a certain opacity regime. By observing at increasing frequency we penetrate the opacity barrier set by synchrotron self-absorption to frequencies lower than it. Image adopted from <a href="#">Lobanov [1996]</a> . . . . .	113
Figure 5.17	Frequency-dependent light curve parameters and their variation with $d$ . From left to right the flare amplitude, flare time scale and cross-band delays are shown, each at three values of $d$ , namely $d = -0.3, 0.0,$ and $0.3$ . The other indices are kept constant with $b = 1.5$ and $s = 2.5$ . For the first and second panels from the left solid lines represent the rising part of the light curve, while dashed lines are used for the slopes of the decaying part. Numerical values for the slopes are shown with that of the decaying part in parenthesis. Image adopted from <a href="#">Fromm et al. [2014]</a> . . . . .	120
Figure 5.18	Parameter space plots for the evolution of frequency-dependent light curve parameters as a function of $s$ and $b$ and for fixed $d$ . Here, maps are related to the rising part of the light curve. . . . .	121
Figure 5.19	Frequency-dependent flare amplitudes. Triangles denote the values obtained through Gaussian process regression and circles those from exponential flare decomposition. Fitted power law functions are also shown following the same color coding and showing the rise and decay wings with respect to frequency. Best-fit power-law indices are shown on the plot. . . . .	123
Figure 5.20	Frequency-dependent flare variability time scales, through the decomposition into exponential flares. Purple circles correspond to the rising part of the light curve at each frequency, while filled green squares to the decaying part. Solid lines, color-coded according to the data, indicate the best-fit power-law of the form $\alpha\nu^b$ . Indices $b = \{\epsilon_{\text{flare time rise exp}}, \epsilon_{\text{flare time decay exp}}\}$ are shown on the plot. . . . .	124

Figure 5.21	Frequency-dependent flare variability time scales, through Gaussian process regression. Purple circles correspond to the rising part of the light curve at each frequency, while filled green squares to the decaying part. Solid lines, color-coded according to the data, indicate the best-fit power-law of the form $a\nu^b$ . Indices $b = \{\epsilon_{\text{flare time rise GP}}, \epsilon_{\text{flare time decay GP}}\}$ are shown on the plot. . . . .	124
Figure 6.1	Radio SED of 1H 0323+342. Data points are connected with line segments to facilitate visual inspection. For the same reason one spectrum every five is colored. The legend shows the observation date of the quasi-simultaneous SED in the form of fractional year. . . . .	128
Figure 6.2	Radio light curves of 1H 0323+342 at all frequency bands employed by the F-GAMMA monitoring program. . . . .	129
Figure 6.3	Spectral energy distributions of AGN and of the $\gamma$ -loud RLNLS1 J0948+0022 (orange data points without fit). Blazar SEDs are shown in colored points along with their respective best-fit SED models. Starting from top (black line) to bottom (blue), one moves from FSRQs to BL Lacs along the "blazar sequence". Also shown for comparison are SEDs of the radio galaxies NGC 6251, Centaurus A, and M87. Image from Foschini et al. [2010]. . . . .	130
Figure 6.4	Uniform-weighted MODELFIT maps of 1H 0323+342 at 15 GHz from the VLBA. Contour levels correspond to $-0.3\%$ , $0.3\%$ , $0.6\%$ , $1.2\%$ , $2.4\%$ , $4.8\%$ , $9.6\%$ , $19.2\%$ , and $38.4\%$ of the highest peak flux density of $0.344$ Jy/beam (epoch 2011.17) as a common reference. All maps are convolved with an average beam with major and minor axes of $0.768$ and $0.481$ mas, respectively with the major axis at a PA of $-5^\circ$ . Also shown, is the coverage for the uv-plane associated to the observation. . . . .	135
Figure 6.4	continued. . . . .	136
Figure 6.4	continued. . . . .	137
Figure 6.4	continued. . . . .	138
Figure 6.5	Position angle (PA) of all fitted components at all epochs. The jet axis remains strikingly stable at a mean PA of $\sim 124^\circ$ over $\sim 3$ yr. Here, only the southernmost region of the plane is shown with $0^\circ$ to the North (not shown). . . . .	139
Figure 6.6	Light curves of all VLBI components. Bottom panel also shows the total intensity single-dish light curve at 15 GHz obtained within F-GAMMA. Note the different flux density scales. Light curve of the quasi-stationary component, S, is plotted in both plot for visual comparison of the different flux density scales. Note the fast variability pattern of 1H 0323+342 and the low-frequency of VLBI sampling compared to it. . . . .	140
Figure 6.7	Temporal evolution of fitted component separation from the core. Line segments represent the best-fit linear model describing each knot's kinematical behavior. Apart from robustly identified knots (C#), open squares denote non-robust features. The new component (NC), visible in the latest epoch only, is shown as a red square right after the quasi-stationary feature S. . . . .	141

Figure 6.8	Intrinsic speed of components, $\beta$ , and viewing angle, $\theta$ , constrained by the observed apparent speed, $\beta_{\text{app}}$ , and the jet-to-counter-jet ratio, $R$ . Shown are the regions of valid $\beta$ and $\theta$ combinations according to highest and lowest observed $\beta_{\text{app}}$ , 6.9 and 0.93, respectively. A further constraint is set by $R$ , measured from the map and required $R_{\text{req}}$ , in order for the Doppler factor to be real-valued. The most stringent constraints are set by the highest apparent speed and jet-to-counter-jet ratio, limiting the region of possible $\beta$ and $\theta$ combinations to the red shaded area. . . . .	144
Figure A.1	Light curves of individual components (left panels) and the core (right panels) at 15, 43, and 86 GHz, from top to bottom, respectively. Component C1 at 15 GHz shows significant variability between 2008 and 2010. Component C3 at 43 and 86 GHz is at its decaying flux density phase. . . . .	157

LIST OF TABLES

---

Table 3.1	Telescopes participating in the GMVA. . . . .	40
Table 4.1	Summary of the 6 observing epochs of PKS 1502+106 at 43 GHz. Data from dedicated GMVA observing sessions. Station designations: VLBA <sub>8</sub> = Br – Fd – Kp – La – Mk – NI – Ov – Pt; <sup>(1)</sup> Peak flux density, off-source rms noise level and total flux density of all MODELFIT components. <sup>(2)</sup> Major and minor axes along with the position angle of the restoring beam. All parameters listed in the table correspond to the final, uniform weighted untapered, MODELFIT image. . . . .	51
Table 4.2	Summary of the 6 observing epochs of PKS 1502+106 at 86 GHz. Data from dedicated GMVA observing sessions. Station designations: VLBA <sub>8</sub> = Br – Fd – Kp – La – Mk – NI – Ov – Pt; Ef – Effelsberg; Mh – Metsähovi; On – Onsala; Pb – Plateau de Bure; Pv – Pico Veleta; Ys – Yebes; <sup>(1)</sup> Peak flux density, off-source rms noise level and total flux density of all components. <sup>(2)</sup> Major and minor axes along with the position angle of the restoring beam. All parameters listed in the table correspond to the final, untapered, uniform weighted, MODELFIT image. . . . .	52
Table 4.3	Summary of the 19 observing epochs at 15 GHz of PKS 1502+106 obtained within the MOJAVE monitoring program. VLBA <sub>10</sub> station designations: Br – Brewster; Fd – Fort Davis; Hn – Hancock; Kp – Kitt Peak; La – Los Alamos; Mk – Mauna Kea; NI – North Liberty; Ov – Owens Valley; Pt – Pie Town; Sc – St. Croix. <sup>(1)</sup> Peak flux density, off-source rms noise level and total flux density of all components. <sup>(2)</sup> Major and minor axes along with the position angle of the restoring beam. All parameters listed in the table correspond to the final, uniform weighted, untapered, MODELFIT image. . . . .	53
Table 4.7	Mean spectral indices for components C1, C2, C3 and the core as obtained by SSA fitting for C1 and a single power-law fit for C2, C3, and the core. . . . .	68

Table 4.8	Physical parameters estimated using causality arguments and observed variability. Columns from left to right: (1) knot designation; (2) elapsed time between maximum and minimum flux density; (3) effective size; (4) variability time scale; (5) Doppler factor; (6) Lorentz factor and (7) viewing angle. . . . .	69
Table 4.9	Apparent and intrinsic jet opening angles deduced from individual MODELFIT components. Columns from left to right: (1) knot designation; (2) number of epochs used for the calculation where the component is resolved; (3) mean separation from the core; (4) critical viewing angle from the component's speed; (5) mean apparent opening angle and (6) intrinsic opening angle. .	72
Table 4.10	Estimated physical parameters for knot C1 and the VLBI core. Columns from left to right: (1) Designation; (2) turnover frequency; (3) turnover flux density; (4) measured size; (5) equipartition critical size; (6) SSA magnetic field; (7) minimum equipartition magnetic field and (8) Doppler factor. . . . .	75
Table 5.1	F-GAMMA program facilities and spectral coverage. . . . .	87
Table 5.2	Calibrator flux densities in Jy, used for the calibration of Effelsberg 100-m and IRAM 30-m F-GAMMA data. The flux density of NGC 7027 is corrected for extended structure, compared to the telescope's primary beam at $\nu > 10.45$ GHz. The table combines values from <a href="#">Angelakis et al. [2015]</a> and <a href="#">Nestoras et al. [in prep.]</a> ; see also references therein. . . . .	89
Table 5.3	The mean fractional impact of each correction step taken, on radio data from the Effelsberg 100-m and IRAM 30-m telescopes. Table adopted from <a href="#">Angelakis et al. [2015]</a> . . . . .	90
Table 5.4	Fit results from exponential flare decomposition. . . . .	97
Table 5.5	Gaussian process regression results after subtracting the minimum flux of the light curve. Columns from left to right: (1) observing frequency; (2) the minimum flux density subtracted prior to the fit; (3) obtained flare amplitude; (4) obtained time of flare maximum; (5) obtained flare rising and (6) decay time. . . . .	102
Table 5.6	Cumulative table containing time lag results from all methods with respect to data at 142.33 GHz. OVRO 15 GHz data come without $\tau_{\text{DCCF}}$ uncertainty since the light curve was used as the initial reference for the DCCF analysis. Columns from left to right: (1) observing frequency; (2) frequency-dependent lime lag from exponential flare decomposition, (3) from Gaussian process regression, and (4) from the DCCF analysis. . . . .	112
Table 5.7	Frequency-dependent "time-lag core shifts" obtained through the flare timing analysis. Time lags are averaged per frequency between $\tau_{\text{GP}}$ and $\tau_{\text{DCCF}}$ . Values are reported without error. All time lags are referenced to the highest well-sampled frequency of 142.33 GHz. Columns from left to right: (1) observing frequency; (2) average time lag between $\tau_{\text{GP}}$ and $\tau_{\text{DCCF}}$ ; (3) the angular offset in units of mas ( $\Delta r = \mu\tau$ ); (4) time-lag-based core position offset; (5) core distance to the vertex of the jet. . .	116
Table 5.8	Equipartition magnetic field strength calculated through time lags and subsequent time-lag core shifts. Values are based on average $\tau$ and are reported without error. Columns from left to right: (1) observing frequency; (2) average time lag between $\tau_{\text{GP}}$ and $\tau_{\text{DCCF}}$ ; (3) magnetic field strength at a distance of 1 pc from the core; (4) core magnetic field strength. . . . .	118

Table 6.1	The seven $\gamma$ -ray-detected RLNLS1 galaxies and their physical characteristics. Columns from left to right: (1) source name under the J2000 designation; (2) redshift; (3) radiative, (4) kinetic, and (5) total jet powers; and finally (6) estimated mass of their SMBH. <b>References:</b> <sup>†</sup> Angelakis et al. [2015]; <sup>‡</sup> Foschini et al. [2015]. . . . .	130
Table 6.2	Summary of the 8 observing epochs at 15 GHz of 1H 0323+342 obtained within the MOJAVE monitoring program. Columns from left to right: (1) date of observation; (2) array elements; (3) peak flux density; (4) RMS noise level; (5) total flux density of components in the MODELFIT image; (6) major and (7) minor axes along with the (8) position angle of the restoring beam. All parameters listed in the table correspond to the final, untapered, uniform-weighted MODELFIT image. VLBA <sub>10</sub> station designations: BR – Brewster; FD – Fort Davis; HN – Hancock; KP – Kitt Peak; LA – Los Alamos; MK – Mauna Kea; NL – North Liberty; OV – Owens Valley; PT – Pie Town; SC – St. Croix. . . . .	133
Table 6.3	Kinematical parameters of all VLBI components of 1H 0323+342. Columns from left to right: (1) knot designation; (2) proper motion in $\text{mas y}^{-1}$ ; (3) Apparent velocity in units of $c$ ; (4) time of zero core separation—i.e. time of component ejection. . . . .	141
Table 6.4	Findings of the single-dish analysis of Angelakis et al. [2015]. Columns from left to right: (1) source name under the J2000 designation; (2) observing frequency; (3) variability brightness temperature and (4) variability Doppler factor. . . . .	146
Table 6.5	Average brightness temperature of components deduced from VLBI. The mean size of components across the 8 observing epochs is used. . . . .	148
Table 6.6	Table of inferred physical parameters. The left column contains measured quantities used in each calculation, leading to the values in the right column. The table is divided in three parts that, from top to bottom, contain the results obtained with the use of VLBI data only, the critical values for the Lorentz factor (minimum value) and the viewing angle, and finally, results obtained through the combination of VLBI and filled-aperture monitoring data. . . . .	149
Table B.1	MODELFIT results 15 GHz. Columns from left to right: (1) observing epoch in fractional year; (2) MJD of the observing epoch; (3) epoch identifier between 1–19; (4) integrated component flux density; (5) radial separation from the core; (6) position angle; (7) component size given as the FWHM of the major axis; (8) component identification label. . . . .	159
Table B.1	continued. . . . .	160
Table B.1	continued. . . . .	161
Table B.2	MODELFIT results at 43 GHz. Columns from left to right: (1) observing epoch in fractional year; (2) MJD of the observing epoch; (3) epoch identifier between 1–6; (4) integrated component flux density; (5) radial separation from the core; (6) position angle; (7) component size given as the FWHM of the major axis; (8) component identification label. . . . .	162



Table B.3	MODELFIT results at 86 GHz. Columns from left to right: (1) observing epoch in fractional year; (2) MJD of the observing epoch; (3) epoch identifier between 1–6; (4) integrated component flux density; (5) radial separation from the core; (6) position angle; (7) component size given as the FWHM of the major axis; (8) component identification label. . . . .	163
Table C.1	1H 0323+342 MODELFIT results at 15 GHz. Columns from left to right: (1) observing epoch in fractional year; (2) integrated component flux density; (3) radial separation from the core; (4) position angle; (5) component size given as the FWHM of the major axis; (6) component identification label. C denotes the core, S the quasi-stationary component and C# the rest of the moving features. . . . .	165
Table C.1	continued. . . . .	166



## A GALAXY AND ITS JET

---

### 1.1 INTRODUCTION

Active Galactic Nuclei (AGN) are the most powerful, persistent emitters of radiation in the Universe. They are—most probably—powered by accretion of matter onto *supermassive black holes* (SMBHs). Those are believed to reside in the centers of most galaxies, including ours—the Milky Way. Their masses in the range  $10^6$ – $10^{10} M_{\odot}$ , make SMBHs the most exotic compact objects known.

AGN come in very many different flavors. Some feature double, opposite-directed and highly-energetic fast plasma outflows, likely driven by the conversion of gravitational potential energy to electromagnetic, while others lack such jets. The common characteristic among all though, is the huge luminosities they possess able to outshine their entire host galaxy. This huge energy output is mostly attributed to non-thermal processes in the sense that emitted light does not come from processes such as nuclear fusion that powers the stellar population of their hosts.

### 1.2 THE DISCOVERY OF ACTIVE GALAXIES

In the last third of the 18th century Charles Messier started cataloging diffuse nebulae in the night sky that were clearly not stars. By the end of the 19th century a great deal of work had been done in deep sky surveys with the publication of the New General Catalog (NGC) and its supplement the Index Catalog (IC), a few years later. These catalogs contained thousands of diffuse nebulae whose nature and distance were, at that time, completely unknown. However, spectroscopic data were available and most of these nebulae were characterized by absorption lines in their optical spectra. It is now known that those lines are produced by the stellar population of normal galaxies.

[Fath \[1909\]](#) made a landmark observation by finding emission lines from the nucleus of NGC 1068 (M77). These lines originate from the atomic transitions of the circumnuclear material of the galaxy. A few years later, [Slipher \[1917\]](#) demonstrated these lines to be very broad, suggesting fast motions in the nucleus of NGC 1068. Velocities of up to  $3600 \text{ km s}^{-1}$  were measured in his spectroscopic observations. Even higher velocities were measured for NGC 4151 by [Campbell and Moore \[1918\]](#). Here, velocities up to  $7500 \text{ km s}^{-1}$  were observed. In 1918 Heber D. Curtis got the first glimpse of a jet through an underexposed photographic plate of M87. This would be the first and for many years only optical jet.

[Seyfert \[1943\]](#) concluded that these nebulae showing broad emission lines and uncommonly bright nuclei constitute a separate class of objects. Much later, [Khachikyan and Weedman \[1971\]](#) came to the conclusion that there exist two distinct classes of so-called Seyfert galaxies—those of Type 1 and those of Type 2. Both Seyfert types have bright narrow emission lines, such as [O III] or [Ne V],

but Seyfert 1 spectra feature significantly broader permitted transition lines than lines from forbidden transitions. Type 2 spectra are characterized by the equally narrow permitted and forbidden transition lines. Later, intermediate Seyfert types were recognized [Seyfert 1.5 to 1.9; e.g. Goodrich, 1989] based on the presence of both narrow and broad hydrogen Balmer lines.

Observational data lend support to the following scenario. The nucleus of these galaxies is a compact, high-luminosity ( $\sim 10^{43}$ – $10^{48}$  erg s $^{-1}$ ), and mass ( $\sim 10^6$ – $10^{10}$   $M_{\odot}$ ) volume ionizing the surrounding material, thus giving rise to emission lines in their spectra, mainly due to hydrogen recombination. The emission line width is due to the high velocity of the material. In the volume around the nucleus of those systems there exist two ionized gas regions—the narrow- and the broad-line region. The narrow-line region (NLR) is believed to be at a distance of  $\sim 100$ – $1000$  pc away from the central engine. It is characterized by velocities of a few hundred kilometers per second and low ambient density. This is where—due to the low density environment—the narrow forbidden lines originate. Much closer to the central engine, typically  $\lesssim 1$  pc, is the region giving rise to the broad emission lines (the BLR). There, velocities are much higher due to the proximity to the supermassive compact object. Typical velocities reach a small fraction of the speed of light and it is the higher density environment and frequent collisions that de-excite atoms and inhibit the generation of forbidden lines. Seyfert 2 objects are either deprived of the BLR or it is much less prominent, being somehow obscured.

### 1.3 DISCOVERIES AT RADIO WAVELENGTHS

After the discovery of radio emission from the center of the Milky Way galaxy by Jansky [1933] and with the advent of radio engineering and technology, it became clear that radio sources are found scattered all over the sky. The new science of radio astronomy was about to be born in the 1950s and surveys of the radio sky were under way. One of the surveys performed in Cambridge, UK yielded the Revised Third Cambridge Catalog (3CR) of radio sources [Bennett, 1962]. It contained all sources of radio emission with flux densities  $\geq 9$  Jy and a limiting declination of  $\geq -5^{\circ}$ , at 178 MHz. Some 328 sources with their positions, luminosities, and distances were contained in 3CR.

Based on the complete sample of the 3CR catalog, Fanaroff and Riley [1974] found a correlation between the luminosity of these sources and their morphological characteristics—i.e. the relative positions of high and low surface brightness features, in interferometric data at 1.4 or 5 GHz. Almost all sources were found to fall into two luminosity classes with a sharp dividing line at about  $10^{41}$  erg s $^{-1}$ . Less luminous sources appeared to have complex morphology with the bulk of their radio emission originating in regions close to the optical counterpart (FRI sources). Powerful radio sources appeared to have simpler structure with straight, double jets ending in two prominent lobes on either side of them. In those, so-called FR II sources, most radio emission was seen to be coming from the central nucleus and also from the lobes. It is currently believed that FRI sources, being less powerful, are unable to efficiently punch through the interstellar and later on intergalactic medium of their hosts, and prone to

interaction with it, produce the edge-brightened, often disrupted radio jet structures observed in contrast to the powerful FR IIs featuring long, straight jets.

#### 1.4 THE FIRST QUASARS

While Seyferts exhibit nuclear luminosity comparable to that of the stellar population of the host galaxy, quasars outshine the host by a factor of hundreds, rendering it invisible.

The first surveys of the radio sky could identify the strongest sources with objects emitting in the optical band. Those were usually galaxies but more often than not radio sources were identified with peculiar star-like objects. 3C 48 was the first source to be identified with a stellar-appearing object of 16th magnitude, based on observations with a two-element interferometer [Matthews and Sandage, 1963] (see Chapter 2 for details on interferometry). The term *quasar* an abbreviation of "quasi-stellar radio source" was coined in the 1960s to name these peculiar sources. It is indicative of the—then—unknown nature of those luminous star-like objects.

Another radio source identified with an optical, star-like counterpart was 3C 273 [Hazard et al., 1963]. This "radio-star" was characterized by an unusual optical spectrum featuring broad emission lines of unidentified elements. The mystery was finally solved by Schmidt [1963], who identified the strange emission lines as shifted hydrogen lines. The whole spectrum was red-shifted by 15.8%; i.e. 3C 273 was moving away from the observers on Earth with a velocity of ~16% of the speed of light. This discovery led to the determination of even higher redshifts for other radio sources [Schmidt, 1965]; e.g. 3C 48 with  $z = 0.367$ , where  $z$  is given by

$$z = \frac{\lambda - \lambda_0}{\lambda_0} = \frac{\lambda}{\lambda_0} - 1 \quad (1-1)$$

Here  $\lambda$  is the observed, cosmologically-redshifted wavelength while  $\lambda_0$  is the lab wavelength. Being at such cosmological distances and with their apparent magnitude and radio brightness, quasars were characterized by extremely high absolute optical and radio luminosities in addition to their rapid variability with time scales which implied very small emission regions.

#### 1.5 UNIFICATION OF ACTIVE GALAXIES

Active galaxies can be divided into two broad categories: Seyfert galaxies and quasars (see Fig. 1.1). From the point of view of radio activity, quasars can be subdivided into radio-loud and radio-quiet, accounting for ~10% and ~90% of the total population, respectively. Radio-loud AGN are those characterized by  $R > 10$  with

$$R \equiv \frac{S_{5\text{GHz}}}{S_B} \quad (1-2)$$

where  $S_{5\text{GHz}}$  and  $S_B$  are the flux densities at 5 GHz and optical B band [Kellermann et al., 1989].

In attempting to unify the large variety of active galaxies, a number of schemes have been proposed. Their common underlying principle is the attempt to attribute the full palette of observational properties, to only a small number of intrinsic parameters.

Such an example is the realization of [Blandford and Königl \[1979\]](#) that compact and extended radio sources are the same class of objects, only seen at different angles,  $\theta$ , between their jet axis and our line of sight. Compact radio sources were directed at a small, while extended lobe-dominated ones, at large  $\theta$ .

The next milestone was the unification of all Seyfert types, again by orientation, by [Antonucci and Miller \[1985\]](#). Using spectropolarimetry, they have determined that most observational properties of Seyfert galaxies could be explained if they were harboring a typical active nucleus, surrounded by a dusty torus, obscuring the BLR. Depending again on  $\theta$ , looking face-on the central region, we are able to discern the spectral features, namely the broad emission lines that arise from the BLR. Looking instead the galaxy edge-on, the torus is blocking the view of BLR clouds and only the NLR, residing at larger distances, is visible (see Fig. 1.2).

Radio-loud AGN can also be unified by orientation. *Flat-spectrum radio quasars* (FSRQ) are the same class of objects as FR II radio galaxies only closely oriented to our line of sight [[Barthel, 1994](#)] and *BL Lacs* are those FRIs viewed at small  $\theta$  [[Urry and Padovani, 1994](#)]. These schemes apart from the obscuring torus invoke relativistic effects as well, to account for the characteristics of powerful *blazars*, a term coined to collectively refer to the beamed population of radio-loud AGN—i.e. FSRQs and BL Lacs (see Section 1.8). For a review on AGN unification schemes refer to [Urry and Padovani \[1995\]](#).

## 1.6 BUILDING BLOCKS OF AGN

The constituents of active galactic nuclei are discussed here. In Fig. 1.3 a sketch of the building blocks of an AGN is shown in order of increasing distance from the central SMBH.

### 1.6.1 *The supermassive black hole*

Let us begin with the “prime mover”—a supermassive black hole (SMBH). It resides at the center of the system setting it in motion. Its immense gravitational pull drags material from its environs that, through an accretion flow, reaches the innermost stable circular orbit (ISCO) and either crosses the black hole’s event horizon or is somehow channeled along the polar axis of the SMBH, fueling the dipolar stream of plasma known as the jet.

### 1.6.2 *Accretion disk*

Accretion flows are known to exist around astrophysical objects of all scales. In the case of AGN, the central gravitational potential causes the material to settle down in a disk configuration with an extent of  $\sim 10^{-3}$ – $10^{-2}$  pc. From there, material spirals inward towards the central gravitating body, in a viscous flow

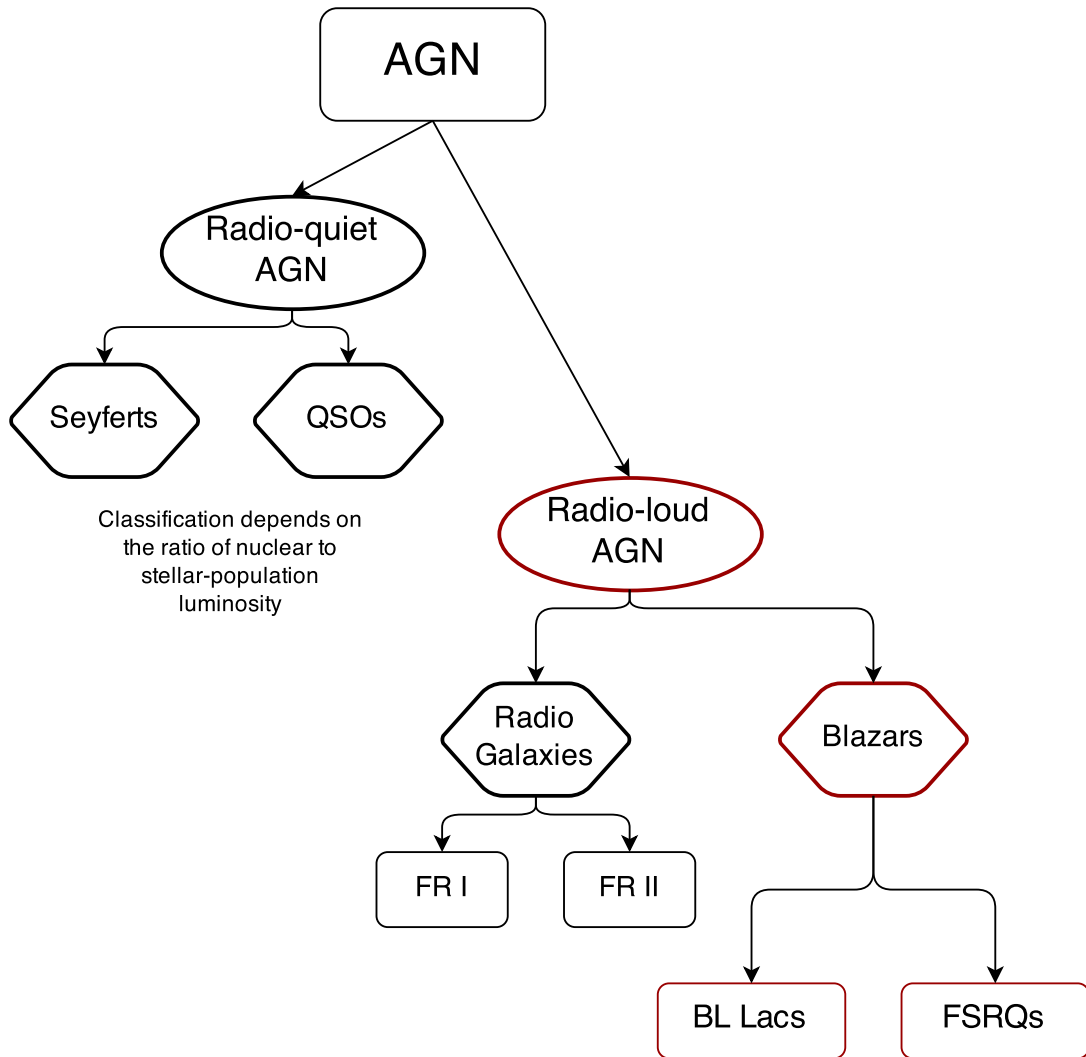


Figure 1.1: Classification of AGN depending on their radio-loudness.

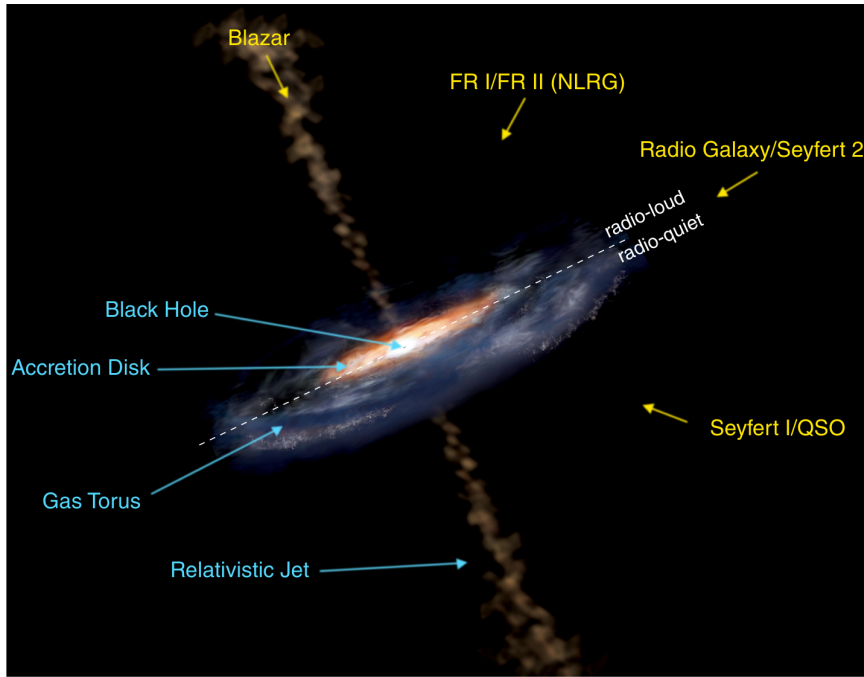


Figure 1.2: AGN unification by orientation. Image credit: NASA/Aurore Simonnet, Sonoma State University.

of increasing temperature, while radiating electromagnetic radiation. Typically, AGN accretion disks emit a large amount of energy as ultra-violet (UV) and X-ray photons, a spectral feature commonly referred to as the “big blue bump”. In the context of certain models, accretion disk radiation can play a significant role in the production of GeV/TeV emission observed from AGN. They can offer a dense reservoir of seed photons for the inverse Compton process to take place (see Section 1.9.2).

### 1.6.3 Broad-line region

Further outwards, below and above the accretion disk at typical distances of 0.01–1 pc there exists a high-density region with electron number density  $n_e \gtrsim 10^9 \text{ cm}^{-3}$ . It is an ensemble of clouds rotating fast within the gravitational potential of the SMBH, with typical speeds in the range 1 000–25 000  $\text{km s}^{-1}$ . Matter gets photoionized due to extensive absorption and reprocessing of accretion disk radiation, resulting also in an ambient temperature of  $T \sim 10^4\text{--}10^5 \text{ K}$  [Peterson, 1997]. The mass contained within the BLR is typically  $\sim 10^3\text{--}10^4 M_\odot$  and as the name suggests, this region is responsible for the production of the Doppler-broadened lines, in the optical spectra of AGN. The size of the BLR has been found to scale with luminosity roughly as

$$R_{\text{BLR}} \propto L^{1/2}. \quad (1-3)$$

The BLR can also provide a potential reservoir for target photons available for inverse Compton up-scattering to high energies (see Section 1.9.2).



#### 1.6.4 *Molecular torus*

The presence of a molecular, geometrically thick, obscuring torus was first invoked in unification schemes by viewing angle. Today, its presence is unambiguous since direct imaging of AGN tori has been achieved [e.g. Jaffe et al., 1993, 1996]. These clumpy, dusty structures at distances between an inner radius of  $\sim 1\text{--}10$  pc and total extent of the order of some hundred parsecs emit mainly at infra-red (IR) wavelengths due to absorption and re-emission as thermal black bodies; i.e. the dust component of such tori is heated by accretion disk optical/UV radiation to temperatures of  $\sim 100\text{--}1000$  K and subsequently re-emits at IR bands. Apart from obscuring the BLR and eventually the nuclear region, they feed material to the inner accretion disk through viscous transport of angular momentum.

#### 1.6.5 *Narrow-line region*

The narrow line region at  $100\text{--}1000$  pc away from the SMBH, is a region or an ensemble of low-density gas clumps ( $n_e \sim 10^3\text{--}10^5 \text{ cm}^{-3}$ ). They follow trajectories of much lower velocity  $< 500 \text{ km s}^{-1}$  and contribute the narrow, forbidden spectral lines in the observed optical spectra. The total mass content is of the order of  $10^6 M_\odot$ .

#### 1.6.6 *The relativistic jet*

The common feature of all radio-loud AGN is the presence of a fast relativistic outflow. Jets are an efficient way of dumping angular momentum and can extend up to several Mpc. Plasma is accelerated within it, reaching speeds very close to that of light. Perturbations injected through the jet nozzle propagate downstream through the steady-state flow and can create shocks, traveling, standing and even backwards moving (trailing shocks). Particles crossing those shocks gain kinetic energy through stochastic acceleration. Finally, the jet terminates when its kinetic energy equals that of the ambient intergalactic medium (IGM) and a termination shock is formed, seen at radio wavelengths as one or two radio lobes at the opposite ends of the jet.

### 1.7 OBSERVATIONAL PROPERTIES OF ASTROPHYSICAL JETS FROM BLACK HOLES

The majority of relativistic jets ought to be symmetric; i.e. they must be born as dipolar outflows. It is an observational fact though, that many jets we are able to directly image appear to be single-sided. A counter-jet is missing. Unification by orientation has solved this paradox by introducing relativistic and geometrical effects that alter the appearance of radio galaxies and "turn" them into blazars, as  $\theta$  decreases.

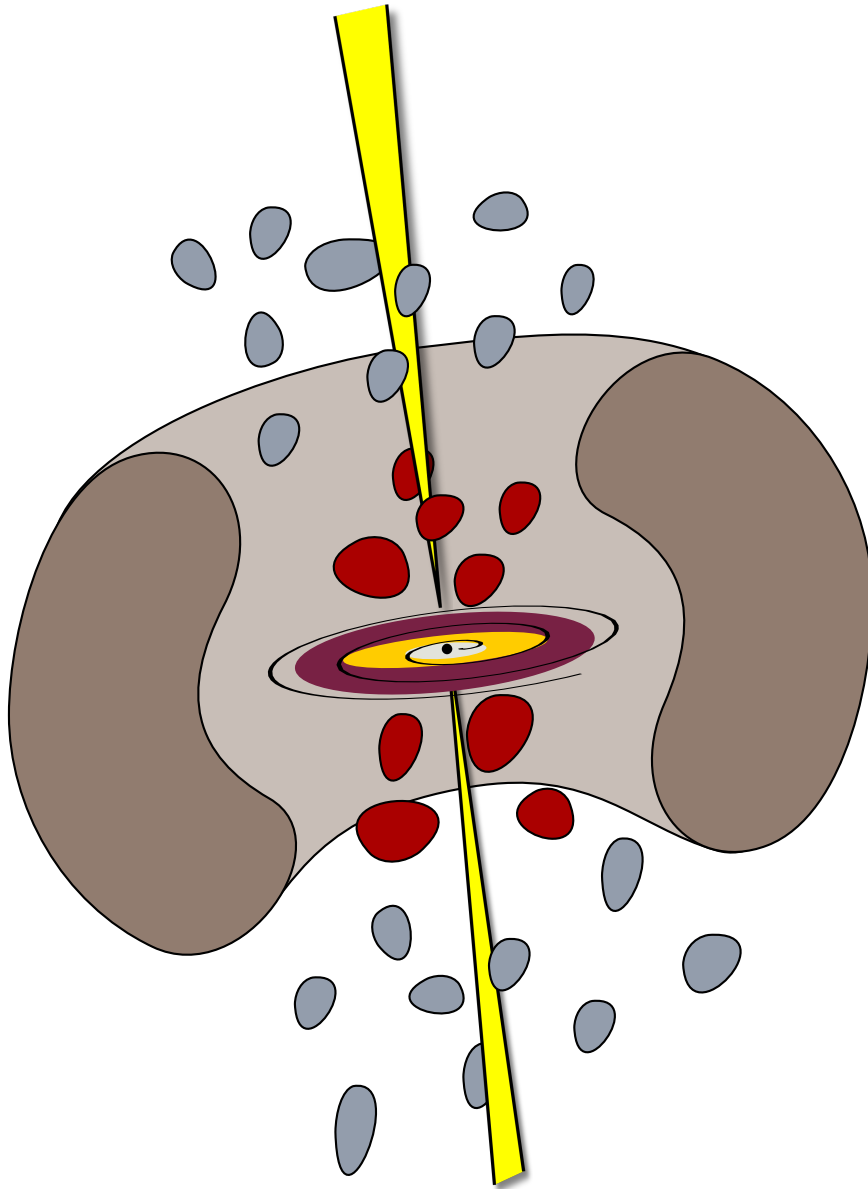


Figure 1.3: The building blocks of an active galactic nucleus. Shown in colors are: (black) the supermassive black hole at the center; (from purple to white) the accretion disk; (red) clouds of the broad-line region (BLR); (light gray and cut in darker shade) the obscuring molecular torus surrounding the system; (light blue) clouds of the narrow-line region (NLR); (bright yellow) the relativistic jet. The sketch is not to scale. For details refer to Section 1.6.

### 1.7.1 *Relativistic beaming*

If the plasma flow constituting the jet is approaching us at a highly relativistic speed and very close to our line of sight, then the extreme brightness and consequently high suppression of the receding jets' brightness can be explained as a phenomenon referred to as Doppler beaming. Under these conditions the radiation emitted by an emission element within the flow is not isotropic, but rather concentrated in a small cone with opening angle

$$\alpha = \frac{1}{\gamma} \quad (1-4)$$

in the direction of motion, where  $\gamma$  corresponds to the bulk Lorentz factor of the element.

The Lorentz factor is a more appropriate measure of the intrinsic velocity of emission elements, since the latter can reach very high values, close to—but never exceeding—the speed of light,  $c$ . The Lorentz factor is defined as

$$\gamma = \frac{1}{\sqrt{1 - \beta^2}} \quad (1-5)$$

with  $\beta = v/c$  and  $v$  the intrinsic linear velocity of the emission element.

Relativistic effects, such as beaming, introduce differences between observed and intrinsic properties. Through our observations we are only able to see apparent luminosities, jet speeds and brightness temperatures that are related to the intrinsic ones—in the emission element's rest frame—through a parameter referred to as Doppler factor. This is defined as

$$\delta = \gamma^{-1} (1 - \beta \cos \theta)^{-1}. \quad (1-6)$$

### 1.7.2 *Apparent luminosity*

The difference between the frequency a photon was emitted at (in the source's rest frame) and the frequency it is observed here on Earth is given by

$$\nu_{\text{obs}} = \delta \nu_{\text{int}}. \quad (1-7)$$

Flux densities in the two frames are related through

$$S_{\text{obs}} = \delta^{n-\alpha} S_{\text{int}}. \quad (1-8)$$

Observed and intrinsic luminosities of AGN are related through

$$L_{\text{obs}} = \delta^{n-\alpha} L_{\text{int}} \quad (1-9)$$

with  $\alpha$  the spectral index of the optically thin part of the emission and  $n$  being in the range 2–3; 2 refers to a continuous and 3 to a blobby jet [Scheuer and Readhead, 1979].

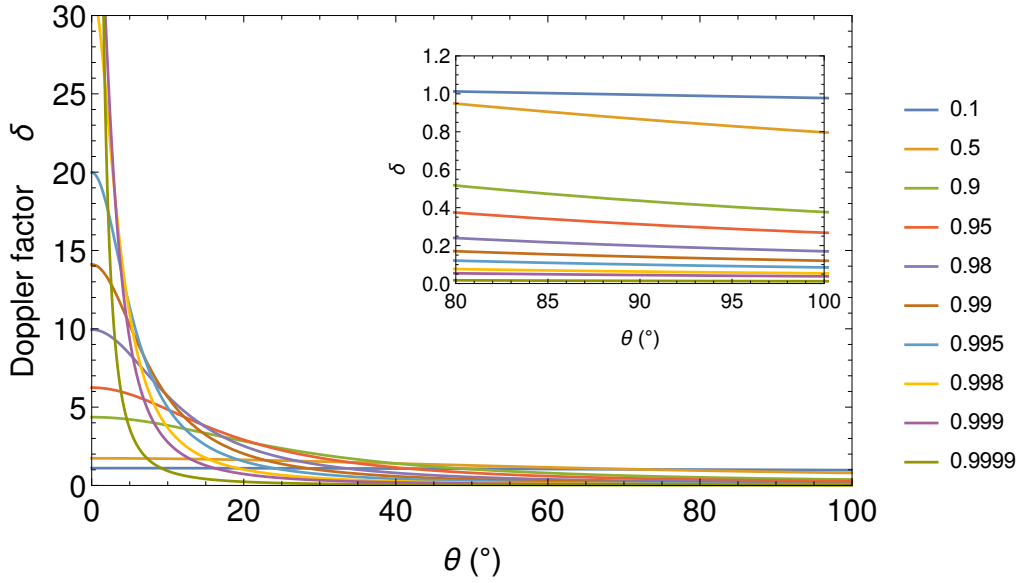


Figure 1.4: Dependence of the Doppler boosting factor on viewing angle for the given range of intrinsic speeds,  $\beta$ , between 0.1 and 0.9999. Inset: Note the deboosting ( $\delta < 1$ ) that occurs for large viewing angles, even close to the plane of the sky, and for high flow speeds.

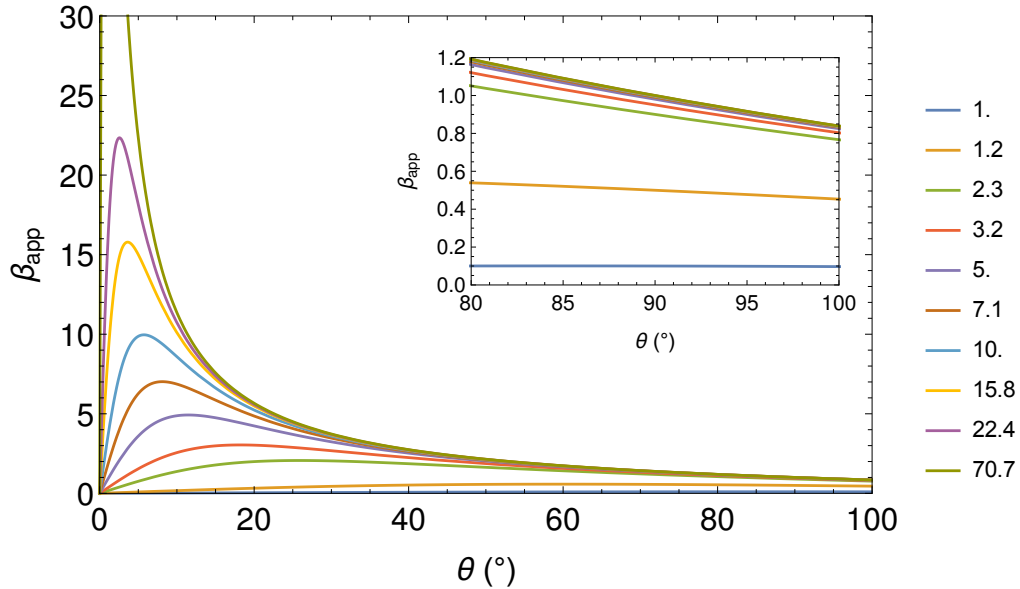


Figure 1.5: Dependence of the observed apparent velocity,  $\beta_{app}$ , on viewing angle for the same range of intrinsic velocities as in Fig. 1.4 only here expressed as the equivalent Lorentz factor.

It is worth noting that as seen in the inset of Fig. 1.4, which shows the dependence of the Doppler factor on viewing angle for a given range of intrinsic flow speeds, the effect of de-beaming or Doppler de-boosting takes place even at large viewing angles, given sufficiently fast intrinsic motion. Even at  $80^\circ$ , for intrinsic speeds above  $0.5c$ , de-boosting is at work; i.e. the Doppler factor is less than unity. This is due to the concentration of radiation into the narrow emission cone. The higher the Lorentz factor, the narrower the cone is, so for large viewing angles, our line of sight could be completely out of the emission cone rendering radiation invisible; e.g. even radio galaxies (typically  $\theta > 30^\circ$ ) are de-beamed for intrinsic speeds  $\beta \gtrsim 0.5$ .

### 1.7.3 Eddington luminosity and limiting mass-accretion rate

The *Eddington luminosity* is the limiting value for the luminosity of a gravitating body, above which radiation pressure is stronger than its gravitational pull and the system is naturally disrupted. Under the assumptions of spherical symmetry within a highly ionized environment of mostly hydrogen, where the mass is dominated by protons while electrons mainly contribute to opacity, the Eddington luminosity is given by

$$L_{\text{Edd}} = \frac{4\pi cGMm_p}{\sigma_T}. \quad (1-10)$$

Here,  $M$  is the mass,  $m_p$  the proton mass, and  $\sigma_T$  the Thomson cross-section. Note that the Eddington luminosity only depends on the object's mass.

An *Eddington accretion rate*,  $\dot{M}_{\text{Edd}}$ , can be inferred from  $L_{\text{Edd}}$  and is the mass accretion rate when a gravitating body emits at its Eddington luminosity limit. It is given by

$$\dot{M}_{\text{Edd}} = \frac{L_{\text{Edd}}}{\epsilon c^2}. \quad (1-11)$$

The radiative efficiency,  $\epsilon$ , is usually assumed to be  $\epsilon \sim 0.1$ .

### 1.7.4 Brightness temperature

The specific intensity,  $I_\nu$ —i.e. intensity per differential frequency element—for a black body in thermal equilibrium with its surroundings is given by Planck's law as

$$I_\nu = \frac{2h\nu^3}{c^2} \frac{1}{e^{\frac{h\nu}{k_B T}} - 1}. \quad (1-12)$$

In radio astronomical applications since  $h\nu \ll kT$ , Planck's law can be approximated through the expansion of the exponential term with the use of

$$e^x = 1 + x + \frac{x^2}{2!} + \dots \quad (1-13)$$

yielding

$$B_{\nu}(T) = \frac{2\nu^2 k_B T}{c^2}, \quad (1-14)$$

commonly referred to as the Rayleigh–Jeans approximation.

As a result, given a certain flux density level and size we are able to infer the temperature of an emitting region even if the process is non-thermal. This is a virtual temperature—not connected to the kinetic energy of its constituents—that the region would be characterized by, if radiating as a black body. The extremely high observed brightness temperatures measured in relativistic jets lead to the conclusion that the processes involved are of non-thermal nature.

Observed and intrinsic brightness temperatures are connected through

$$T_{b,obs} = \delta T_{b,int}. \quad (1-15)$$

Thus, using measured brightness temperatures and limiting values suggested on the basis of physical arguments [Kellermann and Pauliny-Toth, 1969; Readhead, 1994], one can deduce estimates for the Doppler factor by attributing the excess of  $T_b$ , above theoretical limits, purely to Doppler boosting.

#### 1.7.5 Superluminal motion

This is a purely geometric effect, first suggested by Rees [1966] and later observed [Gubbay et al., 1969; Cohen et al., 1971; Whitney et al., 1971; Cohen et al., 1977] (cf. Porcas [1983] for a short review). It comes about simply because while measuring the distance an emission element has traveled, in deducing its speed, we divide by the wrong elapsed time. That is an apparent time interval due to the fact that a knot traveling at an intrinsic speed close to the speed of light, catches up with its own radiation, emitted in a preceding time. Let us imagine the situation depicted in Fig. 1.6. Consider a knot traveling with intrinsic velocity  $u$  and emitting a packet of radiation at position A and time  $t = 0$ . Within a time interval  $dt$ , the knot has reached its next position (B) where it re-emits a second radiation packet. The first wavefront needs time

$$t_1 = \frac{D}{c} + \frac{u \cos \theta dt}{c} \quad (1-16)$$

to reach the observer. Here,  $D$  denotes the distance between the observer and knot position B. Radiation from position B takes time

$$t_2 = dt + \frac{D}{c} \quad (1-17)$$

to reach the observer. Consequently, what we measure as the time interval between the two times of arrival of the two waves is

$$\Delta t = t_2 - t_1 = dt - \frac{u}{c} \cos \theta dt = (1 - \beta \cos \theta) dt \quad (1-18)$$

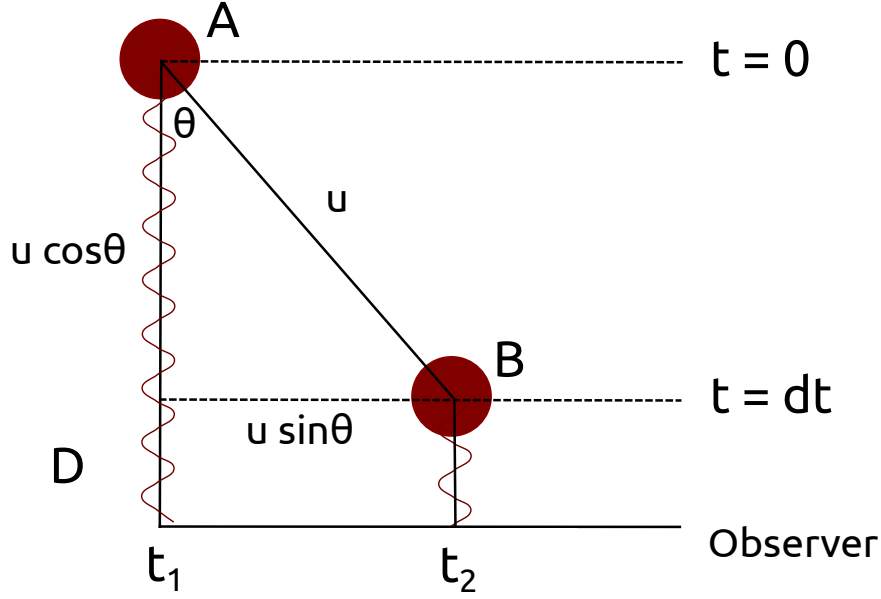


Figure 1.6: Geometry of superluminal motion.

By dividing the projected distance between the two positions,

$$\frac{u}{c} \sin \theta dt \quad \text{or} \quad \beta \sin \theta dt, \quad (1-19)$$

with the apparent time interval  $\Delta t$  we obtain an apparent expansion speed of

$$\beta_{\text{app}} = \frac{\beta \sin \theta}{1 - \beta \cos \theta}. \quad (1-20)$$

In many cases  $\beta_{\text{app}}$  is found to exceed the speed of light  $c$ —i.e. *superluminal motion* is observed. However, this is only an illusion.

## 1.8 BLAZAR PROPERTIES

Blazars constituting the beamed population of radio-loud AGN, represent the most extreme manifestation of active galaxies. The two classes of objects comprising the family of blazars are the FSRQs and the BL Lacs and the dividing line is drawn according to their power, with FSRQs being the powerful sub-class (see Fig. 1.1). Their extreme phenomenology includes fast superluminal motion, observed both at parsec and sub-parsec scales, high degree of radio and optical polarization, rapid broadband flux density, and polarization variability with time scales down to minutes.

The most intriguing aspect of blazars is their intense variability and a large collection of models have been proposed in order to explain it. These are under scrutiny today since the exact mechanisms giving rise to the blazar phenomenon are to date not fully understood. Shocks that are generated and travel downstream the relativistic jet are one possibility [e.g. Marscher and Gear, 1985; Valtaoja et al., 1992; Türler et al., 2000]. At the shocked region acceleration of particles can take place, leading them to relativistic energies and beamed emission of radiation. Shells of plasma colliding with each other due to differential veloc-

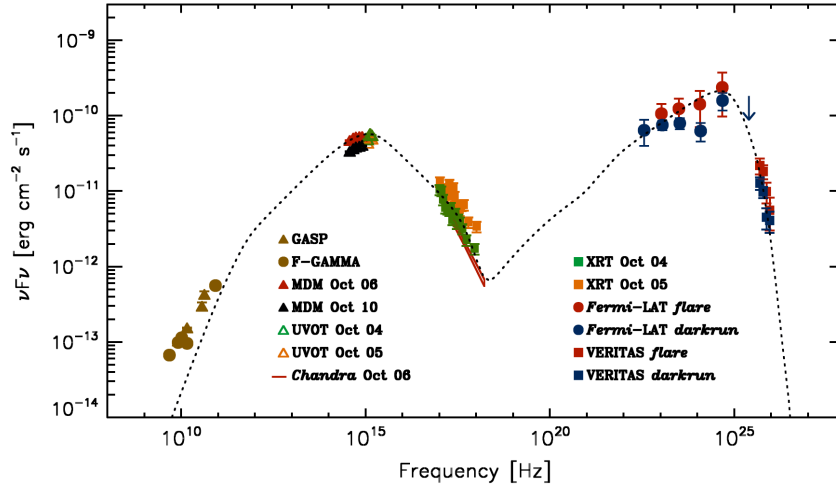


Figure 1.7: Broadband SED of the blazar 3C 66A during a multi-wavelength observing campaign. The fit corresponds to an EC+SSC model (see text). Data contributed from different programs and instruments are shown. Image from [Abdo et al. \[2011\]](#).

ities in the flow are also possible [e.g. [Spada et al., 2001](#)]. In addition to those, geometrical models have been proposed that attribute variability to differential Doppler boosting [due to e.g. precession; [Camenzind and Krockenberger, 1992](#)] and also models attributing observed temporal variations of flux density and structure to instabilities growing in the jet [e.g. [Lobanov and Zensus, 2001](#), and references therein].

The big picture is completed by their double-peaked spectral energy distribution (SED, see Fig. 1.7), first peaking between radio and soft X-rays, due to synchrotron emission and then at keV to GeV energies, likely owing to the Inverse Compton (IC) process [e.g. [Ulrich et al., 1997](#); [Urry, 1999](#); [Georganopoulos et al., 2001](#)]. High-energy emission in the MeV/GeV range is observed thanks to space-bound observatories, the latest of which is the *Fermi* Gamma-ray Space Telescope (*Fermi*-GST). The two main blazar emission mechanisms are discussed in the next section.

On VLBI scales they usually appear as core-dominated, one-sided sources with variable structural dynamics. They feature a compact, inverted or flat spectrum core that is usually variable. Downstream, within the collimated jet, extended components can be identified as they separate from the core at superluminal velocities. Those components are subject to “spectral ageing”; i.e. they become weaker with time, especially at higher frequencies, thus producing a steepening synchrotron spectrum.

## 1.9 RADIATION MECHANISMS

### 1.9.1 Synchrotron radiation

Accelerated charged particles emit electromagnetic radiation. An electron for example, while passing close to an ion, changes its velocity vector and emits. Electromagnetic radiation from ultra-relativistic ( $v \sim c$ ) charged particles that alter their path is called *synchrotron* radiation. Synchrotron radiation was first



observed in particle accelerators on earth (called cyclotrons) but since its discovery (in 1947) it has been also observed to originate in cosmic sources. There is compelling evidence suggesting that cosmic synchrotron emission is due to particles, mainly electrons, gyrating around magnetic field lines [Ginzburg and Syrovatskii, 1965; Pacholczyk, 1970].

But this is only half of the story. Magnetic fields are not prerequisites for the production of synchrotron radiation. In fact, since electrons have mass they could radiate even in a gravitational potential. Let us consider an example<sup>1</sup>. Using Larmor's formula (in cgs units) and substituting already the generic acceleration term,  $a$ , with that coming from a gravitational field characterized by acceleration  $g = 980 \text{ cm s}^{-2}$ . This makes an electron radiate power

$$P_{\text{cyc}} = \frac{2}{3} \frac{e^2 g^2}{c^3} = 5.46 \times 10^{-45} \text{ erg s}^{-1}. \quad (1-21)$$

The same power would be radiated if an electron was accelerated in the electrostatic field of a proton from a distance

$$b = \left( \frac{e^2}{m_e g} \right)^{1/2} = 508 \text{ cm}. \quad (1-22)$$

Consequently, if an electron was free-falling towards Earth, the power it radiates is equal to that radiated from a distance of about 5 meters, if it was accelerated radially due to the electrostatic force of one proton.

In the ultra-relativistic limit, Eq. 1-21 has also a dependence on the Lorentz factor of the particle and becomes

$$P_{\text{syn}} = \frac{2}{3} \frac{q^2}{c^3} \gamma^4 a^2 \quad (1-23)$$

where, now we use a generic acceleration  $a$  and  $q$  denotes the charge of the particle. The main characteristics of synchrotron radiation is that it is beamed and highly polarized, both linearly and circularly. In more convenient SI units the average synchrotron power of a single electron accelerated by a magnetic field, is given by

$$P_{\text{syn}} = \frac{4}{3} \sigma_T \beta^2 \gamma^2 c U_B \quad (1-24)$$

where  $\sigma_T = 8\pi r_e^2/3$  is the Thomson cross section, with  $r_e = e^2/(m_e c^2)$  the classical electron radius,  $\beta$  is the speed in units of  $c$ , and  $U_B = B^2/8\pi$  is the magnetic field energy density.

The low-energy hump of blazar SEDs ( $10^5 \lesssim \nu \lesssim 10^{16}$  Hz) is attributed to synchrotron radiation from gyrating ultra-relativistic, charged particles around magnetic field lines. Observed spectra of blazars can be described by power-laws of the form

$$S \propto \nu^{+\alpha} \quad (1-25)$$

<sup>1</sup> Example from <http://www.astronomy.ohio-state.edu/~ryden/ast822.html>

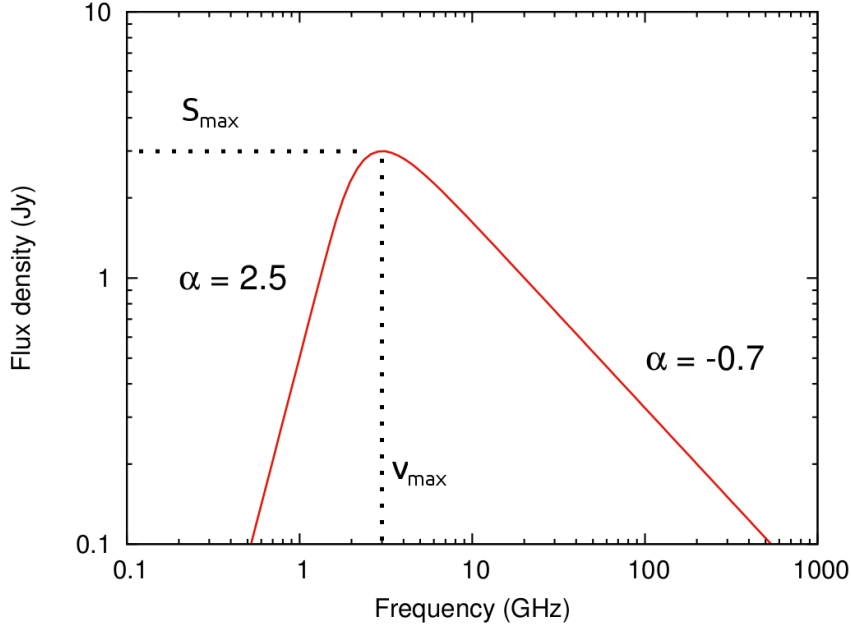


Figure 1.8: Typical synchrotron self-absorption spectrum. Here  $S_{\max} = 3 \text{ Jy}$ ,  $\nu_{\max} = 3 \text{ GHz}$  are the turnover flux density and turnover frequency, respectively. The optically thick and thin spectral indices are shown on the plot and have typical values of  $5/2$  and  $-0.7$ , respectively.

where  $S$  is the flux density in Jy,  $\nu$  is the observing frequency and  $\alpha$  the spectral index.

A cardinal mechanism that shapes the observed spectra is *synchrotron self-absorption* (SSA, see Fig. 1.8). This opacity-driven effect is simple to understand. A single blob of plasma is an ensemble of electrons with randomly distributed—but nevertheless very high Lorentz factors,  $\gamma_e$ . These  $\gamma_e$ , refer to individual electrons. In any case, they radiate due to stochastic acceleration/deceleration, isotropically in the co-moving frame of the blob, as a whole. The synchrotron photons they emit, cannot escape the cloud unless they possess a minimum amount of energy (since  $E = h\nu$ , this translates into “having” a minimum frequency) so that they avoid absorption since as a photon propagates through the plasma on its way out of the blob, there is a probability that it will scatter off one of the electrons and lose its energy. The critical frequency above which, a photon can escape, without being absorbed is called the turnover frequency ( $\nu_{\max}$  in Fig. 1.8). For  $\nu_{\text{obs}} < \nu_{\max}$ , the plasma is optically thick, while for  $\nu_{\text{obs}} > \nu_{\max}$  it is optically thin. Canonical values for the spectral indices in these two regimes are  $\alpha_{\text{thick}} = 5/2$  and  $\alpha_{\text{thin}} = -0.7$ , respectively. Traditionally, blazar spectra characterized by indices  $>0$ , are referred to as inverted, in the range  $0.0$  to  $-0.5$  as flat, and  $<-0.5$  as steep.

Since numerous sources with flat spectra are routinely observed, it is believed that those spectra are due to superposition of a number of individual SSA components (Fig. 1.9). This is especially believed to be the case for the prominent feature referred to as the core, present in all VLBI maps of blazars [e.g. van der Laan, 1966; Marscher, 1995, 1996; Türler et al., 2000]

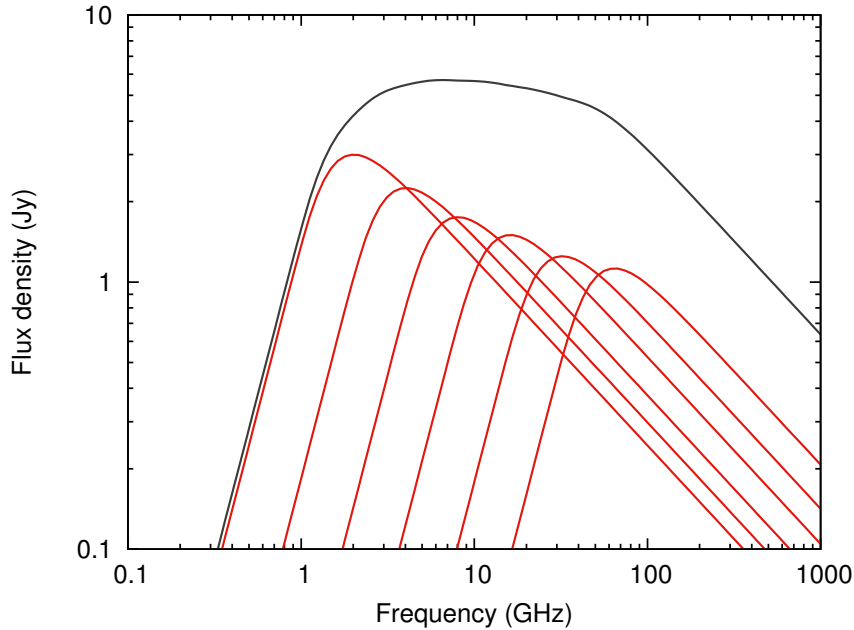


Figure 1.9: Superposition of six SSA spectra, able to produce flat spectral characteristics across a broad frequency band. Here all SSA components are characterized by optically thick and thin parts with indices of 2.5 and  $-0.7$ , respectively. The resulting—from superposition—spectrum is shown in black.

### 1.9.2 Inverse Compton scattering

The high-energy hump of blazar SEDs ( $10^{16} \lesssim \nu \lesssim 10^{26}$  Hz) is commonly ascribed to the process of *inverse Compton scattering*. This is the interaction—collision and exchange of momenta—between a relativistic electron and a photon. During the interaction, a low energy photon is up-scattered to energies up to X- or  $\gamma$ -rays by the high-Lorentz-factor electron.

For the process to be at work in blazars, a target photon field is required. The synchrotron process discussed in Section 1.9.1 produces such candidate photons. These can be up-scattered by the very electrons giving them off, in which case the process is referred to as *synchrotron self-Compton* (SSC). If the seed photon field originates from the external environment of the jet, then it is referred to as *External Radiation Compton* or simply *External Compton* [ERC or EC, see e.g. Sokolov and Marscher, 2005]. Potential reservoirs for EC are the photons from the accretion disk, the hot corona above it, IR photons from the dusty/clumpy torus, those from the BLR or even the cosmic microwave background (CMB) photon field.

The total inverse-Compton power gained by the photon field and lost by the electron is given by

$$P_{\text{IC}} = \frac{4}{3} \sigma_{\text{T}} \beta^2 \gamma^2 c U_{\text{rad}} \quad (1-26)$$

where  $U_{\text{rad}}$  is the energy density of the seed photon field. Energy losses due to the IC process are also referred to as *electron cooling*.

Combining Eq. 1–24 and 1–26, we obtain the ratio

$$\frac{P_{\text{IC}}}{P_{\text{syn}}} = \frac{U_{\text{rad}}}{U_{\text{B}}} \quad (1-27)$$

between the energy densities of the seed photon field and the magnetic field, accelerating the particles.

An alternative for the production of the high-energy component of blazar SEDs is a family of models similar to the logic described above, that differ though in the composition of the relativistic jet. In those, so-called *hadronic* models, both electrons ( $e^-$ ) and heavier protons ( $p^+$ ) are assumed to be accelerated to ultra-relativistic energies. Consequently, protons could easily exceed the energy threshold for the production of pions, ( $\pi^0$ ,  $\pi^+$ , and  $\pi^-$ ), via interactions with seed/target photons in the emission region. In such models the high energy component of blazar SEDs is dominated by synchrotron emission due to relativistic protons, cascades initiated by  $\gamma\gamma \rightarrow e^- + e^+$ , and photons from  $\pi^0$  decays [see e.g. Kirk and Mastichiadis, 1992; Mannheim, 1993; Boettcher, 2010].

## 1.10 FORMATION AND STABILITY OF RELATIVISTIC FLOWS

### 1.10.1 Formation of jets

Although the exact process driving the formation of jets is to date not entirely understood, according to the standard working paradigm astrophysical jets are produced by rapidly rotating objects. The crucial ingredient is the presence of a pressure gradient extending outward from the base of the flow, with the pressure being higher than the particle energy density at the base, so that it can efficiently accelerate them to high Lorentz factors. The consensus is that magneto-hydro dynamic (MHD) acceleration is at play; i.e. the pressure required is magnetic pressure provided by the rotating, astrophysical compact object [Spruit, 2010]. In the case of AGN this can be a rotating accretion disk [Blandford and Payne, 1982] or the black hole itself [Blandford and Znajek, 1977; Komissarov, 2009].

These mechanisms of plasma acceleration require the presence of a large-scale and predominantly poloidal magnetic field threading the object. As the object spins, the magnetic field lines essentially co-rotate with it—inducing no toroidal component—up to the radius of the Alfvén surface<sup>2</sup>. From this point on, co-rotation stops (with magnetic field lines lagging behind the object’s rotation) and magnetic-field lines wound up thus giving rise to a significant toroidal component [for an illustration see Fig. 2 of Spruit, 2010]. The resulting helical magnetic field topology introduces a gradient of the toroidal component of the magnetic field along the poloidal direction, creating a funnel, that accelerates plasma. Via MHD acceleration, plasma flows can reach Lorentz factors of the order 10–100s. Helical topology of the magnetic field is further supported by the Faraday rotation measure gradients observed in various sources [e.g. Asada et al., 2002; Gabuzda et al., 2004; Croke et al., 2010; Hovatta et al., 2012].

<sup>2</sup> The surface where the flow speed is equal to the Alfvén speed.

It is found that jets need to be collimated for efficiently transforming Poynting flux into kinetic flux [e.g. Tchekhovskoy et al., 2009]. Collimation takes place in a zone extending some  $\sim 10^3$  Schwarzschild radii from their base. There exists observational evidence supporting the existence of such a zone [e.g. Junor et al., 1999].

State-of-the-art, global, three-dimensional general relativistic MHD (GRMHD) simulations support the above scenario for the formation and acceleration of relativistic outflows. With an initial setup featuring a supermassive black hole, an accretion disk, and a large-scale poloidal magnetic field (see Fig. 1.10), these simulations can reproduce the observed properties of stable relativistic jets, namely bulk Lorentz factors and morphology (see Fig. 1.10) [e.g. McKinney and Blandford, 2009; McKinney et al., 2012].

If the picture painted above is correct, then jets created from objects on all possible astrophysical scales are one and the same phenomenon, only accordingly scaled up or down, and with few parameters affecting the jet morphology and power, such as the mass of the central source and its putative spin [see e.g. Merloni et al., 2003; Falcke et al., 2004].

### 1.10.2 *Stability of relativistic jets*

From Earth-bound experiments it is known that plasma is highly susceptible to instabilities. For a plasma in equilibrium, these perturbations can grow and oscillate or be dumped out. The observational fact that astrophysical jets can reach sometimes up to Mpcs suggests a unique stability for those jets and an ability for efficient dumping. In the following a few important plasma instabilities, relevant to astrophysical jets, are introduced.

#### 1.10.2.1 *Current-driven "kink" instability*

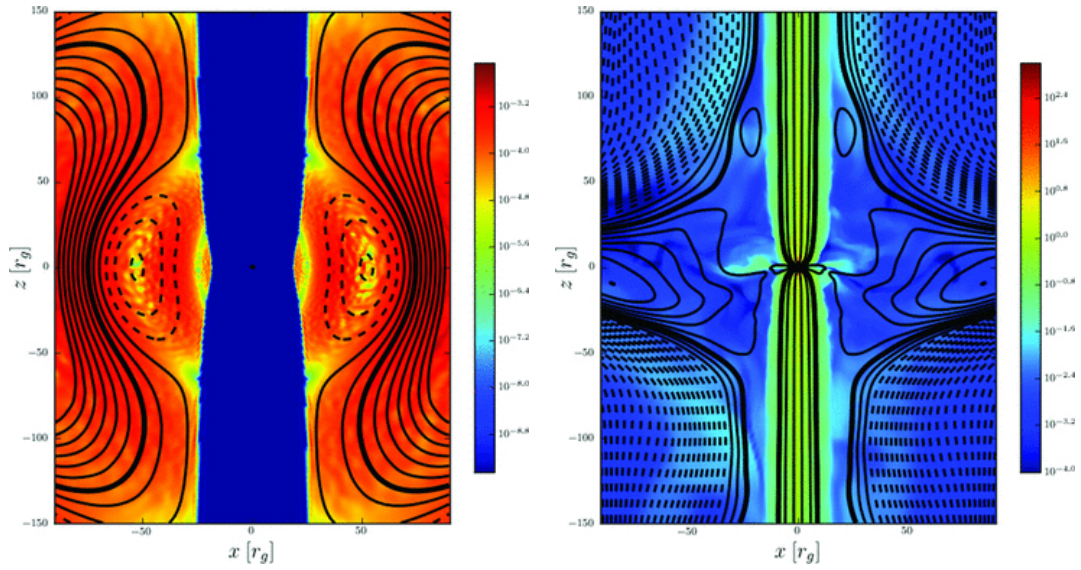
This mode of current-driven instability, also referred to as "kink" instability has the potential to disrupt the jet at its initial stages, when it is still magnetic-energy dominated. It acts by displacing the fluid's center of mass, thus heavily perturbing the cylindrical jet flow, putting it into a spiral oscillatory movement [see e.g. Moser and Bellan, 2012].

#### 1.10.2.2 *Magnetic reconnection*

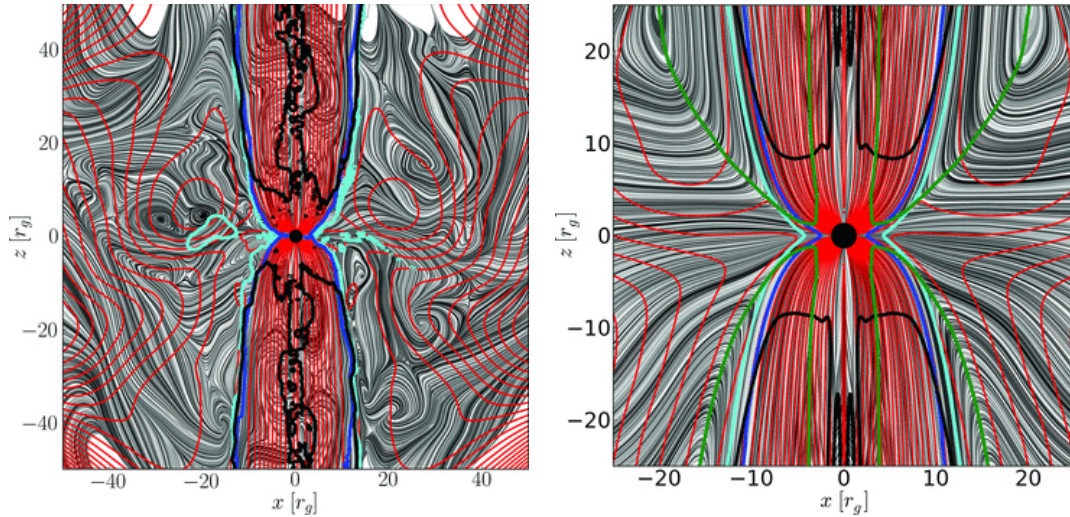
Magnetic reconnection refers to fast re-configuration of the magnetic field topology. The phenomenon is known and seen in solar flares and elsewhere, in situations where highly conducting plasma is involved. Reconnection of magnetic field lines dissipates magnetic field energy into thermal and kinetic energy. Apart from that though, magnetic reconnection has been invoked in models of particle acceleration [see e.g. Giannios, 2013].

#### 1.10.2.3 *Kelvin–Helmholtz instability*

When the jet initiates interactions with its surrounding medium another kind of instability emerges. Kelvin–Helmholtz (K–H) instability is caused by the viscosity shear at the boundary layer between the fast jet and the slow ambient



- (a) Initial state of the model at  $t = 0$ . It comprises a weakly magnetized, thick accretion disk around a spinning black hole (BH) with  $\alpha/M = 0.9375$ . Black lines represent the integrated (over the  $\phi$ -coordinate) magnetic vector potential,  $A_\phi$ . Color-coded is the quantity  $b^2 = 2U_B$  and black lines correspond to field loops with alternating polarity, embedded in the disk. The thick black line tracks the outermost angular part of the black-hole-driven jet (same as in panel 1.10b).
- (b) Evolved state at time  $t \sim 10412 r_g/c$ . The strongly magnetized gas near the BH that launches a vertical jet is seen here as the collimated beam of high electromagnetic energy density. All field lines of the first and second field loops have been accreted or ejected. Field lines of the evolved third and fourth loop are shown as solid and dashed black lines, respectively. The thick line is the same as in panel 1.10a.



- (c) Evolved state at the same time as in panel 1.10b. Here, velocity flow lines are shown in gray-scale, and field lines ( $A_\phi$  integrated over  $\phi$ ) in red. The accretion flow appears turbulent with visible eddies.
- (d) Time-averaged velocity flow field, as in panel 1.10c. Here, the image is zoomed-in on the vicinity of the BH. The BH is threaded by ordered magnetic flux, and the flow shows equatorial symmetry.

Figure 1.10: Realization of a global 3-dimensional GRMHD simulation. A relativistic jet emerges from an initial configuration featuring a spinning SMBH, an accretion disk and a large-scale, poloidal magnetic field. Images from McKinney et al. [2012].

medium. It induces turbulence, along with pinch and helical modes of oscillatory motions [e.g. [Lobanov and Zensus, 2001](#); [Perucho et al., 2004](#)].

### 1.11 OPEN QUESTIONS

Closing this introductory Chapter, let us review a few open questions underlining how lively the field of AGN still is, after a few decades of intense research. Some of these questions we touch upon in the course of the present thesis.

1. Even if theorists and their simulations have led to some agreement as to how jets are formed, still, the issue of the putative SMBH spin and its role in jet formation is—from the observational point of view—open. Is it possible to be proven that SMBHs do have spin and can it be measured?
2. What is the reason that most AGN do not form jets? Is there a connection with the SMBH spin? Is it only maximally-rotating (Kerr) SMBHs that launch energetic jets or Schwarzschild black holes can do so too?
3. How are jets collimated and remain so, for long distances away from their source? Is hydrodynamic launching completely ruled out? To answer this, high-resolution and high-cadence polarization mapping will give some important insights.
4. What is the dominant emission mechanism in blazars? Is it SSC and what is the contribution of EC, if any? Do we have to invoke one- or multi-component SSC models? What is the seed photon reservoir for EC? The BLR, accretion disk, torus or even CMB photons?
5. What about hadronic models? Protons need more energy to be accelerated to the observed Lorentz factors but their presence could explain more naturally the impressive stability of observed collimated beams of plasma (point 3).
6. Which mechanism(s) drive the rapid blazar variability seen across the whole electromagnetic spectrum? Through their observational predictions, different scenarios can be put to the test.
7. Where is the location of the MeV/GeV or higher-energy emission site? Do  $\gamma$  rays originate close to the SMBH or further out, beyond the BLR, parsecs downstream the jet?
8. Are narrow-line Seyfert 1 galaxies (NLS1) (see Chapter 6) just another low-black-hole-mass flavor of the blazar phenomenon? What does their recent detection in  $\gamma$  rays tell us about their nature?
9. Which parameters are relevant for the unification of AGN, after all?

### 1.12 OUTLINE AND IMPACT OF THE PRESENT WORK

In 2008 August, *Fermi*/LAT discovered the blazar PKS 1502+106 showing a rapid and strong  $\gamma$ -ray outburst followed by bright and variable flux over the

next months. The main part of this thesis is largely motivated by this very outburst.

The activity at high energies triggered an intensive multi-wavelength campaign covering also the radio, optical, UV and X-ray bands indicating that the outburst was accompanied by a simultaneous flare at optical/UV/X-rays with a significantly delayed outburst at radio bands as observed by the F-GAMMA program. Due to these findings and the fact that the source already showed a rotation of the VLBI electric vector position angle (EVPA) in 2007/2008 likely as precursor of the  $\gamma$ -ray outburst, additional high-frequency VLBI/GMVA observations at 86 (and 43) GHz have been performed at 6 epochs between 2009 and 2012. Consequently, PKS 1502+106 turns out to be a key source in the framework of detailed studies of the physical connection between the radio and  $\gamma$ -ray emission, particularly probing the emission mechanism and conclusively localizing the  $\gamma$ -ray emitting region.

The present thesis combines the two main tools used in AGN studies; a broadband variability analysis and the Very Long Baseline Interferometry (VLBI) technique. Use of the former approach enables the differentiation between competing variability models, by studying parameters such as the flare amplitudes, time lags and spectral evolution that have specific observational signatures in the time and spectral domain. Furthermore using advanced cross-band correlation techniques, the location where the high-energy emission originates can be constrained. On the other hand the power of VLBI, and mm-VLBI in particular, is revealed through the ability of directly probing the structural dynamics of sources (studies of source kinematics, determination of jet speeds, etc.) thus enabling the correlation between ejected features and flares in multi-wavelength light curves and ultimately getting a handle on the inner workings of the jet of PKS 1502+106 at sub-milliarcsecond scales. VLBI analysis and findings are presented in Chapter 4 while the cross-frequency variability study for the source and discussion of the findings within the framework of the shock-in-jet model in Chapter 5.

A second target of the thesis at hand is the  $\gamma$ -ray- and radio-loud NLS1 galaxy 1H 0323+342. Through VLBI imaging and the densely-sampled F-GAMMA light curves the determination of the viewing angle towards the source is possible. Thus, this thesis is shedding some light to this very important observable in the context of AGN unification schemes (see Chapter 6).

In addition to the above, a thorough introduction to both techniques used here is given. Specifically, in Chapters 2 and 3 theoretical considerations and practical aspects of the reduction of mm-VLBI data are given. The first part of Chapter 5 is also concerned with the theoretical background of the methods used in the light curve analysis.

Finally, a critical summary and concluding remarks of this work are presented in Chapter 7.



## INTERFEROMETRY AND VLBI

---

### 2.1 INTRODUCTION

In the present chapter a basic introduction to astronomical interferometry will be given. Specifically, very-long-baseline interferometry (VLBI) will be introduced, a technique that revolutionized instrumental capabilities in radio astronomy and led to a paradigm shift in our understanding of AGN at their finest scales. An introduction to the VLBI most frequently used “jargon” will be given also, that is among the most troublesome aspects of VLBI, especially to the newcomer.

The angular resolution,  $R$ , of an optical instrument is given by the following relation

$$R \propto \frac{\lambda}{D} \quad (2-1)$$

where  $\lambda$  is the wavelength of the incoming electromagnetic radiation and  $D$  the diameter of the primary mirror of the instrument. In the radio regime in particular, the angular resolution that characterizes a telescope is rather poor for small apertures and long wavelengths or equivalently low observing frequencies (see Fig. 2.1).

Poor angular resolution leads to poor spatial localization of radio sources in the sky. Early attempts to tackle the problem included indirect techniques, for example lunar occultations, which provide an angular resolution of the order of  $1''$  [Hazard, 1961, 1962; Hazard et al., 1963]. These efforts were the first to provide estimates of angular diameters, using the 250-ft radio telescope in Jodrell Bank, UK and the 210-ft Parkes antenna in Australia; with the first radio galaxies to have accurately measured parameters being 3C 212 and 3C 273.

It was this very quest for ever higher angular resolution observations that led to the invention of aperture synthesis by Ryle and Hewish [1960] (Nobel prize in Physics 1974—the first awarded for astronomical research). Using this technique one tries to artificially synthesize a large telescope out of a number of smaller ones, situated in different locations. The distance that separates the elements of the interferometer, commonly referred to as baseline length, can vary between one element diameter up to several thousand or several hundred thousand kilometers, when it comes to very-long-baseline interferometry and space VLBI<sup>1</sup>.

Synthesis refers to the combination of signals arising from each element. The combination can be done in real time and by purely optical means (e.g. mirrors, prisms, beam splitters etc.) as in optical interferometry or off-line and at a different location and time after the observing run as in VLBI (where cross correlation

---

<sup>1</sup> For a comprehensive introduction to the fundamentals of radio interferometry, cf. R. Porcas' lecture during the 2nd MCCT-SKADS training school here: <http://pos.sissa.it/cgi-bin/reader/conf.cgi?confid=65>

of the signals is employed). Different and very special equipment is required in each case. Recent advances in communications technology though, have enabled the real-time connection of telescopes and in some occasions on-line correlation of data (e.g. e-VLBI, e-MERLIN).

Observing in VLBI mode means that each telescope points at the target source, stays on tracking it, integrating, and recording the voltage. Each chunk of on-source data is called a *scan*. Scans can last from a few seconds up to several minutes depending on the sensitivity of the baseline and atmospheric coherence. The sensitivity of a single antenna is given by

$$\Delta T = \frac{2k_B T_{\text{sys}}}{A_{\text{eff}} \sqrt{\Delta\nu \Delta\tau}} \quad (2-2)$$

and the sensitivity of an antenna array comprising  $N$  elements is

$$\Delta T = \frac{2k_B T_{\text{sys}}}{A_{\text{eff}} \sqrt{\Delta\nu \Delta\tau}} \frac{1}{\sqrt{N(N-1)}} \quad (2-3)$$

where

- $\Delta T$  is the root-mean-square noise of the output  $T_{\text{sys}}$ ,
- $k_B$  is the Boltzmann constant,
- $T_{\text{sys}}$  is the system temperature,
- $A_{\text{eff}}$  is the effective aperture of the element,
- $\Delta\nu$  is the observing bandwidth, and
- $\Delta\tau$  is the total, on-source integration time.

Some array-specific efficiency terms may also contribute to sensitivity but are neglected here for simplicity.

The appropriate scan length is specified according to the baseline sensitivity—i.e. an array of two elements—and also the stability of the atmosphere at a given observing wavelength. The reason is that given two identical telescopes, the scan length must ensure that the source is detected by both elements. This is not the case though for a baseline comprising a sensitive and a not-so-sensitive element. In this case it is sufficient for the sensitive one to detect the source. This fact follows from the formula of the baseline sensitivity. Usual scan lengths are of the order of 5 to 10 minutes. Furthermore, the scan length plays a role in the process of *fringe fitting*, discussed further in a subsequent paragraph. Repeated scans of the source of interest within an observing run of several hours result in filling the  $uv$ -plane with the help of Earth's rotation, resulting in higher-fidelity images (see Section 2.2.3).

For VLBI the combination of signals from different telescopes, referred to as stations, is performed by a piece of hardware or software called "correlator". The correlator searches, calculates and applies the correct phase (time) offset to the data of each baseline in order to obtain constructive interference fringes (see Fig. 2.2). Much more effort is needed primarily as observing frequency increases, but also as other observational parameters change.

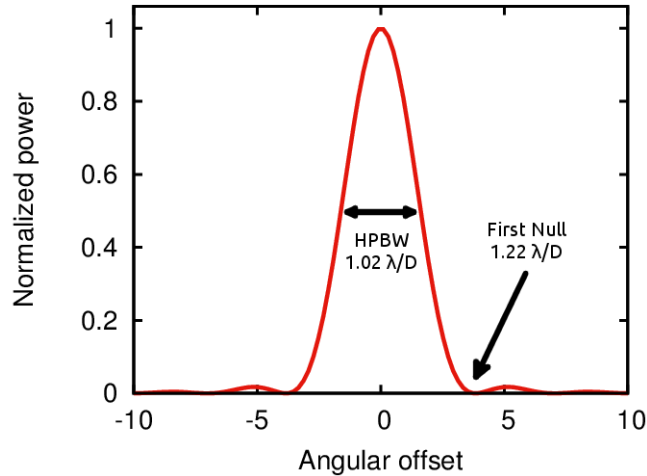


Figure 2.1: Power response of a receiving element to a point source as a function of angular offset from the peak,  $P(\theta)$ . For a uniform circular aperture  $P(\theta) = (J_1(x)/x)^2$  also known as the Airy pattern, where  $J_1$  is the first order Bessel function. The half-power beam width (HPBW) is at  $\sim 1.02 \lambda/D$  and the instrument's resolution is defined by the first null at  $\sim 1.22 \lambda/D$ .

For radio interferometry and for VLBI in particular, correlation takes place after the data acquisition at the correlation facility. A number of institutes around the world host such correlators with the most famous among them being in Bonn (MPIfR, Germany), Dwingeloo (JIVE, The Netherlands), Socorro (NRAO, USA) along with correlators in Moscow, Russia, and Japan.

## 2.2 CORRELATED NOISE AND THE VISIBILITY FUNCTION

The purpose of imaging interferometry is to reconstruct the spatial distribution of sky brightness by measuring as many as possible, different spatial frequencies of this portion of the sky (containing a radio source). In practice, sampling of the spatial frequencies is rather sparse due to the finite and rather limited number of interferometer elements and their positions. An easy and didactic way to understand interferometry is by having in mind the double-slit experiment performed at the beginning of the nineteenth century by Thomas Young [e.g. for an overview [Young, 1802](#)]. Visualizing the two slits as two antennas comprising a baseline, we can imagine that a fringe pattern is "cast" on the plane of the sky with the positive and negative fringes perpendicular to the baseline direction. Evidently such a baseline can only be sensitive in the direction of the alternating fringes and not along them (see Fig. 2.4). It is this special piece of equipment, the correlator, that makes the whole process possible.

### 2.2.1 The correlator input: voltages and noise

For successfully correlating the data from each baseline a number of inputs are needed for the correlator. First and foremost the data itself. These come in hard disks containing the raw, digitized, recorded voltages from each station and an accurate time stamp from a hydrogen maser "clock". For the purposes of VLBI

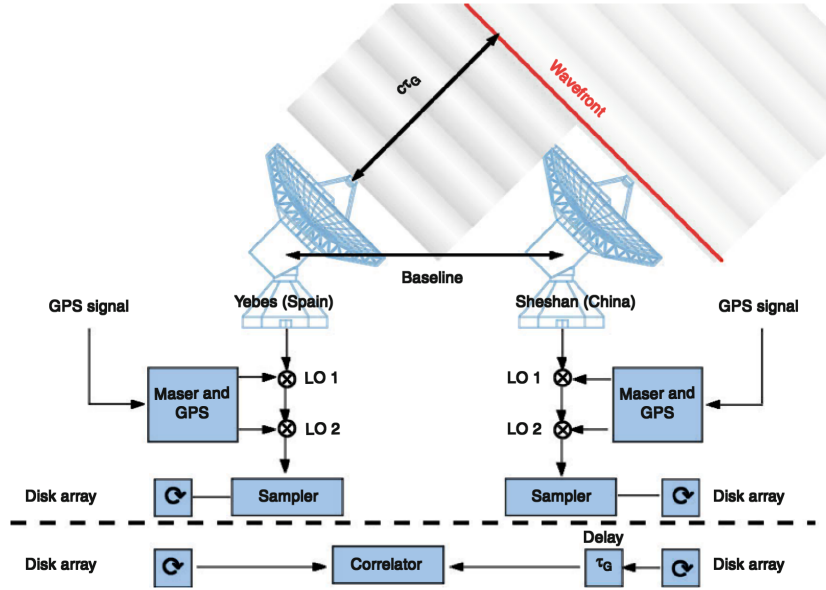


Figure 2.2: Schematic diagram of the two-element, very-long-baseline interferometer. The plane waveform reaches the antennas with a delay  $c\tau_g$  which needs to be compensated in order to coherently (or in-phase) combine the signal of each element with one another. Image from [Wiesemeyer and Nothnagel \[2014\]](#).

the important piece of information is the voltage phase that needs to be recorded at a high rate and with precise time stamps. For this purpose, highly accurate maser clocks are used at each participating VLBI station.

The second most important piece of information is the antenna positions comprising the interferometric array. These need to be known with high precision ( $<1$  mm) especially at higher observing frequencies. Other parameters of the correlator model include, Earth rotation data, the polar motion (UT1  $\pm$  UTC correction), source positions, atmospheric thickness, clock synchronization offsets, tidal effects, Earth tectonic drifts, atmospheric pressure loading along with other higher order effects. The whole process is based on having an—as complete as possible—model in order to calculate the geometric time delay given by

$$\tau_g = \frac{\vec{b} \cdot \vec{s}}{c} \quad (2-4)$$

with  $\vec{b}$  the baseline vector, and coherently mix the signals from  $N$  number of elements and  $N(N-1)/2$  baselines (see Fig. 2.2).

### 2.2.2 The correlator output

The correlator multiplies and then time-averages the recorded signals (i.e. voltages) from two telescopes (a baseline). The two voltages—each coming from a different telescope—have the following form

$$V_1 = V \cos[\omega(t - \tau_g)] \quad \text{and} \quad V_2 = V \cos(\omega t) \quad (2-5)$$

where  $V$  is the maximum amplitude of the oscillation,  $\omega$  is the frequency of the observed signal (otherwise  $\nu = \omega/2\pi$ ),  $t$  is the time variable and the two signals are identical apart from the fact that they are separated by a time interval, the geometric delay (see Fig. 2.2).

The physical principle upon which aperture synthesis is based is the van Cittert-Zernicke theorem<sup>2</sup> [van Cittert, 1934; Zernike, 1938]. The theorem in essence tells us that spatially incoherent radiation, with increasing distance from the source, becomes spatially coherent and can produce constructive or destructive interference patterns. With some simplification it tells us—the not so obvious and rather unexpected fact—that electrons emitting at different times and at different positions, “knowing” nothing about each other, give rise to photons that while initially out-of-phase with each other, in the far field of the source become in-phase and can interfere.

Strictly mathematically speaking it relates the spatial coherence function (or visibility)  $V(\vec{r}_1, \vec{r}_2) = |V|e^{i\phi} = \langle E(\vec{r}_1)E^*(\vec{r}_2) \rangle$ , to the intensity distribution of the incoming radiation  $I(x, y)$  through a Fourier transform

*Introduction  
to the concept  
of visibility*

$$V(\vec{r}_1, \vec{r}_2) \stackrel{\mathcal{F}}{\underset{\mathcal{F}^{-1}}{=}} I(x, y). \quad (2-6)$$

The spatial coherence function,  $V(\vec{r}_1, \vec{r}_2)$ , is the time-averaged complex product of the received electric field  $E(\vec{r}_1)$  and  $E(\vec{r}_2)$  in two antenna positions  $\vec{r}_1$  and  $\vec{r}_2$ . All it tells us is that the brightness distribution of a distant radio source on the plane of the sky ( $x$  and  $y$  denote directions parallel to RA and DEC) can be reconstructed through a Fourier transform of the cross-correlation of the signal received by antennas at different points on the Earth.

Radio interferometric techniques greatly owe to optical interferometry and the pioneering work by Michelson and his collaborators in the last decade of 19th and the first decades of the 20th century [Michelson, 1890, 1920]. They have managed to measure the diameters of nearby stars [Michelson and Pease, 1921] as well as solar system objects [Michelson, 1891]. Recalling again T. Young’s double-slit experiment we can imagine the fringe pattern on the plane of the sky. If the angular diameter of the star is small compared to the spacing of two adjacent fringe pattern maxima then the star is *unresolved*. This also results in the intensity of the fringe minima reaching zero. If, on the other hand, the angular diameter of the star is larger than the fringe spacing then it is *resolved* and the fringe pattern minima do not reach zero intensity (see Fig. 2.3). In the latter case the resulting fringes are a superposition of more than one fringe patterns from spatially-separated, unresolved regions of the source, thus not reaching zero. Concluding, the more resolved the object is, the “worse” the visibility function looks. The terminal case arises when the source size is so large that the interference fringes disappear (i.e. the source is *resolved out*).

According to Michelson’s definition the interferometric fringe visibility is

$$v_f = \frac{\text{intensity of maxima} - \text{intensity of minima}}{\text{intensity of maxima} + \text{intensity of minima}} \quad (2-7)$$

<sup>2</sup> For a very nice and interesting visualization of the van Cittert-Zernicke theorem see the article “Spatial coherence from ducks” by Knox et al. [2010] and the related video at <https://www.youtube.com/watch?v=4o48J4streE>.

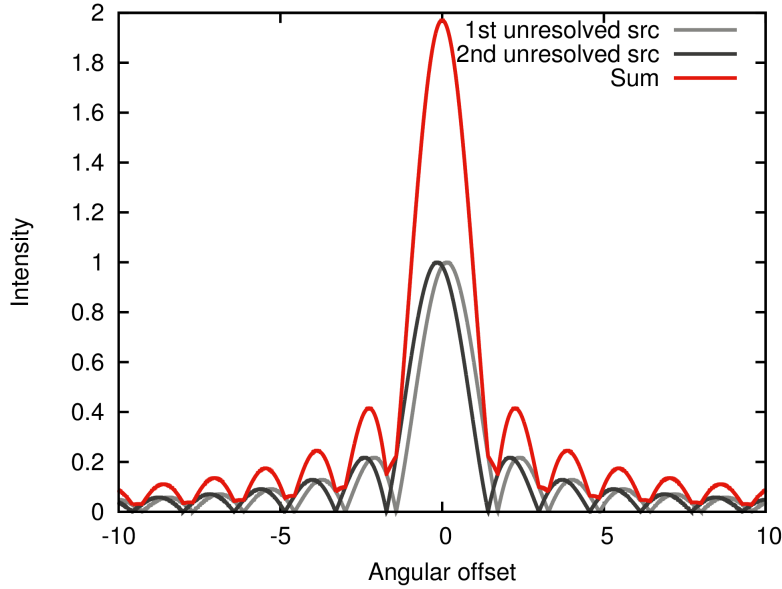


Figure 2.3: Fringe intensity of two unresolved sources and of their sum. While for the unresolved ones the intensity reaches zero, the same does not happen for the resolved one.

and this quantity is at maximum unity ( $v_f = 1$ ) for an unresolved source and less than one ( $v_f < 1$ ) for a resolved one.

*The complex visibility*

Let us now return to the radio domain and discuss the simplest configuration for an interferometer; a two-element, single-baseline instrument (Fig. 2.2). The antennas comprising it, record two discrete signals of the form of Eq. 2-5. These are to be processed by the correlator. The first step is the multiplication with each other that yields

$$V_1 V_2 = \left( \frac{V^2}{2} \right) [\cos(2\omega t - \omega\tau_g) + \cos(\omega\tau_g)] \quad (2-8)$$

which features the rapidly varying term  $\cos(2\omega t - \omega\tau_g)$ . The process of time-averaging within a sufficiently large interval  $\Delta t \gg 1/\omega t$ , eliminates this term.

The correlator by multiplying and time-averaging two signals arising from a set of two telescopes casts a *cosinusoidal* fringe pattern on the sky with the following final form

$$R_{\cos} = \langle V_1 V_2 \rangle = \left( \frac{V^2}{2} \right) \cos(\omega\tau_g). \quad (2-9)$$

This kind of sinusoidal correlation output though, is sensitive only to the even part of the source brightness distribution and has zero response to the odd part. For an illustration see Fig. 2.4. In order to build a useful (functional) instrument that is sensitive to both, even and odd structural information, one needs to be able to produce and combine both types of cross-correlation. To retrieve the

sinusoidal part, a ninety-degree ( $90^\circ$ ) phase offset is introduced to one of the two signals of Eq. 2-5 and the output then becomes

$$R_{\sin} = \langle V_1 V_2 \rangle = \left( \frac{V^2}{2} \right) \sin(\omega\tau_g). \quad (2-10)$$

The concept of the complex visibility comes about by combining the two "complex correlator" data products and using Euler's formula ( $e^{i\phi} = \cos(\phi) + i\sin(\phi)$ ) for convenience, we define it as

$$V \equiv R_{\cos} + iR_{\sin} = Ae^{i\phi} \quad (2-11)$$

where

$$A = \sqrt{R_{\cos}^2 + R_{\sin}^2} \quad \text{and} \quad \phi = \arctan\left(\frac{R_{\sin}}{R_{\cos}}\right) \quad (2-12)$$

are the complex visibility amplitude and phase respectively.

In radio astronomy and under a few simplifying assumptions the complex visibility is written as

$$\mathcal{V}_v(u, v, w \equiv 0) = \iint \frac{I_v(l, m)}{\sqrt{1-l^2-m^2}} e^{-2i\pi(ul+vm)} \, dl dm \quad (2-13)$$

where  $I_v$  is the intensity distribution of the source,  $l$  and  $m$  the directional cosines, and subscript  $v$  arises from considering only one monochromatic component of the electric field. For a complete treatment see Clark [1999]. In the formula above the assumption of a coplanar array is implicit and  $u, v$  are the coordinates of the receiving elements in units of wavelengths, as is customary in interferometry. The formula represents a Fourier transform and is invertible. The consequence of Eq. 2-13 is that having a sufficient number of visibility measurements at different  $u, v$  coordinates (i.e. sufficient sampling of the Fourier components) one can derive  $I_v(l, m)$ .

The task of the correlator is exactly this. Given a set of individual voltage measurements, to provide the complex visibilities (hereafter simply visibilities) out of which the source structure can be later deduced by means of a Fourier transform.

*The correlator*

Visibilities, being complex quantities, are characterized by an amplitude and a phase term. The amplitude represents the amount of correlated noise (see Fig. 3.3) and the phase carries the positional information; "where this amplitude (or power) is located". One needs to be aware of the fact that each visibility datum contains information for the sky brightness distribution everywhere and not only at a given coordinate. In any case, it should be obvious by now, that the correlator model is not quite as accurate and residuals remain. Residuals that need to be further calibrated-out.

### 2.2.3 The $uv$ -plane: Sampling the visibilities, coverage and the dirty beam

The main point of the discussion above is that for every sky brightness distribution  $I(l, m)$ , there exists a visibility function  $V(u, v)$  that is its Fourier transform,

recall Eq. 2–6. The problems start from the fact that due to inherent observational limitations, predominantly telescope positions that make certain baselines available and finite antenna sizes that negate measurements at short and certainly zero spacings, the visibility function is never fully attainable. What is available is a set of visibility measurements; i.e. the visibility function sampled at certain positions. The two-dimensional space of spatial coordinates expressed in wavelengths is called the *uv-plane* and contains the positions where a visibility measurement exists or not (see Fig. 2.5). The density of samples on the *uv-plane* is referred to as the *uv-coverage* of a given interferometric observation [see also Thiébaud, 2009, for a review on optical interferometry techniques].

Each baseline at each time interval (correlator integration time) yields one visibility datum that represents a different Fourier component, thus a different spatial frequency of the source brightness distribution. The whole idea is to have as many as possible, different configurations of baselines so as to sample as many as possible spatial frequencies of the source. A single baseline is not particularly helpful towards this direction but as a consequence of the Earth’s rotation, the projected geometry of the baseline changes with time. It is obvious that this single baseline is able to provide information on more than one spatial frequencies within a maximum range of a 12-hour observation. After that, our single baseline starts to re-sample the same portion of the Fourier plane, provided that the positions of the two antennas remain fixed and the source has not changed (neither its flux nor structure). The same holds for all baselines coming from an array of elements with fixed positions, hence a 12-hour observation provides the maximum *uv-coverage*. Since the brightness distribution of the source is obviously a real-valued function, the visibility is a *Hermitian* one<sup>3</sup>. This leads to every interferometric measurement yielding a visibility point at a certain *uv-coordinate* and its anti-symmetric with respect to the center of the *uv-plane*.

The *uv-coverage* of an observation is a contributing factor to, and a prerequisite for successful imaging. First and foremost, the Fourier transform of the *uv-coverage* determines the response of the interferometer; i.e. its *point spread function* (PSF), *synthesized* or *dirty* beam. The resolution is determined by the longest *uv-spacing* while sensitivity to large scale structure depends on the shortest baselines. Image fidelity—i.e. the ability to reconstruct complex source structure, greatly increases with *uv-coverage* while gaps decisively limit it. Finally, image dynamic range is affected by side-lobes of the synthesized beam, as a result of these gaps.

Deconvolution  
and  
CLEANing

By simply Fourier transforming the visibility data, we obtain an image of the source brightness distribution that is affected by the PSF of the instrument and it is referred to as the “dirty map”. There exist algorithms such as CLEAN [Högbom, 1974], tackling the problem of deconvolving the “dirty beam” from the map, to finally yield an artefact-free image. CLEAN models the source brightness distribution with delta functions (the CLEAN components). It subtracts the dirty beam pattern from the map and substitutes with CLEAN components on a pixel-after-pixel basis in decreasing order of brightness, until either a predefined threshold of flux, or a number of components is reached. The final CLEAN map is produced by convolving the CLEAN components with the CLEAN beam, that

<sup>3</sup> This follows from basic Fourier transform properties.



is a side lobe-free beam matching the resolution of the initial “dirty beam”. Subtraction of the CLEAN map from the initial dirty map yields the residual map that at the end of the process ideally has a random, noise-like appearance.

For the successful application of the Fast Fourier Transform (FFT) algorithm one needs to bin the data in a regular grid with a number of cells in each direction being a power of two. The final parameters of the image strongly depend on the weighting scheme used to quantify the contribution of each visibility datum to the map. Weighting only has to do with the number of individual visibility measurements per bin. Among the most used schemes are *natural* and *uniform* weighting. In the former, higher number of individual visibilities present in a bin, results in higher weight of the cell during the FFT as opposed to a cell with fewer or none which carries zero weight (see Fig. 2.5a). In the latter case, all cells that feature at least one visibility datum are considered equally during the imaging procedure and contribute identically to the formation of the synthesized beam. As a result, uniform weighting optimizes the point source sensitivity and yields higher angular resolution images at the expense of higher image noise level. Other schemes exist as well, such as robust weighting that is a compromise between the two aforementioned schemes (cf. D. Briggs dissertation, 1995<sup>4</sup>).

*Visibility weighting and tapering*

Another word from the VLBI vocabulary deserving some mention is the word *tapering*. Tapering is a form of weighting but this time taking into account the *uv*-distance of the specific visibility datum. It is used in order to down-weight data on long baselines. Using a Gaussian taper will significantly increase the detectability of extended source structure at the expense though, of angular resolution.

### 2.3 VISIBILITY PHASE SELF-CALIBRATION

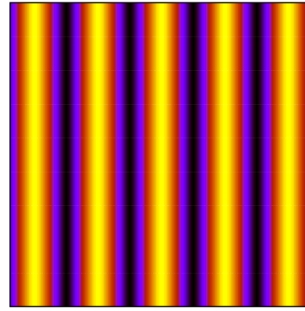
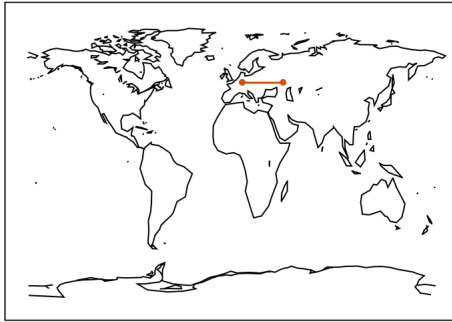
Incomplete knowledge of parameters such as source and array-element positions, atmospheric optical thickness, clock offsets etc. introduce errors in the calculation of visibilities, collectively referred to as corrupting terms. The effect of corrupting terms in visibility data is to scatter power across the image, contributing to a higher-than-expected noise level and degrading image fidelity. The relationship between the observed and real visibilities output by a baseline with elements 1 and 2, can be written as

$$\mathcal{V}_{12}^{\text{obs}}(t) = g_1(t)g_2^*(t) \mathcal{V}_{12}^{\text{true}}(t) + \epsilon_{12}(t) \quad (2-14)$$

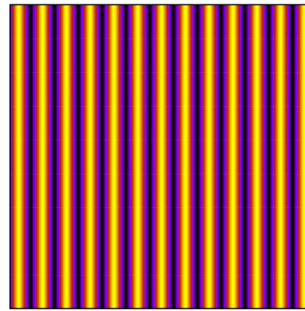
where  $g_1(t)$ ,  $g_2(t)$  are time-dependent, antenna-based terms; the so-called *complex gains* and  $\epsilon_{12}(t)$  represents the thermal noise. Use of the term gain here can be somewhat misleading, nevertheless it is accurately delivering the message that these terms are connected to the performance and external parameters (e.g. weather) of individual antennas. Using the following functional form for the complex gains, for the two antennas of our baseline:

$$g_1 = a_1 e^{i\phi_1} \quad \text{and} \quad g_2 = a_2 e^{i\phi_2} \quad (2-15)$$

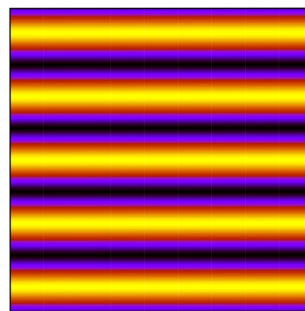
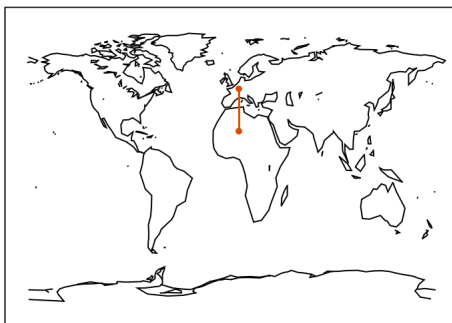
<sup>4</sup> <http://www.aoc.nrao.edu/dissertations/dbriggs/>



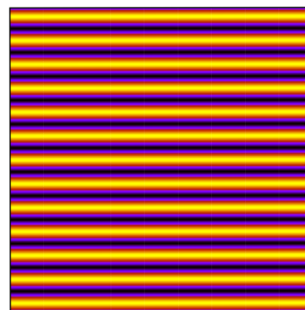
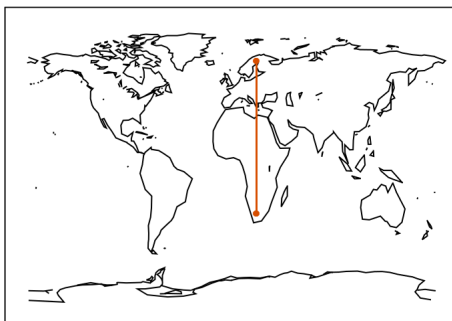
(a) A short East–West baseline (in red). The fringe spacing ( $\lambda/b$ ) is rather loose. This baseline is not sensitive to structure in the North–South direction. Here a cosinusoidal, even fringe pattern is shown.



(b) Long East–West baseline. The fringe spacing ( $\lambda/b$ ) is rather tight resulting to higher angular resolution.

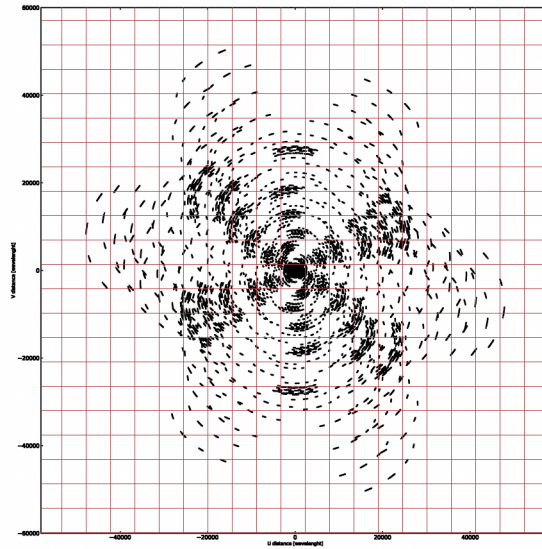


(c) A short North–South baseline. This baseline is not sensitive to source structure on the East–West direction.

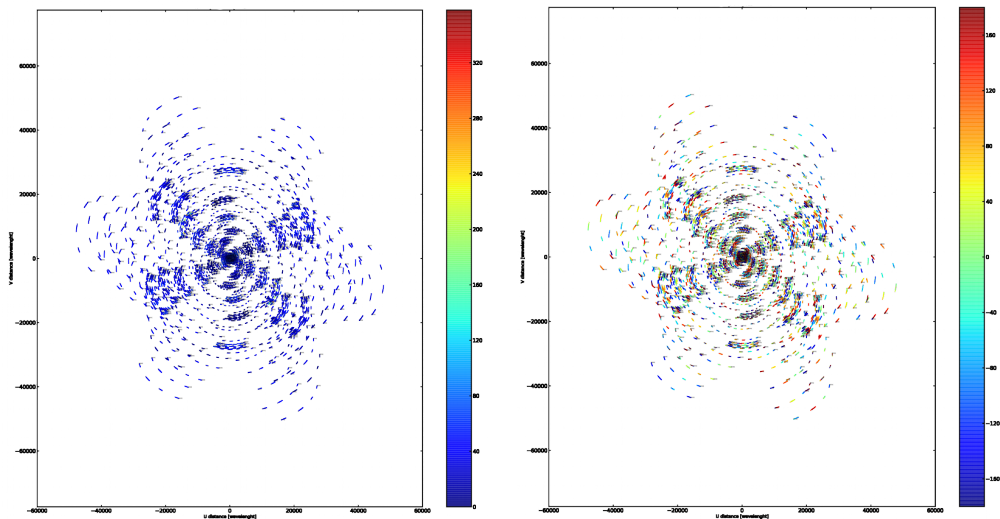


(d) A long North–South baseline.

Figure 2.4: Four hypothetical baseline configurations (with their projected length shown as a red line) and their respective on-sky fringe pattern dictated by their projected length. Here, cosinusoidal fringe patterns are shown. The color code denotes their response with values between 0 (black) and 1 (bright yellow).



(a) Usual representation of the  $uv$ -plane with information on “where” visibility measurements exist. Overplotted is the grid where data is interpolated. Weighting schemes rely on the density of visibility data in each cell.



(b) Same as above but plotting color-coded the complex visibility amplitude.

(c) Same as above but plotting color-coded the complex visibility phase.

Figure 2.5: Example  $uv$ -coverage of a Giant Metrewave Radio Telescope (GMRT) observation. Figures courtesy of Hans-Rainer Klöckner (MPIfR).

we can rewrite Eq. 2-14 as

$$\mathcal{V}_{12}^{\text{obs}}(t) = \left[ a_1(t)a_2(t)e^{i(\phi_1-\phi_2)} \right] \mathcal{V}_{12}^{\text{true}}(t) + \epsilon_{12}(t). \quad (2-16)$$

Self-calibration refers to the process of calculating the complex gains for each antenna of the array, using the target source as calibrator, as opposed to employing a phase-calibration source to perform *phase referencing* [Alef, 1989]. To do that, one needs to proceed with some educated guesses for the source structure and making use of certain tools like the closure relations which will be discussed in the following. Under the assumption that baseline-dependent terms ( $\epsilon_{ij}$ ) are small and can be neglected, the procedure is applied in an iterative way as follows. Usually a point-source structure is assumed as a starting model. With the use of imaging and deconvolution algorithms such as CLEAN, a model for the source is built and the calculation of the complex gains is performed by self-calibration. The model is used as a starting point for the next round of deconvolution and self-calibration until the process converges. Self-calibration requires high *signal-to-noise ratio* in order to be reliable. This, to a certain extent, can be achieved by averaging data in given time intervals. Blazars, as strong sources, allow the use of self-calibration with impressive results.

Given three interferometer elements A, B, C forming a closed triangle of baselines AB, BC, CA (Fig. 2.6a) we have

$$\begin{aligned} \phi_{AB} &= \psi_{AB} + T_A - T_B \\ \phi_{BC} &= \psi_{BC} + T_B - T_C \\ \phi_{CA} &= \psi_{CA} + T_C - T_A \end{aligned} \quad (2-17)$$

where  $\phi_{AB}$  is the observed visibility phase coming from the antenna pair AB,  $\psi_{AB}$  is the real phase that should have been observed without the corrupting station phases that each element of the baseline separately contributes,  $T_A$  and  $T_B$ . Corrupting phases are additive terms (see Eq. 2-16).

Now, addition of the equation set 2-17 around a closed triangle yields

$$\Phi_{ABC} = \phi_{AB} + \phi_{BC} + \phi_{CA} = \psi_{AB} + \psi_{BC} + \psi_{CA}. \quad (2-18)$$

The interpretation of Eq. 2-18 is very interesting and tells us that the sum of observed phases around a closed triangle (Fig. 2.6a) is equal to the sum of corruption-free visibility phases. Eq. 2-18 is referred to as the closure phase for the triangle ABC. For an array of N elements there exist  $(N-1)(N-2)/2$  independent closure phases. The problem to its full extent is degenerate, meaning that we have  $(N-1)(N-2)/2$  good measurements for deducing N telescope corrupting phases. One can reduce this number to  $(N-1)$  by treating one of the antennas as reference. This antenna is assumed to have zero phase offset and all phase corrections are calculated with respect to this antenna. Closure phases are a crucial observable and play a significant role in the process of self-calibration [see Cornwell and Wilkinson, 1981].

An important implication of phase self-calibration is the loss of the absolute positional information in the sky for the source, since one alters the visibility phases.

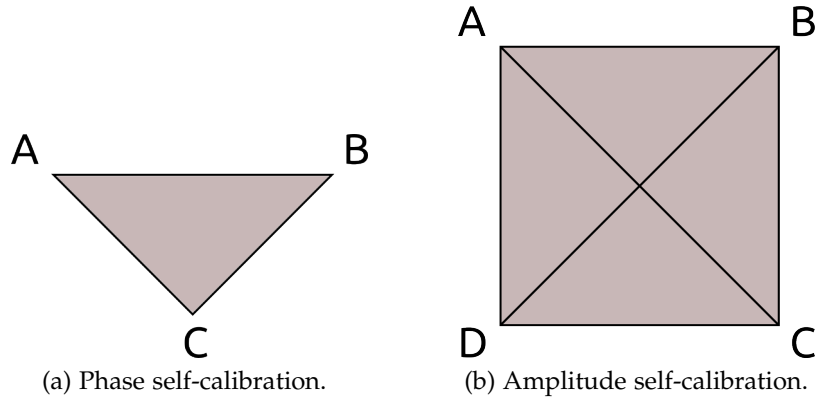


Figure 2.6: Closure relations geometry.

## 2.4 VISIBILITY AMPLITUDE SELF-CALIBRATION

Given four interferometer elements A, B, C and D as in Fig. 2.6b we can write:

$$\begin{aligned}
 A_{AB} &= \Psi_{AB} \times T_A T_B \\
 A_{BC} &= \Psi_{BC} \times T_B T_C \\
 A_{CD} &= \Psi_{CD} \times T_C T_D \\
 A_{DA} &= \Psi_{DA} \times T_D T_A
 \end{aligned} \tag{2-19}$$

where  $A_{AB}$  is the observed visibility amplitude coming from the antenna pair AB and  $\Psi_{AB}$  is the real amplitude that should have been observed without the corrupting amplitudes that each element of the baseline separately contributes,  $T_A$  and  $T_B$ .

In the case of visibility amplitudes the situation is slightly more complicated due to the multiplicative nature of station-based corrupting terms (see Eq. 2-16). By finding the right way to multiply and divide the equations of set 2-19, one can obtain a closure relation between observed and real, or error-free amplitudes

$$A_{ABCD} = \frac{A_{AB} \cdot A_{CD}}{A_{DA} \cdot A_{BC}} = \frac{\Psi_{AB} \cdot \Psi_{CD}}{\Psi_{DA} \cdot \Psi_{BC}} \times \frac{T_A T_B T_C T_D}{\cancel{T_D} T_A T_B T_C}. \tag{2-20}$$

Obviously one needs a minimum number of four elements in order to be able to perform corrections using the closure relation for visibility amplitudes (Fig. 2.6b).

In essence, self-calibration is the process of solving for the “best calibration parameters” that better match a given visibility data set to a model for the source. The model can be obtained through an initial guess, usually a first image of the source. With such a starting point one can perform many iterations of deconvolution and self-calibration. Every iteration yields a better image which is used as the starting point for subsequent imaging and self-calibration iterations. During self-calibration cycles one needs to be extremely cautious. First, the signal-to-noise ratio of the data needs to be high enough so as for the procedure to produce reliable results. Second, the process—especially amplitude self-

calibration—can introduce and “freeze” fake source structure. Consequently, it must be applied with extreme caution.

## 2.5 APPLICATIONS OF VLBI TO BLAZARS

Very-long-baseline interferometry is the only way of directly imaging the central regions in the vicinity (pc to sub-pc scales) of the SMBHs where the bulk of blazar activity takes place. The structure of blazars, as seen in VLBI maps, is typically dominated by a compact core and extended structure—usually a faint jet. The jet is in most cases non-symmetric, in that a counter-jet is rarely visible due to small viewing angle and subsequent de-boosting, and features of enhanced emission, referred to as knots or “blobs”. Further downstream extended and misaligned emission regions, with respect to the jet, may be visible.

Despite its cardinal role in the study of AGN, VLBI is limited by both minimum detectable flux density and minimum required source-compactness. While the first limit is obvious, the second calls for a few more words. Due to the very nature of aperture synthesis there will always be a gap in  $uv$ -coverage located at the center of the  $uv$ -plane. The problem arises from the size and locations of the antennas forming the array. The result of it being that an interferometer is characterized by a maximum source-extension that it can detect; the absence of compact structure renders sources invisible to the interferometer (see Section 2.2.3). In Porcas [2005] the concept of *brightness temperature sensitivity* is presented, that combines the two aforementioned limiting physical parameters ( $T_b \propto S/\nu^2\vartheta^2$  with  $S$  the flux density,  $\nu$  the frequency, and  $\vartheta$  the source size, see also Section 1.7.4). VLBI arrays are limited to the brightness temperature regime in excess of  $10^{6-7}$  K, a fact that makes them ideal observing machines for non-thermal processes, such as synchrotron emission, where  $T_b$  is higher than  $10^{6-7}$  K.

Owing to their extreme variability, understanding the blazar phenomenon calls for multi-frequency, multi-epoch VLBI observations. Combination of the two approaches has yielded insights into the inner workings of blazar jets. Since observations are possible in a broad frequency range, they can reveal the source spectral properties at vastly different scales ranging from sub-parsec to kiloparsecs away from the core (e.g. using the VLA). Observationally, the core usually exhibits a flat or inverted radio spectrum while the jet and the discernible knots downstream show steep power-law spectra reflecting the power-law energy distribution of the emitting particle populations.

It is multi-epoch VLBI that first hinted towards the existence of apparent faster-than-light expansion speeds for sub-milliarcsecond jet components [Gubbay et al., 1969; Cohen et al., 1971; Whitney et al., 1971; Cohen et al., 1977], a property of jets first theorized by Rees [1966]. Key questions that multi-epoch observations can address are whether structural changes can be associated with extreme flux density variations, whether extragalactic jets accelerate or knots follow ballistic motions within the flow, and what is the connection between radio outbursts and intense  $\gamma$ -ray emission. In a large number of sources there appears to be connection between the aforementioned observables. Often times variability can be attributed to traveling or standing features in jets, usually associated with shocks and/or instabilities depending on the physical conditions

of the flow [e.g. Hardee, 2002, 2007; Fromm et al., 2013a]. See Zensus [1997] for a review.

Apart from only total intensity, high-resolution polarimetry can reveal the magnetic field topology of blazar jets, being able to disentangle the contribution of sub-parsec regions to the global picture [see e.g. Gabuzda, 2003, for a review]. Attempts of combining all aforementioned approaches to a large enough sample of sources have the potential to infer statistically significant properties of the blazar population [see e.g. Arshakian et al., 2012; Lister et al., 2013; Homan et al., 2015].

### 2.5.1 Frequency-dependent core position

Most blazar VLBI maps at different frequencies feature one bright, usually unresolved emission region, most often referred to as the VLBI core and an extended jet, provided that sensitivity and angular resolution are sufficient. It has been shown both observationally and theoretically that the position of this core feature is not frequency-independent, a phenomenon discovered by Marcaide and Shapiro [1984] and afterwards studied by many researchers [Zensus et al., 1995a; Lobanov, 1998; Hada et al., 2011]. This “core” does not coincide with the nucleus or the central engine of the AGN, but rather a point near—or not so near—to the base of the jet where the transition between optically thick and thin regime occurs for the given observing wavelength. This point is situated closer to the jet base as frequency increases, with a frequency dependence that roughly scales as  $r_c(\nu) \propto \nu^{-1/k_r}$  [Lobanov, 1998], where  $\nu$  is the observing frequency. For a synchrotron self-absorbed core in equipartition, the index  $k_r$  is equal to 1 [Blandford and Königl, 1979].

Systematic study of the *core-shift* effect has the potential of revealing basic physical properties of the jet’s ultracompact flow such as the magnetic field strength, and the true distance of the core from the base of the jet. Additionally core-shift measurements can put competing theoretical models of jet formation and variability to the test (see Lobanov [2010] and references therein).





## PRACTICAL MILLIMETER-VLBI CALIBRATION AND IMAGING

---

### 3.1 MILLIMETER-VLBI OBSERVATIONS AND THE GMVA

High angular resolution is the main scientific driver for the advent of radio interferometric techniques. This goal can be achieved by either making use of longer baselines or by employing higher-frequency observations. Both approaches are challenging and are limited in the former case by the size of the Earth and in the latter by technical difficulties that need to be overcome. Space-VLBI missions are an extreme example of ultra-long baseline use, having shown significant success and yielded important scientific results [see e.g. Hirabayashi et al., 1998; Lobanov and Zensus, 2001; Gwinn et al., 2014].

But high resolution is only part of the objective. Observations at millimeter bands can penetrate the opacity barrier set by synchrotron self-absorption at lower frequencies, thus enabling emission regions close to the central engines of AGN to be imaged in the highest detail. This way one can gain important insights into the physical processes of these, otherwise self-absorbed and therefore inaccessible to longer wavelengths, regions. With the bulk of blazar activity taking place in regions close to the central engine, very-long-baseline interferometry at mm wavelengths (mm-VLBI) is essential for addressing questions as discussed in Section 1.11, being able to deliver both the highest angular resolution and penetrate the opacity barrier inaccessible to lower-frequency observations.

The global millimeter-VLBI array<sup>1</sup> (GMVA) is a heterogeneous *ad hoc* array formed by telescopes in Europe and the Very Long Baseline Array (VLBA) in USA, that come together into one instrument twice per year for VLBI observations at a frequency of 86 GHz (see Table 3.1). The angular resolution of the GMVA at 3 mm can reach down to  $\sim 50 \mu\text{as}$  and the linear scales it can probe depend on distance. Indicatively, at redshift equal to one,  $50 \mu\text{as}$  correspond to less than 0.5 pc. Stations that participate in GMVA runs in Europe are: Effelsberg 100-m, Onsala 20-m, IRAM Pico Veleta 30-m, Plateau de Bure interferometer ( $6 \times 15$ -m, phased array), Metsähovi 14-m, Yebes 40-m. In USA: VLBA  $8 \times 25$ m and the GBT 100-m. Future plans for the expansion of the array include the Korean VLBI Network KVN ( $3 \times 21$  m), LMT 50-m, Noto 32-m, and ultimately the phased ALMA that is going to greatly enhance the sensitivity of the array and the fidelity of data products.

At millimeter wavelengths, factors such as short atmospheric coherence times (variable at each station), the dry and wet component of the atmosphere and specific weather conditions, small number of low-effective-area antennas, high system temperatures, and even complicated scheduling requirements render VLBI experiments extremely difficult. However, observations with the GMVA at a frequency of 86 GHz can deliver angular resolutions down to  $\sim 50 \mu\text{as}$  and enhanced sensitivity. Typical detection threshold is in the range 0.05–0.3 Jy. The

<sup>1</sup> <http://www3.mpifr-bonn.mpg.de/div/vlbi/globalmm/>

TELESCOPE	LOCATION	EFFECTIVE DIAMETER (m)	SEFD (Jy)	POL.
Effelsberg	Germany	80	1500	Dual
Pico Veleta	Spain	30	700	Dual
Plateau de Bure	France	34	500	Dual
Metsähovi	Finland	14	17500	Dual
Onsala	Sweden	20	5500	LCP
Yebes	Spain	40	1700	LCP
VLBA ( $\times 8$ )	USA	25	2000	Dual

Table 3.1: Telescopes participating in the GMVA. The eight VLBA stations participating in GMVA runs are: BR – Brewster; FD – Fort Davis; KP – Kitt Peak; LA – Los Alamos; MK – Mauna Kea; NL – North Liberty; OV – Owens Valley; PT – Pie Town (see Fig. 3.5). The Plateau de Bure interferometer is a phased array comprising  $6 \times 15$ -m antennas.

lack of sensitivity and short atmospheric coherence at mm wavelengths can be overcome by increasing the observing bandwidth (see Eq. 2–3).

### 3.2 PRACTICAL MILLIMETER-VLBI DATA REDUCTION AND THE RATIONALE BEHIND IT

Upon completion of correlation, data collected by different antennas at different locations on the globe can be thought of and treated as, a single data set. But attempting to image such a “raw” data set is generally a fruitless exercise. This is where the main complication of mm-VLBI arises. Dealing with short wavelengths, the correlator has to feature an extremely detailed model for geometric delay compensation. Accuracy to a fraction of the observed wavelength translated in time delay is of uttermost importance. Such a model is almost never available; even if it is, unpredictable propagation delays in the atmosphere, time standard offsets, and even recent earthquakes can alter the characteristics of individual observations. As such, after correlation, visibility phases need to be further corrected for residual delays and visibility amplitudes that also need to be converted from arbitrary correlator units to radio astronomy relevant units, namely Jy.

#### 3.2.1 *A priori calibration in AIPS*

The amplitude and phase calibration is performed with the National Radio Astronomy Observatory’s (NRAO) Astronomical Image Processing System (AIPS) [Greisen, 1990]. AIPS is a widely used suite of general purpose tasks intended for interferometric data reduction. An important point to keep in mind when working with AIPS has to do with its philosophy. All calibration actions do not directly alter the data; they are rather stored in so-called calibration or extension tables and it is these tables that are applied to the data in the very final step of reduction. The extension tables follow a nomenclature according to the specific

effect they have on the data. For example bandpass correction (with BPASS) creates the BP table or those that are created by flagging tasks are called FG tables and so on. In the following, text in upper case refers to AIPS tasks.

Fig. 3.2 shows a flow chart of indicative calibration steps. The first step is to load the raw data, using the task FITLD. They come usually in the form of a multi-source, *uvfits* file. If data is not properly arranged, one needs to index and sort them in chronological order using INDXR. A list of all scans with start and end times along with the target source can be accessed through LISTR. Provided that sub-arrays are not present we continue to the next step. However, data from GMVA are very often obtained using the technique of sub-arraying. That is, having some telescopes of the array observing a source while others, either perform pointing scans to ensure correct pointing or observe another source due to observability constraints (e.g. low declination for a specific station). This is evident from the output of LISTR. If duplicate scan time ranges are present, then sub-arrays were used and data need to be re-arranged accordingly. In this case the task USUBA, that automatically identifies and assigned data to different sub-arrays, is used. INDXR needs to be invoked once more to index the visibilities. The next step is the first to affect the data. It is the parallactic angle correction with CLCOR, as a result of the alt-azimuth mounts most radio telescopes use. Here we apply a correction for the diurnal turning of phase due to the use of circular polarization feeds in VLBI stations. Special care must be taken for telescopes that are equipped with linear polarization feeds like the 30-m telescope at Pico Veleta, Spain. This is done with the tasks PRTAN and TABED before the use of CLCOR.

*Sub-arraying*

### 3.2.2 *Manual phase calibration and fringe fitting*

At this point the process branches out into two calibration phases, one for the visibility phase and one for the amplitude (see Fig. 3.2). They can be performed in a interchangeable order. Starting with phases we incrementally apply an initial manual phase calibration. This is needed due to presence of residual phase delays in the data (e.g. due to clock offsets) causing the phases to vary with frequency. Manual phase calibration is performed (i) to remove the slopes caused by delays and (ii) to align the phase offsets between IFs. Fig. 3.1 shows data before and after the application of a manual phase calibration. The process is as follows. After inspecting the data and finding a time range where a strong source is observed and fringes are established, with the task FRING we calculate single subband phase rates and delays [see e.g. [Martí-Vidal et al., 2012](#)]. The manual phase calibration is first performed for the american stations (VLBA) and then by connecting to european stations and adding baselines, where fringes are clearly seen, we gradually build an initial solution table that takes care of the chief phase corrupting effects with respect to the preselected reference antenna. The selection of a reference antenna is a parameter that plays an important role in the whole process and needs to be carefully chosen. It ideally is an antenna that is known to perform well and most baselines with it show fringes. An antenna at the center of the array is also preferred but in VLBI this is a tricky notion.

For the estimation of multi-band delays and rates, the approach of fringe fitting was invoked [[Schwab and Cotton, 1983](#); [Alef and Porcas, 1986](#); [Cotton,](#)

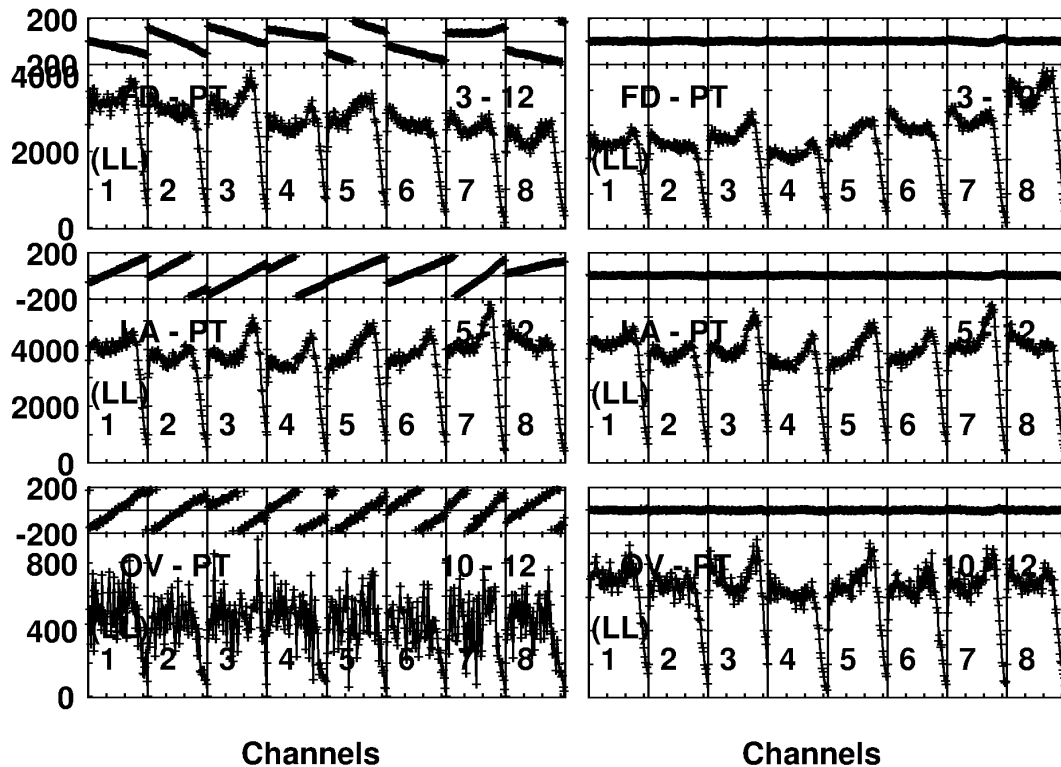
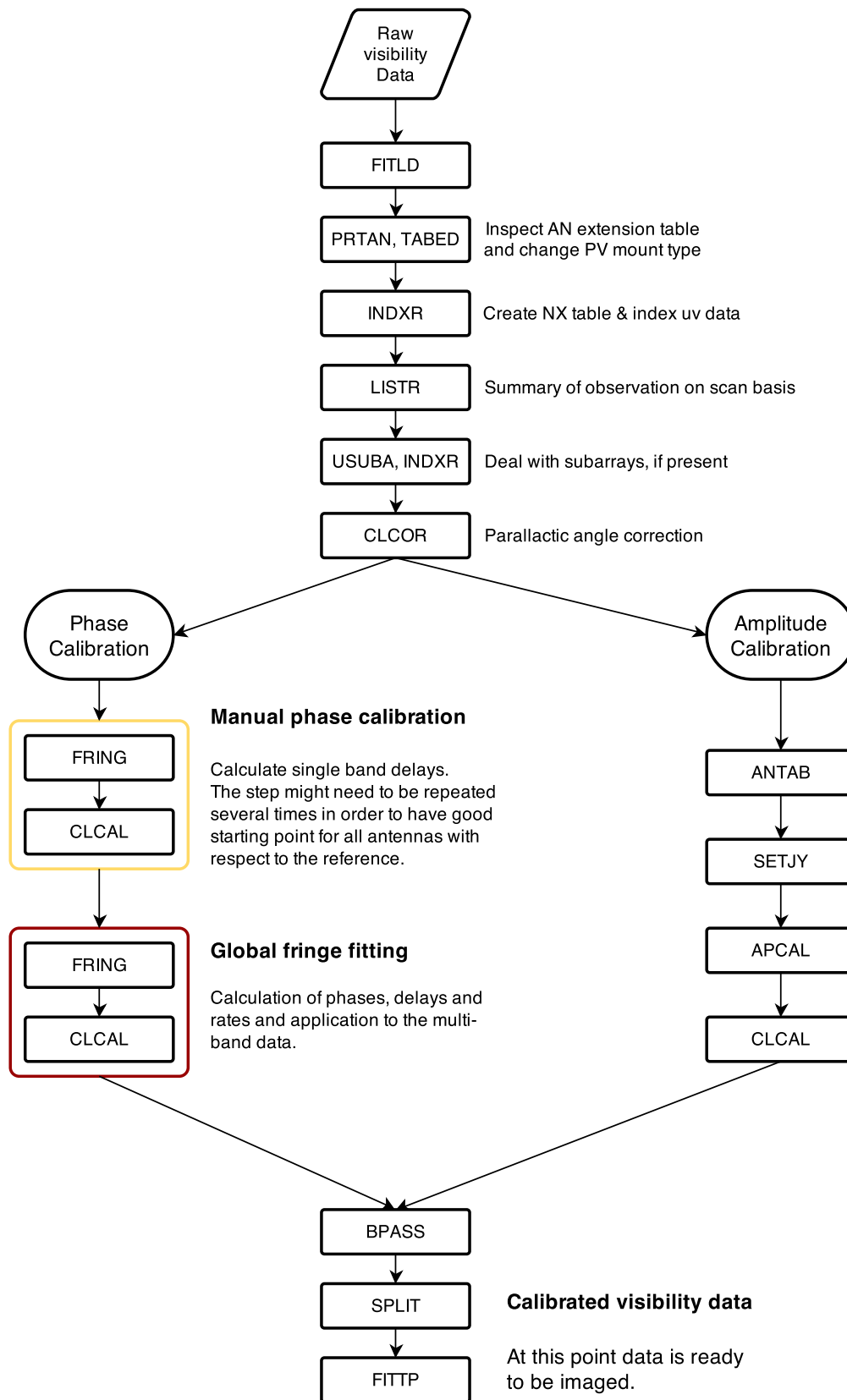


Figure 3.1: The effect of manual phase calibration on the data. Here, cross-power spectra of three VLBA baselines are shown. Those between FD–PT, LA–PT, and OV–PT for 3C 454.3. Data on the left are before the application of manual phase calibration, while on the right, after it. Note the slopes in phases (upper panels) that are gone after application of manual phase calibration. Original image courtesy of Dhanya G. Nair (MPIfR).

1995; Zensus et al., 1995b]. A linear fit to the phase variation across time and frequency is performed yielding the aforementioned estimates to be applied to the data. The fit is performed in a *solution interval*—that is the time for which the phase varies almost linearly—thus a simple linear fit is a reasonable approximation. Within AIPS the solution interval can be varied to reach the SNR needed but it cannot exceed the scan length. Changes to the data, produced by each task, must be constantly monitored for undesired effects. Generic data inspection packages, in order of frequency of usage are: SNPLT, POSSM, LISTR, PRTAN and others; The former two are to be used most often to plot the solution (SN) and calibration (CL) tables after every correction step. Corrupted beyond recovery data can be flagged with tasks such as UVFLG or TVFLG. Extension tables can be deleted using the verb EXTDEST and files can be removed invoking ZAP.

### 3.2.3 Amplitude calibration

The prime purpose of this step is to convert visibility amplitudes from arbitrary correlator units into usable flux density units (Jy). Before doing so though, signal attenuation due to propagation through the Earth’s atmosphere and elevation-dependent gain variations, at each station, have to be taken into account. Atmospheric attenuation, showing increasing severity with frequency, is due to

Figure 3.2: Flow chart of the *a priori* visibility data calibration procedure.

absorption of incoming radiation at certain bands. At 43 GHz and 86 GHz signal loss is rather significant and needs to be rectified. Visibility data from the GMVA come with tabulated values for the recorded  $T_{\text{sys}}$ , atmospheric conditions, and gain curves in polynomial form. These are read into AIPS with the task ANTAB (see Fig. 3.2) that outputs the system temperature (TY) and gain curve (GC) tables. Before proceeding, the Stokes I flux density of all sources in the multi-source file need to be specified with SETJY (e.g. from single-dish measurements). The four Stokes parameters quantify the polarization state of incident radiation [see e.g. Pacholczyk, 1970]. If interested in polarization imaging, all Stokes parameters (I, Q, U, V) flux densities have to be provided. The task APCAL performs the actual amplitude calibration and opacity correction given the receiver temperatures and a zenith opacity as starting points. This mode of APCAL requires the dedicated weather information (WX) file coming from each station in order to generate the SN table to be applied to the data with the task CLCAL. The temperatures present in the WX file are used for the calculation of the atmospheric temperature,  $T_{\text{atm}}$ , which is needed for converting the slope of the skydip plot into atmospheric opacity. The procedures for opacity and elevation-dependent gain correction are equivalent to those applied in the case of single-dish data. For a treatment in the context of single-dish observations see Section 5.2.1.

After the visibility amplitudes are corrected, using the measured system temperatures and elevation-dependent gain curves, we proceed with conversion from correlator units into Jy. Each of the telescopes comprising a baseline records a certain noise signal. In VLBI, it is the amount of correlated noise that constitutes the visibility amplitude. That is because antennas comprising a given baseline can be—and in practice are—so far away from each other that rarely suffer from the same interference sources. Each antenna at its recording end, registers a system temperature  $T_{\text{sys}}$  that is the contribution of all noise sources along with that of the source of interest (see Fig. 3.3a). It is the task of the correlator to report the amount of correlated noise and then by—in essence—multiplying with the recorded  $T_{\text{sys}}$ , one has a figure for the visibility amplitude (see Fig. 3.3b). More specifically, the conversion between correlator units,  $S_{\text{cor}}$ , and flux density in Jy,  $S_{\text{Jy}}$ , is done as:

$$S_{\text{Jy}} = S_{\text{cor}} \frac{1}{\eta} \frac{\sqrt{\text{SEFD}_A \text{SEFD}_B}}{\sqrt{2 \Delta\nu \Delta\tau}} \quad (3-1)$$

where  $\eta$  is a loss factor due to data sampling ( $\eta = 0.64$  for 1 bit sampling and 0.88 for 2 bit sampling). The system equivalent flux density (SEFD) is defined for each station as

$$\text{SEFD}_A = \frac{T_{\text{sys},A}}{g_A} \quad (3-2)$$

here for station A, with  $g$  the station gain.

Due to the properties of the electronic components used, the bandpass shows variable response with frequency. Thus the last step is the determination of the bandpass response. This is done by the task BPASS with the use of a strong observed source. Initial calibration of visibility data is now completed and sources

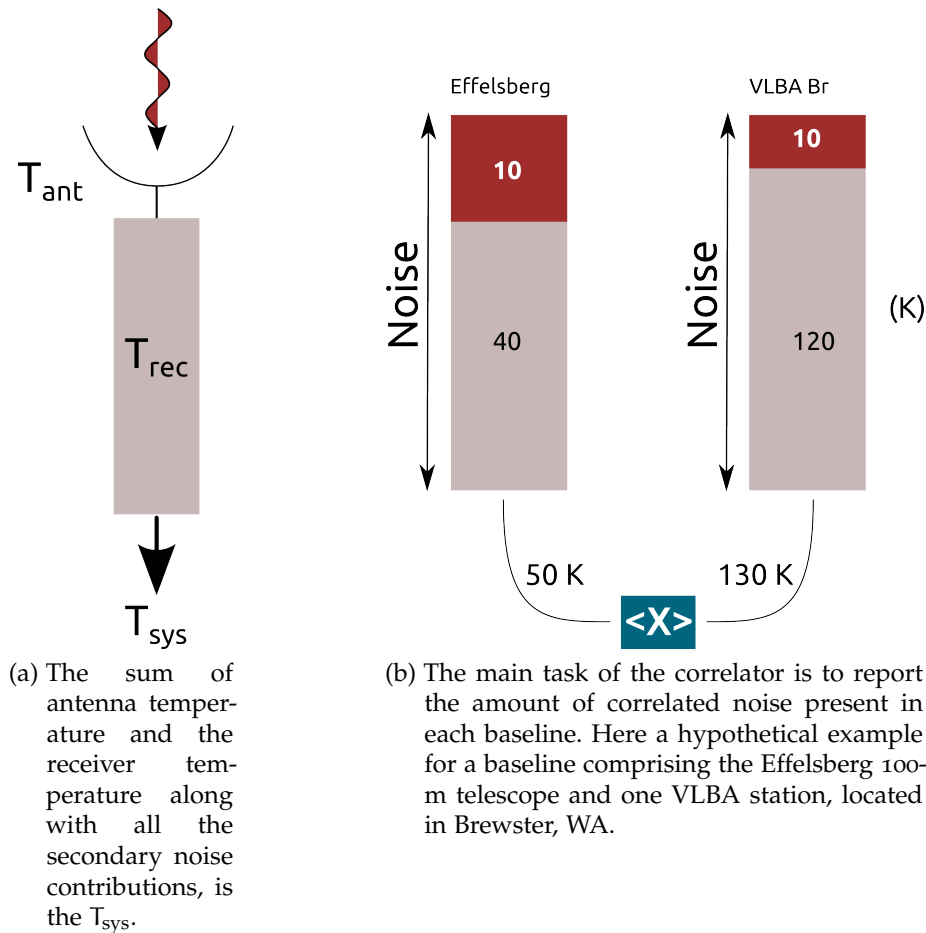


Figure 3.3: System temperature and other noise contributions, with the amount of correlated noise being the important observable of VLBI.

can be separately extracted from the large multi-source file with SPLIT which averages the data in frequency and time. Time averaging is also possible in DIFMAP<sup>2</sup> [Shepherd et al., 1994; Shepherd, 1997]. With FITTP the resulting uv-data can be saved in the convenient *fits* format for later further processing and imaging with DIFMAP.

#### 3.2.4 Imaging and model fitting with DIFMAP

For the subsequent imaging and analysis of data we have used the DIFMAP software [Shepherd, 1997; Shepherd et al., 1994]. After importing the visibility data, continuous deconvolution cycles are performed with the application of the CLEAN algorithm [Högbom, 1974] followed by phase self-calibration. Amplitude self-calibration, with decreasing integration time, is performed after every sequence of CLEAN and phase self-calibration and only when a representative model for the source is obtained. Extreme caution has to be exercised in order not to artificially and/or irreversibly alter the morphology of the source, by introducing or eliminating spurious/fake or real source features. This is accomplished by constant inspection of the results and by preventing the standard deviation of visibility amplitudes to vary more than a certain figure (e.g. 10%).

<sup>2</sup> DIFMAP is a stand-alone imaging program, not part of the AIPS suite.

In order to parameterize each image and quantitatively handle the relevant quantities, the MODELFIT algorithm within DIFMAP can be employed. The procedure involves fitting two-dimensional Gaussian components directly to the fully calibrated visibility data. In principle, each two-dimensional Gaussian component is described by six parameters. Here, circular components were used in order to reduce the number of free parameters which in this case are: the component flux density, its size expressed as the full width at half maximum (FWHM) of the two-dimensional Gaussian and its position angle (PA) expressed in degrees from North to South, between  $0^\circ$  and  $180^\circ$  in the clockwise and  $0^\circ$  to  $-180^\circ$  in the counterclockwise direction. The data at each frequency and each observing epoch are modeled separately. To simplify the analysis and reduce the number of unconstrained parameters during the data reduction, only circular Gaussian components are used. Initially, the number of components is unrestricted. The limit to the number of components was set by testing whether the presence of an additional one causes the  $\chi^2$  value for the fit to decrease significantly.

MODELFIT components do not necessarily represent physical jet emission features. In fact, they could just accommodate a mathematical requirement of the model, trying to describe the complex structure of an extragalactic jet [Lister et al., 2009]. Particularly here, where the time baseline of 43/86 GHz data spans three years and sampling is rather sparse. Consequently, we adopted the criterion that a physical region of enhanced emission within the jet should repeatedly appear in three consecutive observing epochs. We relax this criterion for 86 GHz data and only when images in specific intermediate epochs suffer from low dynamic range, preventing us from discerning a component whose presence is indicated by data in adjacent epochs.

Uncertainties of model fitting are taken as follows. For the component flux density an uncertainty of 10% is a reasonable and conservative estimate that is widely adopted [Lister et al., 2009, 2013]. The error in the position is set to 1/5 of the epoch beam size, if the component is unresolved, otherwise we take 1/5 of the component size as an estimate of the uncertainty. The beam size for each observing epoch is calculated through  $b_\phi = \sqrt{b_{\text{maj}} b_{\text{min}}}$  [Lobanov, 2005].

Uncertainty in the PA is the direct translation of the positional uncertainty ( $\Delta XY$ ) from mas to degrees using the simple trigonometric formula  $\Delta PA = \arctan(\Delta XY/r)$ , with  $r$  the radial separation in mas.

Positive identification of jet emission features, across epochs and frequencies, is a laborious and ambiguous task as a result of the process of phase self-calibration (loss of absolute position information) and the inherent complex nature of extragalactic jets. In the process of obtaining the final kinematical model for the source at each frequency, the component separation, size and flux density were used as parameters combined with the requirement that they should vary smoothly and in a way dictated by physical processes.



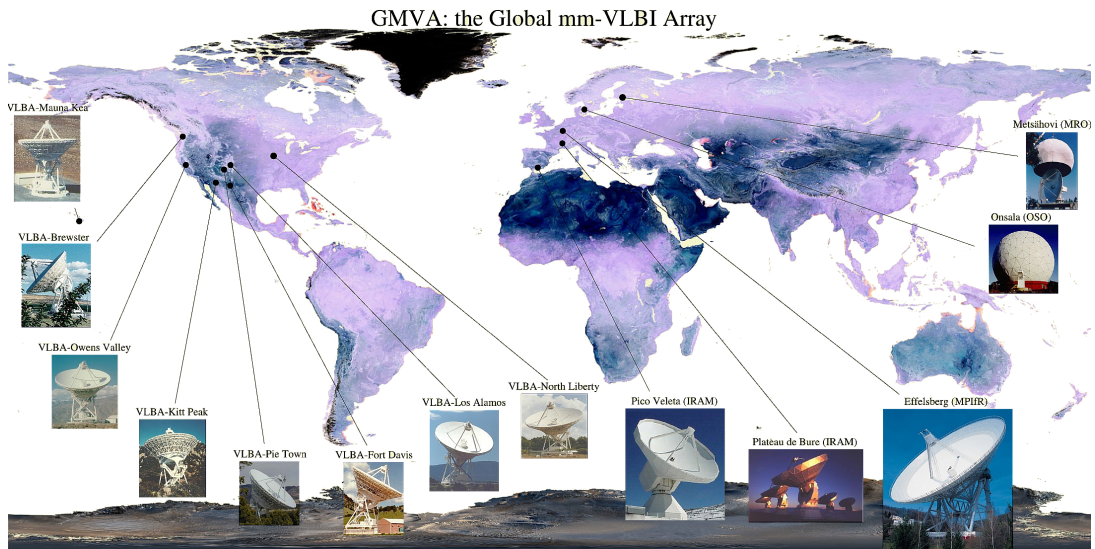


Figure 3.4: The Global Millimeter-VLBI Array (GMVA). Original image: T. P. Krichbaum (MPIFR).

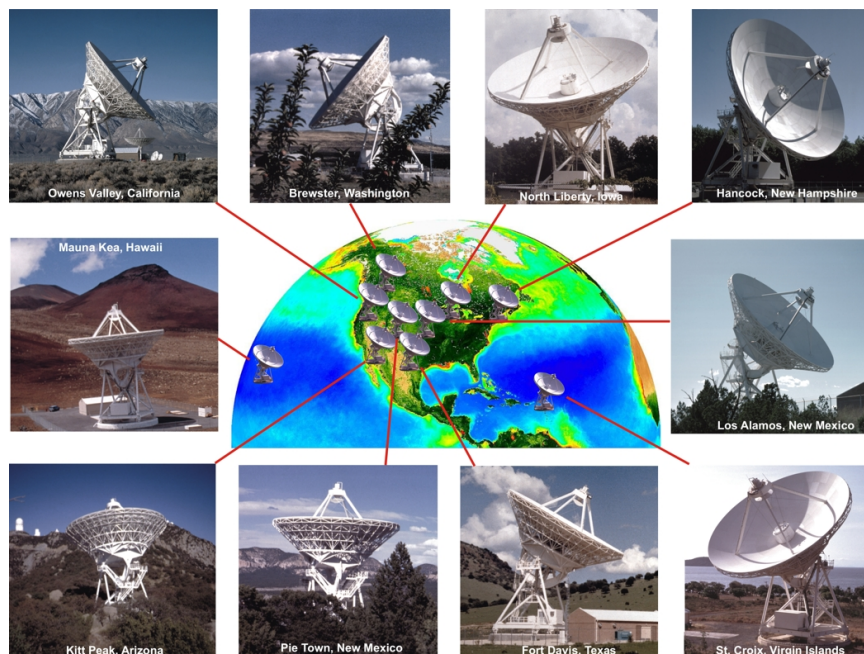


Figure 3.5: The Very Long Baseline Array (VLBA). Image courtesy of NRAO, AUI and Earth image courtesy of the SeaWiFS Project NASA, GSFC and ORBIMAGE.



---

#### 4.1 INTRODUCTION

Blazars are among the most copious and variable emitters of radiation in the Universe. They inherently feature double, opposite-directed fast plasma outflows, most likely driven by the conversion of gravitational potential energy to electromagnetic, in the immediate vicinity of spinning supermassive black holes (SMBHs) [Blandford and Znajek, 1977] or from the accretion disk surrounding them [Blandford and Payne, 1982, cf. Meier et al. [2001]; Blandford [2001]; Meier [2003] for reviews]. The linear extent of those jets greatly exceeds the dimensions of their hosts and can reach undisrupted, up to a few million parsecs (pc).

Their double-humped spectral energy distribution (SED), first peaks between radio and soft X-rays, due to synchrotron emission and then at keV to GeV energies, likely owing to the Inverse Compton (IC) process [see e.g. Ulrich et al., 1997; Urry, 1999; Georganopoulos et al., 2001]. However, the detailed processes giving rise to their characteristics are still under intense debate. Outstanding questions—among others—include: (i) which mechanism(s) drive their rapid variability across the whole electromagnetic spectrum, (ii) where in the jet does the high-energy emission originate and (iii) what is the target photon field for IC up-scattering; the dusty torus infra-red (IR) radiation, broad-line region (BLR) or accretion disk photons? Through their observational predictions, different scenarios can be put to the test. Theoretical considerations indicate that the bulk of  $\gamma$ -ray emission should be emanating from regions of low ambient density otherwise the pair production process,  $\gamma + \gamma \rightarrow e^- + e^+$ , would prohibit  $\gamma$ -ray photons to escape the MeV/GeV production region, introducing a high  $\gamma$ -ray opacity environment [Dermer et al., 2012; Tavecchio and Ghisellini, 2012]. Nonetheless, observational evidence is still conflicting, indicating that GeV-emission can be produced close to the central engine, within the broad-line region (BLR), or even in the vicinity of the accretion disk some 100 Schwarzschild radii from the SMBH [e.g. Blandford and Levinson, 1995]. Other findings lend support to the “larger-distance scenario”, whereby MeV/GeV photons originate from shocks, shock-shock interaction or turbulent cells within the plasma flow parsecs downstream the jet [see e.g. Valtaoja and Teräsranta, 1995; Marscher, 2014].

Correlated variability and flare timing analyses, between the radio and  $\gamma$ -ray bands place the production site of  $\gamma$  rays few pc upstream of the mm-band unit-opacity surface [Fuhrmann et al., 2014; Max-Moerbeck et al., 2014], while other findings point towards shocked regions further downstream the jet [Valtaoja and Teräsranta, 1995; León-Tavares et al., 2013]. With the bulk of blazar activity taking place in regions close to the central engine, very-long-baseline interferometry (VLBI) at mm wavelengths is essential for addressing those questions, being able to deliver both the highest angular resolution and penetrate the opacity barrier inaccessible to low-frequency observations. As an example,

work based on 7 mm-VLBI and flux monitoring of OJ287 places the  $\gamma$ -active region more than 14 pc away from its central engine [Agudo et al., 2011].

The blazar PKS 1502+106 was detected by the *Fermi* Gamma-ray Space Telescope [Ritz, 2007] in 2008 August during a rapid and strong  $\gamma$ -ray flare. This was followed by high and variable flux over the subsequent months [Ciprini, 2008; Abdo et al., 2010], triggering an intensive multi-wavelength campaign covering the radio, optical, UV, and X-ray bands [Pian et al., 2011]. The flare appeared simultaneously at optical/UV/X-rays in contrast to its radio counterparts which appeared significantly delayed [Fuhrmann et al., 2014, see also Chapter 5].

PKS 1502+106 (OR 103, S3 1502+10, J1504+1029) at a redshift of  $z = 1.8385$ ,  $D_L = 14176.8$  Mpc [Adelman-McCarthy et al., 2008], is a powerful blazar classified as a Flat Spectrum Radio Quasar (FSRQ) with the mass of its central engine  $\approx 10^9 M_\odot$  [Abdo et al., 2010, and references therein]. In X-rays, it is a known and significantly variable source [George et al., 1994]. Radio interferometric observations with the VLA at 1.4 GHz reveal the large-scale morphology of PKS 1502+106, with a straight jet at a position angle (PA) of about  $-160^\circ$  [Cooper et al., 2007]. Previous VLBI findings suggest instead, a curved, asymmetric jet and a multi-component, core-dominated source [Fey et al., 1996] with very fast apparent superluminal motion of up to  $\approx 37 \pm 9 c$  [An et al., 2004].

In the following, we present a full VLBI study of PKS 1502+106 at three frequencies, namely 15, 43, and 86 GHz (wavelengths of 20, 7 and 3 mm, respectively). Our millimeter VLBI monitoring of PKS 1502+106 was triggered by the period of flaring activity that the source underwent and started in early 2008. Data at 43 and 86 GHz span the time period between 2009 May and 2012 May. VLBI monitoring at mm wavelengths is complemented by 19 epochs of VLBA observations at 15 GHz from the MOJAVE program [Lister et al., 2009].

Throughout the chapter we adopt  $S \propto \nu^\alpha$  and the following cosmological parameters:  $H_0 = 71 \text{ km s}^{-1} \text{ Mpc}^{-1}$ ,  $\Omega_m = 0.27$ ,  $\Omega_\Lambda = 0.73$ . An angular separation of 1 milliarcsecond (mas) translates into a linear distance of 8.53 pc. At the redshift of PKS 1502+106 a proper motion of 1 mas/yr corresponds to an apparent superluminal expansion speed of 79.04 c.

## 4.2 OBSERVATIONS AND COMPLEMENTARY DATA

### 4.2.1 High frequency 43 GHz and 86 GHz GMVA data

The mm-VLBI observations with the Global Millimeter VLBI Array (GMVA) comprise 6 epochs spanning the period between 2009 May 7 and 2012 May 18 with observations obtained twice per year, apart from 2010 October. The experiment included the following stations. In Europe: Effelsberg(100 m, Ef), Onsala (20 m, On), Pico Veleta (30 m, Pv), Plateau de Bure ( $6 \times 15$  m phased array, Pb), Metsähovi (14 m, Mh), Yebes (40 m, Ys); in the USA, all Very Long Baseline Array (VLBA) stations that are equipped with 86 GHz receiving systems, namely Br, Nl, Pt, La, Fd, Kp, Ov, and Mk ( $8 \times 25$  m). For a complete presentation of the observational layout refer to Tables 4.1 and 4.2. The GMVA experiment was carried out in dual polarization mode at the stations where this setup is available (Ys and On record only LCP) at a bit rate of 512 Mbits/s. The observing strategy at 86 GHz included 7 minute scans of PKS 1502+106 bracketed by

OBS. DATE	ARRAY	$S_{\text{peak}}^{(1)}$ (Jy beam <sup>-1</sup> )	rms <sup>(1)</sup> (mJy beam <sup>-1</sup> )	$S_{\text{total}}^{(1)}$ (Jy)	$b_{\text{maj}}^{(2)}$ (mas)	$b_{\text{min}}^{(2)}$ (mas)	PA <sup>(2)</sup> (°)
2009-05-08 <sup>I</sup>	VLBA <sub>8</sub>	3.47	0.9	3.70	0.56	0.17	-21.0
2009-10-13 <sup>II</sup>	VLBA <sub>8</sub>	2.20	1.2	2.56	0.73	0.17	-17.7
2010-05-07 <sup>III</sup>	VLBA <sub>8</sub>	0.53	0.7	0.65	0.60	0.18	-20.7
2011-05-08 <sup>IV</sup>	VLBA <sub>8</sub>	0.93	0.9	1.18	0.61	0.24	-20.2
2011-10-09 <sup>V</sup>	VLBA <sub>8</sub>	0.95	0.7	1.13	0.58	0.18	-21.8
2012-05-18 <sup>VI</sup>	VLBA <sub>8</sub>	0.82	0.8	0.92	0.61	0.20	-18.2

Table 4.1: Summary of the 6 observing epochs of PKS 1502+106 at 43 GHz. Data from dedicated GMVA observing sessions. Station designations: VLBA<sub>8</sub> = Br – Fd – Kp – La – Mk – Nl – Ov – Pt; <sup>(1)</sup> Peak flux density, off-source rms noise level and total flux density of all MODELFIT components. <sup>(2)</sup> Major and minor axes along with the position angle of the restoring beam. All parameters listed in the table correspond to the final, uniform weighted untapered, MODELFIT image.

equally lengthed scans of calibrator sources for the full duration of the session. The 43 GHz scans using only the VLBA were performed during the time when European stations were performing scans for pointing correction. Data were correlated at the MPIfR facility in Bonn, Germany and reduced according to the methods described in Chapters 2 and 3.

#### 4.2.2 15 GHz MOJAVE survey data

In this work, we have made use of the publicly available data from the Monitoring Of Jets in Active galactic nuclei with VLBA Experiments (MOJAVE) program<sup>1</sup> [Lister et al., 2009]. Data on PKS 1502+106 comprise 19 observing epochs that span the period between 2002 August 12 to 2011 August 15 and apart from few occasions all ten VLBA stations participate in the observations (see Table 4.3). Data are provided as fully self-calibrated visibilities and as such the necessary steps of imaging and model fitting were performed, following the steps described in Section 3.2.2 of the previous chapter.

#### 4.2.3 Single-dish 15, 43 and 86 GHz F-GAMMA data

Single-dish, multi-frequency monitoring data were obtained within the framework of the long-term *Fermi*-GST AGN Multi-frequency Monitoring Alliance (F-GAMMA) program<sup>2</sup> [Fuhrmann et al., 2007; Angelakis et al., 2010; Fuhrmann et al., 2014]. F-GAMMA is the coordinated effort for simultaneous observations at 11 bands in the range between 2.64 GHz to 345 GHz. Regular monthly observations including the Effelsberg 100-m and IRAM 30-m telescopes are closely coordinated to ensure maximum coherency. The observing strategy utilizes *cross-scans*; that is slewing over the source in both, azimuth and elevation, directions. After initial flagging, pointing offset, opacity, sensitivity, and gain-curve corrections are applied to the data as described in the dedicated chapter on single-dish

<sup>1</sup> <http://www.physics.purdue.edu/MOJAVE/>

<sup>2</sup> <http://www3.mpifr-bonn.mpg.de/div/vlbi/fgamma/fgamma.html>

OBS. DATE	ARRAY	$S_{\text{peak}}^{(1)}$ ( $\text{Jy b}^{-1}$ )	$\text{rms}^{(1)}$ ( $\text{mJy b}^{-1}$ )	$S_{\text{total}}^{(1)}$ (Jy)	$b_{\text{maj}}^{(2)}$ (mas)	$b_{\text{min}}^{(2)}$ (mas)	$\text{PA}^{(2)}$ ( $^{\circ}$ )
2009-05-07 <sup>I</sup>	VLBA <sub>8</sub> + Pb, Pv, On, Ef	2.23	0.6	2.85	0.27	0.06	−3.9
2009-10-13 <sup>II</sup>	VLBA <sub>8</sub> + Pv, Pb, On, Ef	0.88	0.9	1.10	0.20	0.05	−5.2
2010-05-06 <sup>III</sup>	VLBA <sub>7</sub> –NI + Pv, Pb, On, Mh, Ef	0.49	0.4	0.61	0.32	0.08	−10.4
2011-05-07 <sup>IV</sup>	VLBA <sub>8</sub> + Pv, Pb, On, Mh, Ef	0.76	0.5	0.89	0.29	0.07	−4.8
2011-10-09 <sup>V</sup>	VLBA <sub>8</sub> + Ys, Pv, On, Ef	0.57	1.7	0.65	0.20	0.07	−4.2
2012-05-17 <sup>VI</sup>	VLBA <sub>7</sub> –Fd + Ef, On, Pv, Ys	0.54	1.2	0.62	0.24	0.06	−5.8

Table 4.2: Summary of the 6 observing epochs of PKS 1502+106 at 86 GHz. Data from dedicated GMVA observing sessions. Station designations: VLBA<sub>8</sub> = Br – Fd – Kp – La – Mk – NI – Ov – Pt; Ef – Effelsberg; Mh – Metsähovi; On – Onsala; Pb – Plateau de Bure; Pv – Pico Veleta; Ys – Yebes; <sup>(1)</sup> Peak flux density, off-source rms noise level and total flux density of all components. <sup>(2)</sup> Major and minor axes along with the position angle of the restoring beam. All parameters listed in the table correspond to the final, untapered, uniform weighted, MODELFIT image.

data of the present thesis and in [Fuhrmann et al., 2014; Angelakis et al., 2015; Nestoras et al., in prep.].

From the broad F-GAMMA frequency coverage, in the current chapter, only the bands matching our mm-VLBI frequencies, namely those at 14.60, 43.00 and 86.24 GHz, are employed.

#### 4.2.4 Fermi/LAT $\gamma$ -ray data

*Fermi*-GST (hereafter *Fermi*) is the latest generation space-bound telescope, built for and dedicated to detailed observations of the high-energy sky. Since its launch in 2008 the Large Area Telescope (LAT) on board scans the sky every 3 hours in the energy range between  $\sim 20$  MeV to  $>300$  GeV, providing unprecedented spatial, spectral, and temporal coverage.

Specifically, the LAT is a pair conversion telescope equipped with an anti-coincidence shield, sensitive to cosmic-ray, electrically charged particles which should be rejected [Atwood et al., 2009]. Incident  $\gamma$ -ray photons, convert to  $e^-e^+$  pairs while passing through the bulk of high atomic number material. The localization of the source is achieved by reconstruction of the trajectories of the  $e^-e^+$  pairs.

In the analysis to follow, we make use of the monthly-binned  $\gamma$ -ray light curve of PKS 1502+106 already presented in Fuhrmann et al. [2014], covering the time period between MJD 54707 (2008.66) and MJD 55911 (2011.96). Details of the light curve and  $\gamma$ -ray data analysis are given in the aforementioned reference [see also Abdo et al., 2010].

OBS. DATE	ARRAY	$S_{\text{peak}}^{(1)}$ (Jy beam $^{-1}$ )	rms $^{(1)}$ (mJy beam $^{-1}$ )	$S_{\text{total}}^{(1)}$ (Jy)	$b_{\text{maj}}^{(2)}$ (mas)	$b_{\text{min}}^{(2)}$ (mas)	PA $^{(2)}$ ( $^{\circ}$ )
2002-08-12	VLBA $_{10}$	1.17	1.5	1.62	0.97	0.44	-2.8
2003-03-29	VLBA $_{10}$	1.29	1.5	1.18	0.95	0.43	1.4
2004-10-18	VLBA $_{10}$	0.56	1.0	0.10	1.05	0.42	-8.0
2005-05-13	VLBA $_{10}$	0.51	0.9	0.87	1.04	0.46	-8.2
2005-09-23	VLBA $_{10}$ -NI	0.77	0.6	1.12	0.93	0.41	-0.7
2005-10-29	VLBA $_{10}$	0.85	0.5	1.14	1.03	0.46	-8.8
2005-11-17	VLBA $_{10}$ -Br	0.90	1.0	1.18	1.21	0.46	-11.8
2006-07-07	VLBA $_{10}$	1.16	1.8	1.53	1.09	0.45	-9.6
2007-08-16	VLBA $_{10}$	1.10	0.8	1.51	0.97	0.49	-7.8
2008-06-25	VLBA $_{10}$ -Br	1.33	0.8	1.74	1.10	0.40	-7.7
2008-08-06	VLBA $_{10}$	1.33	0.8	1.71	1.04	0.48	-7.3
2008-11-19	VLBA $_{10}$	1.58	0.7	1.98	1.04	0.50	-6.4
2009-03-25 <sup>I</sup>	VLBA $_{10}$ -Hn	2.79	0.9	3.17	1.12	0.50	-3.2
2009-12-10 <sup>II</sup>	VLBA $_{10}$	1.19	0.8	1.48	1.02	0.47	-12.7
2010-06-19 <sup>III</sup>	VLBA $_{10}$	0.71	0.6	0.98	1.14	0.47	-12.8
2010-08-27	VLBA $_{10}$	0.74	0.5	0.99	0.99	0.44	-5.7
2010-11-13	VLBA $_{10}$	0.86	0.6	1.12	1.05	0.42	-9.4
2011-02-27 <sup>IV</sup>	VLBA $_{10}$	0.98	0.7	1.23	0.93	0.42	0.5
2011-08-15 <sup>V</sup>	VLBA $_{10}$	1.11	0.9	1.35	1.17	0.44	-1.1

Table 4.3: Summary of the 19 observing epochs at 15 GHz of PKS 1502+106 obtained within the MOJAVE monitoring program. VLBA $_{10}$  station designations: Br – Brewster; Fd – Fort Davis; Hn – Hancock; Kp – Kitt Peak; La – Los Alamos; Mk – Mauna Kea; NI – North Liberty; Ov – Owens Valley; Pt – Pie Town; Sc – St. Croix. <sup>(1)</sup> Peak flux density, off-source rms noise level and total flux density of all components. <sup>(2)</sup> Major and minor axes along with the position angle of the restoring beam. All parameters listed in the table correspond to the final, uniform weighted, untapered, MODELFIT image.

### 4.3 PKS 1502+106 JET PHENOMENOLOGY

#### 4.3.1 *Parsec-scale jet morphology*

Modelfit VLBI maps at 15, 43 and 86 GHz are presented in Fig. 4.1, 4.2 and 4.3, respectively. Evidently, PKS 1502+106 exhibits a pronounced core-dominated morphology with a continuous one-sided jet at parsec scales, owing to relativistic beaming.

The entire series of VLBI images—at all frequencies—features a distinct region of enhanced emission responsible for the bulk of observed flux density (see Section 4.3.3). To this brightest feature at all instances, we refer to as the core. For the purposes of our analysis we assume it stationary for the full length of our observations and across-frequencies. This is consistent with our finding of non-significant, within the positional uncertainties, frequency-dependent core-shifts at our observing frequencies (see Section 4.5.2).

In addition to the core component, the 15 GHz jet can be decomposed into 3 to 4 distinct model-fit components at each observing epoch. At 43 GHz the jet is better represented by 3 components, while at 86 GHz we have used a number of model-fit components ranging between 2 and 4 due to varying dynamic range of the images and intrinsic structural and flux density changes of the source. Nevertheless, we are able to cross-identify 2 components between all three frequencies and 3, only between 43 and 86 GHz. In our analysis we use the following nomenclature. At 15 GHz, five jet features can be identified (Fig. 4.1). The three earliest-visible are labeled Ca, Cb, and Cc owing to their estimated ejection times being consistent with a separation from the 15 GHz core prior to or close in time, to the first observing epoch we employ (see Table 4.4 and Section 4.3.2 on obtaining the kinematical parameters). We use arithmetic labeling (C<sub>1</sub>, C<sub>2</sub>, C<sub>3</sub>) for components that can be positively cross-identified between, at least, two frequencies. More specifically, C<sub>1</sub> and C<sub>2</sub> are present at 15, 43 and 86 GHz, while component C<sub>3</sub> is only visible at the latter two frequencies due to blending effects at 15 GHz.

Overall, the maximum angular extension of the jet at 15 GHz reaches about 3 to 4 mas towards the southeast direction with the inner jet, up to a distance of  $\sim 2$  mas, laying at a smaller position angle (PA) and more towards the easterly direction (see Fig. 4.1). An apparent misalignment between inner and outer jet is evident from the VLBI maps at 43 and 86 GHz as seen in Fig. 4.2 and 4.3. This finding is further supported by the relative RA and DEC positions of fitted Gaussian components (XY positions) shown in Fig. 4.4 at both high frequencies, where the regions closer to the core are resolved. Consequently, observations at 43 and 86 GHz reveal the more aligned inner jet at its highest detail.

#### 4.3.2 *VLBI kinematics at 15, 43 and 86 GHz*

To obtain each knot's proper motion,  $\mu$ , through the narrow, curved jet of PKS 1502+106 we perform a weighted, linear least-squares fit to their epoch-to-epoch radial separation from the respective core at each frequency. Component radial separations from the core are shown in Fig. 4.5 for 15, 43 and 86 GHz respectively, where the linear fits are also visible. The inferred values of apparent



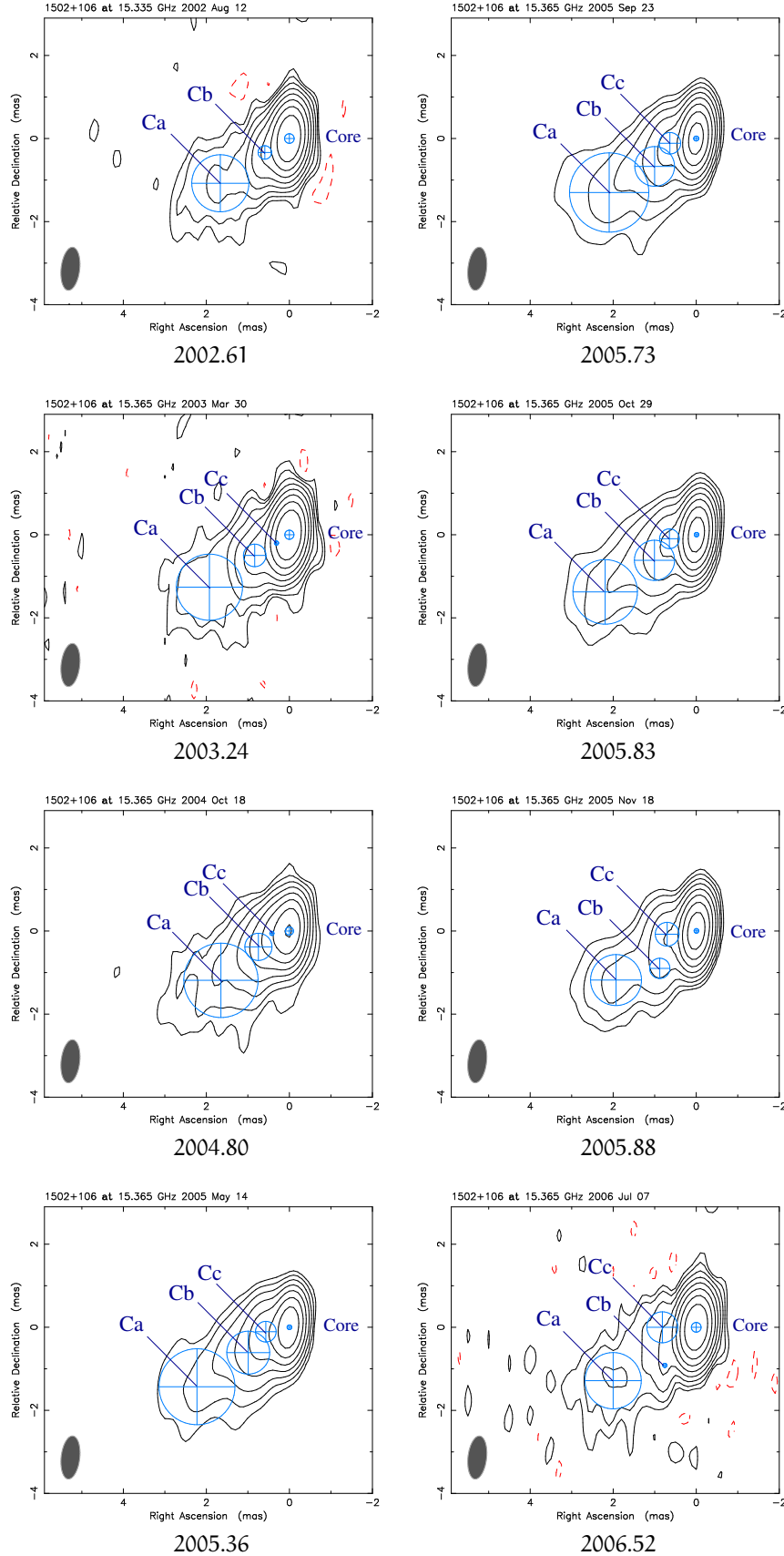


Figure 4.1: Uniform weighted, untapered MODELFIT images of the blazar PKS 1502+106, at 15 GHz. Contour levels correspond to  $-0.15\%$ ,  $0.15\%$ ,  $0.3\%$ ,  $0.6\%$ ,  $1.2\%$ ,  $2.4\%$ ,  $4.8\%$ ,  $9.6\%$ , and  $19.2\%$  of the highest peak flux density of  $2.79$  Jy/beam (epoch 2009.23) as a common reference. The restoring beam has FWHM of  $1.04$  mas  $\times$   $0.45$  mas at a position angle of  $-6.4^\circ$ . Unmarked components indicate non-robust features. Time progresses from top to bottom and from left to right.

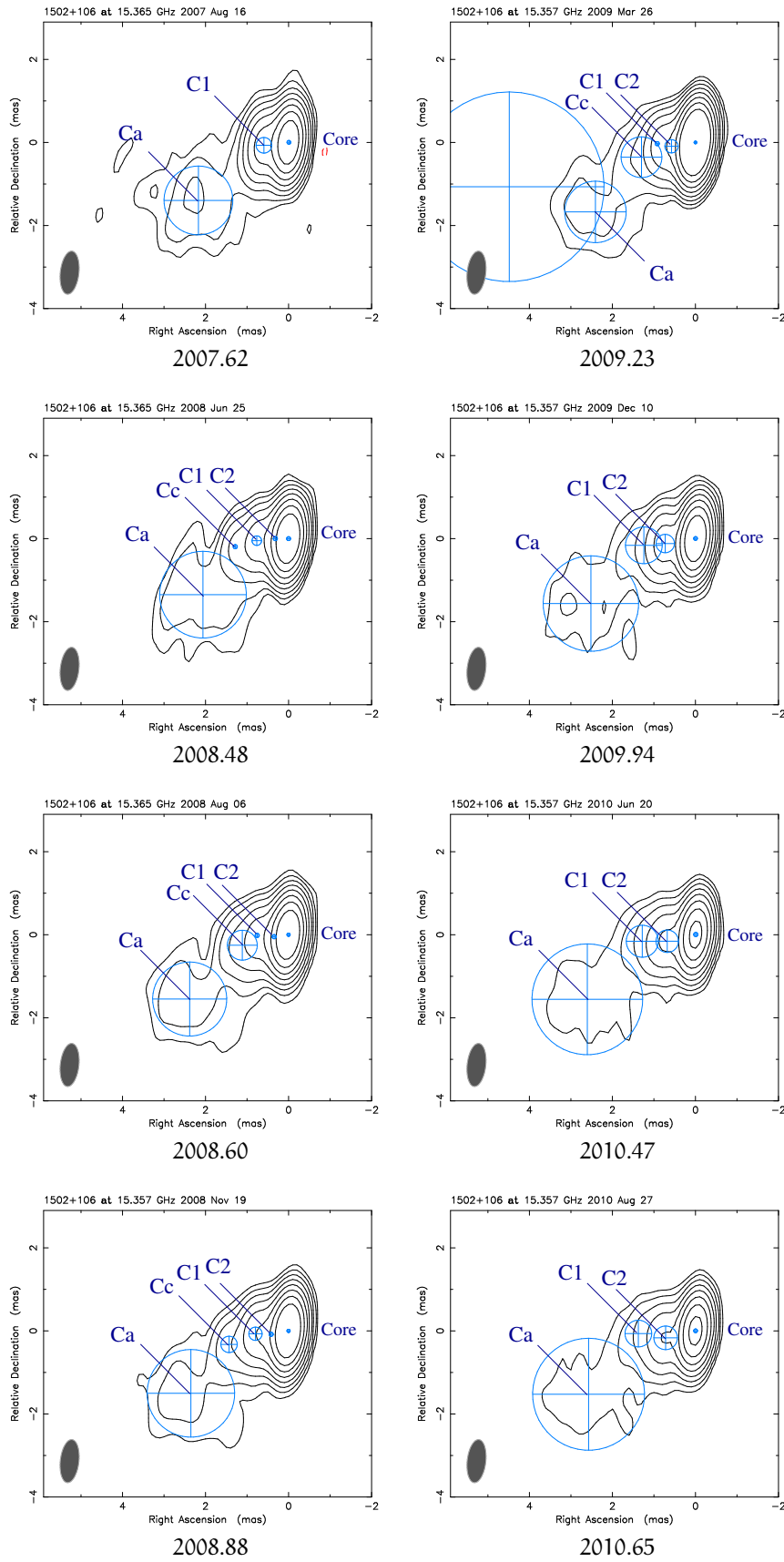


Figure 4.1: continued.

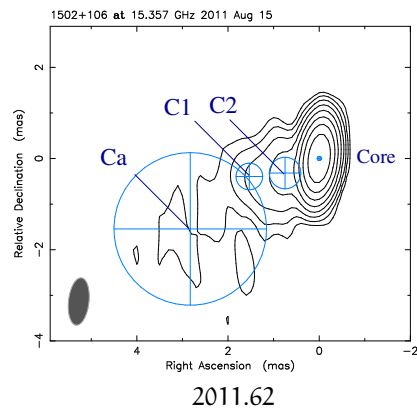
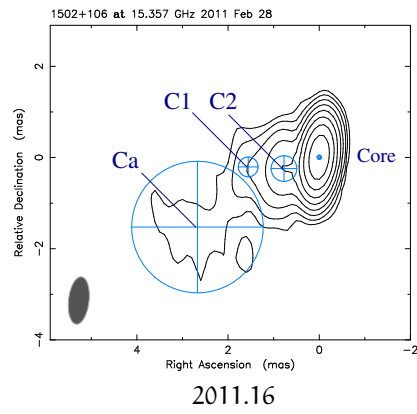
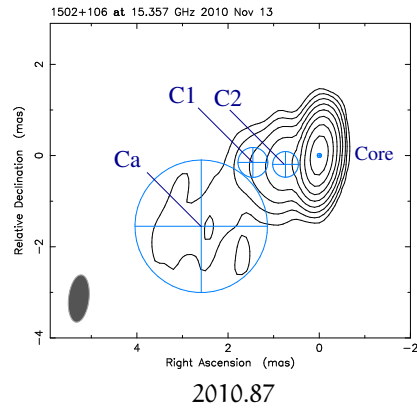


Figure 4.1: continued.

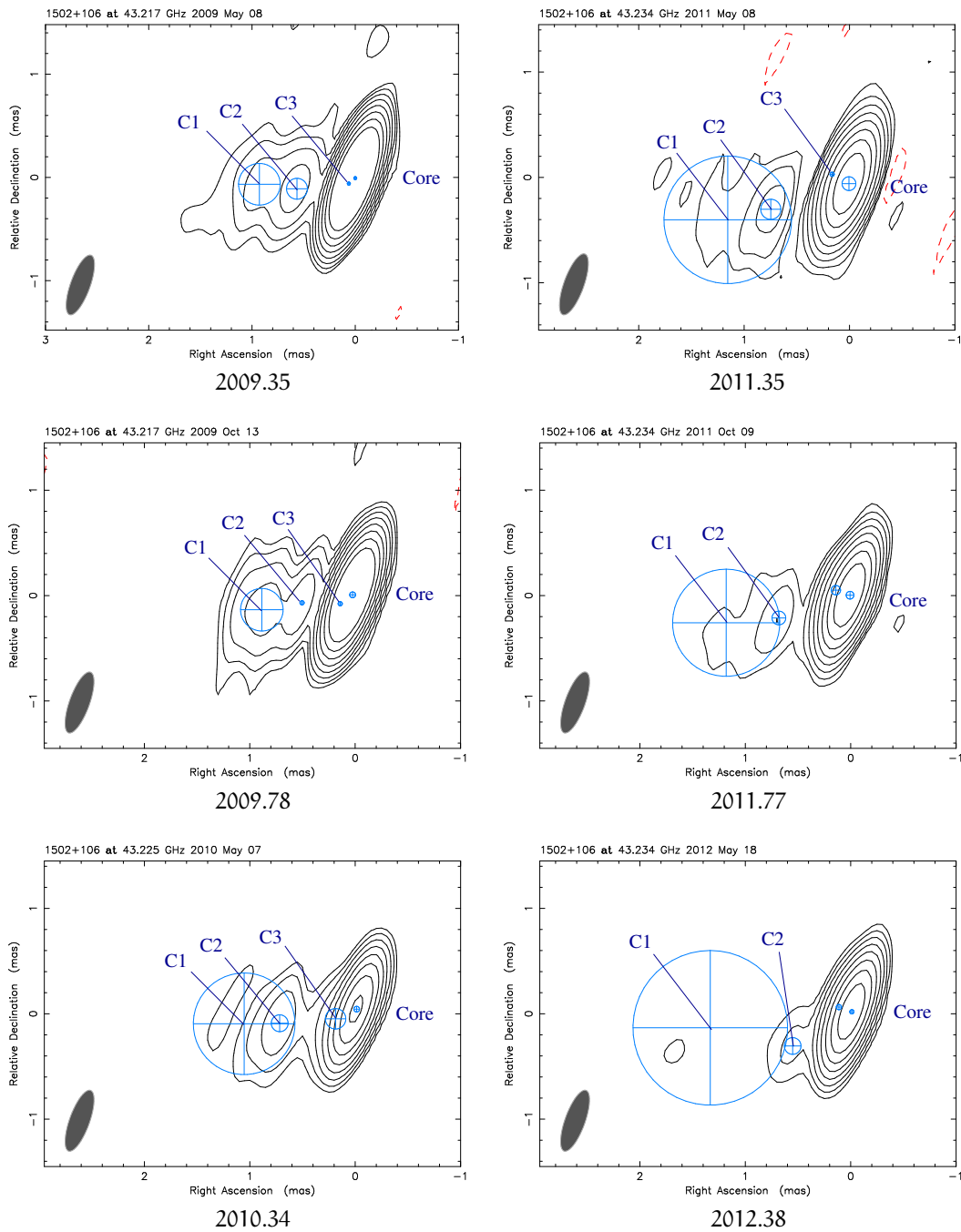


Figure 4.2: Uniform weighted, untapered MODELFIT images of the blazar PKS 1502+106, at 43 GHz. Contour levels correspond to  $-0.1\%$ ,  $0.1\%$ ,  $0.2\%$ ,  $0.4\%$ ,  $0.8\%$ ,  $1.6\%$ ,  $3.2\%$ ,  $6.4\%$ , and  $12.8\%$  of the peak flux density of  $3.47 \text{ Jy/beam}$  (epoch 2009.35) as a common reference. The restoring beam is shown at the bottom left of each image, with FWHM  $0.61 \text{ mas} \times 0.19 \text{ mas}$  at a position angle of  $-19.9^\circ$ . Unmarked components indicate non-robustly cross-identified features. Time progresses from top to bottom and from left to right.

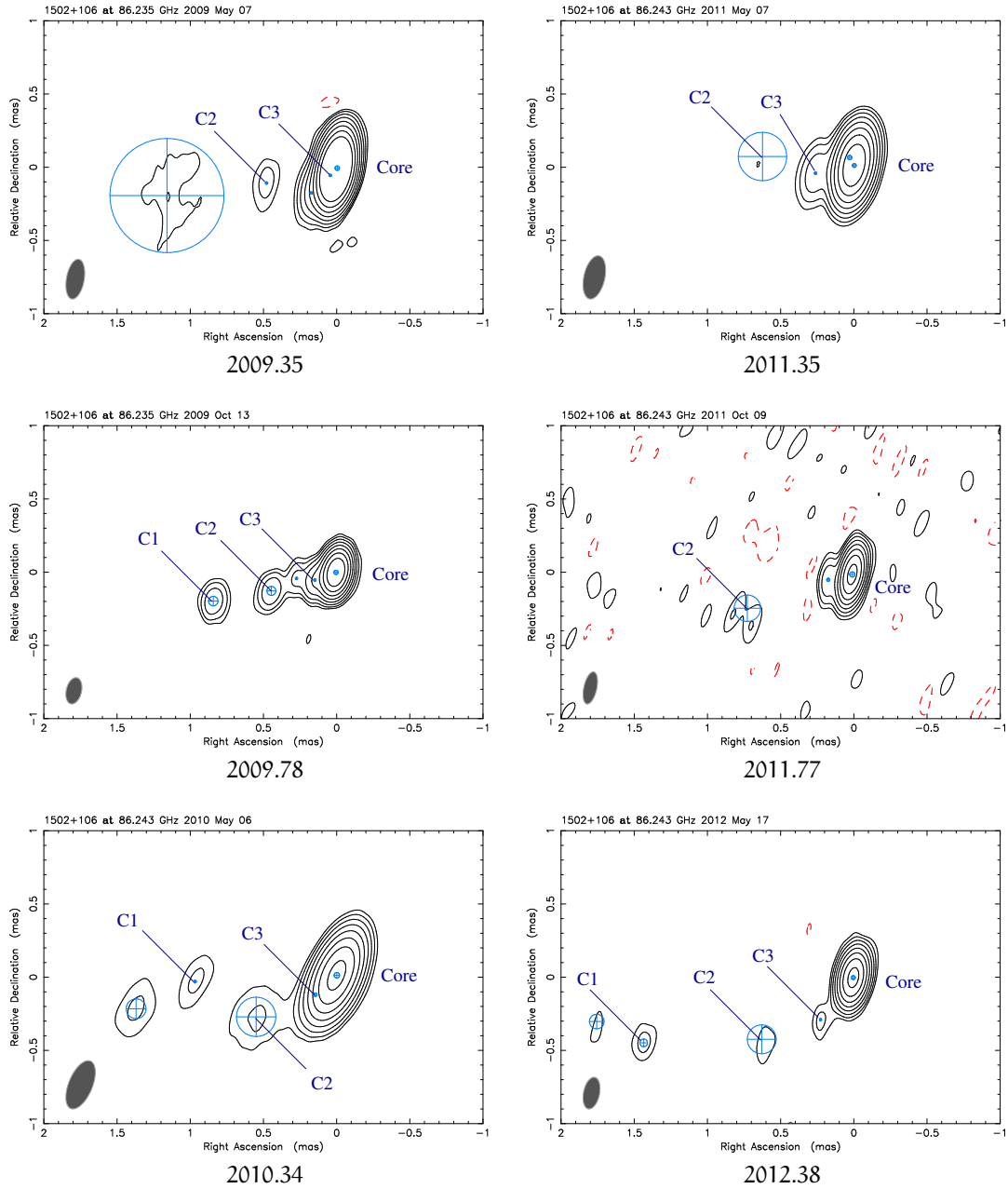
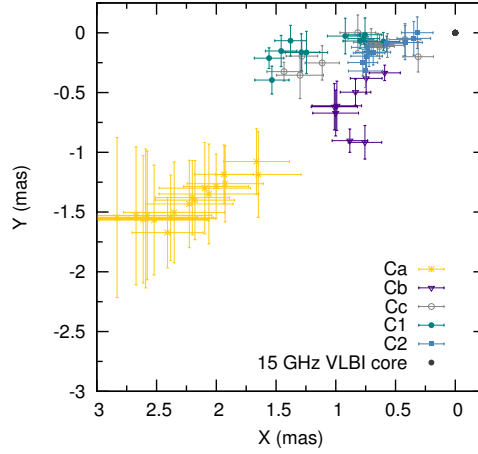
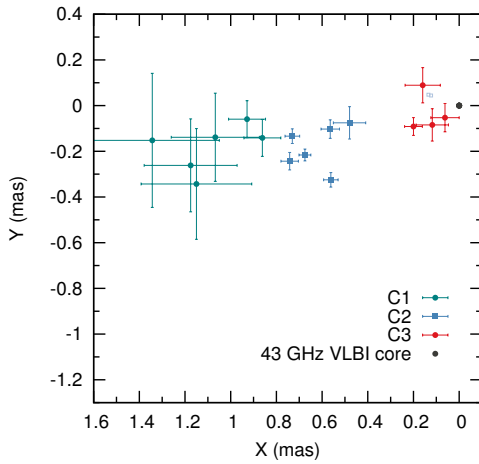


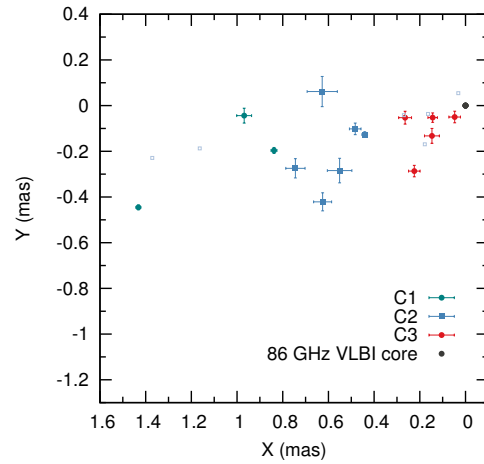
Figure 4.3: Uniform weighted, tapered MODELFIT images of the blazar PKS 1502+106, at 86 GHz. Contour levels correspond to  $-0.15\%$ ,  $0.15\%$ ,  $0.3\%$ ,  $0.6\%$ ,  $1.2\%$ ,  $2.4\%$ ,  $4.8\%$ ,  $9.6\%$  and  $19.2\%$  of the peak flux density of  $2.23 \text{ Jy/beam}$  (epoch 2009.35) as a common reference. The restoring beam is shown at the bottom left of each image. Unmarked components indicate non-robustly cross-identified features. Time progresses from top to bottom and from left to right.



(a) X and Y separation at 15 GHz



(b) X and Y separation at 43 GHz



(c) X and Y separation at 86 GHz

Figure 4.4: X and Y coordinates (relative RA and DEC with respect to the core) of all robustly identified components at the frequencies of 15, 43, and 86 GHz.

speed in mas/yr and in units of speed of light ( $\beta_{\text{app}} = v_{\text{app}}/c$ ), along with ejection date for all robust jet features are reported in Tables 4.4, 4.5 and 4.6. Compared to the kinematical results of the MOJAVE program presented in [Lister et al. \[2013\]](#), our component identification is slightly different. It is also based in the cross-identification with the high-frequency data but the overall picture does not differ significantly and knot speeds along with their ejection dates are in very good agreement.

The apparent expansion speed,  $\beta_{\text{app}}$ , of each component is then given by:

$$\beta_{\text{app}} = \frac{\mu D_L}{c(1+z)} \quad (4-1)$$

where:

- $\mu$  is the proper motion in rad/s,
- $D_L$  the luminosity distance in m,
- $c$  speed of light in m/s
- $z$  the redshift of the source.

As evident from Fig. 4.5 and Tables 4.4 through 4.6, PKS 1502+106 is characterized by extremely fast superluminal motion of features within the jet flow. Measured apparent velocities are in the range of  $\approx 10$ – $22$  c at 15 GHz, while at 43 GHz the range is  $\approx 2$ – $11$  c and from  $\approx 7$ – $20$  c for 86 GHz. The maximum  $\beta_{\text{app}}$  per frequency is  $\beta_{\text{app}}^{15\text{GHz}} = (22.1 \pm 1.1)$ ,  $\beta_{\text{app}}^{43\text{GHz}} = (10.9 \pm 2.8)$ ,  $\beta_{\text{app}}^{86\text{GHz}} = (19.5 \pm 0.4)$ , all characterizing the motion of superluminal feature C1.

The independently deduced kinematical models per frequency are generally in agreement, with only a few, worthy of discussion, discrepancies. These are mainly encountered at our mid-frequency of 43 GHz for components C1 and C2. Here, C1 appears to be traveling downstream the jet with only about half the speed observed at 15 and 86 GHz, where the measurements agree with the observational uncertainties. This can be attributed to the large positional uncertainties but also to the fact that our high frequency VLBI observations are limited in number and especially at 43 GHz, also limited in uv-coverage. Consequently, the presence or absence of even a single data point can drastically affect the quality of the fit and the deduced kinematical parameters.

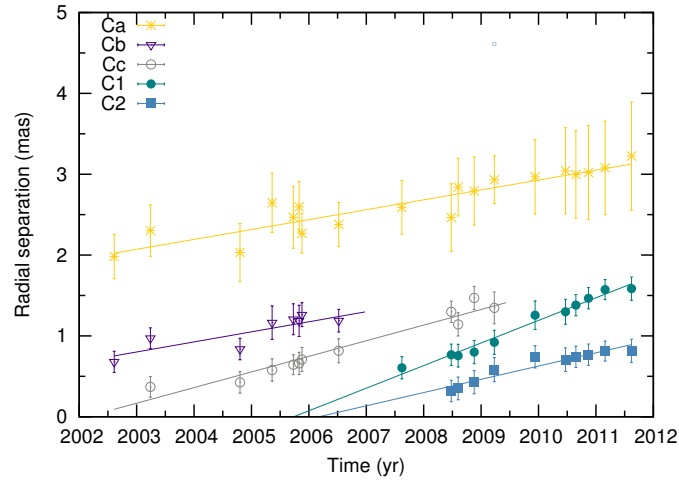
Inferred apparent component speeds allow for a study of the  $\beta_{\text{app}}$  profile along the radial direction of the jet. This is presented in Fig. 4.6. Up to a distance of  $\approx 1.5$  mas away from the core the apparent speeds observed follow an almost monotonically increasing trend, peaking at about 1 mas at all frequencies. In the region  $> 1.5$  mas downstream, the rising trend seems to break with only one, though robust, measurement at 15 GHz for the historical component Ca having only a  $\beta_{\text{app}} = (9.7 \pm 1.2)$  at a radial separation of  $\approx 2.8$  mas. Indicating a change of physical conditions within the flow—e.g. deceleration and/or a change of the viewing angle.

In the immediate vicinity of the core, knot C3 moves outwards with an apparent superluminal speed of  $(5.0 \pm 3.7)$  c and  $(7.1 \pm 0.7)$  c, at 43 and 86 GHz respectively.

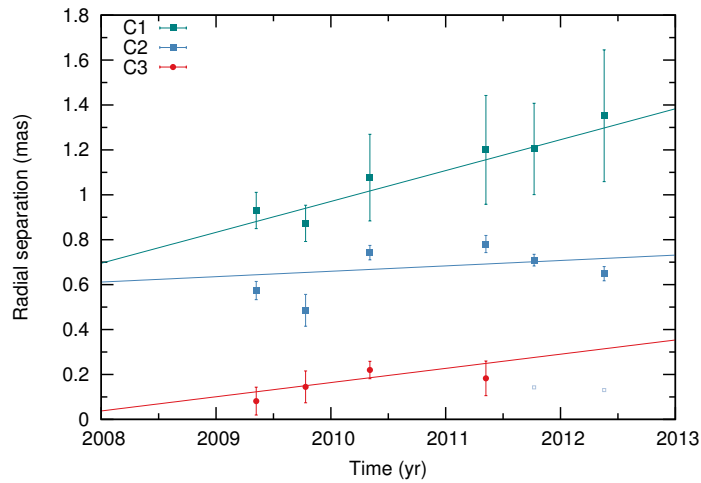
The XY (RA-DEC) position and the radial separation plots presented in Fig. 4.4 and 4.5 reveal the erratic, wobbly trajectory of superluminal feature C2 both at 43 and 86 GHz. The emerging pattern is not inconsistent and could in fact hint towards the scenario that C2 is following a helical expansion path. A scenario though, that cannot be corroborated due to the limited number of observations and the consequently low sampling rate of the underlying motion.

Other physical effects may also contribute to small, observed differences. Such uncertainties include the small aspect angles under which blazars are viewed, having the potential of greatly magnifying relativistic aberration effects on position and/or the position of the core which itself can constitute a non-stationary feature, subject to erratic motion, though such an effect is not clearly seen by the motion of other superluminal components.

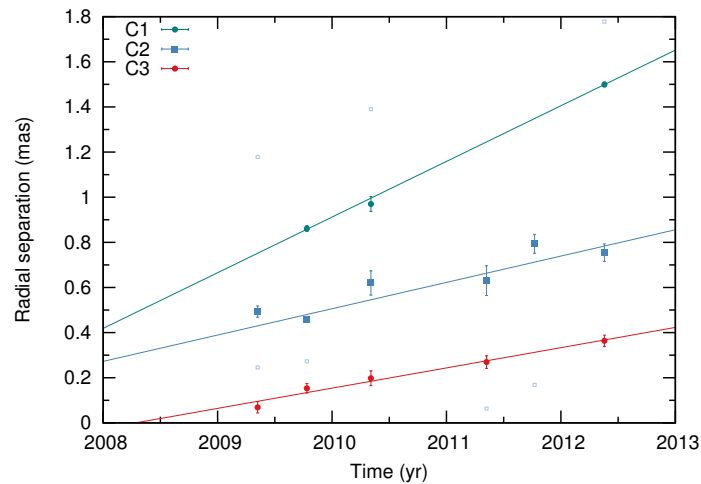
For those jet components that can be identified across observing frequencies, ejection dates are again in good agreement with the exception of C2 whose wobbly motion does not allow for a good estimate of the ejection date at 43 GHz. Components C1, C2 and C3 have been separated from the core in the time period covered by the VLBI monitoring. C1 and C2 separated in  $\sim 2006$  while C3 in  $\sim 2008$  at a time close to the onset of the multi-frequency outburst of PKS 1502+106.



(a) Component separation at 15 GHz



(b) Component separation at 43 GHz



(c) Component separation at 86 GHz

Figure 4.5: Temporal evolution of component radial separation from the core at—from top to bottom—15, 43 and 86 GHz. While the long-term kinematical behavior of PKS 1502+106 is visible at the lowest frequency, 43 and 86 GHz observations allow for a high resolution view towards the inner jet of PKS 1502+106. Components C1 and C2 being identifiable across all frequencies can be seen using the same color code.



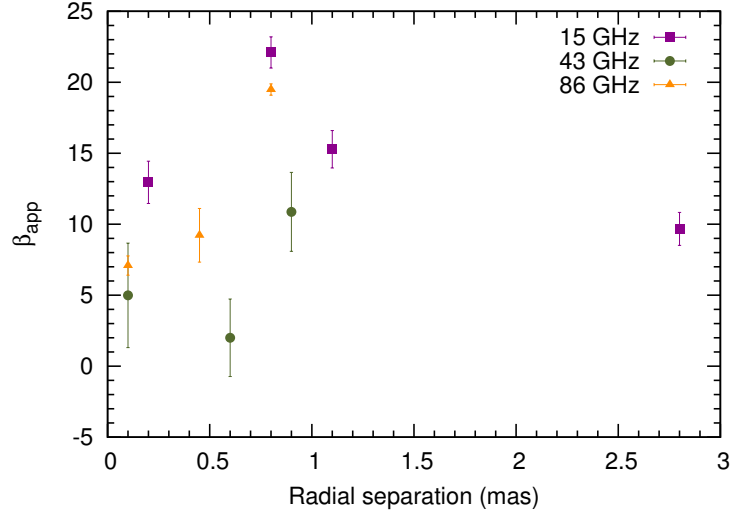


Figure 4.6: Apparent speed profile of superluminal components as a function of radial separation from the core.

KNOT	$\mu$ (mas yr <sup>-1</sup> )	$\beta_{\text{app}}$ (c)	$t_{\text{ej}}$ (yr)
Ca	$0.122 \pm 0.015$	$9.7 \pm 1.2$	$1986.1 \pm 2.6$
Cb	$0.125 \pm 0.033$	$9.8 \pm 2.6$	$1996.6 \pm 2.2$
Cc	$0.193 \pm 0.017$	$15.3 \pm 1.3$	$2002.1 \pm 0.4$
C1	$0.280 \pm 0.014$	$22.1 \pm 1.1$	$2005.7 \pm 0.2$
C2	$0.164 \pm 0.019$	$13.0 \pm 1.5$	$2006.2 \pm 0.5$

Table 4.4: Deduced kinematical parameters of jet components at 15 GHz

KNOT	$\mu$ (mas yr <sup>-1</sup> )	$\beta_{\text{app}}$ (c)	$t_{\text{ej}}$ (yr)
C1	$0.138 \pm 0.035$	$10.9 \pm 2.8$	$2002.9 \pm 1.9$
C2	$0.024 \pm 0.035$	$2.0 \pm 2.7$	$1982.5 \pm 41.5$
C3	$0.063 \pm 0.047$	$5.0 \pm 3.7$	$2007.4 \pm 2.2$

Table 4.5: Deduced kinematical parameters of jet components at 43 GHz

KNOT	$\mu$ (mas yr <sup>-1</sup> )	$\beta_{\text{app}}$ (c)	$t_{\text{ej}}$ (yr)
C1	$0.247 \pm 0.005$	$19.5 \pm 0.4$	$2006.3 \pm 0.1$
C2	$0.117 \pm 0.024$	$9.2 \pm 1.9$	$2005.7 \pm 1.0$
C3	$0.090 \pm 0.009$	$7.1 \pm 0.7$	$2008.3 \pm 0.3$

Table 4.6: Deduced kinematical parameters of jet components at 86 GHz

### 4.3.3 Radio flux density decomposition

The flare in PKS 1502+106 is dominated by a single, clearly visible event from  $\gamma$ -ray energies down to radio frequencies, between MJD 54689 and MJD 55295. The upper panel of Fig. 4.7 features the *Fermi*/LAT  $\gamma$ -ray light curve and following panels depict the total intensity radio data at 15, 43 and 86 GHz, both from the filled-aperture F-GAMMA observations and from cm/mm-VLBI monitoring. The total, single-dish flux density is decomposed into individual VLBI core and jet-component light curves. We show those of the positively cross-identified components C1, C2 and C3, omitting the historical components, at 15 GHz, and any non-robust jet features.

The core dominates the total flux density at VLBI scales at all frequencies. Radio flux density decomposed into core and MODELFIT components accounts for the largest fraction of the total single-dish flux density and follows nicely the overall flare evolution. Only in few cases, the sum of flux density of all MODELFIT components deviates from the total single-dish flux density. This is attributed to the low cadence of mm-VLBI monitoring and the source extreme variability behavior. Evidence for it, is the presence of substructure in the well-sampled F-GAMMA and  $\gamma$ -ray light curves.

Our mm-VLBI monitoring reveals that emission from the core is the dominant component of the whole radio flare, which at 15 GHz has varied in flux density by a factor of  $\sim 3$  with a time scale of approximately 2 years (see Fig. 4.7). The same behavior persists also at 43 and 86 GHz where its flux density varies by a factor of  $\sim 6$ – $7$  and  $\sim 4$ – $5$ , respectively within our GMVA monitoring period.

At 43 and 86 GHz, where resolution allows, it is clear that the flare is not an attribute of the core only. Here, the recently ejected component C3 appears to be in a decaying phase already during the first mm-VLBI observing epoch (see lower panels of Fig. 4.7 and Fig. A.1), but still shows significantly higher flux densities compared to all later epochs. Despite the limited number of data for C3, it can be clearly seen that—apart from the core—it is the only moving jet feature that is flaring, with its flux density dropping by a factor of  $\sim 20$ , at both frequencies. Knot C3 is the only component (apart from the core) that can be associated with the radio flare, given its estimated ejection time. For clarity and completeness all individual component light curves are shown in Appendix A.

### 4.3.4 Spectra of individual knots

While our high-frequency GMVA data at 43 and 86 GHz are simultaneous, this is not the case for the 15 GHz VLBA data. In order to assemble quasi-simultaneous spectra of individual superluminal components within the jet of PKS 1502+106, we select the 15 GHz epochs closest in time to each of the six 43/86 GHz GMVA observing runs. The quasi-simultaneous data forming each of the six spectra are labeled, I to VI, in Tables 4.1 through 4.3. The mean separation between the 15 GHz and 43/86 GHz observing epochs composing the spectral data is  $\sim 51$  days.

Components C1 and C2 are positively cross-identified between all three observing frequencies (Section 4.3.1) and hence quasi-simultaneous spectra were assembled for those. Knot C1 is the only sufficiently sampled component that

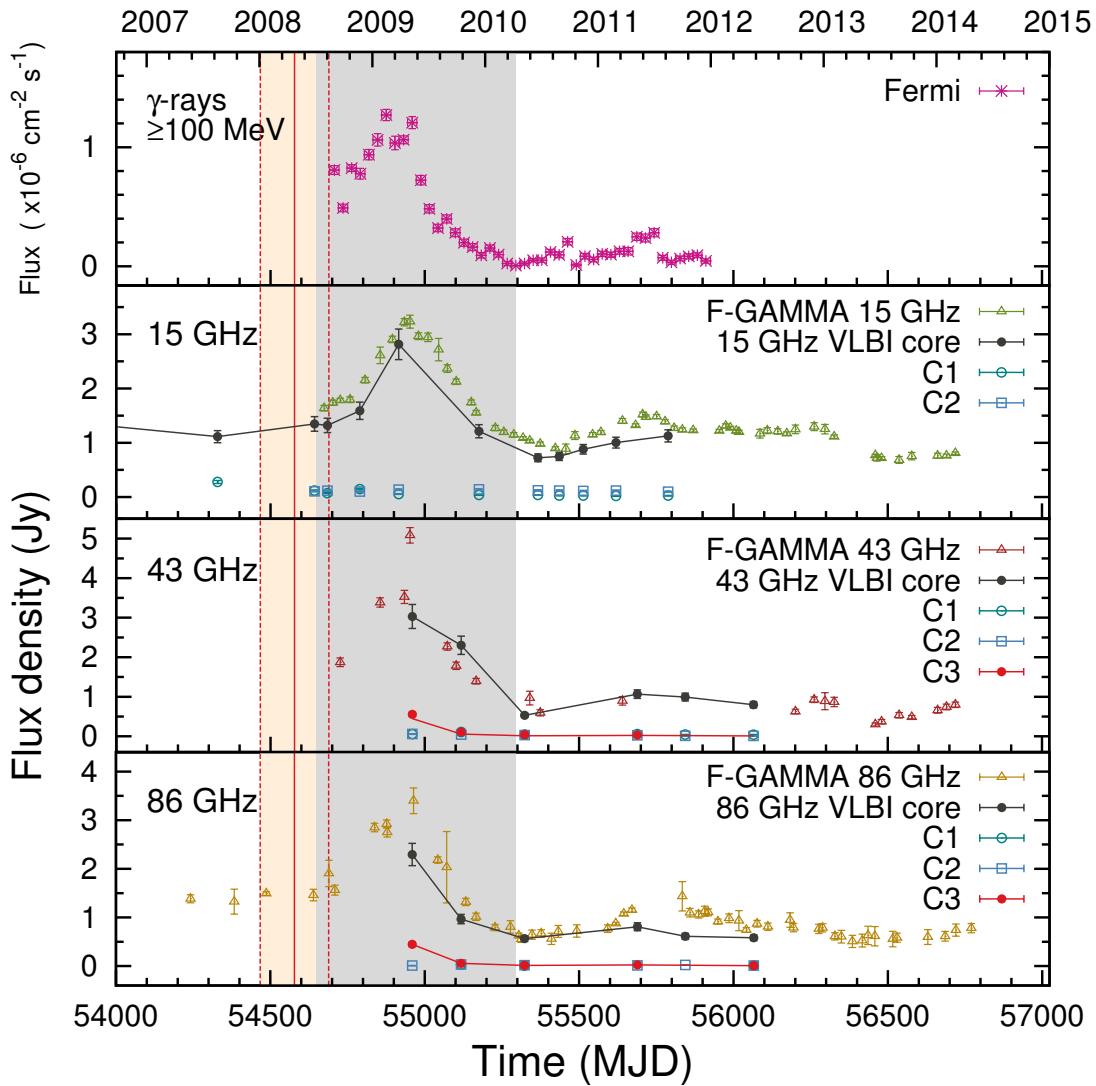


Figure 4.7: Light curves of PKS 1502+106. From top to bottom are shown: the *Fermi*/LAT  $\gamma$ -ray light curve at  $E > 100$  MeV; F-GAMMA single-dish radio light curve at 15 GHz with the core and component light curves from the VLBI flux density decomposition; same as before but at 43 GHz and (lower panel) at 86 GHz. Note the VLBI knot C3, only visible at the two highest frequencies, at its decaying flux density phase. The gray shaded area delineates the full duration of the flare  $\sim 650$  days. The red shaded area marks the estimated ejection interval of knot C3 with the red solid line designating its  $t_{ej}$ .

shows evidence of a synchrotron self-absorbed spectrum (SSA) featuring a spectral break at the turnover frequency,  $\nu_m$  and flux density  $S_m$ . In order to obtain  $S_m$  and  $\nu_m$ , along with the optically-thin spectral index we fit a model SSA spectrum of the following form [e.g. [Türler et al., 2000](#)]:

$$S_\nu = S_m \left( \frac{\nu}{\nu_m} \right)^{\alpha_t} \frac{1 - \exp[-\tau_m (\nu/\nu_m)^{\alpha - \alpha_t}]}{1 - \exp(-\tau_m)} \quad (4-2)$$

where:

- $\nu_m$  is the turnover frequency in GHz,
- $S_m$  is the turnover flux density in Jy,
- $\tau_m \approx 3/2 \left( \sqrt{1 - \frac{8\alpha}{3\alpha_t}} - 1 \right)$  is the optical depth at  $\nu_m$
- $\alpha_t$  is the spectral index of the optically thick part of the emission, and
- $\alpha$  the optically-thin spectral index.

The spectral index for the optically thick part is fixed to the canonical value  $\alpha_t = 5/2$ . We fit the observed spectra of C1 simultaneously and obtain  $S_m = (0.08 \pm 0.01)$  Jy,  $\nu_m = (33.2 \pm 2.0)$  GHz and  $\alpha = -(2.46 \pm 0.41)$ , as the average spectrum. The spectral index characterizing knot C1 is arguably very steep. To obtain the same parameters during the highest state of the knot, the fit is performed once more, at epoch 2009.9 only. Resulting parameters are as follows:  $S_m = 0.133$  Jy,  $\nu_m = 36.7$  GHz and  $\alpha = -1.98$ . These were used for the calculation of the magnetic field from SSA in Section 4.4.5.

For components C2 and C3 showing no sign of a SSA break, a power-law fit is performed separately at each observing epoch and the mean optically thin spectral index  $\langle \alpha \rangle$ , characterizing the time-averaged spectrum, along with its standard error are reported in Table 4.7.

C2 is also a well-sampled feature that during the whole length of our VLBI monitoring is characterized by a steep optically-thin spectrum with a mean power-law index of  $\langle \alpha \rangle = -(1.03 \pm 0.2)$  and a peak at  $\leq 15$  GHz. However, the situation is less constrained for component C3 that is only seen at 43 and 86 GHz due to the resolution limit of the 15 GHz observations. Here the analysis yielded an optically-thin, two-point spectral index  $\langle \alpha \rangle = -(0.84 \pm 0.34)$ .

The core is the the most compact, stationary feature at each frequency and it is characterized by a flat spectrum; i.e.  $\alpha \geq -0.5$ . However, at epoch 2009.9 it appears to exhibit an SSA turnover at  $\nu_m \sim 43$  GHz. The mean spectral index of the core is found to be  $\langle \alpha \rangle = -(0.22 \pm 0.07)$ , indicative of unresolved substructure.

#### 4.4 INFERRED PHYSICAL PARAMETERS

In the present Section, we deduce physical parameters of the jet of PKS 1502+106, given the phenomenological characteristics of the source and the findings of our VLBI analysis presented in Section 4.3. We touch upon the Doppler factor, viewing angle, brightness temperature distribution along the jet, and magnetic field estimates.

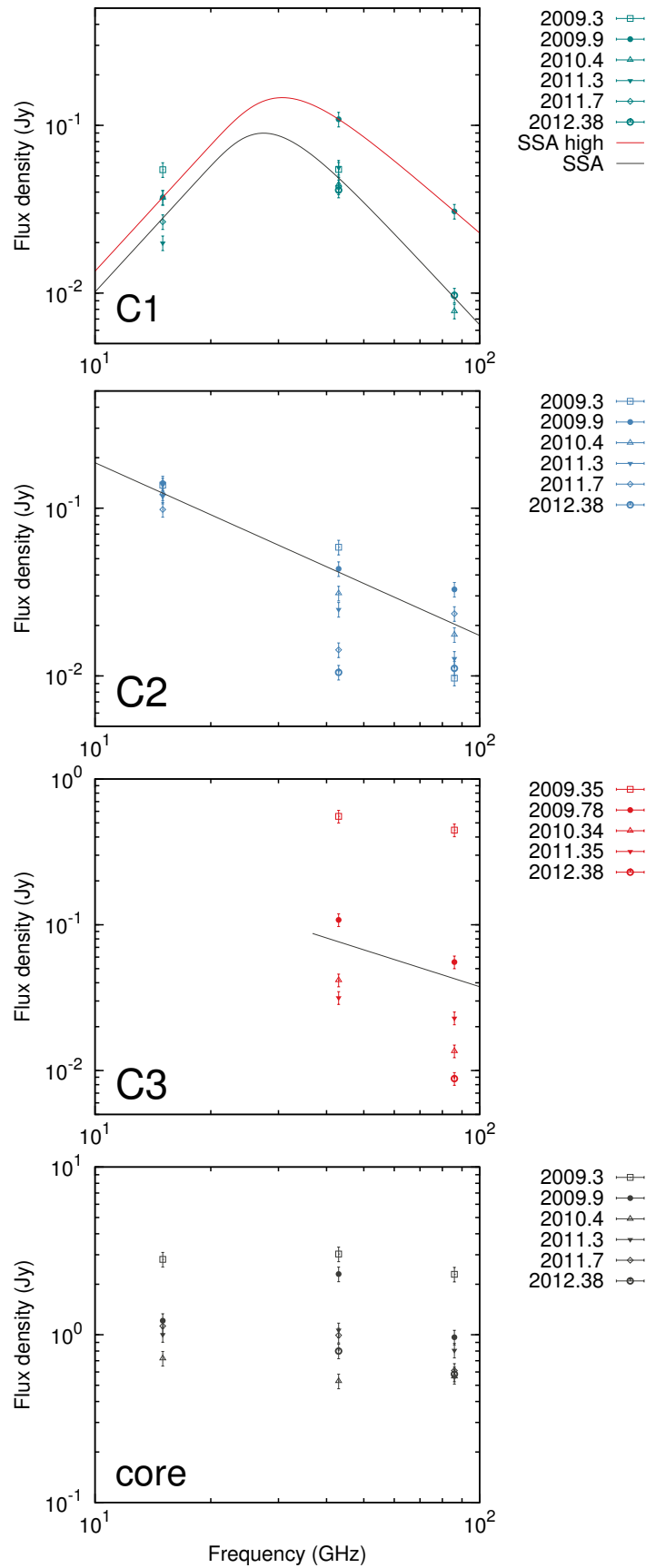


Figure 4.8: Three-point spectra of knots C1, C2, the VLBI core and their temporal evolution. For C3 spectra are only available at 43 GHz and 86 GHz since it is blended at 15 GHz. Black lines represent the time-averaged spectra of components and their slopes are reported in Table 4.7. For component C1 the fitted SSA model spectra are also shown. The red curve is a SSA fit during its highest state, while the black corresponds to the mean SSA spectrum.

KNOT	$\langle \alpha \rangle$
C1	$-2.46 \pm 0.41$
C2	$-1.03 \pm 0.26$
C3	$-0.84 \pm 0.34$
Core	$-0.22 \pm 0.07$

Table 4.7: Mean spectral indices for components C1, C2, C3 and the core as obtained by SSA fitting for C1 and a single power-law fit for C2, C3, and the core.

#### 4.4.1 Doppler and Lorentz factor estimates

As shown in Section 4.3.2, the highest apparent speed measured in the jet of PKS 1502+106 is  $\beta_{\text{app}} \approx 22$  and corresponds to the expansion velocity of component C1 present only in the 15 and 43 GHz data. From here we can readily estimate the minimum Lorentz factor that characterizes the flow [e.g. Urry and Padovani, 1995]. It follows that  $\gamma \geq \gamma_{\text{min}}$  for the jet with the minimum Lorentz factor given by

$$\gamma_{\text{min}} = \sqrt{\beta_{\text{app}}^2 + 1} \quad (4-3)$$

and for the observed maximum apparent velocity we obtain  $\gamma_{\text{min}} = 22.1$ . Consequently, the Doppler boosting factor can be estimated as well since  $\delta_{\beta_{\text{app}}, \text{C1}} \approx \beta_{\text{app}, \text{C1}} \approx 22.1$  at 15 GHz. For knots C2 and C3, it is  $\delta_{\beta_{\text{app}}} \approx \gamma_{\text{min}, \text{C2}} = 9.3$  and  $\delta_{\beta_{\text{app}}} \approx \gamma_{\text{min}, \text{C3}} = 7.2$ , from the 86 GHz observations.

In addition to the Doppler factor estimate obtained from the minimum Lorentz factor, under the valid assumption of causality one can arrive to another estimate of the Doppler factor,  $\delta_{\text{var}}$ , using the temporal variation of the flux density of individual components. For details on this method see Jorstad et al. [2005] and references therein. The variability Doppler factor is given by

$$\delta_{\text{var}} = \frac{d_{\text{eff}} D_L}{c \Delta t_{\text{var}} (1+z)} \quad (4-4)$$

where:

- $d_{\text{eff}}$  is the effective angular size of the component in radians
- $D_L$  the luminosity distance in m,
- $c$  speed of light in  $\text{m s}^{-1}$  and
- $\Delta t_{\text{var}} = dt / \ln(S_{\text{max}}/S_{\text{min}})$  the variability timescale with  $dt$  the time between  $S_{\text{max}}$  and  $S_{\text{min}}$ .
- $z$  is the source's redshift.

Components C1 and C3 can be used for this purpose. Both components suffer from under-sampled light curves, and are unresolved; that is, being smaller than the beam size at the epoch of their highest respective flux densities at all three observing frequencies.

KNOT	t	dt <sub>eff</sub> (mas)	Δt <sub>var</sub> (yr)	δ <sub>var</sub>	γ <sub>var</sub>	θ <sub>var</sub> (°)
15 GHz						
C <sub>1</sub>	2007.6–2011.2	≤0.9	≥1.3	≤51.4	≤30.5	≥0.8
43 GHz						
C <sub>3</sub>	2009.4–2011.3	≤0.1	≥0.7	≤12.1	≤7.1	≥3.4
86 GHz						
C <sub>3</sub>	2009.4–2011.3	≤0.1	≥0.7	≤15.0	≤9.2	≥2.9

Table 4.8: Physical parameters estimated using causality arguments and observed variability. Columns from left to right: (1) knot designation; (2) elapsed time between maximum and minimum flux density; (3) effective size; (4) variability time scale; (5) Doppler factor; (6) Lorentz factor and (7) viewing angle.

In all cases (for C<sub>1</sub> at 15 GHz and C<sub>3</sub> at 43 and 86 GHz) we have used the minor axis of the restoring beam as the upper limit for the component angular size. This selection is based on the fact that the minor axis is positioned almost parallel to the jet axis, thus allowing the highest resolution to be achieved along it. Specifically, for the higher frequencies and component C<sub>3</sub> the minor axis of the 86 GHz beam was selected, since it yields the most stringent upper limit to its size.

By a simple inspection of the light curves one can readily see that component flux density variations are not adequately sampled and the point of maximum flux density most probably precedes our first observing epoch. This fact sets a lower limit to the variability time scale, Δt<sub>var</sub>, with dt obtained directly from the light curves of individual components. As a result of the above considerations, calculation of the variability Doppler factor at high frequencies can only yield upper limits for δ<sub>var</sub>.

Along the same argumentation an estimate of the variability Lorentz factor can be obtained by

$$\gamma_{\text{var}} = \frac{\beta_{\text{app}}^2 + \delta_{\text{var}}^2 + 1}{2\delta_{\text{var}}} \quad (4-5)$$

Results of the calculations are summarized in Table 4.8. Component C<sub>1</sub> is characterized by the highest variability Doppler (δ<sub>var</sub> ≤ 51.4) and Lorentz (γ<sub>var</sub> ≤ 30.5) factors. All figures are consistent with the estimates of the minimum Lorentz factor, γ<sub>min</sub>, presented previously. Knot C<sub>3</sub> is also found to have consistent behavior at both high frequencies with δ<sub>var</sub><sup>43 GHz</sup> ≤ 12.1 and γ<sub>var</sub><sup>43 GHz</sup> ≤ 7.1, while at 86 GHz the estimation yields δ<sub>var</sub><sup>86 GHz</sup> ≤ 15 and γ<sub>var</sub><sup>86 GHz</sup> ≤ 9.2.

An additional Doppler factor estimate can be obtained from the spectra of individual components—i.e. the relative magnetic field strength given by synchrotron self-absorption and equipartition. This is discussed in Section 4.4.5.

#### 4.4.2 The viewing angle towards PKS 1502+106

Jets orientation with respect to the the observer's line of sight is a contributing factor to their appearance and observed physical characteristics. Using the observed apparent expansion speed we can set constraints to the aspect angle under which a jet is viewed.

The first approach is by calculating the critical angle maximizing the observed  $\beta_{\text{app}}$ . The apparent speed is given by [Rees, 1966]

$$\beta_{\text{app}} = \frac{\beta \sin \theta}{1 - (\beta \cos \theta)} \quad (4-6)$$

where  $\beta$  is the intrinsic expansion velocity in units of  $c$  and  $\theta$  is the viewing angle. With the help of the definition of the Doppler factor,  $\delta = [\gamma(1 - \beta \cos \theta)]^{-1}$ , Eq. 4-6 can be rewritten as

$$\beta_{\text{app}} = \beta \gamma \delta \sin \theta \quad (4-7)$$

and  $\beta_{\text{app}}$  is maximized (i.e.  $\beta_{\text{app,max}} = \beta \gamma$ ) for  $\sin \theta_c = \gamma^{-1}$  or  $\sin \theta_c = \delta^{-1}$ , since for this angle  $\theta_c$ ,  $\gamma = \delta$ . Using the minimum Lorentz factor,  $\gamma_{\text{min}} \approx 22$  calculated above we arrive to the following figure for the critical angle:

$$\theta_c = \arcsin \left( \frac{1}{\gamma_{\text{min}}} \right) = 2.6^\circ \quad (4-8)$$

The approach of using variability arguments can be applied in the estimation of the viewing angle towards the source, as well. The "variability viewing angle",  $\theta_{\text{var}}$  is given by

$$\theta_{\text{var}} = \arctan \left( \frac{2\beta_{\text{app}}}{\beta_{\text{app}}^2 + \delta_{\text{var}}^2 - 1} \right) \quad (4-9)$$

Analysis was performed for all components with significant variability (see Fig. A.1) and yields viewing angles for each component separately. The results are shown in the last column of Table 4.8. For the fastest superluminal knot, C1, we obtain the smallest viewing angle  $\theta_{\text{var}} \geq 0.8^\circ$ . For C3 we obtain consistent values at 43/86 GHz of  $\geq 3.4^\circ$  and  $\geq 2.9^\circ$ , respectively. Interestingly, components C1 and C3 are traveling with very different apparent speeds (Section 4.3.2) at two different region of the jet—in the outer jet ( $r > 1$  mas) and inner ( $r < 0.5$  mas), respectively. This fact in combination with the difference of their inferred Doppler factors may hint towards a "two-region scenario", wherein physical conditions differ intrinsically. This possibility is further discussed in the following.

#### 4.4.3 Opening angle of the jet

In the present section we investigate the apparent and intrinsic opening angles of the jet,  $\phi_{\text{app}}$  and  $\phi_{\text{int}}$ , respectively employing two different approaches. First, we use all MODELFIT components at all three frequencies and perform a simultaneous linear fit to their deconvolved sizes in order to obtain the jet opening



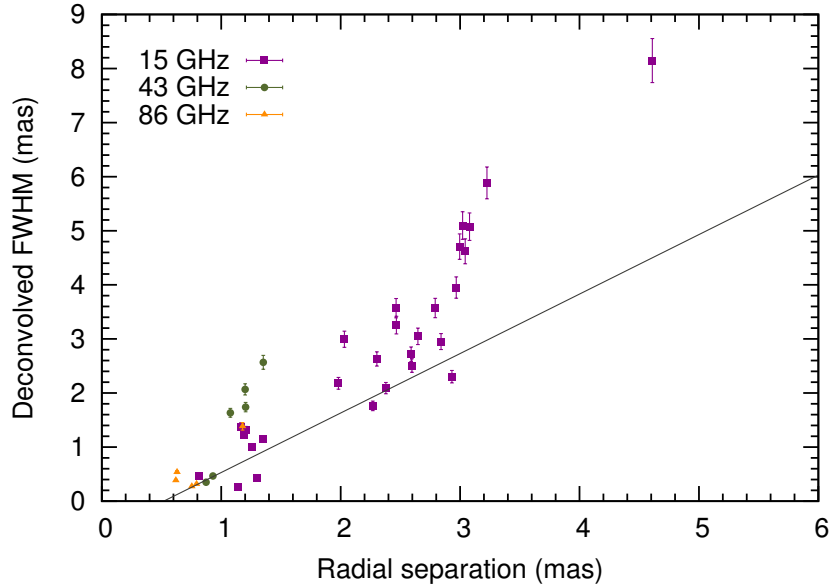


Figure 4.9: Deconvolved FWHM of all resolved jet components with respect to radial separation from the core at all available frequencies. The black solid line represents the best linear fit to the data.

rate. In the second approach we deduce  $\phi_{\text{app}}$  from each individual MODELFIT component based on its size and kinematical characteristics.

#### 4.4.3.1 Opening angle from a simultaneous fit to component deconvolved sizes

In Fig. 4.9 the deconvolved effective size,  $d_{\text{eff}} = 1.8 \text{FWHM}_d$  [Fromm et al., 2013a], where  $\text{FWHM}_d = \left(\text{FWHM}^2 - b_\phi^2\right)^{1/2}$ , of all resolved MODELFIT components at all three frequencies is shown as a function of radial separation from the core. We fit  $d_{\text{eff}}$  with respect to radial core separation, using a simple linear model assuming a constant jet opening angle. The least-squares fit yields a slope of  $(0.61 \pm 0.09)$  translating to an apparent half-opening angle of  $(17.2 \pm 2.6)^\circ$  and an apparent full-opening angle of  $\phi_{\text{app}} = (34.4 \pm 5.2)^\circ$ . The de-projected opening angle is then given by

$$\phi_{\text{int}} = \phi_{\text{app}} \sin \theta \quad (4-10)$$

which for  $\theta = \theta_c = 2.6^\circ$  (see Section 4.4.2), Eq. 4-10 yields  $\phi_{\text{int}} = (1.6 \pm 0.2)^\circ$ .

#### 4.4.3.2 Opening angle from each individual component separately

We performed the analysis on the uv-plane, utilizing the component size,  $\text{FWHM}_d$ , and radial distance,  $r$ , from the core. First we calculate the opening angle corresponding to each MODELFIT component separately. Assuming the component fills the entire jet cross section,  $\phi_{\text{app}}$  is given by

$$\phi_{\text{app}}^{\text{comp}} = 2 \arctan \left( \frac{\text{FWHM}_d}{2 \langle r \rangle} \right). \quad (4-11)$$

KNOT	# EPOCHS	$\langle r \rangle$ (mas)	$\theta_c$ ( $^\circ$ )	$\langle \phi_{\text{app}} \rangle$ ( $^\circ$ )	$\langle \phi_{\text{int}} \rangle$ ( $^\circ$ )
15 GHz					
Ca	19	2.66	5.9	38.4	4.0
Cb	3	1.19	5.8	34.1	3.5
Cc	3	1.10	3.8	17.2	1.1
C1	2	1.28	2.6	17.8	0.8
43 GHz					
C1	6	1.11	6.2	37.5	1.9
86 GHz					
C2	4	0.70	2.9	17.6	1.9

Table 4.9: Apparent and intrinsic jet opening angles deduced from individual MODELFIT components. Columns from left to right: (1) knot designation; (2) number of epochs used for the calculation where the component is resolved; (3) mean separation from the core; (4) critical viewing angle from the component's speed; (5) mean apparent opening angle and (6) intrinsic opening angle.

Then, we average over deconvolved size and distance, thus obtaining the average opening angle of a given component at a mean radial distance from the core. The intrinsic opening angle of the jet, making use of the viewing angle corresponding to each component, according to its apparent expansion speed at each frequency, is given by Eq. 4-10. The results are shown in Table 4.9. The mean intrinsic opening angle for the jet, deduced by averaging the  $\langle \phi_{\text{int}} \rangle$  of all components is  $(2.2 \pm 1.3)^\circ$ .

#### 4.4.4 Radial brightness temperature distribution

The brightness temperature of a given VLBI component in the source rest frame is given by [see e.g. [Lähteenmäki et al., 1999](#)]:

$$T_b = 1.22 \times 10^{12} \frac{S_\nu}{\nu^2 d_{\text{eff}}^2} (1+z) \quad (\text{K}) \quad (4-12)$$

where:

- $S_\nu$  is the component's flux density in Jy,
- $d_{\text{eff}}$  the effective size of the emitting region in mas, and
- $\nu$  the observing frequency in GHz.

In Fig. 4.10 the radial distribution of observed brightness temperatures along the jet of PKS 1502+106 is presented. The brightness temperature,  $T_b$ , is calculated for each component and epoch. What can be readily realized are the

frequency-dependent  $T_b$  values, with the highest observed brightness temperatures calculated from the lowest-frequency VLBI data.

Observed brightness temperatures approach and mostly exceed the equipartition limit [Readhead, 1994] of about  $5 \times 10^{10}$  K for the core, at all frequencies (see Fig. 4.10). The core is at all times unresolved and thus the  $T_b$  values represent lower limits.

The same trend of high  $T_b$  persists throughout the first milliarcsecond downstream of the core, with a few components being resolved. Specifically, in the regions

- between 0 and 1 mas we estimate high  $T_b$  at all frequencies deduced from lower limits, with a handful of measured values of lower brightness temperature as observing frequency increases, in the range from  $10^7$  K at 86 GHz to slightly above  $10^9$  K at 15 GHz.
- Between 1 and 2 mas, the division persists, indicative of the sampling of different portions of the jet. Here the measurements at 15 GHz are clustered in the range  $10^9$ – $10^{10}$  K while at both high frequencies the  $T_b$  is significantly lower,  $T_b \geq 10^7$  K
- Further than 2 mas downstream, the jet is observable only at 15 GHz and the distribution of  $T_b$  is characterized by a decreasing trend from  $10^9$  K to  $10^8$  K at a distance of 4.6 mas.

The mean—over time—core brightness temperature at our 3 observing frequencies is:  $\langle T_{b,\text{core}}^{15\text{GHz}} \rangle \geq (3.8 \pm 1.5) \times 10^{10}$ ,  $\langle T_{b,\text{core}}^{43\text{GHz}} \rangle \geq (1.5 \pm 1.0) \times 10^{10}$ , and  $\langle T_{b,\text{core}}^{86\text{GHz}} \rangle \geq (7.4 \pm 5.0) \times 10^9$ . Overall, brightness temperatures along the jet (Fig. 4.10) exhibit a decreasing trend with radial separation. Inference of a slope is difficult due to the presence of a large number of lower limits for the  $T_b$  due to unresolved components. However, there exist no evidence to support any increase of  $T_b$ , as we move along the jet.

#### 4.4.5 Magnetic field estimates

Estimates of the magnetic field strength for individual components can be obtained under the assumption that synchrotron self-absorption (SSA) is the dominant process shaping the observed spectra. Following Marscher [1983] the strength of the magnetic field can then be calculated as

$$B_{\text{SSA}} = 10^{-5} b(\alpha) \vartheta^4 \nu_m^5 S_m^{-2} \left( \frac{\delta}{1+z} \right) \quad (\text{G}) \quad (4-13)$$

where:

- $b(\alpha)$ , is a tabulated spectral index-dependent parameter [see Marscher, 1983, Table 1]
- $\vartheta$  the component size in mas,
- $\nu_m$  the spectral turnover frequency in GHz, and

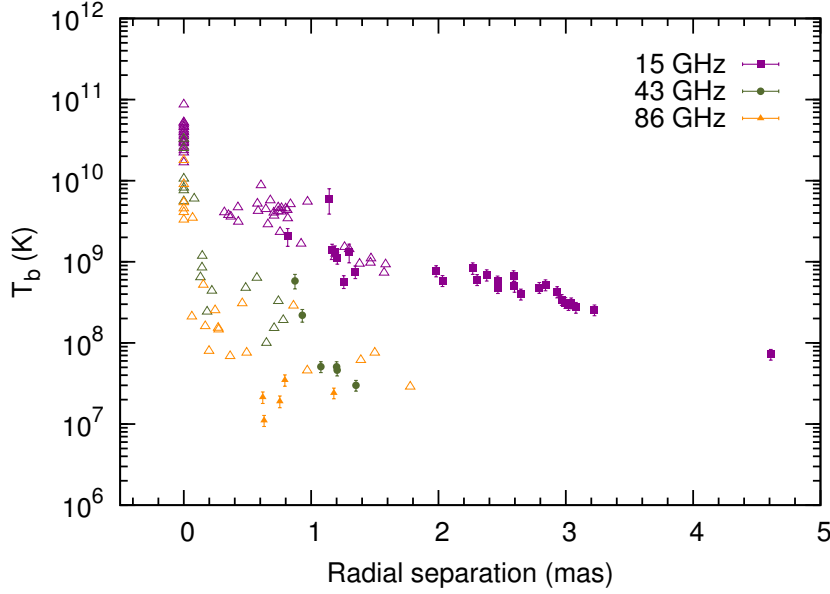


Figure 4.10: Brightness temperature,  $T_b$ , distribution with respect to radial separation from the core at all observing frequencies. Filled symbols represent  $T_b$  measurements, while open symbols represent lower limits.

- $S_m$  the spectral turnover flux density in Jy.

Given the strong dependencies of  $B_{SSA}$ , mainly on  $\nu_m$  and  $\vartheta$ , we note that measurement uncertainties of those quantities, translate into large uncertainty of the magnetic field estimated through Eq. 4–13. Nevertheless, we attempt the estimation for those components that the turnover frequency and flux density are somewhat constrained, namely knot C1 and the core. Even if a Doppler factor  $\delta$ , correction is not applied, an apparent value along the jet can be obtained [Bach et al., 2005]. In Table 4.10 we summarize our findings.

C1 appears to exhibit a strong magnetic field of  $\approx 5.0 \delta$  G. This large value could be an indication of a highly-magnetized traveling disturbance along the jet. Its high apparent expansion velocity of  $\approx 22 c$  and high Doppler factor ( $22.1 \leq \delta \leq 51.4$ , see Section 4.4.1) may hint towards the plausibility of this scenario.

The VLBI core is the bright compact region featured in every blazar VLBI map. Its characteristic spectral flatness is traditionally attributed to the superposition of a number of individual SSA components, each with a distinctly peaked spectrum. The spectral shape of the core at epoch 2009.9 (see Fig. 4.8) hints for the presence of an SSA peak close to a frequency of  $\sim 43$  GHz. Taking this as the turnover frequency and with  $S_m = 2.3$  Jy we obtaining an SSA magnetic field estimate  $B_{SSA} \sim 2 \delta$  mG.

Another constraint to the magnetic field can be set assuming equipartition between radiating relativistic particles ( $E_e \propto B^{-1.5}$ ) and the energy contained in the magnetic field ( $E_B \propto B^2$ ). The equipartition magnetic field that minimizes the total energy content  $E_{tot} = (1 + k)E_e + E_B$  is [see e.g. Bach et al., 2005]

$$B_{eq} = \left[ 4.5 (1 + k) f(a, \nu_a, \nu_b) L R^3 \right]^{2/7} \quad (4-14)$$

where:

KNOT	$\nu_m$ (GHz)	$S_m$ (Jy)	$\vartheta$ (mas)	$\vartheta_{\text{eq}}$ (mas)	$B_{\text{SSA}}/\delta$ (G)	$B_{\text{eq}}$ (G)	$\delta_{\text{eq}}$
C1	36.7	0.13	0.10	$\approx 0.01$	5.0	0.3	$\approx 50$
Core	$\sim 43$	2.3	0.06	0.1	0.002	1.2	...

Table 4.10: Estimated physical parameters for knot C1 and the VLBI core. Columns from left to right: (1) Designation; (2) turnover frequency; (3) turnover flux density; (4) measured size; (5) equipartition critical size; (6) SSA magnetic field; (7) minimum equipartition magnetic field and (8) Doppler factor.

- $k$  is energy ratio between electrons and heavy particles,
- $f$  is a tabulated function of  $\alpha$ , and upper and lower synchrotron frequency cutoffs,  $\nu_a, \nu_b$  in GHz,
- $L$  is the synchrotron luminosity of the source given by  $L = 4\pi D_L^2 \int_{\nu_a}^{\nu_b} S d\nu$ , and
- $R$  is the size of the knot in cm.

For  $k \approx 100$  and  $f(-0.5, 10^7, 10^{11}) = 1.6 \times 10^7$ , we obtain the following expression

$$B_{\text{eq}} = 5.37 \times 10^{12} (S_m \nu_m D_L^2 R^{-3})^{2/7}. \quad (4-15)$$

Knot C1 is characterized by a moderate  $B_{\text{eq}} \approx 0.3$  G and the core features the highest equipartition magnetic field with  $B_{\text{eq}} \approx 1.4$  G and  $B_{\text{eq}} \approx 2.6$  G, respectively. Results are summarized in Table 4.10.

The two magnetic field estimates have a different dependence on the Doppler factor. On the one hand,  $B_{\text{SSA}} \propto \delta$  for the magnetic field strength calculated from SSA, and  $B_{\text{eq}} \propto \delta^{(2/7\alpha+1)}$  for the minimum, equipartition magnetic field. We use those to get an estimate of  $\delta_{\text{eq}}$ , when possible, from the ratio  $B_{\text{eq}}/B_{\text{SSA}} = \delta_{\text{eq}}^{2/7\alpha}$ . The estimated equipartition Doppler factor for C1,  $\delta_{\text{eq}, \text{C1}} \approx 50$ , is also in good agreement with  $\delta_{\text{var}} \leq 51.4$ . Given the assumptions, all values are in reasonable agreement.

## 4.5 DISCUSSION

### 4.5.1 The $\gamma$ -ray/radio flare

The monthly-binned *Fermi*/LAT data adopted from Fuhrmann et al. [2014] and shown in Fig. 4.7 (top panel) span the time period between MJD 54707 (2008.66) through MJD 55911 (2011.96). The source is already at high state, since the beginning of our monitoring period. From then on, the rising trend continues until MJD 54875 (2009.12), when the absolute maximum in  $\gamma$ -ray photon flux of  $\sim 1.3 \cdot 10^{-6} \text{ cm}^{-2} \text{ s}^{-1}$  is reached. In fact, there exists some amount of sub-structure in the  $\gamma$ -ray light curve. A second—local—maximum is reached on MJD 54959 (2009.35) with comparable flux. Altogether, activity at high energies,

from its start until the first—and absolute—minimum is reached on MJD 55295 (2010.27), lasts for almost 650 days (shaded area in Fig. 4.7).

In Savolainen et al. [2002] the generic connection between flux density outbursts and newly ejected jet features has been made, with most radio flares accompanied by the ejection of one or more components. While usually the brightness of knots associated with flares decays fast, here we follow the evolution of one thanks to the enhanced resolution of mm-VLBI. As discussed in Section 4.3.3 component C<sub>3</sub>, visible at 43 and 86 GHz only, is in fact characterized by a decaying light curve with an initial flux density level—at epoch 2009.35—almost 10 times higher than that of the other two components (C<sub>1</sub>, C<sub>2</sub>) present in the flow and seen also at both high frequencies.

Observations analyzed here are consistent with C<sub>3</sub> having an apparent speed of  $\approx 7.1 c$  (Section 4.3.2) and its ejection year, based on the kinematical models at 43 and 86 GHz, is  $2007.4 \pm 2.2$  and  $2008.3 \pm 0.3$ , respectively. C<sub>3</sub>'s time of zero separation (red vertical line in Fig. 4.7) coincides with the onset of the  $\gamma$ -ray flare when extrapolating the rate of  $\gamma$ -ray flux change, as it rises linearly, back in time. We conclude, based on the ejection date of superluminal component C<sub>3</sub>, that it is most probably associated with the  $\gamma$ -ray flare and its radio counterpart. Since its separation from the core, it is traveling downstream the jet with an apparent superluminal velocity of 7.1  $c$  at 86 GHz and a consistent velocity at 43 GHz (see Table 4.6). We note the larger uncertainty in the knot's time of ejection at 43 GHz as compared to observation at 86 GHz. That is due to the sparser sampling at this frequency and the higher impact to the fit due to the very last data point in the radial separation plot (middle panel of Fig. 4.5). In any case, the two figures are consistent with each other.

Assuming the speed of knot C<sub>3</sub> to remain constant, at the times of the two  $\gamma$ -ray photon flux maxima, in 2009.2 and 2009.4 (at MJD 54897 and 54959) the knot is  $\sim 0.7$  and  $\sim 0.8$  pc downstream the 3-mm core, respectively.

A plausible scenario is that a disturbance originating at the jet nozzle of PKS 1502+106, while still upstream of the 3-mm core—i.e. the unit-opacity surface at 86 GHz—it produces an increase of  $\gamma$ -ray emission. As it continues to move outwards, it becomes optically thin as it crosses the 3-mm VLBI core hence producing the radio flare. Alternatively, the core may represent the first conical recollimation shock of the flow [Daly and Marscher, 1988; Gómez et al., 1995; Bogovalov and Tsinganos, 2005; Marscher, 2008], in which case the flare can be attributed to shock–shock interaction and subsequent enhancement of emission. In any case, as the disturbance moves further downstream we observe it as knot C<sub>3</sub> at its decaying flux density phase.

#### 4.5.2 Distance estimates to the central engine

The long-standing debate as to where in the jet the high-energy emission originates, is presently far from being considered resolved. In this paper, combining radio single dish monitoring data and our findings from the VLBI analysis of PKS 1502+106 presented here, we explore and further constrain the region where the pronounced GeV activity of 2009 takes place and compare with the SED modeling results of Abdo et al. [2010].

Under the assumption that the core takes up the entire jet cross section, the de-projected distance of the 86 GHz core from the vertex of the hypothesized conical jet can be estimated using the following expression

$$d_{\text{core}} = \frac{1.8 \langle \text{FWHM}_{\text{core}} \rangle}{2 \tan(\phi_{\text{int}}/2)} \quad (4-16)$$

With an average size for the core  $\langle \text{FWHM}_{\text{core}} \rangle = 0.03$  mas and a nominal opening angle between  $\phi_{\text{int}} = 2.2^\circ$  and  $\phi_{\text{int}} = 1.6^\circ$  (Section 4.4.3), the 86 GHz core is constrained to distances between  $\leq 12$  pc and  $\leq 16.5$  pc away from the vertex of the jet, respectively. These distances constitute upper limits since the core is at all times unresolved, and the size we report is an upper limit of its angular size.

Using a cross-correlation function analysis, Fuhrmann et al. [2014] find significantly correlated variability for PKS 1502+106 between the  $\gamma$ -ray and 86 GHz single-dish light curves, shown in Fig. 4.7. Radio lags behind  $\gamma$  rays by  $14 \pm 11$  days at a significance level above 99%. This time lag translates into a distance of  $\sim 2.1$  pc between the  $\gamma$ -ray emitting region and the  $\tau = 1$  surface at 86 GHz. Assuming that the core in our 86 GHz images coincides with the same surface of opacity transition from the optically thick to thin regime in the jet, we conclude that the  $\gamma$ -ray emitting region is located at  $\leq 10$ – $15$  pc or  $\leq 3$ – $4.6 \times 10^{19}$  cm away from the vertex of the hypothesized conical jet. These figures represent also upper limits for the distance between the black hole and the  $\gamma$ -ray production region, due to the uncertain—but likely small—separation between the black hole horizon and the base of the jet.

From the Mg II line profile the bulk BLR radius of PKS 1502+106 is estimated to be  $R_{\text{BLR}} = 2 \times 10^{17}$  cm [see Abdo et al., 2010, and references therein]. The distance of  $\leq 3$ – $4.6 \times 10^{19}$  cm corresponds to a region at the outer edge or further downstream from the BLR of the source. The upper limit reported here does not contradict the findings of Abdo et al. [2010], where the external radiation Compton mechanism (ERC) with the BLR photon field as the target for IC up-scattering, has a significant contribution to the high-energy part of the SED. As such, the MeV/GeV-active region must be within or at the edge of the BLR. However, the  $\gamma$ -ray flare discussed in Abdo et al. [2010] precedes by few weeks the one we analyze here and most likely belongs to the pre-main-flare period shown in Fig. 4.7.

The precision we can obtain from the VLBI data at hand is not sufficient for the estimation of core-shifts, magnetic fields and other relevant physical parameters, using the effect of frequency-dependent position of the VLBI core component [Marcaide and Shapiro, 1984; Lobanov, 1998]. It is worth noting that the results of Pushkarev et al. [2012] place the 15 GHz core at a distance of  $\sim 8$  pc from the vertex of the jet. Consequently, since the unit-opacity surface at 86 GHz ought to be closer to the jet base than the core at 15 GHz, the upper limits reported above constrain rather loosely the 86 GHz core distance to the vertex. A point that should be taken into account when estimating such distances through VLBI when the core is unresolved. The upper limits deduced from VLBI will be discussed in the next chapter where we obtain the distance of the 3-mm core from the vertex of the jet through a detailed, multi-frequency light curve timing analysis.

### 4.5.3 Intrinsic jet properties

Given the Doppler factor and apparent speed for superluminal knots C<sub>1</sub> and C<sub>3</sub>, estimated in Section 4.3.2 and 4.4.1, we explore the jet properties of PKS 1502+106. From the expressions of both the Doppler factor and Lorentz factor and making use of Eq. 4–6, we obtain the expressions of the Doppler factor as a function of apparent speed given the viewing angle,  $\delta = f(\beta_{\text{app}}|\theta)$ , and given the Lorentz factor,  $\delta = f(\beta_{\text{app}}|\gamma)$ . The loci in Fig. 4.11 represent these two functions for a range of viewing angles and Lorentz factors (see caption for details). Overplotted are regions of estimated  $\delta$  and  $\beta_{\text{app}}$ . These help us in constraining the intrinsic properties of the flow in terms of viewing angle and the Lorentz factor.

Component C<sub>1</sub> is characterized by an extreme variability Doppler factor of  $\sim 51$ . The figure is an upper limit calculated from causality arguments but agrees well with  $\delta_{\text{eq}}$  (see Tables 4.8 and 4.10). The same variability analysis for knot C<sub>3</sub>, suggests comparable results from both 43 and 86 GHz, with an upper limit for the Doppler factor  $\sim 12$ – $15$  (Table 4.8). Fig. 4.11 is indicative of the extreme characteristics of the relativistic jet flow. Clearly, especially for C<sub>1</sub>, we are in the small  $\theta$ –extreme  $\beta$  regime, with the deduced parameters being  $\geq 0.8^\circ$  for the viewing angle and  $\beta > 0.99$ . However, the same considerations for knot C<sub>3</sub> give more moderate results, with  $\theta \geq 3.4^\circ$  and  $\beta > 0.98$ .

Differences in the inferred aspect angle and intrinsic speed, between these two knots, may reflect physical differences in the jet flow of PKS 1502+106. First, the jet portion we observe at high frequencies—knot C<sub>3</sub>—is possibly still in its accelerating phase (see also the apparent speed profile in Fig. 4.6). This could explain the differences seen between knots C<sub>3</sub> and C<sub>1</sub>, with the latter being some 1 mas downstream of the core. The jet, as revealed from the maps and the overall structure, appears to bend thus the high Doppler factor further out, traced by knot C<sub>1</sub>, could also be attributed to differential Doppler boosting. Taking into account only the 86 GHz data (red rectangle in Fig. 4.11) the two regions wherein components C<sub>3</sub> and C<sub>1</sub> are traveling are completely incompatible, when it comes to viewing angle and intrinsic speed.

The difference between the Doppler boosting factors in two regions, at two different viewing angles  $\theta_1$  and  $\theta_2$ , keeping  $\beta$  constant is given by

$$\delta_2 - \delta_1 = \frac{\sqrt{1 - \beta^2}(\beta \cos \theta_2 - \beta \cos \theta_1)}{(1 - \beta \cos \theta_2)(1 - \beta \cos \theta_1)}. \quad (4-17)$$

Here, we test whether the change of Doppler factor of  $\sim 40$ , between the inner and outer jet, at distances  $< 0.5$  mas and  $> 1$  mas can be caused only by a jet bending towards our line of sight. Components C<sub>3</sub> and C<sub>1</sub> are traveling in those two regions, respectively. The Doppler factor is estimated from variability—for both—and also from comparing the SSA and equipartition magnetic field for C<sub>1</sub>. C<sub>3</sub> is characterized by  $\delta_{\text{var}} \sim 12$ – $15$  while the two independent estimates agree very well for the Doppler factor of C<sub>1</sub> to an extreme value of  $\sim 50$ . From Fig. 4.11 the intrinsic speed of C<sub>3</sub> is constrained between  $\beta \sim 0.95$  and  $\beta \sim 0.995$  ( $\gamma = 3$  and  $\gamma = 10$ , respectively). Taking even the highest value for  $\beta$ , keeping it constant and applying Eq. 4–17 between  $\theta_1 = 0.8^\circ$  and  $\theta_2 = 3.4^\circ$  (the maximum range observed), we obtain that the difference in Doppler factor of about 40 be-



tween the two regions cannot be reconciled only by changing the viewing angle. For these numbers only a  $\delta_2 - \delta_1 \sim 6$  can be expected. Thus, the two regions are characterized by both a change in the viewing angle and also by acceleration—i.e. change of Lorentz factor. This can also be seen directly from the plot in Fig. 4.11, since only a few loci can lead from one region to the other and only for the less constrained region for C<sub>3</sub>, coming from the kinematics at 43 GHz. Converting the aforementioned intrinsic velocities to the more convenient Lorentz factor, we obtain that even for the highest  $\beta = 0.995$  (for C<sub>3</sub>) and for  $\beta = 0.999$  (for C<sub>1</sub>), we obtain that a change of Lorentz factor, at least, from  $\gamma \sim 10$  to  $\gamma \sim 22$  takes place in the region between roughly 0.3 to 1.1 mas.

In estimating the viewing angle, it is worth noting that the critical value,  $\theta_c$ , might not be a good proxy for the angle between the jet and the observer's line of sight. This is the case for small kinematical Lorentz factors ( $\gamma_{\min}$ ), deduced by low observed apparent speeds. In fact, the viewing angle can be larger than  $\theta_c$  for a flow at a larger viewing angle but intrinsically faster. However, the critical angle does not largely differ from the true  $\theta$  for ultra-relativistic flows. This conclusion draws from the behavior of  $\beta_{\text{app}}$  with respect to the viewing angle (cf. any plot of  $\beta_{\text{app}}$  vs.  $\theta$ ) and the following energetics argument. An electron traveling at 0.6  $c$  has only 1.5 times more (relativistic) kinetic energy than an electron at 0.5  $c$ . The same electron at 0.999  $c$  or  $\gamma \approx 22$ , possesses 3.4 times more energy as compared to an  $e^-$  traveling at a speed of 0.99  $c$  or  $\gamma \approx 7$ . Obviously, it is harder to accelerate the electron in the latter case as opposed to the former, making the minimum Lorentz factor and consequently the critical angle good proxies for the intrinsic values when very high apparent speeds are observed.

The variability viewing angle  $\theta_{\text{var}} \geq 0.8^\circ$ , calculated for C<sub>1</sub> seems small compared to the critical one  $\theta_c = 2.6^\circ$ . These are not inconsistent findings though because the critical viewing angle represents an upper limit as well, calculated from the fastest component—here being C<sub>1</sub>. Estimation of a variability viewing angle is also possible combining single-dish flux density measurements and VLBI kinematics as in Hovatta et al. [2009], where the authors estimate  $\theta_{\text{var}} = 4.7^\circ$  for PKS 1502+106. However, this figure is based on a smaller  $\beta_{\text{app}} = 14.6$  measured at 22 GHz and 37 GHz in the period from 1990.5 to 1995.5 [cf. Terasranta et al., 1998].

Pushkarev et al. [2009] calculate a slightly larger intrinsic opening angle for the jet of PKS 1502+106. The reason is twofold. First, they obtain a slightly larger intrinsic opening angle of  $37.9^\circ$  which they subsequently de-project using the variability viewing angle reported in Hovatta et al. [2009], thus obtaining an intrinsic jet opening angle of  $3.11^\circ$ . The differences with the values we report here, of an opening angle between  $1.6^\circ$  and  $2.2^\circ$ , are justified by the higher apparent speed of component C<sub>1</sub> seen in our data, traveling with  $\beta_{\text{app}} \approx 22$ .

The radial brightness temperature distribution cannot corroborate nor falsify the "two-region scenario", since in the first mas beyond the core, most figures reported constitute lower limits. This arises from the sizes of components being unresolved at all three frequencies. In any case, what is evident is only the decaying trend at distances  $\geq 1$  mas (see Fig. 4.10). Consequently, the scenario of acceleration within the first mas from the core, supported by both kinematics and variability, cannot be tested through the dependence of  $T_b$  on distance. The case where the part of the jet probed by the 86 GHz VLBI data is still at

its accelerating phase [see e.g. Lee, 2013], with the Doppler factor increasing downstream of the 86 GHz core, is not incompatible with the radial  $T_b$  profile. Additionally, note that there is no evidence for any overall rising trend of  $T_b$  with distance, as we move away from the core, but rather a steady decay is seen at all frequencies.

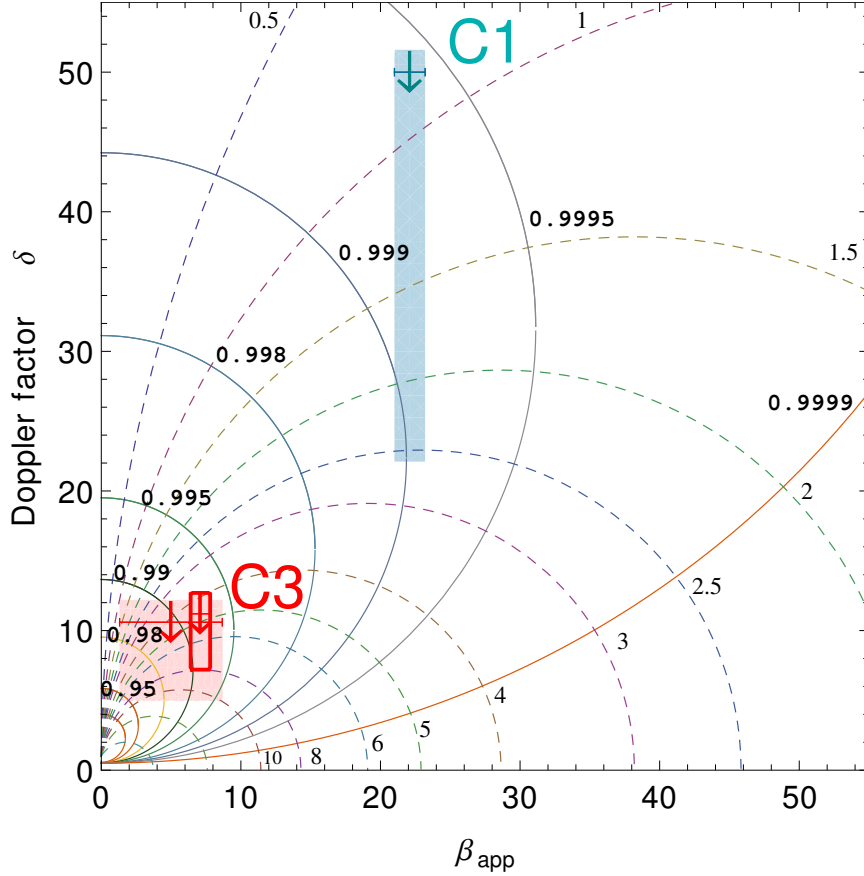


Figure 4.11: Doppler factor as a function of apparent speed for given viewing angle,  $\delta = f(\beta_{\text{app}}|\theta)$ , and given intrinsic speed  $\beta$ ,  $\delta = f(\beta_{\text{app}}|\beta)$ . Loci represent these two functions for a range of  $\theta$  and  $\beta$ . The values of intrinsic speeds plotted are  $\beta = 0.9, 0.95, 0.98, 0.99, 0.995, 0.998, 0.999, 0.9995, \text{ and } 0.9999$  shown as solid lines. For the viewing angle the values are  $\theta = 0.5^\circ, 1^\circ, 1.5^\circ, 2^\circ, 2.5^\circ, 3^\circ, 4^\circ, 5^\circ, 6^\circ, 8^\circ, 10^\circ, 15^\circ, \text{ and } 30^\circ$  shown as dashed lines. Note the two different jet regions, in terms of physical characteristics, where components C1 and C3 are traveling. Shaded areas represent the observables from our VLBI monitoring, namely the Doppler factor and the apparent velocity for each of the two knots.

#### 4.5.4 Particle versus magnetic field dominated jet

We explore the dominance of magnetic field versus magnetic-field energy by: (i) the ratio of equipartition over measured brightness temperature and finally (ii) comparing the equipartition critical size of VLBI components and their observed size.

From the ratio of observed to equipartition brightness temperature ( $T_{\text{eq}} = 5 \times 10^{10}$  K) we can explore the dominance of particle versus magnetic field energy in the regions of the jet of PKS 1502+106. Using Eq. 5d from [Readhead \[1994\]](#), the ratio of the two energy densities can be estimated through

$$\eta = \frac{u_p}{u_B} = \left( \frac{T_{\text{eq}}}{T_b} \right)^{-17/2} \quad (4-18)$$

with  $u_p$  and  $u_B$  the energy density of relativistic particles and magnetic field, respectively and  $T_b$  the observed brightness temperature. Using the mean values for the core brightness temperature reported in Section 4.4.4, we obtain  $\eta_{15\text{GHz}} = 9.7 \times 10^{-2}$ ,  $\eta_{43\text{GHz}} = 3.6 \times 10^{-5}$  and  $\eta_{86\text{GHz}} = 8.9 \times 10^{-8}$ . Magnetic field dominates, on average, in the ultracompact region of the core, at all frequencies, with a decreasing ratio ( $u_p/u_B$ ) as we move towards 86 GHz. This is consistent with the findings of [Lee \[2013\]](#), who argues that while initially the jet at 86 GHz is magnetic-field dominated, as we move further downstream of the high-frequency core, towards regions probed by observations at lower frequencies, magnetic-field energy is converted to kinetic flux and an increase in the brightness temperature is to be expected.

The size of a source in equipartition, at the synchrotron turnover; i.e. the 'equipartition critical size',  $\vartheta_{\text{eq}}$  [[Scott and Readhead, 1977](#)] is given as

$$\vartheta_{\text{eq}} = F(\alpha)[1 - (1+z)^{-1/2}]^{-1/17}(1+z)^{(2\alpha+15)/34} S_m^{8/17} \nu_m^{(2\alpha-35)/34} \quad (4-19)$$

where:

- $F(\alpha)$  is a spectral-index dependent parameter from [Scott and Readhead \[1977\]](#),
- $\alpha$  the optically-thin spectral index,
- $S_m$  the flux density at the synchrotron turnover, and
- $\nu_m$  the turnover frequency

The equipartition critical size offers another means for estimating the energy density dominance in a given source. In case  $\vartheta > \vartheta_{\text{eq}}$ , in the region with observed size  $\vartheta$ , the magnetic field energy dominates. In the opposite case it is the relativistic particles that contribute the most to the region's energy density. Using the spectral values obtained in Section 4.3.4, we calculate the following critical size for the core and knot C1:  $\vartheta_{\text{eq,C1}} \approx 0.01$ ,  $\vartheta_{\text{eq,core}} \leq 0.07$  mas. The aforementioned values allow us to conclude that superluminal knot C1 appears to be magnetic field dominated. Finally, for the core it is  $\vartheta_{\text{eq,core}} \sim 0.1$  mas, while its measured size at the turnover seen for epoch 2009.9  $\vartheta \leq 0.06$  mas. This figures suggest particle energy dominance for the core at 43 GHz. Our results are summarized in Table 4.10.

#### 4.6 CHAPTER SUMMARY AND CONCLUDING REMARKS

In the present chapter a full, three-frequency (15, 43, and 86 GHz) VLBI study of the  $\gamma$ -ray blazar PKS 1502+106 was presented, using GMVA and additional data

from the MOJAVE monitoring program. Furthermore, we have made use of the densely-sampled F-GAMMA single-dish light curves at matching frequencies along with the *Fermi*/LAT monthly-binned light curve at energies  $>100$  MeV. The work presented above allows us to follow the multi-frequency flare of 2008–2010 and conclude the following:

1. PKS 1502+106 exhibits a compact, core-dominated morphology at all three frequencies with a one-sided, bent, parsec-scale jet. The jet can be decomposed into 3 ( $C_1$ ,  $C_2$ , and  $C_3$ ) at 43 and 86 GHz and 5 ( $C_a$  to  $C_e$  and  $C_1$ ,  $C_2$ ) at 15 GHz MODELFIT components characterized by extreme superluminal motion in the range 5–22 c. The most extreme example is component  $C_1$  traveling downstream the jet at about 22 c at 15 GHz and comparable speed at 43/86 GHz.
2. Doppler and Lorentz factor estimates for individual components within the flow of PKS 1502+106 are obtained using variability and VLBI kinematical arguments. The minimum Doppler boosting factors are  $\delta_{\beta_{\text{app}}, C_1} \approx \beta_{\text{app}, C_1} \approx 22.1$  at 15 GHz. For knots  $C_2$  and  $C_3$ , it is  $\delta_{\beta_{\text{app}}} \approx \gamma_{\text{min}, C_2} = 9.3$  and  $\delta_{\beta_{\text{app}}} \approx \gamma_{\text{min}, C_3} = 7.2$ , from the 86 GHz observations. For knot  $C_1$ , showing significant variability at 15 GHz the calculations yield ( $\delta_{\text{var}} \leq 51.4$ ) and Lorentz ( $\gamma_{\text{var}} \leq 30.5$ ) factors. Knot  $C_3$  is also found to have consistent behavior at both high frequencies with  $\delta_{\text{var}}^{43 \text{ GHz}} \leq 12.1$  and  $\gamma_{\text{var}}^{43 \text{ GHz}} \leq 7.1$ , while at 86 GHz the estimation yields  $\delta_{\text{var}}^{86 \text{ GHz}} \leq 15$  and  $\gamma_{\text{var}}^{86 \text{ GHz}} \leq 9.2$ . All figures are consistent with the estimates of the minimum Doppler and Lorentz factors. Doppler factor estimates are strikingly different for knot  $C_3$  at  $r < 0.5$  mas and  $C_1$  at a distance  $r > 1$  mas.
3. An additional Doppler factor estimate from the different dependencies of  $B_{\text{SSA}}$  and  $B_{\text{eq}}$  on  $\delta$  can be calculated. The estimate for  $C_1$  is in agreement with the estimates from kinematics and variability.
4. Using variability arguments we are able to constrain the viewing angle towards the source to  $\theta \geq 3.4^\circ$  for the inner and  $\theta \geq 0.8^\circ$  for the outer portions of the jet, after about 1 mas. Calculation of the critical viewing angle—i.e.,  $\theta_c$ , minimizing the Lorentz factor for a given  $\beta_{\text{app}}$ —for knot  $C_1$  at 15 GHz yields  $\theta_c = 2.6^\circ$ .
5. We calculate the opening angle of the jet of PKS 1502+106 with two methods. First by a linear fit to the deconvolved size of all resolved knots with respect to radial separation from the core and second by averaging the size of each component and calculating the opening angle of each one separately and finally averaging. The estimated de-projected opening angle is between  $1.6^\circ$  and  $2.2^\circ$ .
6. The differences in apparent speed and viewing angle point towards a jet bending after the first mas. This results in differential Doppler boosting—i.e. increasing  $\delta$  from  $\sim 12$ – $15$  to  $\sim 50$  as traced by components  $C_3$  and  $C_1$  traveling at radial distances of  $<0.5$  mas and  $>1$  mas from the core, respectively. However, the Doppler factor gradient cannot be explained on the grounds of bending only. Acceleration must also be at play within the first mas of the jet (see next item).

7. Constraining the intrinsic  $\beta$  and viewing angle,  $\theta$ , from the the limits calculated for the Doppler factor and the measured apparent velocity we can clearly distinguish between two regions of the jet of PKS 1502+106. These are visible in Fig. 4.11, wherein the two knots C1 and C3 are traveling. Specifically, close to the core at a distance  $\leq 0.5$  mas the parameters obtained for C3 at 43 GHz constrain the parameters of the flow to  $0.95 \leq \beta \leq 0.995$  and  $1.5^\circ \leq \theta \leq 10^\circ$ . The same component at 86 GHz sets slightly stringer constraints to the viewing angle with  $4^\circ \leq \theta \leq 8^\circ$ . On the other hand in the region where C1 is traveling its observed Doppler factor and apparent velocity constrain the flow to  $\beta \geq 0.999$  and  $0.8^\circ \leq \theta \leq 2.5^\circ$ . Thus setting clearly a division between the two jet regions. Hence, we conclude that the jet of PKS 1502+106 bends towards us in the region beyond  $\sim 1$  mas downstream of the core and accelerates as well.
8. The radial brightness temperature profile shown in Fig. 4.10 indicated very high  $T_b$  for the core region at all three frequencies. We find though a trend of decreasing  $T_b$  as we go towards higher observing frequency and with increasing distance from the core with no increasing trend whatsoever. This could indicate a magnetically-dominated core region probed by the 86 GHz observations where Poynting flux has not yet fully converted to kinetic flux.
9. Spectra of individual components allow for the calculation of the magnetic field strength in different regions of the jet. Component C1 exhibits a distinctive SSA peak. The core shows a flat spectrum with  $\langle \alpha \rangle \approx -0.22$  but at one epoch (2009.9) signs of a turnover at  $\sim 43$  GHz. To obtain  $S_m$  and  $v_m$  we fit an SSA model to the spectrum of C1 and assume a turnover at about 43 GHz for the core. Through the comparison between the SSA and equipartition, minimum magnetic field we conclude that for component C1  $B_{SSA}$  is much stronger than  $B_{eq}$ , indicating a high degree of Doppler boosting. Finally, for the core it is  $B_{SSA}/\delta \geq 2$  mG and  $B_{eq} = 1.2$  G.
10. From the contrast between the observed and equipartition critical size we conclude that knot C1 is magnetic field dominated. The analysis for the core suggests a particle energy dominated region at 43 GHz.
11. Radio flux density decomposition into distinct VLBI components and comparison with the single-dish radio flux density outburst indicates that the bulk of radio emission originates from the core at all frequencies while another component, C3, only resolved at 43 and 86 GHz contributes also to the flare emission and during the period of mm-/cm-VLBI monitoring appears in a flux density decaying phase. Apart from the core at 43/86 GHz, C3 shares a significant radio flux density level. Component C3 is not resolved at 15 GHz due to blending with the core.
12. Given the radio flux density decomposition and the estimated ejection time of knot C3—coincident with the single-dish mm flare onset—we conclude that it is responsible for the radio flare observed in PKS 1502+106 during the period 2008–2010. Furthermore, the previously established correlation between the radio flare and  $\gamma$  rays indicates that component C3

is responsible for the  $\gamma$ -ray flare and its radio counterparts. Arguably, the 2008–2010 flare of PKS 1502+106 is an event originating in a disturbed region at the jet nozzle. While still upstream of the 3-mm core it produces the increased  $\gamma$ -ray emission observed and as it continues to move, it becomes optically thin (at 86 GHz) close to the 3-mm VLBI core thus enhancing its brightness. It then continues on and after the 86 GHz optically thick region, is seen as knot C<sub>3</sub> at its decaying flux density phase.

13. We conclude that the  $\gamma$ -ray emitting region is located at  $\leq 10$ – $15$  pc or  $\leq 3$ – $4.6 \times 10^{19}$  cm away from the vertex of the hypothesized conical jet. These estimates are upper limits for the distance between the SMBH and the  $\gamma$ -ray production region, due to the uncertain distance between the black hole horizon and the base of the jet.

Concluding, PKS 1502+106 represents a source whose complex structural dynamics needs to be further investigated with higher-cadence, high-resolution imaging at mas and sub-mas scales.

## THE BROADBAND OUTBURST OF PKS 1502+106: WHAT CAN IT TELL US?

---

### 5.1 INTRODUCTION

The present chapter is concerned with the presentation and analysis of the single-dish data set on PKS 1502+106 covering the broadband 2008–2010 outburst. The set includes multi-epoch and multi-wavelength observations from the *Fermi*-GST AGN Multi-frequency Monitoring Alliance (F-GAMMA) program<sup>1</sup>, along with light curves from the OVRO 40 m blazar monitoring program<sup>2</sup> and the available data from the high-frequency SMA calibrator list archive<sup>3</sup> at a central frequency of 226.5 GHz.

The regularly sampled F-GAMMA data set, presented and analyzed in the following, spans the frequency range between 2.6 GHz to 142.33 GHz and the time baseline covers approximately six years in length, with the bulk of observations starting in 2008 June and continuing until 2014 April and some high frequency light curves starting as early as 2007 May. The data set features a mean cadence of  $\sim 30$  days.

The multi-wavelength approach has a significant impact in blazar physics and has been employed by many authors in previous studies, offering a tool towards an—as complete as possible—understanding of blazar phenomenology [see e.g. [Hartman et al., 1992](#); [Urry, 1999](#); [Ferrarese and Ford, 2005](#)] through different theoretical models. Testing the feasibility and/or validity of such models translates into quantitatively contrasting the observational signatures of the mechanisms they invoke with actual observations. Dense, long-term, multi frequency monitoring of these extreme manifestations of AGN activity offer a unique opportunity for putting blazar variability models to the test and comparing with the predictions of theoretical frameworks that attempt to explain the emission and overall observed characteristics of those sources.

The scope here is to parameterize the observed outburst seen in the light curves and extract its relevant parameters such as flare amplitudes, time scales, and cross-band delays. First, the use of observed cross-band and frequency-dependent time lags allows us to estimate the core shifts—i.e. the frequency-dependent position of the core—with an approach other than via traditional multi-frequency VLBI measurements. With the core shift at hand, an opacity profile of the source is obtained and, under the assumption of equipartition, physical parameters such as the magnetic field at each respective core region and at a distance of 1 pc away from it are also estimated. Furthermore, the distance of each core to the vertex of the jet in combination with the observed delay between radio and  $\gamma$  rays allow for decisively constraining the location of the high-energy emission.

---

<sup>1</sup> <http://www3.mpifr-bonn.mpg.de/div/vlbi/fgamma/fgamma.html>

<sup>2</sup> <http://www.astro.caltech.edu/ovroblazars/>

<sup>3</sup> <http://sma1.sma.hawaii.edu/callist/callist.html>

Second, using the deduced flare parameters a direct comparison with the predictions of the shock-in-jet scenario is attempted, through the results of analytical simulations within its framework. This approach also allows for better constraining the physical parameters such as the evolution of the Doppler factor and the magnetic field topology with distance, in the assumed conical jet of PKS 1502+106.

## 5.2 RADIO OBSERVATIONS AND THE F-GAMMA PROGRAM

Data used in this work have been collected within the framework of the F-GAMMA program [Fuhrmann et al., 2007; Angelakis et al., 2010; Fuhrmann et al., 2014]. It is the coordinated effort for the contemporaneous monitoring of a sample comprising approximately 60 *Fermi* detected blazars at three radio telescopes, namely the Effelsberg 100-m (EB), Institut de Radioastronomie Millimétrique, IRAM 30-m (at Pico Veleta, PV, Spain) and Atacama Pathfinder EXperiment (APEX) 12-m, at Llano de Chajnantor, Chile. Since its initiation in 2007, the F-GAMMA program followed the evolution of the total intensity and polarization of this population of extreme objects enabling detailed studies of broadband variability, emission mechanisms, spectral evolutionary paths and the long sought connection between radio emission and  $\gamma$  rays.

The complete frequency coverage spans 11 bands between 2.64 and 345 GHz; 2.64 to 43.0 GHz available from observations at EB, 86.24 and 142.33 GHz at PV and 345.00 GHz at APEX (for details see Table 5.1). The monthly observations at EB and PV were performed in a quasi-simultaneous manner with a typical separation of days to ensure maximum spectral coherency. Allocated F-GAMMA observing runs were complemented by the general flux monitoring conducted at PV and in close collaboration with the local staff [Ungerechts et al., 1998]. A subsample of 25 F-GAMMA sources were observed from APEX along with a number of interesting low-declination *Fermi* blazars and other AGN, that are not observable from the sites of EB and PV. A detailed description of EB and PV observations and data reduction is provided in Fuhrmann et al. [2008, 2014]; Angelakis et al. [2015]; Nestoras et al. [in prep.]. In the following the essential reduction steps are presented in an abridged but comprehensive way.

### 5.2.1 Effelsberg 100-m telescope data analysis

EB data are obtained using the heterodyne receivers mounted at the secondary focus of the 100-m telescope (see Table 5.1). Receivers at 4.85, 10.45, and 32.00 GHz are multiple-feed equipped systems allowing differential (beam-switched) measurements. EB observations are conducted with *cross-scans*, that is slewing over the radio source in the directions of azimuth and elevation. A necessary number of sub-scans is commanded accordingly, thus enabling the necessary signal-to-noise ratio (SNR) to be reached. After acquisition of raw data, an initial data quality control or "flagging" is performed, at sub-scan level, ensuring that sub-scans fulfill some minimum quality criteria.

Later, sub-scans of each observed source are averaged together and finally a Gaussian fit is applied in order to extract the relevant parameters used in



FACILITY	WAVELENGTH (mm)	FREQUENCY (GHz)	ENERGY (GeV)
Effelsberg 100-m	110	2.64	...
	60	4.85	...
	36	8.35	...
	28	10.45	...
	20	14.60	...
	13	23.05	...
	9	32.00	...
	7	43.00	...
IRAM 30-m	3	86.24	...
	2	142.33	...
APEX 12-m	0.8	345.00	...
<i>Fermi</i> /LAT	...	...	0.1–300

Table 5.1: F-GAMMA program facilities and spectral coverage.

subsequent reduction steps described below. The steps of the post-measurement data reduction procedure are as follows:

1. **Pointing offset correction.** This is meant to account for the power loss due to the discrepancy between the telescope pointing model and the real source position. The correction is applied through the following formula:

$$T_{i,\text{poi}} = T_{i,\text{obs}} \exp \left[ 4 \ln 2 \left( \frac{\Delta p_j}{\text{FWHM}_\nu} \right)^2 \right] \quad (5-1)$$

where,

- $i, j$  are the scan driving direction indices  $i, j = \{\text{AZI}, \text{ELV}\}$  with  $i \neq j$ ,
  - $T_{i,\text{poi}}$  the antenna temperature in direction  $i$  after pointing correction,
  - $T_{i,\text{obs}}$  is the observed antenna temperature prior to pointing correction,
  - $\Delta p_j$  is the pointing offset obtained by a Gaussian fit in the  $j$  direction, and
  - $\text{FWHM}_\nu$  is the extracted FWHM of the Gaussian at observing frequency  $\nu$ .
2. **Atmospheric opacity correction.** This accounts for the missing flux due to transmission of the observed radiation through the Earth's atmosphere. It is applied as:

$$T_{\text{opc}} = T_{\text{obs}} \exp(\tau_{\text{atm}}) \quad (5-2)$$

where,

- $T_{\text{obs}}$ , is the observed antenna temperature prior to opacity correction,

- $T_{\text{opc}}$  is the resulting antenna temperature after opacity correction,
- $\tau_{\text{atm}}$  is the atmospheric opacity at the source elevation.

The atmospheric opacity,  $\tau_{\text{atm}}$ , is a function of zenith angle only

$$\tau_{\text{atm}} = \tau_{\text{zen}} \cdot \chi(z) = \tau_z \sec z \quad (5-3)$$

where,

- $z$  is the zenith angle corresponding to elevation  $\text{ELV} = 90^\circ - z$ ,
- $\tau_{\text{atm}}$  is the opacity at the source elevation ELV,
- $\tau_{\text{zen}}$  the zenith opacity, and
- $\chi(z)$  the airmass as a function of zenith angle.

The calculation of zenith opacity is done for every observing epoch individually by fitting the lower envelope of the recorded  $T_{\text{sys}}$  as a function of elevation.

3. **Elevation-dependent gain compensation.** Telescope gain is a strong function of its elevation due to gravitational deformation of the main primary reflecting element, resulting in excursions of its geometry from that of an ideal paraboloid. At the Effelsberg 100-m, the effect is largely reduced thanks to construction considerations (use of the homology principle), but nevertheless small residual effects are present, due to its gross size and weight. The elevation-dependent gain compensation or simply gain correction is applied according to the following formula:

$$T_{\text{gc}} = T_{\text{obs}} \cdot G^{-1} \quad (5-4)$$

where,

- $T_{\text{obs}}$ , is the observed antenna temperature prior to gain correction,
- $T_{\text{gc}}$  is the gain-corrected antenna temperature,
- $G$  is the elevation-dependent gain curve.

The gain curve at each observing frequency is given by a second-order polynomial with parameters  $A_0$ ,  $A_1$  and  $A_2$ , of the form:

$$G(\text{ELV}) = A_0 + A_1 \cdot \text{ELV} + A_2 \cdot \text{ELV}^2 \quad (5-5)$$

Parameters  $A_0$ ,  $A_1$  and  $A_2$  are recorded and provided by the telescope staff<sup>4</sup>.

4. **Absolute flux density calibration.** The final step towards a fully calibrated data set is the conversion of the final, corrected antenna temperature from Kelvin to Jy. The procedure is commonly referred to as *sensitivity correction*. It is achieved through the use of standard flux density calibrators which provide the conversion factor between K and Jy. This is done simply by assigning each calibrator's constant flux density to the observed antenna temperature. Flux densities of these calibrators are reported in the literature (see Table 5.2).

<sup>4</sup> <https://eff100mwiki.mpifr-bonn.mpg.de/doku.php>

SOURCE	3C 48	3C 161	3C 286	3C 295	NGC 7027	K3-50A	W3(OH)
Effelsberg 100-m							
S <sub>2.64</sub>	9.51	11.35	10.69	12.46	3.75	...	...
S <sub>4.85</sub>	5.48	6.62	7.48	6.56	5.48	...	...
S <sub>8.35</sub>	3.25	3.88	5.22	3.47	5.92	...	...
S <sub>10.45</sub>	2.60	3.06	4.45	2.62	5.92	...	...
S <sub>14.60</sub>	1.85	2.12	3.47	1.69	5.85	...	...
S <sub>23.05</sub>	1.14	1.25	2.40	0.89	5.65	...	...
S <sub>32.00</sub>	0.80	0.83	1.82	0.55	5.49	...	...
S <sub>43.00</sub>	0.57	0.57	1.40	0.35	5.34	...	...
IRAM 30-m							
S <sub>86.00</sub>	...	...	...	...	2.92	3.23	2.19
S <sub>142.33</sub>	...	...	...	...	4.16	3.85	4.32

Table 5.2: Calibrator flux densities in Jy, used for the calibration of Effelsberg 100-m and IRAM 30-m F-GAMMA data. The flux density of NGC 7027 is corrected for extended structure, compared to the telescope’s primary beam at  $\nu > 10.45$  GHz. The table combines values from [Angelakis et al. \[2015\]](#) and [Nestoras et al. \[in prep.\]](#); see also references therein.

The fractional impact of each correction step taken is shown in Table 5.3 for the two main facilities used by the F-GAMMA program.

### 5.2.2 IRAM 30-m telescope data analysis

IRAM 30-m F-GAMMA observations employ calibrated cross-scans using the “B” and “C” SIS (until 2009 March) and the Eight Mixer Receiver (EMIR) heterodyne receivers. Before the use of EMIR, SIS had the capability of delivering 0.5 GHz of bandwidth at 86.2 GHz and 1 GHz at 142.33 GHz and 228.93 GHz, with linear polarization. The EMIR receiving system is characterized by significantly larger bandwidth, of 8 and 4 GHz at 86.24 and 142.33, respectively and horizontal/vertical polarization configuration. However, during our observations the NBC backend was employed, offering a bandwidth of 1 GHz [[Nestoras et al., in prep.](#)]. The downtime for the IRAM 30-m part of the F-GAMMA program due to the receiver upgrade, from SIS to EMIR, was approximately 1.7 months, between 2009 March 8 and 2009 April 28. Calibration follows along the same lines as with Effelsberg data with the exception of atmospheric opacity correction, that at IRAM 30-m is done automatically using a chopper-wheel-like scheme discussed below. Within the *Mira* software package a Gaussian fit is also performed in order to extract the observed parameters (amplitude, FWHM, and position offset) of each sub-scan. After a first round of flagging at sub-scan level, sub-scans are averaged per direction (AZ-ELV). A reliable measurement of antenna temperature is then obtained by averaging over both directions and performing a Gaussian fit. The post-measurement corrections for compensation

FREQUENCY (GHz)	POINTING (%)	OPACITY (%)	GAIN (%)
Effelsberg 100-m			
2.64	0.5	2.3	0.0
4.85	0.4	2.5	1.2
8.35	0.5	2.5	0.9
10.45	1.2	3.1	1.2
14.60	1.3	2.9	1.3
23.05	1.6	8.1	2.1
32.00	3.1	7.9	2.9
43.00	5.1	20.0	2.1
IRAM 30-m			
86.24	1.0	...	5.0
142.33	4.0	...	5.0

Table 5.3: The mean fractional impact of each correction step taken, on radio data from the Effelsberg 100-m and IRAM 30-m telescopes. Table adopted from [Angelakis et al. \[2015\]](#).

of pointing offsets and elevation-dependent antenna gain are applied similarly to those for Effelsberg 100-m data. At the IRAM 30-m, conversion to the standard flux density scale is done through frequent observations of primary (Mars, Uranus) and secondary (W<sub>3</sub>OH, K<sub>3-50A</sub>, NGC 7027) flux density calibrators.

#### 5.2.2.1 *Calibrated cross scans*

To calibrate our data the standard method implemented for heterodyne receivers at the IRAM 30-m is used [[Downes, 1989](#); [Mauersberger et al., 1989](#)]. Prior to the acquisition of target source data, a calibration scan with three measurements is performed. These are the counts registered for two loads of known temperature, at  $T_{\text{cold}}$  for the cold load, at  $T_{\text{amb}}$  for the load at ambient temperature, along with the sky temperature,  $T_{\text{sky}}$ , near the target source. Measuring the counts generated by the receiving system, the conversion from backend counts to antenna temperature ( $T_{\text{A}}^*$  [K]) is achieved for the subsequent on-source pointing scan. This is instantaneously corrected for atmospheric opacity and antenna forward efficiency. It is additionally equivalent to that traditionally derived from the “chopper wheel calibration” [see e.g. [Penzias and Burrus, 1973](#); [Kutner and Ulich, 1981](#)].

#### 5.2.2.2 *Wobbler switching*

Up until the receiver change from SIS to EMIR, beam switching with a frequency of  $\sim 5$  Hz was used for data acquisition with the IRAM 30-m telescope. Instead, in the EMIR era the wobbler switching method for cross-scans is used.

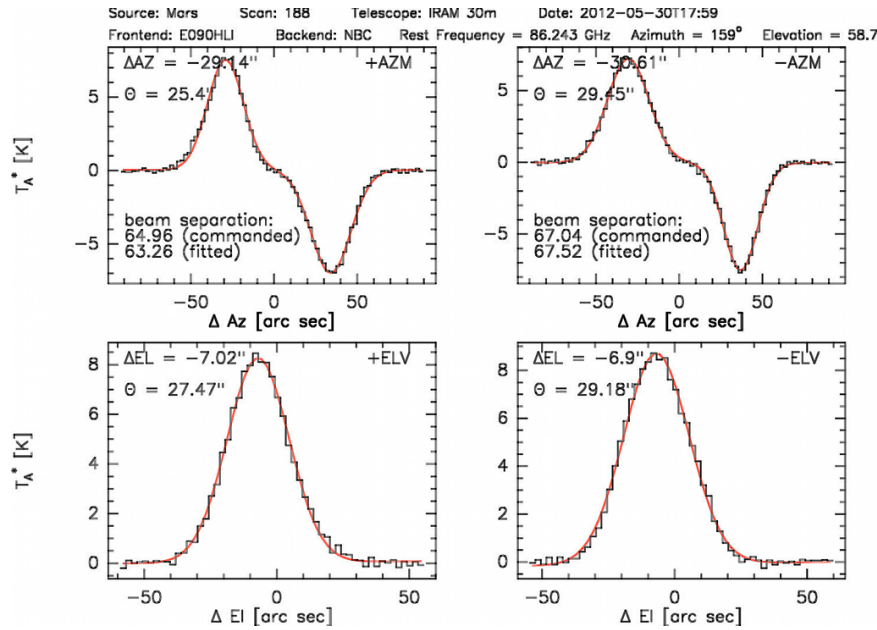


Figure 5.1: Example of a real-life PV sub-scan. Image courtesy of I. Nestoras (MPIfR).

The wobbling—in azimuth—sub-reflector of the 30-m telescope is used as follows. During the course of each sub-scan along the azimuth direction—i.e. while the telescope is driving over the source in AZ—the secondary mirror switches between  $\pm 33''$  along the same direction (AZ) at a frequency of  $\sim 2$  Hz. Each extreme position of the wobbler is referred to as a *wobbler throw*. The source signal is given by the difference between the measurements at each wobbler throw and ensures a very stable and flat baseline (see Fig. 5.1). The use of wobbler switching leads to a significant improvement in data quality, in particular during unstable weather conditions<sup>5</sup>. For an adequate SNR to be achieved a number between 2–4 sub-scans per direction was used within each scan that typically lasts between 30 and 45 s.

### 5.2.3 APEX 12-m data

At APEX the Large APEX Bolometer Camera (LABOCA) is used at a wavelength of 0.83 mm [Siringo et al., 2009]. LABOCA comprises 295 channels and offers a field of view of  $11.4'$  at 345 GHz, with a bandwidth of 60 GHz. For details on the source sample, observing technique and data reduction see Larsson et al. [2012].

## 5.3 FERMI-GST $\gamma$ -RAY OBSERVATIONS

For the purposes of the present chapter the *Fermi* monthly-binned  $\gamma$ -ray light curve of PKS 1502+106 is used. The light curve covers the time period between MJD 54707 (2008.66) and MJD 55911 (2011.96). It has been introduced and discussed in the previous chapter [see Section 4.2.4 and Fuhrmann et al., 2014].

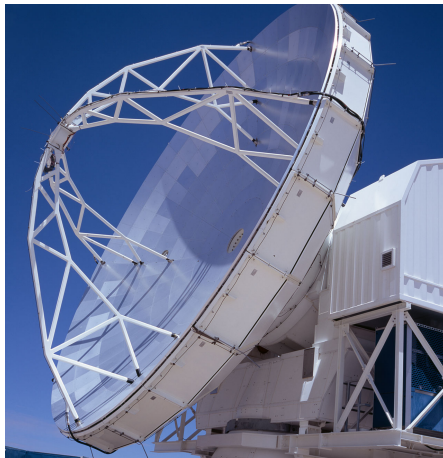
<sup>5</sup> See also the telescope's control system manual here: <http://www.iram.es/IRAMES/documents/ncs30mPako/Current/PDF/pako.pdf>



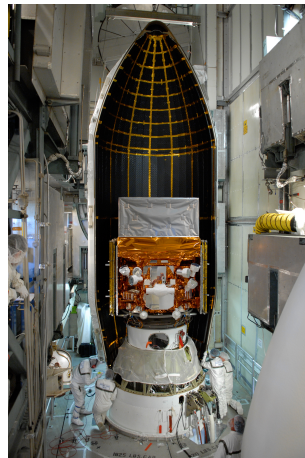
(a) the Effelsberg 100-m radio telescope, Germany.



(b) the IRAM 30-m telescope, Pico Veleta, Spain. Credit: IRAM



(c) the APEX telescope, Chile. Credit: ESO



(d) the *Fermi* telescope in its orbital delivery vehicle. Credit: NASA

Figure 5.2: Facilities used by the F-GAMMA blazar monitoring program.

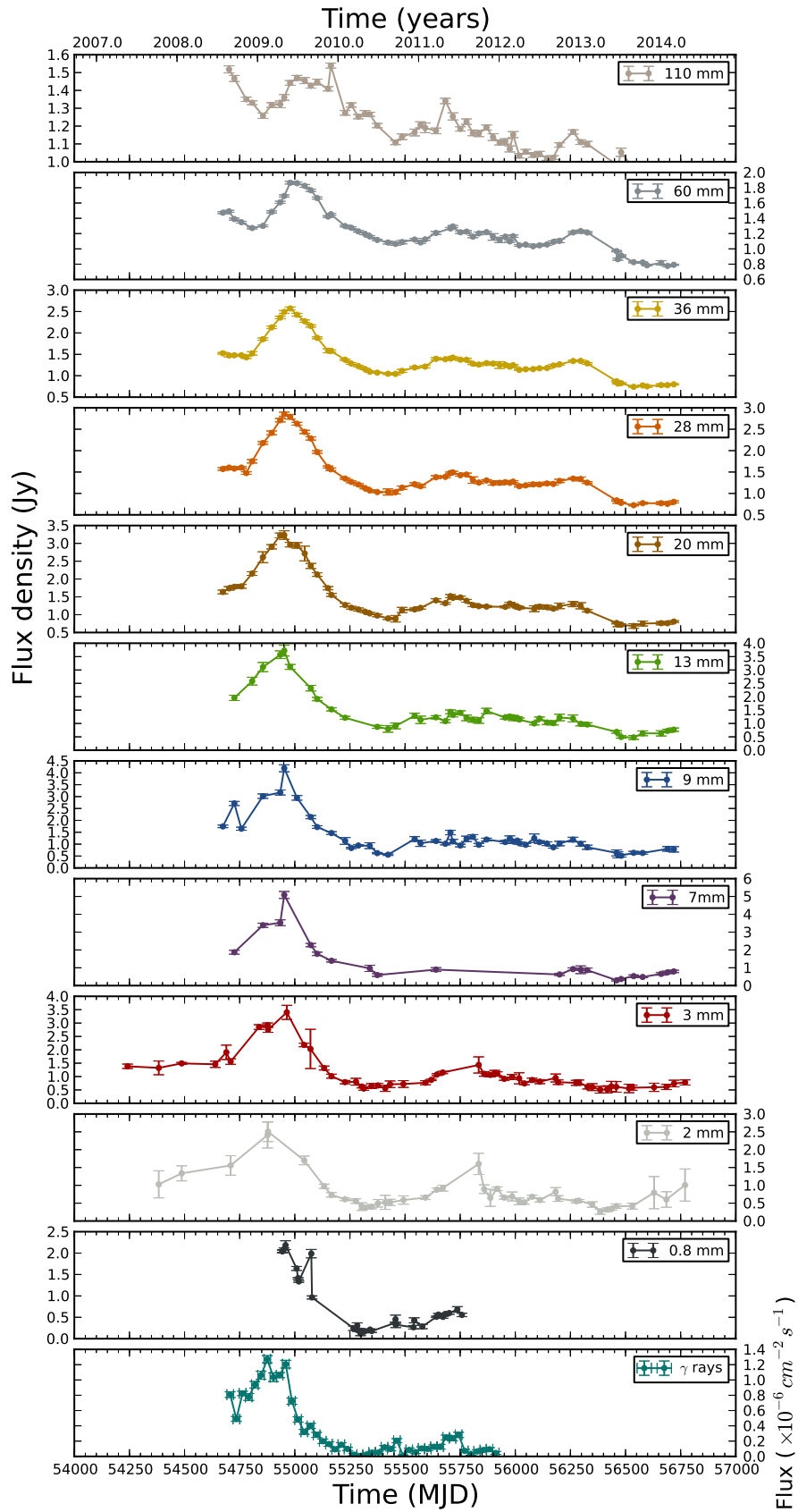


Figure 5.3: Multi-wavelength light curves at radio frequencies from the F-GAMMA program and the  $\gamma$ -ray light curve from *Fermi*. From top to bottom data are shown from: the Effelsberg 100-m at 2.64 GHz, 4.85 GHz, 8.35 GHz, 10.45 GHz, 14.60 GHz, 23.05 GHz, 32.00 GHz, and 43.00 GHz; the IRAM 30-m at 86.24 GHz and 142.33 GHz; APEX 12-m at 345.00 GHz. The bottom panel features the monthly-binned light curve from *Fermi*/LAT at  $E > 100 \text{ MeV}$ . See also Table 5.1.

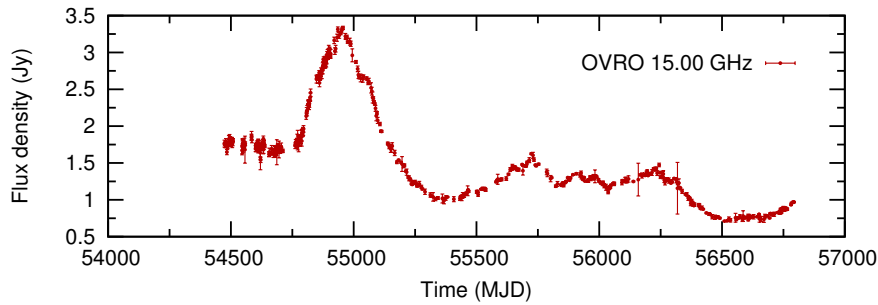


Figure 5.4: Light curve at 15.00 GHz from the OVRO 40 m blazar monitoring program [Richards et al., 2011]. See Section 5.1 for details.

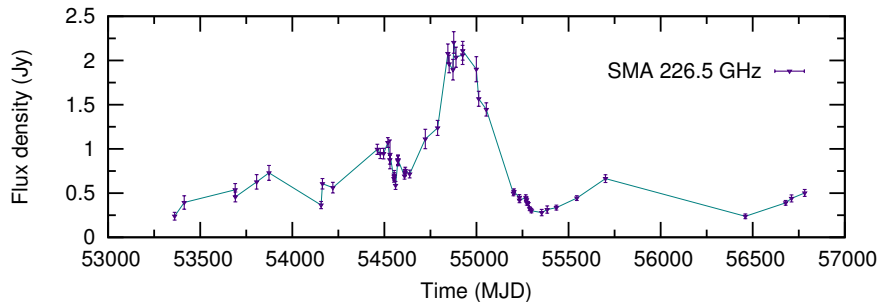


Figure 5.5: Light curve at a central frequency of 226.50 GHz from the high-frequency SMA calibrator list archive [see e.g. Gurwell et al., 2007]. See Section 5.1 for details.

#### 5.4 LIGHT CURVE TIME SERIES ANALYSIS

The importance of light curve parameters lies in the fact that different blazar variability models predict different behavior in the time and frequency domain. Here, the relevant parameters of the broadband outburst seen in PKS 1502+106 are extracted from observations using three independent approaches, namely decomposition into exponential flares, a Gaussian process regression, and a cross-frequency relative timing analysis of the flare with the application of the discrete cross-correlation function.

##### 5.4.1 Decomposition into exponential flares

The first method we employ, in order to obtain the flare parameters from the multi-frequency light curves, is a decomposition of flux density variations into exponential flares. This has been used in the past and under certain assumptions it can lead to estimates of jet parameters derived from flare characteristics, such as the Doppler boosting factor and Lorentz factors along with the viewing angle towards an extragalactic source [see e.g. Lähteenmäki and Valtaoja, 1999; Hovatta et al., 2009; Valtaoja et al., 1999].

Here we employ the same approach and we extract the relevant flare characteristics. These are the variability time scale of the 2008–2010 flare, its amplitude at each observing frequency, and the cross-band delays.

The flaring activity in PKS 1502+106 is dominated by a single, clearly visible event across frequencies (see Fig. 5.3). Despite the fact that substructure could be present—data points prior and after, but close in time to the peak flux density



may hint towards this case—the event is largely unaffected by it. This putative substructure appears more pronounced at higher radio frequencies and also seen in the double-peaked  $\gamma$ -ray light curve. In any case, the isolated flare facilitates our study and gives us the opportunity to follow the behavior of a “clean” outburst, free of heavy blending, an effect often seen in the complex light curves and overall activity of other blazars [e.g. S5 0716+714, [Rani et al., 2013](#)].

For the purposes of the fitting process, only observations within the time interval of the flaring event are considered. This is justified and follows from the discussion above, on the well-defined nature of the outburst in question. Then the quiescent level is subtracted. This is an assumed constant flux density level that accounts for the underlying, steady-state jet flow and is equal to or smaller than the minimum flux density of the light curves. Here, the minimum flux of each light curve is subtracted (see [Table 5.4](#)). An alternative of fitting a linear baseline level taking into account the lowest flux density points bracketing the outburst was also considered. This is not a good approach in the case of PKS 1502+106 since, as often is the case, consequent outbursts start without necessarily reaching a quiescent level prior to the onset of a new one—i.e. different flares are superimposed on each other [[Valtaoja et al., 1999](#)]. It also implicitly assumes that flares are superposed on a quiescent flux density level which is a linear function of time (and diminishes if the slope of the linear fit is negative), a notion that lacks a physical basis.

The expression fitted to the data is

$$g(t) = \begin{cases} S_{\max} e^{(t-t_{\max})/t_r}, & t < t_{\max} \\ S_{\max} e^{-(t-t_{\max})/t_d}, & t > t_{\max} \end{cases} \quad (5-6)$$

where the free parameters are

- $S_{\max}$ , the peak flux density in Jansky,
- $t_{\max}$ , the time when  $S_{\max}$  is reached in days with respect to the reference MJD 54300,
- $t_r$ , the rise time in days and
- $t_d$ , the decay time in days

When the procedure converges, the best fitting set of the above parameters is returned with the errors in each one, representing the standard fitting error. The radio flare data along the exponential rise and decay model fitted to the data are shown in [Fig. 5.6](#) and [5.7](#). The fit agrees reasonably with the data in most cases apart from a few exceptions especially at high observing frequencies. Though the model used for the flare decomposition usually gives good estimates for the flare amplitude this is not the case for other parameters such as the cross-frequency delay, which is systematically underestimated compared to the other two methods we employ (see coming sections and [Table 5.6](#)). This could hint that the flare seen in PKS 1502+106 does not show an evolution that can be modeled though an exponential functional form (see e.g. the 15 GHz OVRO data and the model). Results are summarized in [Table 5.4](#).

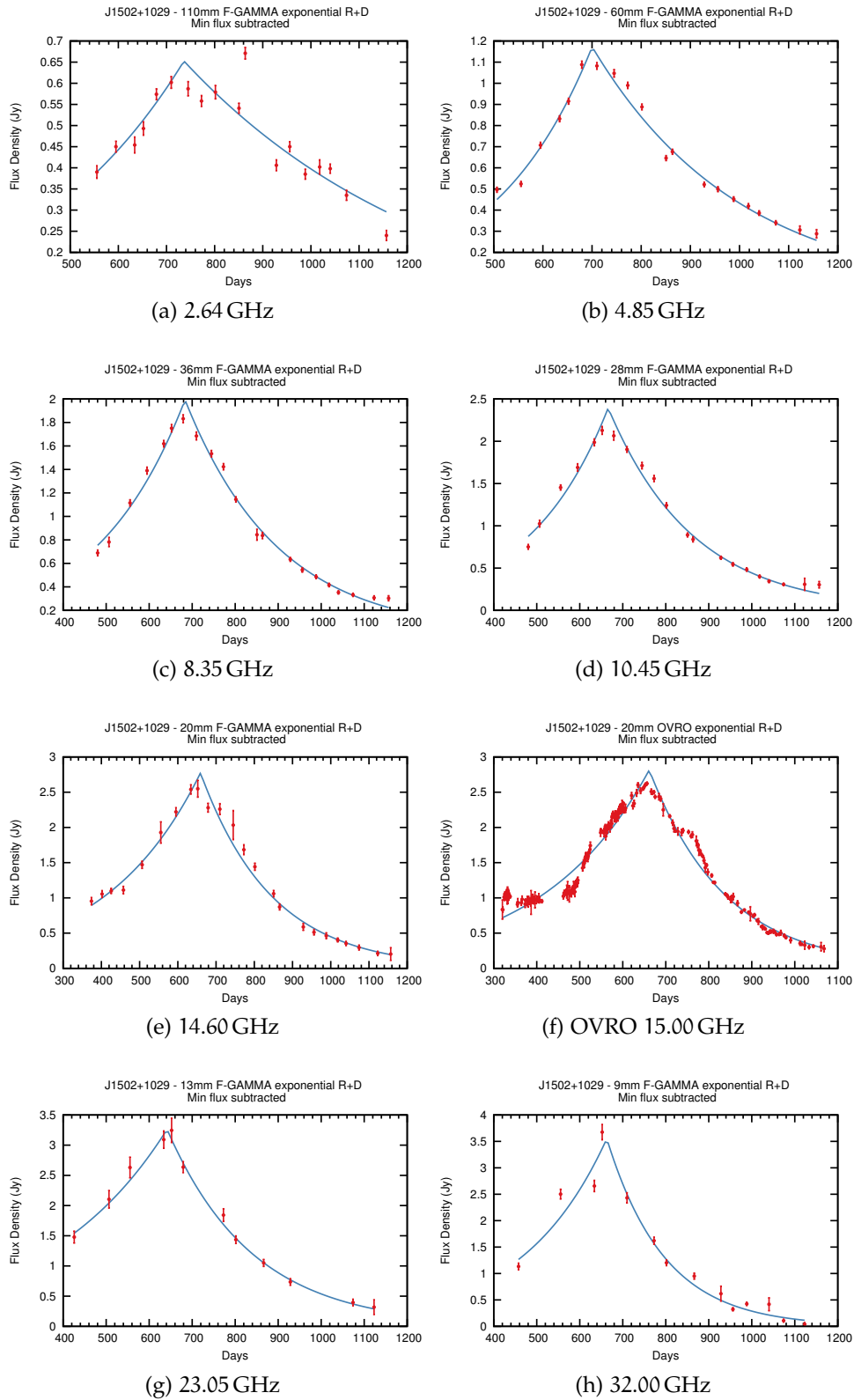


Figure 5.6: Flare decomposition into exponential rise and decay parts. Here from top to bottom and left to right, frequencies in the range 2.64–32.00 GHz are shown. The reference date is MJD 54300.

FREQUENCY (GHz)	MIN. FLUX (Jy)	$S_{\max}$ (Jy)	$t_{\max}$ (MJD 54300+)	$t_r$ (days)	$t_d$ (days)
2.64	0.868	$0.653 \pm 0.032$	$736.3 \pm 22.1$	$351.6 \pm 114.4$	$531.6 \pm 78.5$
4.85	0.777	$1.172 \pm 0.026$	$700.2 \pm 5.6$	$202.2 \pm 16.7$	$300.8 \pm 12.8$
8.35	0.740	$1.993 \pm 0.040$	$683.3 \pm 4.3$	$208.9 \pm 14.6$	$216.5 \pm 6.8$
10.45	0.725	$2.394 \pm 0.061$	$666.1 \pm 4.9$	$184.6 \pm 15.0$	$197.7 \pm 6.5$
14.60	0.683	$2.774 \pm 0.067$	$659.3 \pm 5.1$	$251.9 \pm 13.9$	$187.1 \pm 6.5$
15.00	0.711	$2.816 \pm 0.027$	$661.6 \pm 2.1$	$250.1 \pm 5.3$	$177.2 \pm 3.4$
23.05	0.478	$3.263 \pm 0.086$	$641.6 \pm 5.8$	$288.1 \pm 27.3$	$198.6 \pm 7.3$
32.00	0.516	$3.552 \pm 0.251$	$663.0 \pm 11.6$	$198.9 \pm 35.3$	$134.3 \pm 12.4$
43.00	0.299	$4.098 \pm 0.485$	$652.2 \pm 29.6$	$268.4 \pm 61.3$	$160.2 \pm 43.7$
86.24	0.507	$3.367 \pm 0.185$	$669.8 \pm 9.5$	$269.9 \pm 35.4$	$105.7 \pm 10.5$
142.33	0.263	$2.590 \pm 0.231$	$670.4 \pm 14.1$	$493.5 \pm 106.5$	$123.3 \pm 7.7$
226.50	0.238	$2.377 \pm 0.125$	$659.2 \pm 9.1$	$233.2 \pm 14.2$	$111.5 \pm 6.9$

Table 5.4: Fit results from exponential flare decomposition after subtraction of the light curve absolute minimum at each frequency. Only data points corresponding to the flare are fitted and not light curve data points. Columns from left to right: (1) observing frequency; (2) the minimum flux density subtracted prior to the fit; (3) obtained flare amplitude; (4) obtained time of flare maximum; (5) obtained flare rising and (6) decay time.

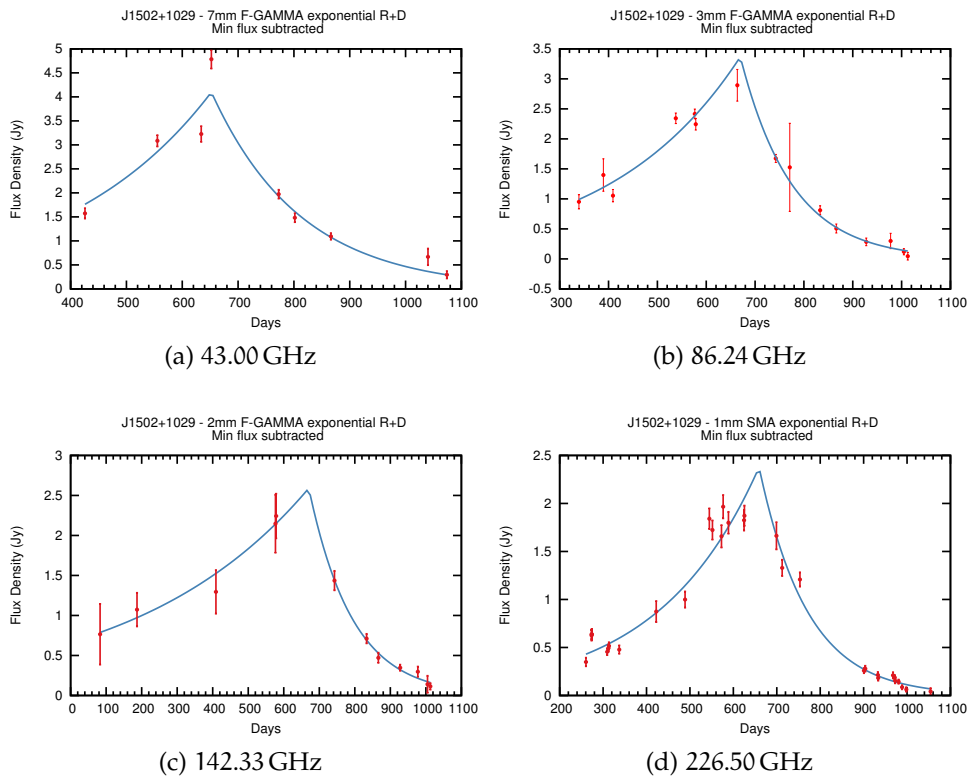


Figure 5.7: Flare decomposition into exponential rise and decay parts. Here from top to bottom and left to right, frequencies in the range 43.00–226.5 GHz are shown. The reference date is MJD 54300.

### 5.4.2 Gaussian process regression

In Section 5.4.1, the standard approach to attacking a generalized regression and prediction problem is exploited. That is, one wants to extract (or learn, as in machine learning applications) the properties of a system—put simply, a function  $f$  that describes the system well enough—from a given set of observations referred to as the training data set. In trying to do so there exist two approaches.

The traditional one and most heavily applied is to obtain the target function  $f$ , by preselecting a class of functions, e.g. linear, and minimizing the residuals between the target function and the training data. The predicting power of the acquired model is restricted by how well the target function is modeled by the preselected class. One can increase the complexity of this class, for example by considering higher-degree polynomials, but is running the danger of overfitting.

A second way to learn  $f$  from the data is by assigning a *prior* probability to all functions one considers to be more likely, for example on the grounds of their smoothness. This non-parametric Bayesian approach, may seem to suffer from the obvious problem of having to deal with an infinite set of functions, but this is not the case. Instead, it can be implemented thanks to a *stochastic* process called *Gaussian process* [cf. Chapter 2 of [Rasmussen and Williams, 2005](#), and [Ivezić et al., 2014](#)].

A Gaussian process (GP) is a probability distribution over functions. It constitutes the generalization of the Gaussian distribution of random variables or vectors, into the space of functions. In Fig. 5.8a, twenty random samples are drawn from a prior distribution defined by a Gaussian process that considers smooth functions; i.e. infinitely differentiable.

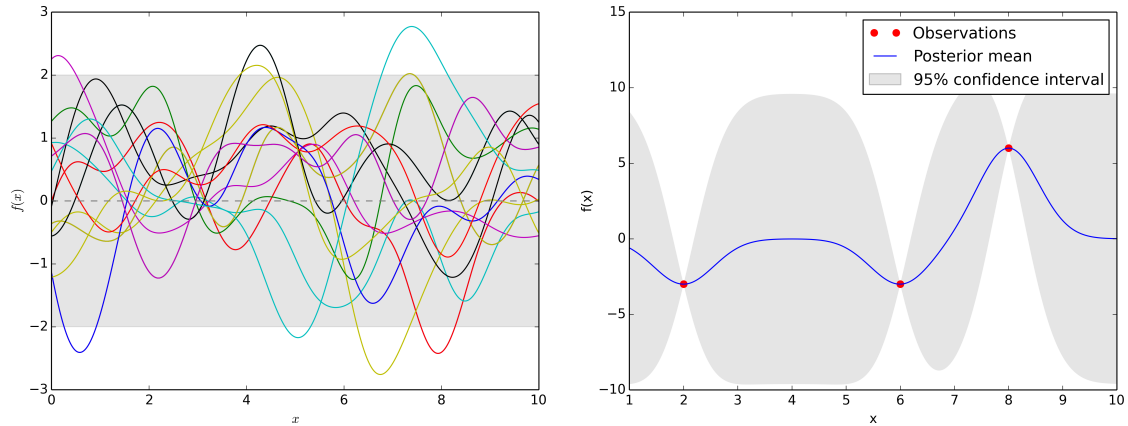
Gaussian process regression is also referred to—especially in the scientific field of geostatistics—as Kriging, following from the pioneering work of Danie G. Krige on plotting distance-weighted averages at the Witwatersrand gold reef complex in South Africa in the 1950s. Krige’s objective was to estimate the most likely distribution of gold, based on sparse samples from a limited number of boreholes<sup>6</sup> [[Agterberg, 2014](#)].

In the case of AGN light curve fitting, the problem has the form of one-dimensional regression with the observables being flux density levels at certain times. Given a set of three observations or training data points

$$\mathcal{D} = \{(x_1, y_1), (x_2, y_2), (x_3, y_3)\} \quad (5-7)$$

as in Fig. 5.8b, our problem reduces to finding the functions, drawn from the prior distribution, that pass through all the training points. This distribution of functions is the *posterior* distribution and its mean, being the expected value, can be considered as the “best-fit function”. Use of the word function here is inappropriate since the outcome of the procedure is a set of the posterior mean values at certain input positions  $x_i$ , rather than a mathematical relation with a functional form. The strong point of Gaussian process regression is its ability to deliver robust error estimates. The shaded area in Fig. 5.8b represents the  $2\sigma$  or 95% confidence interval.

<sup>6</sup> <http://en.wikipedia.org/wiki/Kriging>



(a) The prior: Twenty samples selected randomly from the prior distribution with zero mean and  $\sigma = 1$ , with a squared exponential covariance kernel. (b) The posterior: Result after training the GP with three error-free data points.

Figure 5.8: Gaussian process prior and posterior distributions. Shaded area is delineating a range of 2 standard deviations above and below the mean. For the purposes of this illustration the length scale hyperparameter was set to  $l = 0.8$  (see text for discussion).

It is obvious that the selection of prior is of crucial importance to the final outcome since it governs the properties of functions used for inference. Similar to a multivariate Gaussian distribution—and before conditioning on data—a Gaussian process is defined by its mean,  $\mu$ , and covariance,  $k$ . Without loss of generality one can always assume that  $\mu = 0$  since the data set can always be trivially shifted to accommodate for this assumption.

In the context of Gaussian processes the *covariance function*, *covariance kernel* or simply *kernel*,

$$\text{Cov}[f(x_i), f(x_j)] = k(x_i, x_j) \quad (5-8)$$

is used to define the covariance between any two function values at points  $x_i$  and  $x_j$ ; i.e. the similarity between data points. It is chosen on the basis of our prior beliefs for the function to be learned. Essentially the kernel defines the class of functions that are likely to appear in the prior distribution which in turn determine the kind of structure that the specific GP is able to model correctly. There exists a large number of available kernels each of which can capture different structural information, according to the problem in hand. Kernels have their own set of parameters, called *hyperparameters*, since they define the properties of the prior distribution over functions instead of the functions themselves. There exist simple kernels, such as the squared exponential kernel, with only two hyperparameters and more complex ones with larger sets of hyperparameters. A very useful property of kernels is that addition and multiplication between two or more of them, also produce valid covariance kernels. As such, there is always the option of constructing a covariance kernel that fits the characteristics of the modeling problem<sup>7</sup>. Some examples of simple covariance kernels

<sup>7</sup> For a complete treatment of the subject of describing structure with kernels see <http://mlg.eng.cam.ac.uk/duvenaud/cookbook/>

are the squared exponential, the periodic, and the linear. The former will be discussed in the next paragraph while the two latter from their intuitive naming hint towards the kind of structure they are able to deal with.

The squared exponential kernel has the functional form:

$$k(x_i, x_j) = \sigma^2 \exp\left(\frac{-(x_i - x_j)^2}{2l}\right) \quad (5-9)$$

where the hyperparameters are

- $l$ , the characteristic length scale which determines the length of the wiggly pattern (see Fig. 5.8a) in the functions comprising the prior and
- $\sigma^2$ , is the variance, that maps the mean distance of the function away from its mean value. In this framework it serves only as a scaling factor.

The most widely used kernel is the squared exponential, owing to its generality and smoothness. The latter is the only assumption when using it and is everything but a problem, since most time series arising from physical processes have no reason not to be smooth.

Noisy  
observations

While in Fig. 5.8 we dealt only with noiseless data, it is most often the case that our observations are of the form

$$\mathcal{D} = \{(x_i, y_i + \epsilon_i) \mid i = 1, \dots, n\} \quad (5-10)$$

where  $\epsilon$  here denotes the noise term affecting each data point. Accommodating for noise is a natural consequence of kernel properties, in that one needs only to add it in the noiseless covariance kernel

$$\mathbf{k}_n(x_i, x_j) = \mathbf{k}(x_i, x_j) + \sigma^2 \mathbf{I} \quad (5-11)$$

where  $\mathbf{I}$  is the identity matrix [Roberts et al., 2012].

As an end note, it is worth noting that procedures such as linear regression, spline interpolation and Kalman filtering can be considered as—and in fact are—Gaussian processes arising from different covariance kernels.

#### 5.4.2.1 Training the Gaussian process

Since hyperparameters define the properties of the prior distribution through the covariance kernel, they play a significant role in accurately modeling the data, depending on the complexity of the kernel selected; i.e. the number of hyperparameters it employs. The process of selecting the best set of hyperparameters using the data themselves is referred to as *training the GP* or, more generally, *Bayesian model selection*. In essence, one wants to update the prior knowledge in light of a training data set.

One way of doing so is by maximizing the *marginal likelihood* [Williams and Rasmussen, 1996]. Letting  $\theta$  denote the vector of hyperparameters, then in the case of the squared exponential kernel (Eq. 5-9) we have:

$$\theta = \{l, \sigma^2\}. \quad (5-12)$$

Then, the probability (or evidence) of the training data,  $\mathbf{y}$ , given the hyperparameters vector  $\theta$  is:

$$p(\mathbf{y} | \mathbf{x}, \theta) \quad (5-13)$$

and the log marginal likelihood is given by

$$\mathcal{L} = \log p(\mathbf{y} | \mathbf{x}, \theta) = -\frac{1}{2} \mathbf{y}^\top \mathbf{k}_n^{-1} \mathbf{y} - \frac{1}{2} \log |\mathbf{k}_n| - \frac{n}{2} \log 2\pi. \quad (5-14)$$

In the general case of a hyperparameter vector  $\theta = \{\theta_j | j = 1 \dots n\}$ , the derivatives of the log marginal likelihood with respect to each  $\theta_j$  are

$$\frac{\partial \mathcal{L}}{\partial \theta_j} = \frac{1}{2} \mathbf{y}^\top \frac{\partial \mathbf{k}_n}{\partial \theta_j} \mathbf{k}_n^{-1} \mathbf{y} - \frac{1}{2} \text{Trace} \left( \mathbf{k}_n^{-1} \frac{\partial \mathbf{k}_n}{\partial \theta_j} \right). \quad (5-15)$$

Equation 5-15 can be used with any numerical gradient optimization algorithm in order to maximize the log marginal likelihood and return the set of best hyperparameter values for the problem at hand. The schematic description of the algorithmic steps to be taken can be found in [Rasmussen and Williams \[2005\]](#), Ch. 2, p. 19.

#### 5.4.2.2 Application of GP regression to the light curves of PKS 1502+106

For the application of the method to the radio light curves of PKS 1502+106, a variant of the algorithm presented in [Pedregosa et al. \[2011\]](#) has been used, developed specifically for this purpose. The original suite of machine learning programs can be accessed online<sup>8</sup>.

Here, we consider the full length of each available light curve, without limiting ourselves to the time period bracketing the flare, as in the case of decomposition into exponential flares. Again, for the reasons discussed in Section 5.4.1, before proceeding with the Gaussian process regression, we subtract the minimum flux density level observed at each frequency from the corresponding light curve. To ensure the best unbiased result we perform the process with 100 random initializations of the length scale parameter. Upon completion, the posterior mean distribution is returned along with a robust uncertainty estimate in the form of a 95% confidence interval for the flux density, and the set of hyperparameters maximizing the log marginal likelihood. Consequently, we are able to extract the flare amplitude,  $S_{\max}$ , the time of maximum flux density,  $t_{\max}$ , and the cross-band delay,  $\tau_{\text{GP}}$ . Additionally, by the flare rising and decay time are extracted from the times of the two flux-density minima bracketing the flare maximum. Fig. 5.9 and 5.10 visualize the results of regression at each frequency, while  $S_{\max}$ ,  $t_{\max}$  and  $t_{\text{rise}}$ , and  $t_{\text{rise}}$  values characterizing the flare are visible in Table 5.5. According to the results the flare amplitude,  $S_{\max}$ , shows an increasing trend with frequency, up to 43 GHz whereafter the flare amplitudes start falling again as seen for 86.00, 142.33 and 226.5 GHz (see also Fig. 5.19). As will be discussed later in this chapter there exists a clear tendency for the flare to be visible earlier at higher-frequencies, an effect attributed to opacity (see also Fig. 5.15). The flare rising times while initially increase with frequency, in the

<sup>8</sup> <http://scikit-learn.org/stable/index.html>

FREQUENCY (GHz)	MIN. FLUX (Jy)	$S_{\max}$ (Jy)	$t_{\max}$ (MJD)	$t_{\text{rise}}$ (days)	$t_{\text{decay}}$ (days)
2.64	0.868	$0.593 \pm 0.032$	55095.148	239.848	366.752
4.85	0.777	$1.084 \pm 0.031$	55016.808	201.808	383.192
8.35	0.740	$1.764 \pm 0.043$	54980.390	230.890	435.910
10.45	0.725	$2.055 \pm 0.062$	54968.684	234.884	435.016
14.60	0.683	$2.414 \pm 0.088$	54954.377	288.077	467.623
15.00	0.711	$2.570 \pm 0.026$	54952.276	276.176	391.724
23.05	0.478	$2.856 \pm 0.189$	54921.861	390.761	457.039
32.00	0.516	$2.590 \pm 0.277$	54916.658	447.858	446.542
43.00	0.299	$3.542 \pm 0.454$	54925.763	383.363	527.237
86.24	0.507	$2.439 \pm 0.144$	54912.756	331.256	437.244
142.33	0.263	$1.987 \pm 0.254$	54888.044	313.544	444.456
226.50	0.238	$1.823 \pm 0.102$	54914.307	300.307	460.793

Table 5.5: Gaussian process regression results after subtracting the minimum flux of the light curve. Columns from left to right: (1) observing frequency; (2) the minimum flux density subtracted prior to the fit; (3) obtained flare amplitude; (4) obtained time of flare maximum; (5) obtained flare rising and (6) decay time.

frequency range further than 32.00 GHz they show decreasing trend. Finally, in terms of the flare decay times they seem to be following a slightly increasing trend with frequency in the whole frequency range employed here (see also Fig. 5.21).

### 5.4.3 The discrete cross-correlation function (DCCF)

Putative correlated variability across observing bands based on “sampling-rate-limited” time series can be investigated and quantified using the *discrete cross-correlation function* (DCCF). The approach is discussed in detail in [Edelson and Krolik \[1988\]](#) and along with other cross-correlation methods, it has been used for assessing correlated variability in light curves and spectra by a number of investigators [cf. [Gaskell and Sparke, 1986](#); [Gaskell and Peterson, 1987](#); [Maoz and Netzer, 1989](#)].

The *cross correlation function* (CCF), as a function of time lag  $\tau$  for two discrete, evenly sampled light curves  $x(t_i)$  and  $y(t_i)$  is given by

$$\text{CCF}(\tau) = \frac{1}{N} \sum_{i=1}^N \frac{[x(t_i) - \bar{x}][y(t_i - \tau) - \bar{y}]}{\sigma_x \sigma_y} \quad (5-16)$$

where,

- $\bar{x}$ , is the mean of light curve  $x(t_i)$ ,
- $\sigma_x$ , its standard deviation,



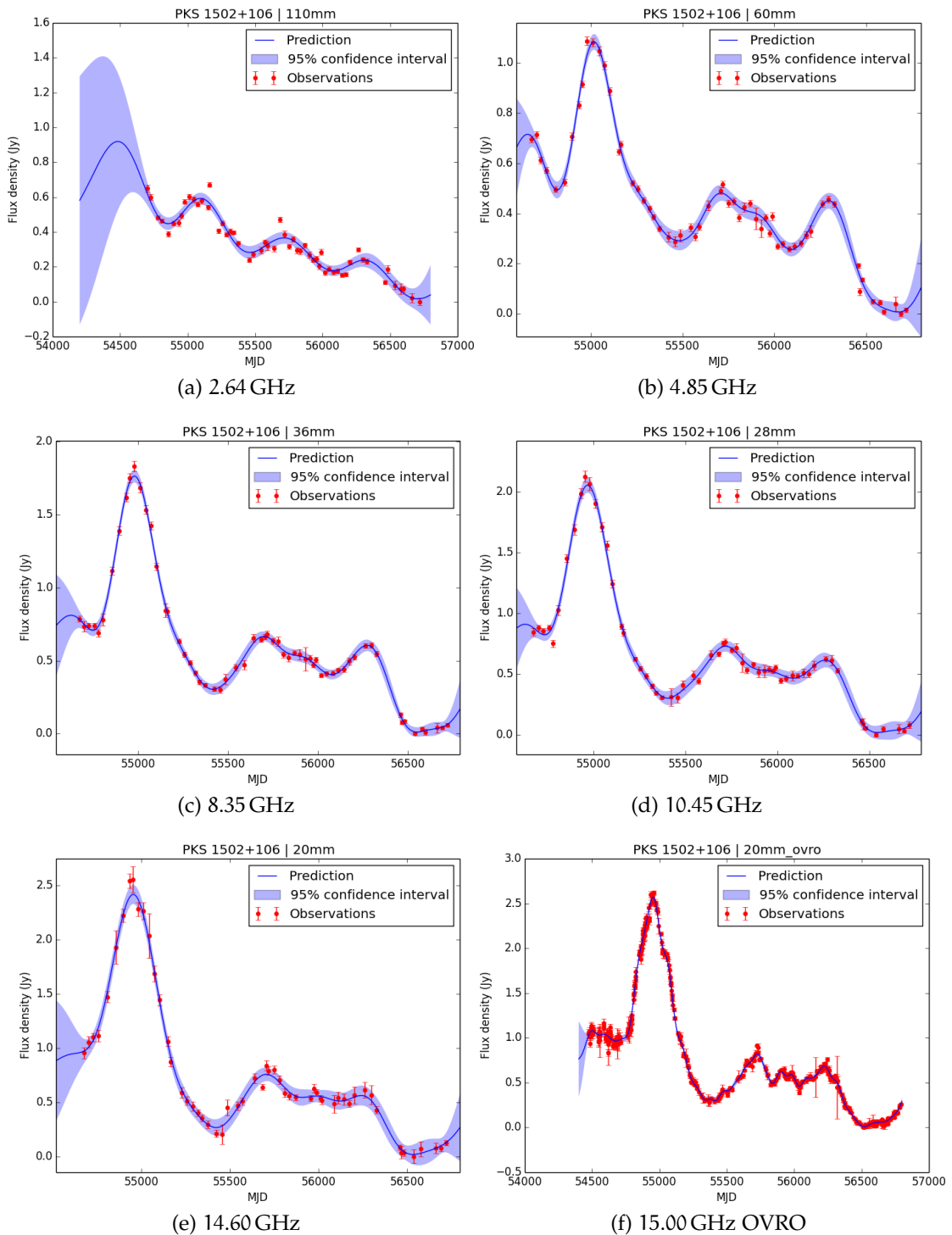


Figure 5.9: Gaussian process regression curves for the radio light curves in the range 2.64–15.00 GHz. Data points are shown in red, the prediction curve in dark blue and the 95% confidence interval is the lighter blue shaded area.

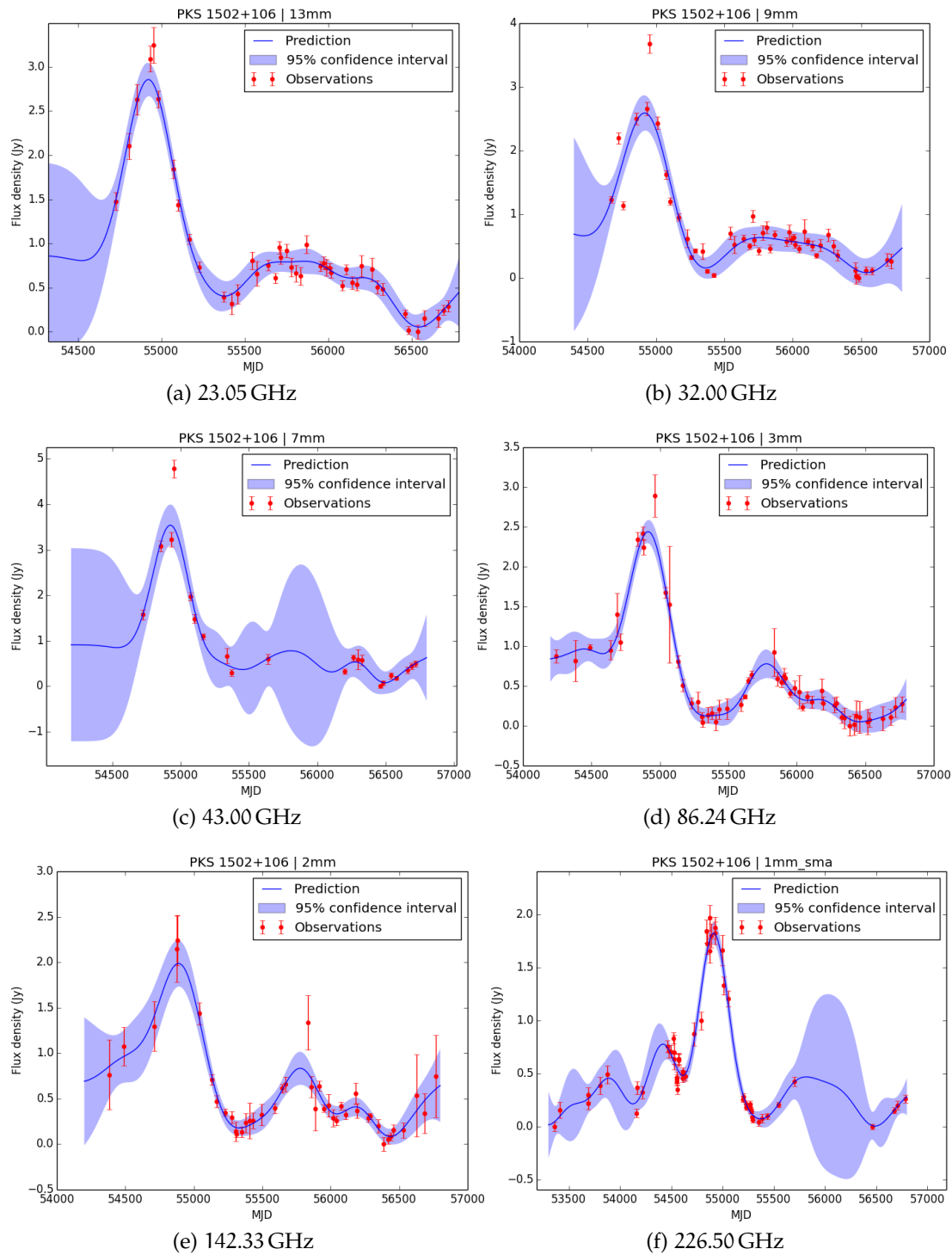


Figure 5.10: Gaussian process regression curves for the radio light curves in the range 23.05–226.50 GHz. Data points are shown in red, the prediction curve in dark blue and the 95% confidence interval is the lighter blue shaded area.

- $\bar{y}$ , is the mean of light curve  $y(t_i)$  and
- $\sigma_y$ , is the standard deviation of light curve  $y(t_i)$ .

The nature of light curves discussed here and most frequent case, especially for light curves obtained through long-term monitoring of blazars, is that they are unevenly sampled. This fact introduces the need for the discrete cross-correlation function [Edelson and Krolik, 1988, see also Larsson, 2012]. In contrast to linear interpolation methods, the DCCF takes into consideration only the data points themselves. In essence, the operation is to slide the two light curves against each other with respect to time, while computing the correlation value for each pair of data and with respect to each sliding interval or *time lag*,  $\tau$ . For two irregularly sampled light curves with  $n$  and  $m$  number of observations respectively, the aforementioned operation yields the *unbinned cross-correlation function* (UCCF)

$$\text{UCCF}_{ij}(\tau) = \frac{(x_i - \bar{x})(y_i - \bar{y})}{\sigma_x \sigma_y}. \quad (5-17)$$

Averaging the UCCF in time lag bins yields the DCCF. Positive DCCF values indicate a positive correlation with an average time shift  $\tau$ , while negative values imply anti-correlation.

In previous work by Fuhrmann et al. [2014], the DCCF technique has been used in search of possible correlation between the radio wavebands and *Fermi*  $\gamma$ -ray observations of the F-GAMMA blazar sample. This study has demonstrated a significant existence of radio/ $\gamma$ -ray correlated variability in blazars through a DCCF stacking analysis and also quantified the average frequency-dependent time lags between observations at the F-GAMMA radio frequencies. Specifically, for PKS 1502+106 a 3 mm/ $\gamma$ -ray correlation is detected at a significance level above 99%, with a time of arrival delay of  $14 \pm 11$  days (see Fig. 5.11). Meaning that the mm-radio emission is lagging behind  $\gamma$  rays. The aforementioned difference of time of arrival for each band translates to a de-projected radial separation of the corresponding emitting regions of 2.1 pc.

One of the targets of the present study is to built on these previous findings and quantify the correlated variability beyond the mm/sub-mm band towards all observed radio frequencies, taking full advantage of the wealth of the F-GAMMA data set (see Fig. 5.3.) The DCCFs have been calculated between the 15 GHz light curve of the OVRO 40 m Blazar Monitoring Program (OVRO) and all available light curves from SMA<sup>9</sup> at 226.5 GHz down to 2.64 GHz, the lowest frequency the F-GAMMA is observing at. Here, a positive lag  $\tau_{\text{DCCF}}$  implies that the peak of activity, lags behind the reference frequency by  $\tau_{\text{DCCF}}$ , measured in days. Hereafter, we refer to the cross-correlated light curves as the reference (OVRO 15 GHz) and the target (all the rest). The selection of the OVRO 15 GHz data as the reference light curve is due to the better sampling.

#### 5.4.3.1 Estimation of time lags

In addition to assessing the presence of correlations, DCCFs quantify it by means of reporting where it occurs in the time lag domain. Various methods

<sup>9</sup> The Submillimeter Array (SMA) operates in the frequency range between 180 GHz and 700 GHz and comprises eight 6 m antennas in configurations with baselines up to 509 m. It is an 8-element radio interferometer located on the top of Mauna Kea, Hawaii.

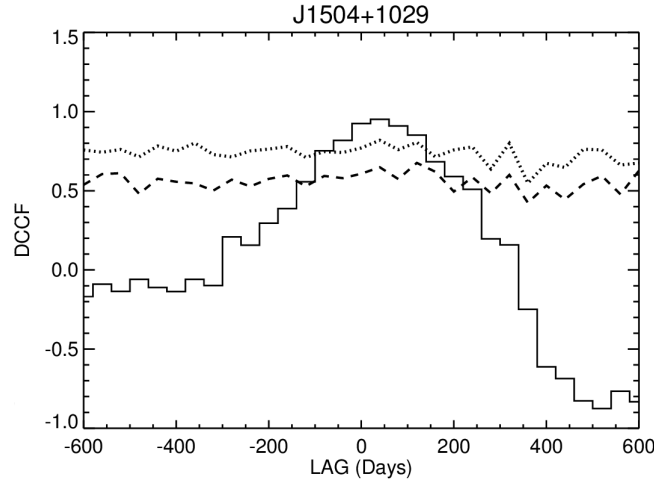


Figure 5.11: DCCF of PKS 1502+106 between light curves at 86.24 GHz and  $\gamma$  rays. Lines represent significance levels above correlation by chance, at 99% (dotted line) and 90% (dashed line) levels. Image adopted from [Fuhrmann et al. \[2014\]](#)

can be employed for this purpose [see e.g. [Larsson, 2012](#)]. In the following we use a Gaussian fit to obtain the DCCF peak and its position. Since the value of interest is the peak of the DCCF, the Gaussian fit is performed in the time lag range that ensures better peak determination. The peak of the Gaussian is the value of time lag  $\tau_{\text{DCCF}}$  reported in Table 5.6. Left panels of Fig. 5.12 through 5.14 show all calculated DCCFs with respect to our selected reference frequency along with the Gaussian fit.

The results confirm the presence of strongly correlated activity across all radio frequencies. In all cases, a strong positive peak is clearly visible. In this way the  $\tau_{\text{DCCF}}$  between all light curves and the reference light curve at 15 GHz is obtained. Subsequently, these time lags are referenced to our highest-frequency, well-sampled light curve at 142.33 GHz.

#### 5.4.3.2 Estimates of time-lag uncertainty

Any reported time lag calculated through the DCCF has to be accompanied by an estimate of the measurement uncertainty. This is not a trivial task and there exists no universally accepted way of doing so. For the purposes of our study we use the model-independent Monte Carlo approach introduced by [Peterson et al. \[1998\]](#).

The two main sources of uncertainty in cross-correlation analyses—in addition to limited data trains and consequently limited number of events—are: (i) flux uncertainties and (ii) uncertainties associated with the uneven sampling of the light curves under investigation for putative correlated variability. The method is comprised of two parts; that of the *flux redistribution* (FR), and that of *random sample selection* (RSS), accounting for (i) and (ii) respectively. The algorithm is essentially as follows:

1. Introduction of Gaussian deviates to the data, constrained by the maximum flux measurement error.

2. Use of a re-sampling with replacement scheme to randomly select data points and create an equally long light curve; i.e. use of a bootstrap-like procedure.
3. Calculation of the DCCF and determination of the time lag corresponding to its peak through a weighted Gaussian fit.
4. After a number of  $N$  Monte Carlo realizations, obtain the *cross-correlation peak distribution* (CCPD).

The uncertainty,  $\pm\Delta\tau_{68\%}$  or simply  $\pm\Delta\tau$ , can be obtained directly from the CCPD and corresponds to the time lag interval of  $\tau_{\text{median}} - \Delta\tau$  and  $\tau_{\text{median}} + \Delta\tau$ , such that 68% of the realizations yield results within this interval. This estimate is equivalent to  $1\sigma$  error, in the case of a Gaussian distribution [Peterson et al., 1998]. Here, a number of 5000 Monte Carlo simulations were performed.

One final remark is needed since the procedure of re-sampling with replacement might not be familiar to the reader. In statistical applications the way one draws samples from a population in order to arrive to conclusions concerning the population as a whole is a complicated and challenging operation. *Bootstrapping* is one option and relies on creating different samples of the population essentially from a single initial or parent sample. A given light curve is, for example, a sample drawn from the underlying process, that is the full flux density variability pattern of the source; i.e. the infinitely populated light curve. One then can create secondary samples of the underlying process by randomly drawing data points from the light curve and creating another one. The primary purpose of bootstrapping is to test the performance of different statistical estimators. Depending on whether each drawn datum is *replaced*, i.e. put back to the initial sample, the procedure is characterized as re-sampling with replacement or re-sampling without replacement. In the former the same datum can be randomly drawn more than once, while in the latter each datum can be randomly selected only once and then is disregarded during subsequent random selections. The important implication of the two above approaches is that in re-sampling with replacement, the resulting distributions—the two new light curves—are statistically independent. As already mentioned, a re-sampling with replacement scheme is employed here.

## 5.5 FREQUENCY-DEPENDENT TIME LAGS

Time delays between flare maxima are often seen and usually attributed to the effect of optical depth. Flare onsets and maxima appear first at higher frequencies and successively progress towards the lower end of the observing frequency range. This is usually connected to the motion of disturbances that as they move downstream the jet and expand adiabatically, the optical depth decreases and lower frequency (hence energy) photons are able to escape the synchrotron-emitting region.

The DCCFs shown in Fig. 5.12 through 5.14 confirm the presence of a correlation between the outburst across observing frequencies, with time lags between the reference frequency of 15.00 GHz and all other light curves. In Table 5.6 the results are referenced to the highest well-sampled frequency of 142.33 GHz. In

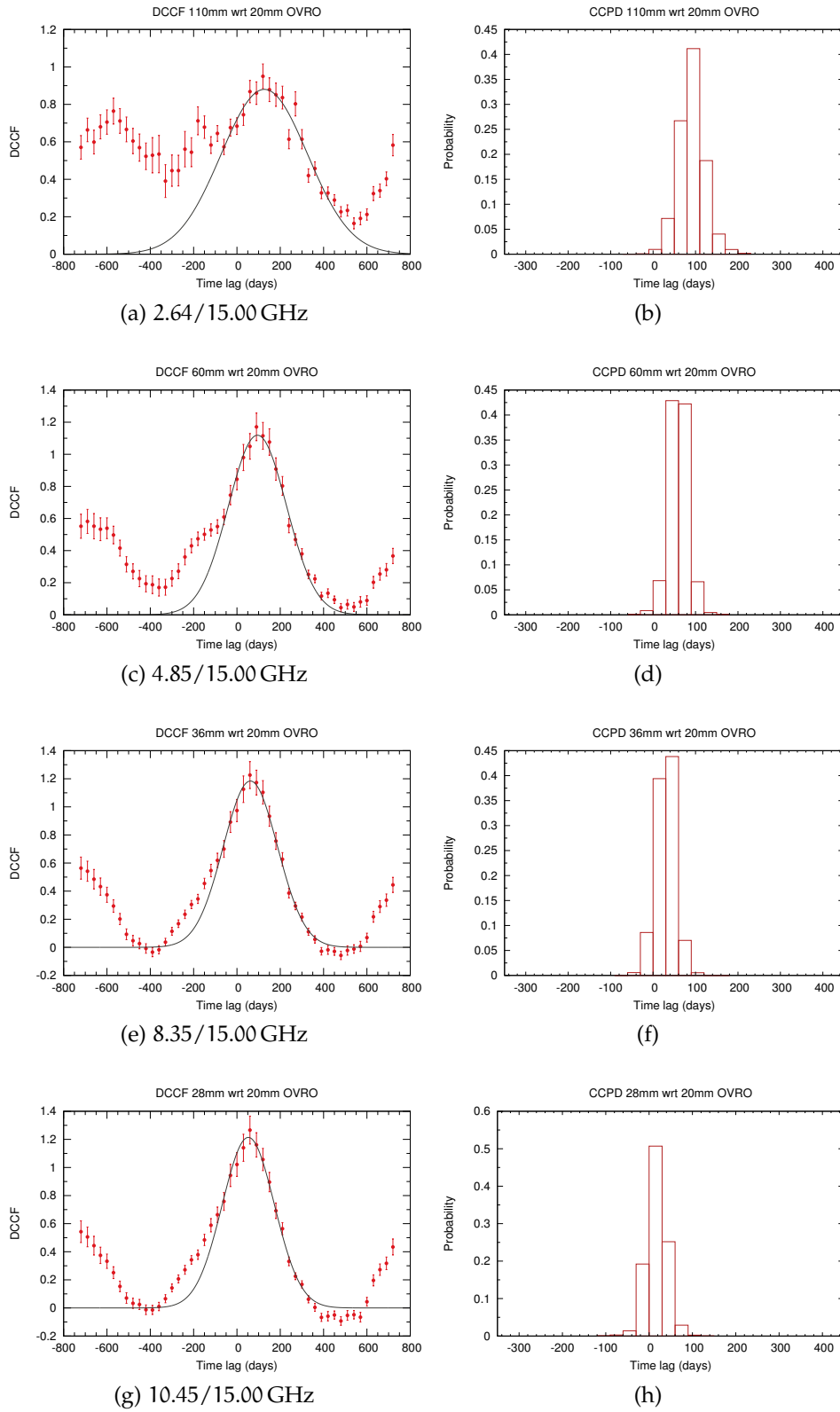


Figure 5.12: DCCFs for the light curves in the frequency range 2.64–10.45 with respect to the 15.00 GHz OVRO light curve. Also shown is the best-fit Gaussian function, the peak of which corresponds to the time lag.

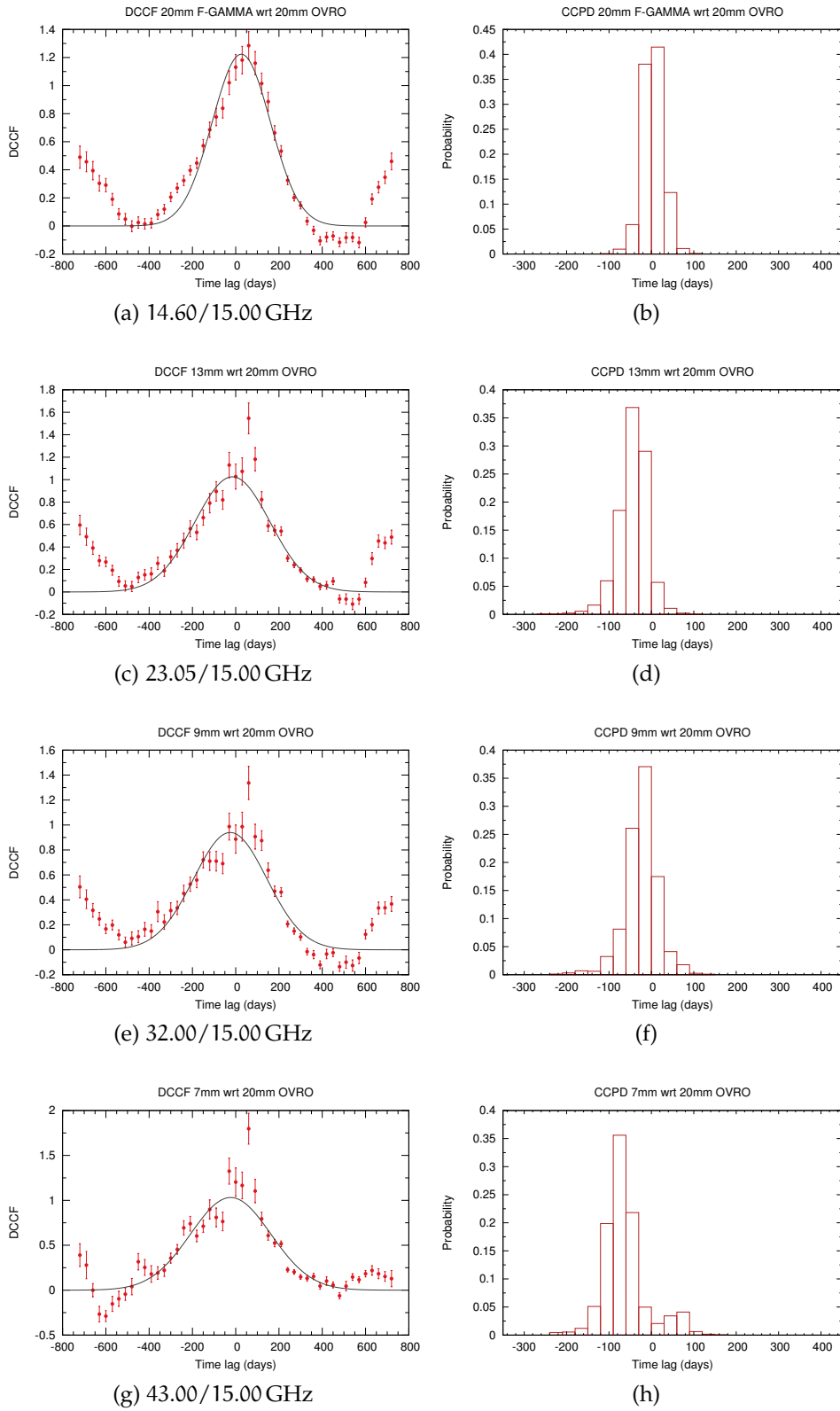


Figure 5.13: DCCFs for the light curves in the frequency range 14.60–43.00 with respect to the 15.00 GHz OVRO light curve. Also shown is the best-fit Gaussian function, the peak of which corresponds to the time lag.

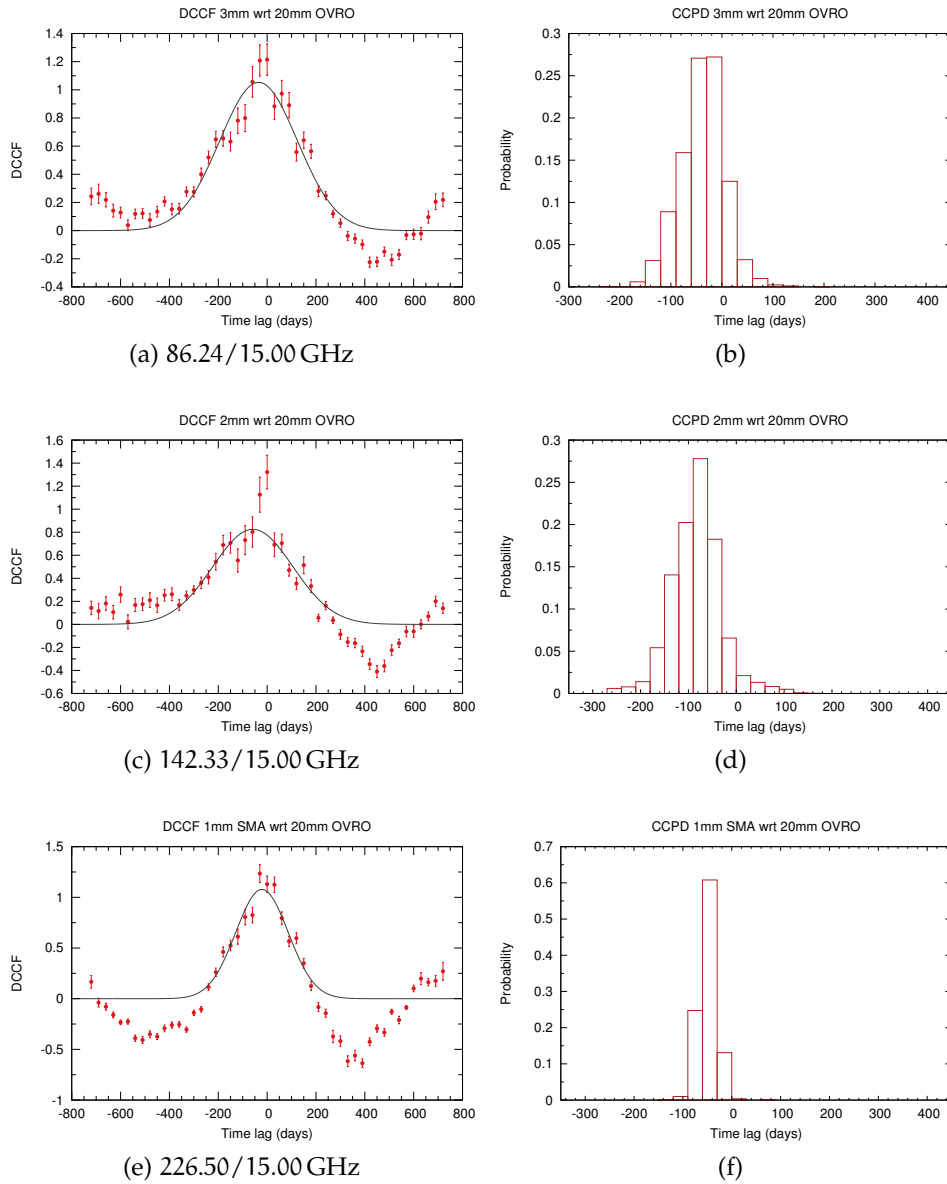


Figure 5.14: DCCFs for the light curves in the frequency range 86.24–226.50 with respect to the 15.00 GHz OVRO light curve. Also shown is the best-fit Gaussian function, the peak of which corresponds to the time lag.



Fig. 5.15 the delays obtained with all three methods are shown, namely results from the decomposition into exponential flares, the Gaussian process regression, and the DCCF analysis.

The light curve decomposition into exponential flares grossly underestimates the cross-frequency time lag due to the shape of the light curve that cannot be well approximated by Eq. 5–6 and also due to the under-sampled flare peak, especially at high frequencies. On the other hand, Gaussian process regression and the discrete cross-correlation function analysis yield conclusive results that are—within the uncertainties—in very good agreement with each other (see Fig. 5.15).

After averaging the time lags obtained through the GP regression and the DCCF analysis, the longest delay is seen for 2.64 GHz being  $\sim 200$  days. A decreasing trend is clearly visible towards higher frequencies with a time lag of  $\sim 140$  days at 4.85 GHz and for 8.35 GHz being  $\sim 110$  days on average. Between the highest frequency of 142.33 and 86.24 GHz it is  $\tau_{\text{DCCF}} \sim 24$  days. The last positive time lag between 226.5 and 142.33 GHz is attributed to the low sampling rate of the SMA light curve rendering it also unusable as high-frequency reference.

This decay trend is described well by a power-law. In order to obtain its index, the frequency-dependent delays are fitted by a power-law of the form  $\alpha\nu^{-1/k_r}$  using a weighted list-squares procedure. The results for index  $k_r$  are for the GP regression  $k_{r,\text{GP}} = (1.4 \pm 0.1)$  and  $k_{r,\text{DCCF}} = (1.8 \pm 0.2)$  for the DCCF results. They both are shown, along with the best-fit curves, in Fig. 5.15. The importance of index  $k_r$  will be discussed in the following section.

## 5.6 TIME-LAG CORE SHIFTS AND OPACITY STRUCTURE OF PKS 1502+106

Through the technique of VLBI, discussed in previous chapters, sub-parsec-scale imaging of extragalactic radio jets is possible and parsec-scale imaging typically achieved [e.g. Zensus, 1997]. Like most blazars PKS 1502+106 features a flat-spectrum core, indicative of the superposition of optically thick synchrotron components [e.g. Kaiser, 2006]. In addition to the scenario that the observed core is the first stationary hotspot (recollimation shock) of the jet [Daly and Marscher, 1988; Gómez et al., 1995], a widely accepted interpretation is that this core is the point of the continuous flow where the photons at a given frequency have enough energy, hence are able to escape the opacity barrier. Under this scenario the core is interpreted as the surface where the optical depth is close or equal to unity at a given frequency [e.g. Königl, 1981].

The standard relativistic jet paradigm [Blandford and Königl, 1979; Königl, 1981] predicts that the apparent position of this unit-opacity surface depends on observing frequency (see Fig 5.16). Therefore, according to the interpretation for the core discussed above, its position must also be frequency-dependent. This “core-shift effect” was first observed by Marcaide and Shapiro [1984] and ever since it is often observed with multi-frequency VLBI [e.g. Lobanov, 1998; Kovalev et al., 2008; Sokolovsky et al., 2011; Pushkarev et al., 2012; Fromm et al., 2013b].

The importance of core-shift measurements lies in the fact that they can provide us with critical insights into the structure and physics of ultracompact jets,

FREQUENCY (GHz)	$\tau_{\text{exp}}$ (days)	$\tau_{\text{GP}}$ (days)	$\tau_{\text{DCCF}}$ (days)
2.64	$65.9 \pm 26.3$	207.104	$185^{+29}_{-29}$
4.85	$29.8 \pm 15.2$	128.764	$153^{+19}_{-20}$
8.35	$12.9 \pm 14.7$	92.346	$120^{+21}_{-22}$
10.45	$-4.3 \pm 14.9$	80.640	$111^{+23}_{-21}$
14.60	$-11.1 \pm 15.0$	66.333	$84^{+26}_{-20}$
15.00	$-8.8 \pm 14.3$	64.232	$58^{+43}_{-51}$
23.05	$-28.8 \pm 15.2$	33.817	$43^{+28}_{-34}$
32.00	$-7.4 \pm 18.3$	28.614	$33^{+34}_{-30}$
43.00	$-18.2 \pm 32.8$	37.719	$35^{+41}_{-31}$
86.24	$-0.6 \pm 17.0$	24.712	$23^{+36}_{-48}$
142.33	0.0	0.0	0.0
226.50	$-11.2 \pm 16.8$	26.263	$37^{+16}_{-19}$

Table 5.6: Cumulative table containing time lag results from all methods with respect to data at 142.33 GHz. OVRO 15 GHz data come without  $\tau_{\text{DCCF}}$  uncertainty since the light curve was used as the initial reference for the DCCF analysis. Columns from left to right: (1) observing frequency; (2) frequency-dependent time lag from exponential flare decomposition, (3) from Gaussian process regression, and (4) from the DCCF analysis.

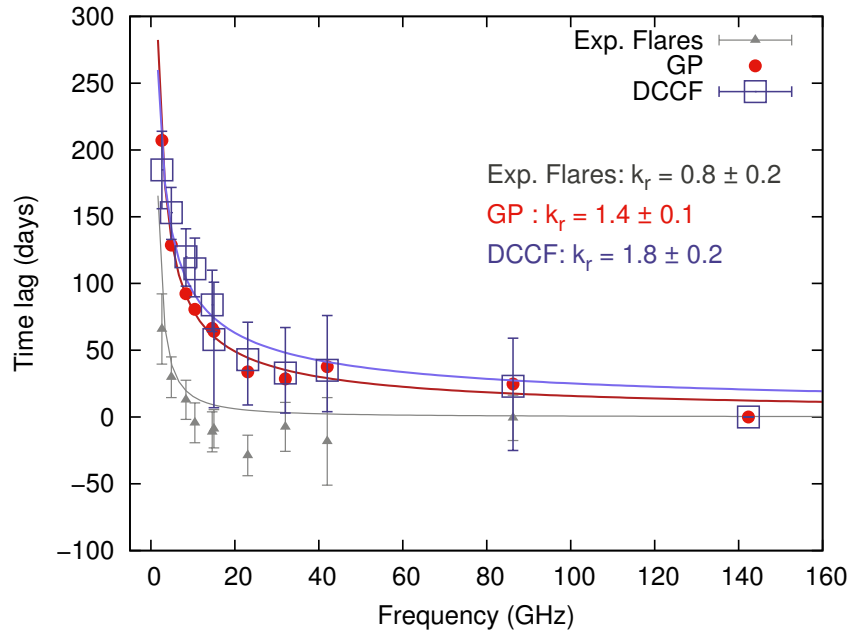


Figure 5.15: Frequency-dependent time lags with respect to the 142.33 GHz data obtained through the three methods employed here. Open squares denote the values obtained from the DCCF analysis, red circles those from the Gaussian process regression and gray triangles the time lags from the exponential flare decomposition. The trend of decreasing time lag as observing frequency increases is evident with the use of all methods. Solid lines of the same color represent the best fit curves of the form  $\alpha\nu^{-1/k_r}$  and indices  $k_r$  are shown on the plot for each method.

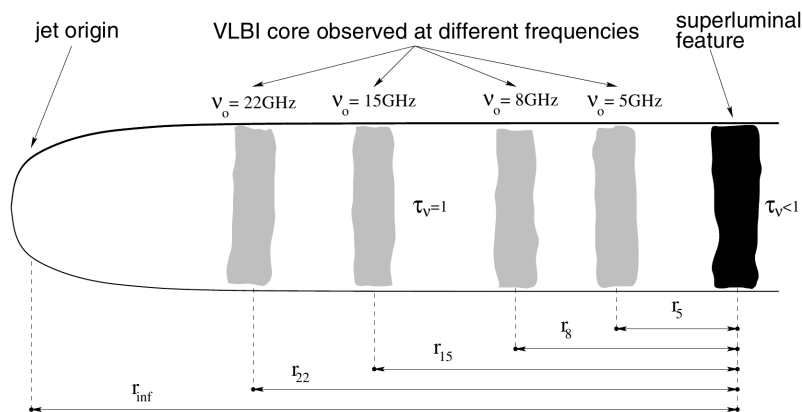


Figure 5.16: Illustration of the frequency-dependent core position effect seen in VLBI images obtained at different frequency bands. Each frequency is "sensitive" to a certain opacity regime. By observing at increasing frequency we penetrate the opacity barrier set by synchrotron self-absorption to frequencies lower than it. Image adopted from Lobanov [1996].

such as the position of the core at each frequency relative to the jet base and the magnetic field in different portions of the relativistic flow [e.g. [Lobanov, 1998](#); [Hirotoni, 2005](#)]. Unfortunately, the difficulty of obtaining accurate core-shift data through VLBI is proportional to their high value since highly accurate positions are required, especially at higher frequencies. Usually the price to pay comes in the form of time-consuming and complicated phase-referencing observations, which nevertheless when successful yield extremely interesting results such as those for the jet of M 87 by [Hada et al. \[2011\]](#).

Relative timing of total flux density outbursts, as seen in single-dish radio observations, presents a viable alternative to VLBI core-shifts. Let us return back to the standard jet model. Here, a disturbance originating at the jet base will propagate outwards along the jet. As this disturbance or shock moves away from the base it crosses the sequence of physically separated regions where the jet flow becomes optically thin—i.e. the VLBI cores, as seen at a given sequence of observing frequencies. When the disturbance reaches a given unit-opacity surface for a given frequency  $\nu_i$ , the synchrotron flare emission most likely becomes optically thin at  $\nu_i$ . This is observed in single-dish light curves as a total intensity outburst, while in VLBI maps these traveling shocks could be manifested as regions of enhanced emission after the core, so-called VLBI components or knots [[Marscher and Gear, 1985](#)]. Since the times of maxima in single-dish light curves correspond to the flare emission becoming optically thin at the unit-opacity surface for a given frequency, it follows that these times are frequency-dependent as well and carry information on the opacity of each core region. In other words, through relative timing of the same flaring event seen at different bands one can obtain a tomography of the jet in terms of nuclear opacity, similar to VLBI core-shift measurements. For details see also [Kudryavtseva et al. \[2011\]](#); [Bach et al. \[2006\]](#) and for applications [Kutkin et al. \[2014\]](#) and [Fuhrmann et al. \[2014\]](#).

An important consideration to be taken into account is that the method is based on the absence of any optically thick component downstream of the core. If there was any, it would sooner or later induce an opacity-driven enhancement of flux density due to its expansion and subsequent drop of density at a region further away from the core, the position of which we try to constrain. Essentially, the emission needs to become optically thin when it reaches each respective unit-opacity surface. In that respect and given the spectra of VLBI components presented in Section 4.3.4, component C<sub>3</sub> which is used for our calculations is optically thin, at least between 43 and 86 GHz.

Based on [Lobanov \[1998\]](#), a "time-lag core-shift" between two frequencies  $\nu_1$  and  $\nu_2$ , with  $\nu_2 > \nu_1$ , can be defined as follows [see also [Kudryavtseva et al., 2011](#)]

$$\Omega_{rv} = 4.85 \times 10^{-9} \frac{\mu \Delta t D_L}{(1+z)^2} \left( \frac{\nu_1^{1/k_r} \cdot \nu_2^{1/k_r}}{\nu_2^{1/k_r} - \nu_1^{1/k_r}} \right) \quad (\text{pc GHz}) \quad (5-18)$$

where

- $\mu$  is the VLBI jet proper motion in  $\text{mas yr}^{-1}$ ,
- $\Delta t$  is the observed time lag between the frequency pair  $\nu_1$  and  $\nu_2$  in yr,
- $D_L$  is the luminosity distance in pc,

- $z$  is the redshift,
- $\nu_1, \nu_2$  are the first and second observing frequency, both expressed in GHz.
- $k_r$  is the power-law index obtained by fitting the cross-band delays (see previous Section). Here,  $k_r = [(3 - 2\alpha)m + 2n - 2]/(5 - 2\alpha)$  with  $m$  and  $n$  denoting the index of the power-law dependence of the magnetic field  $B(r) \propto r^{-m}$  and the electron number density  $N_e(r) \propto r^{-n}$ , respectively at distance  $r$  along the jet. Finally,  $\alpha$  denotes the optically thin spectral index. In case of external density gradients and/or free-free absorption, it is  $k_r > 1$ . For SSA dominated opacity and equipartition between particle energy and magnetic field energy,  $k_r = 1$  for  $m = 1$  and  $n = 2$  independently of  $\alpha$ .

The angular offset in units of mas is given by  $\Delta r = \mu\tau$ . That is the distance traveled by the respective disturbance within the time interval  $\tau$ . Using  $\Omega_{rv}$  and following the works of [Lobanov \[1998\]](#), [Hirovani \[2005\]](#), and [Kudryavtseva et al. \[2011\]](#) we can obtain expressions for the magnetic field and distance between the core and the vertex of the assumed-conical jet. The frequency-dependent distance of the core—at any desired frequency  $\nu$ —is given by

$$r_{\text{core}}(\nu) = \frac{\Omega_{rv}}{\sin \theta} \nu^{-1/k_r}. \quad (5-19)$$

We employ Eq. 5-18 and 5-19 to infer the separation of the radio core at each frequency from the vertex of the conical jet. In that, we use  $k_r = (1.6 \pm 0.2)$  the average  $k_r$  calculated based on two different methods, the DCCF analysis and the Gaussian process regression. The full range of  $k_r$  obtained from all three methods is rather wide with  $0.8 \lesssim k_r \lesssim 1.8$ . Nevertheless, GP and DCCF results agree very well with each other indicating that  $k_r > 1$ . This implies the possible presence of jet external density gradients and/or foreground free-free absorption (e.g. due to the BLR). Other parameters used are  $\mu = 0.09 \text{ mas yr}^{-1}$  which corresponds the proper motion of component C<sub>3</sub> at 86 GHz, responsible for the flare under scrutiny (see Section 4.3.2),  $\theta = 2.6^\circ$  the critical viewing angle (see Section 4.4.2),  $z = 1.8385$ , and  $D_L = 14177 \text{ Mpc}$ . Results of the calculation are shown in Table 5.7 and reveal the opacity structure of PKS 1501+106. The larger distance of  $\sim 10.0 \text{ pc}$  is reported for the 2.64 GHz core, as expected, and distances diminish as we go towards higher frequencies. At observing frequencies between 23.05 and 43.00 GHz the light curves become slightly more sparsely sampled due to the fact that weather effects and poorer system performance of the Effelsberg 100-m telescope at those bands play an increasingly important role. Nevertheless, the trend continues up to 86.24 GHz where the core is about 4.1 pc away from the base of the jet.

### 5.6.1 Localizing the $\gamma$ -ray emission region

The ultimate goal of pinpointing the  $\gamma$ -ray emission region is reached by combining the findings of the present study with those of [Fuhrmann et al. \[2014\]](#) who localize the  $\gamma$ -ray active region at about 2.1 pc upstream of the 86.00 GHz unit-

FREQUENCY (GHz)	AVERAGE $\tau$ (days)	$\Delta r$ (mas)	$\Omega_{rv}$ (pc GHz)	$r_{\text{core}}$ (pc)
2.64	196.1	0.048	0.825	10.0
4.85	140.9	0.035	0.904	7.4
8.35	106.2	0.026	1.014	5.9
10.45	95.8	0.024	1.085	5.5
14.60	75.2	0.019	1.113	4.6
15.00	61.1	0.015	0.925	3.8
23.05	38.4	0.009	0.845	2.6
32.00	30.8	0.008	0.932	2.4
43.00	36.4	0.009	1.525	3.2
86.24	23.9	0.006	3.031	4.1
142.33	0.0	...	...	...

Table 5.7: Frequency-dependent “time-lag core shifts” obtained through the flare timing analysis. Time lags are averaged per frequency between  $\tau_{\text{GP}}$  and  $\tau_{\text{DCCF}}$ . Values are reported without error. All time lags are referenced to the highest well-sampled frequency of 142.33 GHz. Columns from left to right: (1) observing frequency; (2) average time lag between  $\tau_{\text{GP}}$  and  $\tau_{\text{DCCF}}$ ; (3) the angular offset in units of mas ( $\Delta r = \mu\tau$ ); (4) time-lag-based core position offset; (5) core distance to the vertex of the jet.

opacity surface. Here, based on the opacity-driven time lags across the eleven observing frequencies, the distance of the 86.00 GHz core from the vertex of the assumed-conical jet is constrained to  $\sim 4.1$  pc. From the combination follows that the  $\gamma$ -ray emission region is located at approximately 2 pc away from the jet base, well beyond the bulk of BLR material of PKS 1502+106, placed at  $R_{\text{BLR}} \approx 0.1$  pc [Abdo et al., 2010]. A  $\gamma$ -ray emission region placed so far away from the BLR almost negates the notion that BLR photons alone can be used as the target photon field for IC up-scattering to  $\gamma$ -rays, thus other or additional seed photon fields (e.g. torus, SSC) need to be involved in the process.

### 5.6.2 Equipartition magnetic field

Under the assumption of equipartition between the energies of the magnetic field and of particles—i.e. setting  $k_r = 1$ —and with a spectral index  $\alpha = -0.5$ , the following expression yields the magnetic field strength at a distance of 1 pc from the vertex of the jet

$$B_{1 \text{ pc}} \approx 0.025 \left( \frac{\Omega_{rv}^3 (1+z)^2}{\delta^2 \phi \sin^2 \theta} \right)^{1/4} \quad (\text{G}) \quad (5-20)$$

where

- $\delta$  is Doppler factor and
- $\phi$  is the jet’s half-opening angle.

The magnetic field strength at the core can be estimated through

$$B_{\text{core}}(\nu) = B_{1\text{ pc}} r_{\text{core}}^{-1} \quad (5-21)$$

Use of Eq. 5-20 and 5-21 allows for the calculation of the magnetic-field strengths at a distance of 1 pc and at the point of each respective radio core. We employ the values for the Doppler factor and half opening angle deduced and reported in Section 4.4 of  $\delta = 10$  and  $\phi/2 = 0.95^\circ$ , respectively corresponding to components traveling within the inner jet of PKS 1502+106 (see Section 4.3.2). Resulting values for  $B_{1\text{ pc}}$  and  $B_{\text{core}}$  are summarized in Table 5.8. Inferred magnetic field strengths are higher at higher frequencies, when approaching the jet base. Magnetic field strength values range between 3 and 16 mG for the 2.64 (furthest) and 86.24 (closest) cores, respectively, assuming equipartition.

Results presented here are in reasonable agreement with the core shift measurements derived by Pushkarev et al. [2012] who employ standard VLBI techniques and obtain a separation of  $\sim 8$  pc between the 15 GHz VLBI core and the vertex of the jet. Some discrepancies can be seen in the—inferred from VLBI core shifts—physical parameters of the jet, such as the magnetic field at a distance of 1 pc and in the 15 GHz core ( $B_{1\text{ pc}}$  and  $B_{\text{core}}$ ), but these can be explained through the different kinematical parameters used. Specifically, Pushkarev et al. [2012] make use of the fastest non-accelerating, component apparent speed measurement from data covering the period 1994 August to 2007 September, as reported by Lister et al. [2009]. However, in the present thesis we use the result for the proper motion,  $\mu$ , of the component most likely responsible for the multi-wavelength flare of 2008/2010 (knot C<sub>3</sub>), as we showed in the previous chapter, whose apparent angular velocity—while traveling in the inner jet of PKS 1502+106—is almost half of what Pushkarev et al. [2012] use.

## 5.7 COMPARISON WITH SHOCK-IN-JET MODEL SIMULATIONS

The origin of blazar variability and its extreme characteristics is still a matter of intense debate. A multitude of different mechanisms have been proposed in order to explain it. Among those are shocks generated and propagating along the relativistic jet [e.g. Marscher and Gear, 1985; Valtaoja et al., 1992], colliding relativistic plasma shells [e.g. Spada et al., 2001], precession of the jet itself due to the presence of binary black holes [e.g. Camenzind and Krockenberger, 1992] or Kelvin–Helmholtz instabilities developing within the relativistic outflow [e.g. Lobanov and Zensus, 2001, and references therein].

Different variability mechanisms predict different dependencies of observed parameters in the time and frequency domain—i.e. light curves and broadband spectra. In the following we compare our findings in the time domain and the extracted light curve parameters with the predictions of analytical simulations based on the shock-in-jet model [Fromm et al., 2014].

### 5.7.1 *The shock-in-jet scenario and flare evolution*

The central assumption of the classical shock-in-jet model [Marscher and Gear, 1985] is the propagation of a shock within the relativistic jet of an AGN. The

FREQUENCY (GHz)	AVERAGE $\tau$ (days)	$B_{1\text{ pc}}$ (G)	$B_{\text{core}}$ (G)
2.64	196.1	0.025	0.003
4.85	140.9	0.027	0.004
8.35	106.2	0.030	0.005
10.45	95.8	0.031	0.006
14.60	75.2	0.032	0.007
15.00	61.1	0.028	0.007
23.05	38.4	0.026	0.010
32.00	30.8	0.028	0.012
43.00	36.4	0.040	0.013
86.24	23.9	0.067	0.016
142.33	0.0	...	...

Table 5.8: Equipartition magnetic field strength calculated through time lags and subsequent time-lag core shifts. Values are based on average  $\tau$  and are reported without error. Columns from left to right: (1) observing frequency; (2) average time lag between  $\tau_{\text{GP}}$  and  $\tau_{\text{DCCF}}$ ; (3) magnetic field strength at a distance of 1 pc from the core; (4) core magnetic field strength.

jet itself is assumed to have a conical geometry; i.e. its radius,  $R$ , and distance along it,  $r$ , are directly proportional with  $R \propto r^\rho$  where  $\rho = 1$ . At the shock front conditions are appropriate for the acceleration of particles up to relativistic energies. After interaction with the shock those particles travel behind the shock front, while at the same time lose energy through the mechanisms of Compton, synchrotron and adiabatic (non-radiative) energy losses [see e.g. [Valtaoja et al., 1992](#); [Türler et al., 2000](#); [Fromm et al., 2011](#)]. The emitted synchrotron spectrum evolves and its shape is dictated by the relative dominance of each energy loss mechanism. The turnover frequency,  $\nu_{\text{max}}$ , of the synchrotron spectrum follows a characteristic three-stage path in the turnover frequency – turnover flux density plane ( $\nu_{\text{max}}-S_{\text{max}}$ ) with  $\nu_{\text{max}}$  sweeping the frequency range from higher to lower values. In parallel, the peak flux density of the spectrum,  $S_{\text{max}}$ , is evolving as follows:

1. First, at higher frequencies, it rises during the stage of Compton losses,
2. it then reaches a plateau where it stays approximately constant for as long as synchrotron losses dominate, and
3. finally, towards the low-frequency end, it decays during the final stage when adiabatic losses dominate.

The physical quantities of the model are parameterised with the use of power laws. The energy distribution of relativistic electrons is given by

$$N(E) = KE^{-s} \tag{5-22}$$



where  $K$  is a normalisation factor,  $E$  the energy, and  $s$  the power-law index. The variation of the magnetic field along the jet is given by

$$B \propto R^{-b}. \quad (5-23)$$

Index  $b$  also carries information on the topology of the magnetic field in the flow. For a toroidal magnetic field  $b = 1$ , while for poloidal topology  $b = 2$ . The variation with distance of the aforementioned normalisation factor is given by

$$K \propto R^{-k}. \quad (5-24)$$

Finally, the evolution of the Doppler factor is given by

$$\delta \propto R^{-d}. \quad (5-25)$$

Here, negative exponents for the two power laws in Eq. 5-24 and 5-25 denote that the quantities described by them increase with distance along the jet—e.g. for  $d < 0$  the jet is accelerating, for  $d = 0$  the Doppler factor is constant, while  $d > 0$  implies deceleration. According to the model, it is these power-law indices through which the observed patterns of blazar variability can be largely understood.

### 5.7.2 Analytical model simulations

From an observer's point of view, the main observables—as far as multi-frequency radio light curves are concerned—are the flare amplitude, its time scale (rise and decay time scales) and putative delays between flare maxima at different bands. These light curve parameters are observing-frequency dependent (see Fig. 5.15, 5.19, and 5.20 and 5.21).

Based on the original shock-in-jet scenario of Marscher and Gear [1985], Fromm et al. [2014] have performed a series of simulations yielding synthetic blazar light curves at the frequency range matching the F-GAMMA spectral coverage, namely in twelve bands between 2.6 and 345.00 GHz. Those light curves were produced for a spectrum of different values of the indices  $s$ ,  $b$ , and  $d$  ( $k$  is given by  $k = 2(s + 2)/3$ , thus reducing the number of free parameters of the model). The ranges for each of the three indices were selected based on physical arguments and observational findings [for a full account see Fromm et al., 2014] and they are  $2 < s < 3$ , hence  $2.7 < k < 3.3$  for the spectral slope,  $-0.45 < d < 0.45$  for the Doppler factor, and  $1 < b < 2$  for the index describing the magnetic field topology (toroidal, helical or poloidal). From the synthetic light curves, predictions for "observables" such as the flare amplitude, flaring time scale and delay between different bands are deduced in each case.

Given a data set comprising radio light curves at different bands, we are offered the chance for a direct comparison between the observed parameters (flare amplitude, flaring time scale and cross-band delays) and those arising from the simulated light curves. We can thus constrain the model indices and ultimately get a handle on the evolution of physical parameters of the jet and the shock producing the outburst (see Section 4.6). As an example, in Fig. 5.17 extracted light curve parameters of Fromm et al. [2014] are shown, for three

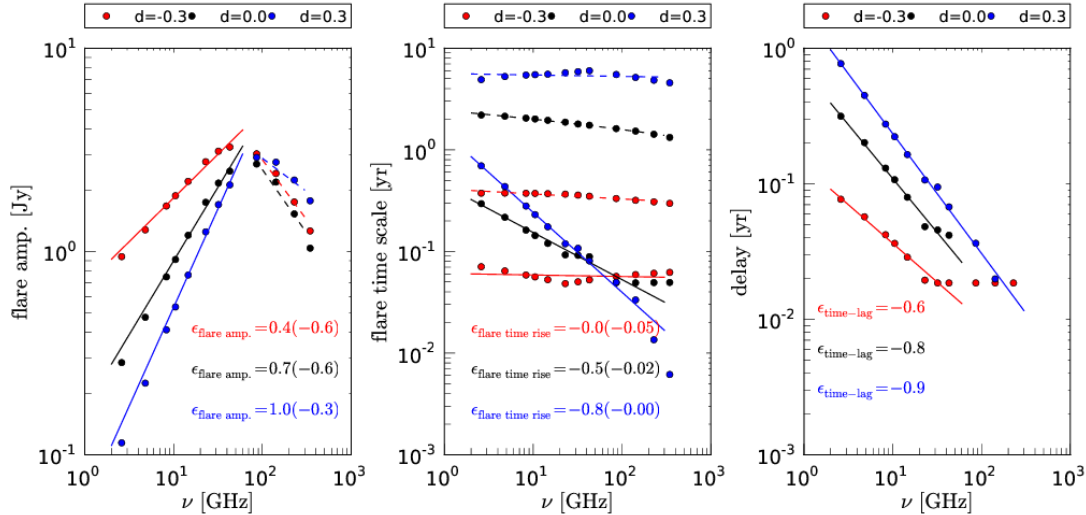


Figure 5.17: Frequency-dependent light curve parameters and their variation with  $d$ . From left to right the flare amplitude, flare time scale and cross-band delays are shown, each at three values of  $d$ , namely  $d = -0.3$ ,  $0.0$ , and  $0.3$ . The other indices are kept constant with  $b = 1.5$  and  $s = 2.5$ . For the first and second panels from the left solid lines represent the rising part of the light curve, while dashed lines are used for the slopes of the decaying part. Numerical values for the slopes are shown with that of the decaying part in parenthesis. Image adopted from Fromm et al. [2014].

different values of the Doppler factor index  $d$ . From the slopes obtained through observed light curves, the values of  $s$ ,  $b$ , and  $d$  can be constrained.

This is what we do in the sections to follow.

### 5.7.3 Results

Overall, the slopes extracted from the multi-wavelength light curves indicate a good agreement of trends with expectations of the shock-in-jet model. A fact advocating for a shock origin of the 2008/2010 flare of PKS 1502+106. In the following paragraphs the observed light curve parameters (cross-band delays, flare amplitudes and time scales) are presented and discussed in conjunction with the results of the analytical shock-in-jet model simulations [Fromm et al., 2014]. The slopes for all light curve parameters extracted through the power law fits are as follows: for the cross-frequency delays  $\epsilon_{\text{time-lag}} \approx -0.6$  (see Fig. 5.15), for the rising and decaying part of the flare, obtained through the GP regression time scale  $\epsilon_{\text{flare time rise GP}} \approx 0.08$  and  $\epsilon_{\text{flare time decay GP}} \approx 0.04$ , respectively. For the same parameter the decomposition into exponential flares gives  $\epsilon_{\text{flare time rise exp}} \approx 0.06$  and  $\epsilon_{\text{flare time decay exp}} \approx -0.3$ . Finally, for the flare amplitudes we obtain (averaging between the results of GP regression and exponential flares)  $\epsilon_{\text{flare amp rise}} \approx 0.7$  and  $\epsilon_{\text{flare amp decay}} \approx -0.3$ , respectively. In the following we search the parameter space and try to constrain the shock physical parameters their evolution.

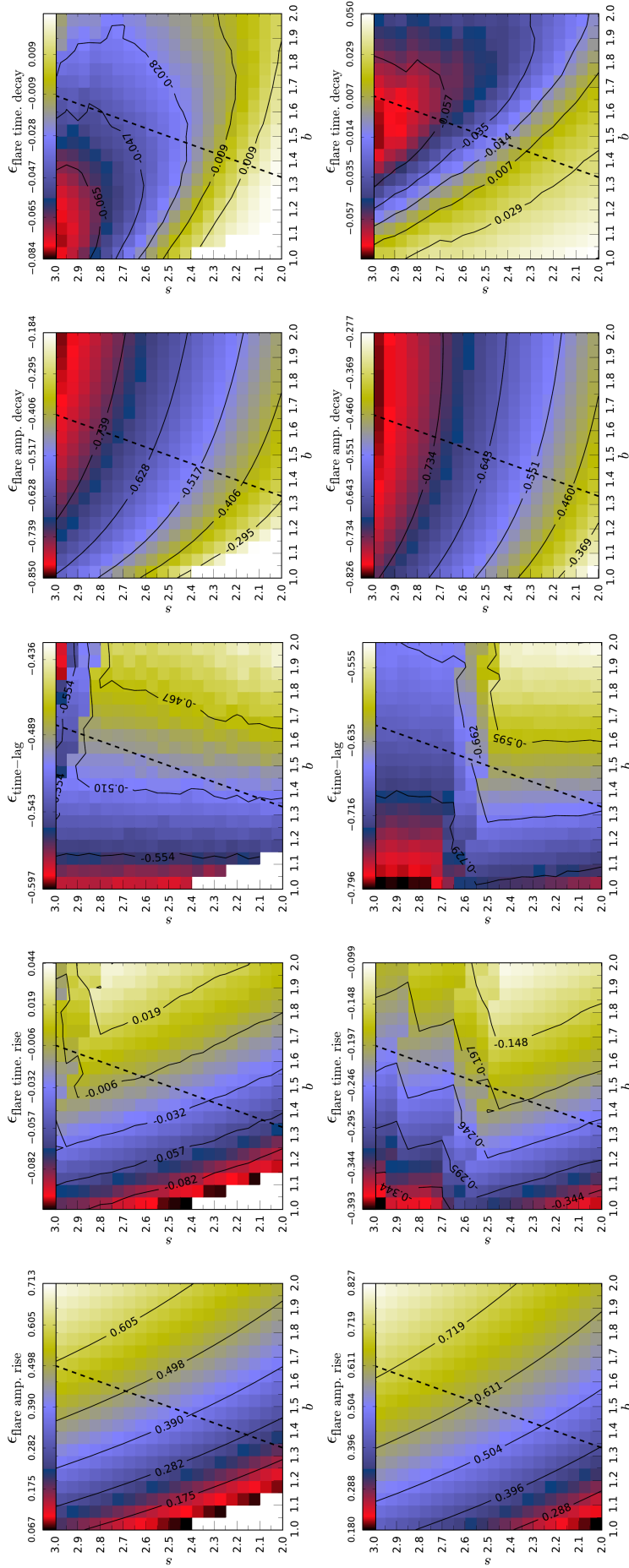


Figure 5.18: Parameter space plots for the evolution of frequency-dependent light curve parameters as a function of  $s$  and  $b$  and for fixed  $d$ . Top row corresponds to  $d = -0.30$  while the bottom to  $d = -0.15$ . The first two columns refer to the rising part of the light curves, middle row refers to the cross-band delay, and the last two rows refer to the decaying part of the light curves. From left to right are shown the slopes:  $\epsilon_{\text{flare amp. rise}}$ ,  $\epsilon_{\text{flare time rise}}$ ,  $\epsilon_{\text{flare amp. decay}}$ ,  $\epsilon_{\text{flare time decay}}$ , and  $\epsilon_{\text{flare time decay}}$  (see Section 5.7.3 and original publication for details). Image adopted from [Fromm et al. \[2014\]](#).

### 5.7.3.1 Cross-band delays

The frequency-dependent time lags,  $\tau$ , obtained through our relative flare timing analysis have already been shown in Fig. 5.15 and used to estimate the distance of each radio core—or unit-opacity surface—to the vertex of the conical jet and the magnetic field strengths along it. Here, we compare these values with the predictions for cross-band delays obtained through the simulations of Fromm et al. [2014].

Firstly, a general good agreement is found between the frequency dependence of  $\tau$ , shown in Fig. 5.15, and the shock model predictions shown in Fig. 5.17 (right). The most stringent constraint to the physical parameters of the jet of PKS 1502+106 is set by the power-law slope of the observed time lags,  $\epsilon_{\text{time-lag}} = -1/k_r$  (see Section 5.5). That is because only a limited area of the parameter space can accommodate for the obtained value  $\epsilon_{\text{time-lag}} \approx -0.6$  (see Fig. 5.15). This value is obtained by averaging over the two values arising from the GP regression and the DCCF analysis and is in accord with the pattern expected from the shock model. From a comparison with the parameter space plots provided in Fig. 11, 12, 13, and 14 of Fromm et al. [2014], we obtain the value of parameter  $d$ , being in the range of slopes  $\epsilon_{\text{time-lag}}$ , consistent with  $d = -0.15$ . Although a slightly higher (absolute) value between  $-0.15$  and  $-0.3$  cannot be excluded. In Fig. 5.18 the aforementioned figures of Fromm et al. [2014] are partially reproduced for visualization of the results. Through the slope of the frequency-dependent cross-band delays, one can safely exclude the scenario of a decelerating jet. Our findings in fact suggest the presence of a certain degree of acceleration taking place within the relativistic jet of PKS 1502+106.

### 5.7.3.2 Flare amplitude

The frequency dependence of flare amplitudes as obtained in Section 5.4 is shown in Fig. 5.19. Results from both GP regression and decomposition into exponential flares are visible on the same plot. Flare amplitudes rise with frequency until they culminate at a frequency of about 43 GHz, after which the amplitude of the flare drops. The rise and decay wings follow a trend that is well described by a broken power law in very good agreement with the shock model expectations (cf. Fig. 5.17 (left) and 5.19). Fig. 5.19 also shows the slopes extracted for each method via a power-law fit. Both approaches (GP and exponential flare decomposition) yield very consistent results with the slopes being  $\epsilon_{\text{flare amp rise}} \approx 0.7$  for the rising part of the flare amplitude as frequency increases and  $\epsilon_{\text{flare amp decay}} \approx -0.3$  for the decaying part.

With the Doppler factor adequately constrained from the slope of observed time lags, we proceed by comparing the two slopes  $\epsilon_{\text{flare amp rise}}$  and  $\epsilon_{\text{flare amp decay}}$  with the simulation results in order to constrain the values of parameters  $b$  and  $s$ , governing the evolution of the magnetic field and its topology and the electron energy distribution, respectively. From Fig. 5.18 we conclude that parameter  $b$ , using  $\epsilon_{\text{flare amp rise}} \approx 0.7$ , can be accurately constrained within the range  $1.5 \lesssim b \lesssim 2.0$ . However, the slope of the decaying part allows for a small range of  $1 \lesssim b \lesssim 1.3$ . As such, the magnetic field configuration cannot be adequately constrained since it relies heavily on those slopes and the Doppler factor. The sit-

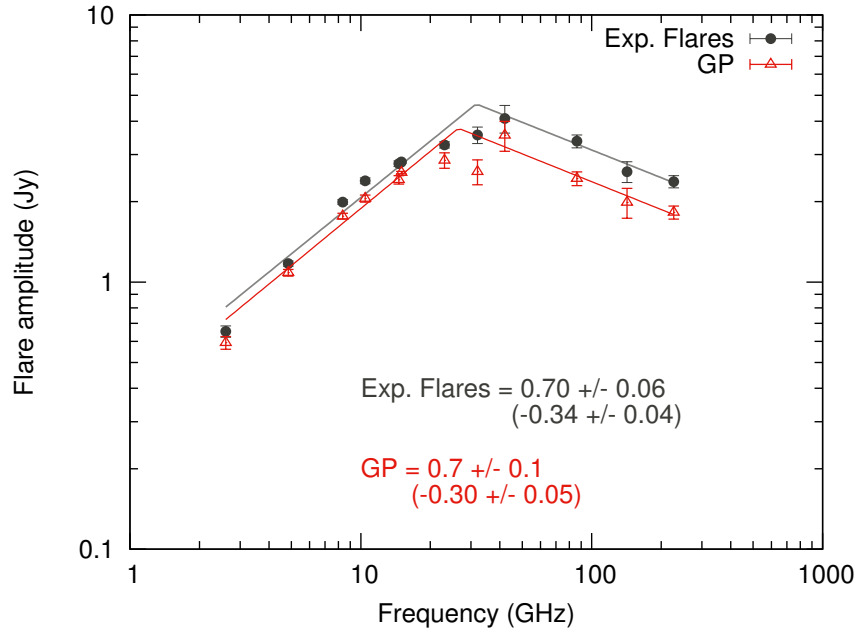


Figure 5.19: Frequency-dependent flare amplitudes. Triangles denote the values obtained through Gaussian process regression and circles those from exponential flare decomposition. Fitted power law functions are also shown following the same color coding and showing the rise and decay wings with respect to frequency. Best-fit power-law indices are shown on the plot.

uation is, in essence, the same for parameter  $s$  to which also poor constraints can be set.

### 5.7.3.3 Flare time scales

In Fig. 5.20 and 5.21 we show the observed frequency-dependent flare time scales obtained through decomposition into exponential flares and Gaussian process regression, respectively. Results do not agree well with each other. A power-law fit is nevertheless attempted yielding the slopes for the rise and decay time through GP regression  $\epsilon_{\text{flare time rise GP}} \approx 0.08$  and  $\epsilon_{\text{flare time decay GP}} \approx 0.04$ . Flare rise and decay slopes obtained from flare decomposition values are  $\epsilon_{\text{flare time rise exp}} \approx 0.06$  and  $\epsilon_{\text{flare time decay exp}} \approx -0.3$ . The time scale of the flare decay cannot be adequately described by a power law. Nevertheless, we show an attempt in both cases but we do not use it for any inference.

The power-law slopes of the rising part of the flare with both methods give comparable results. Comparing with the model simulations we obtain a slightly higher (absolute) value for the Doppler factor parameter being consistent with  $d = -0.45$ .

## 5.8 CHAPTER SUMMARY AND CONCLUDING REMARKS

In the preset chapter we exploited the dense, long-term F-GAMMA radio light curves in the frequency range 2.64–142.33 GHz obtained with the Effelsberg 100-m and IRAM 30-m. Additionally, light curves at 15.00 and 226.6 GHz were used from the OVRO 40 m monitoring program and the Submillimeter Array. Finally,

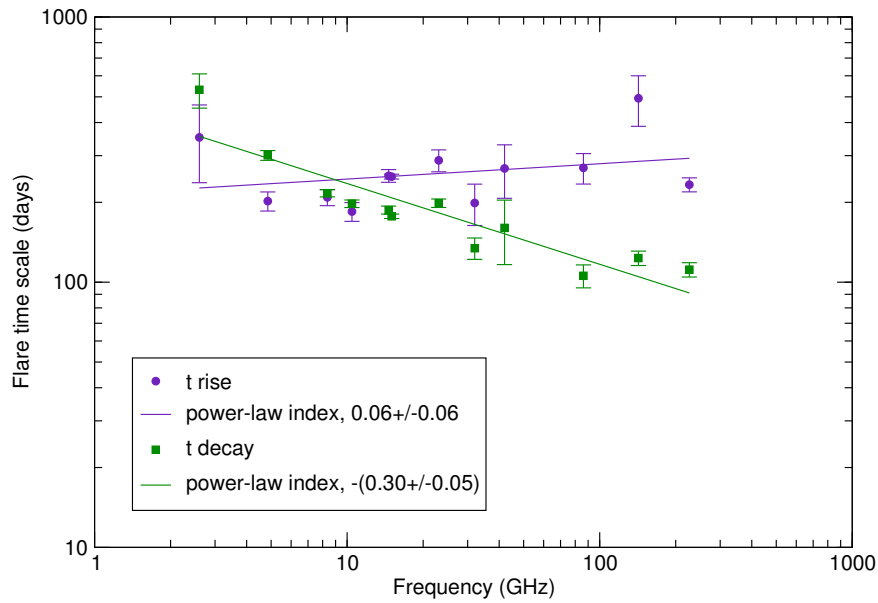


Figure 5.20: Frequency-dependent flare variability time scales, through the decomposition into exponential flares. Purple circles correspond to the rising part of the light curve at each frequency, while filled green squares to the decaying part. Solid lines, color-coded according to the data, indicate the best-fit power-law of the form  $\alpha\nu^b$ . Indices  $b = \{\epsilon_{\text{flare time rise exp}}, \epsilon_{\text{flare time decay exp}}\}$  are shown on the plot.

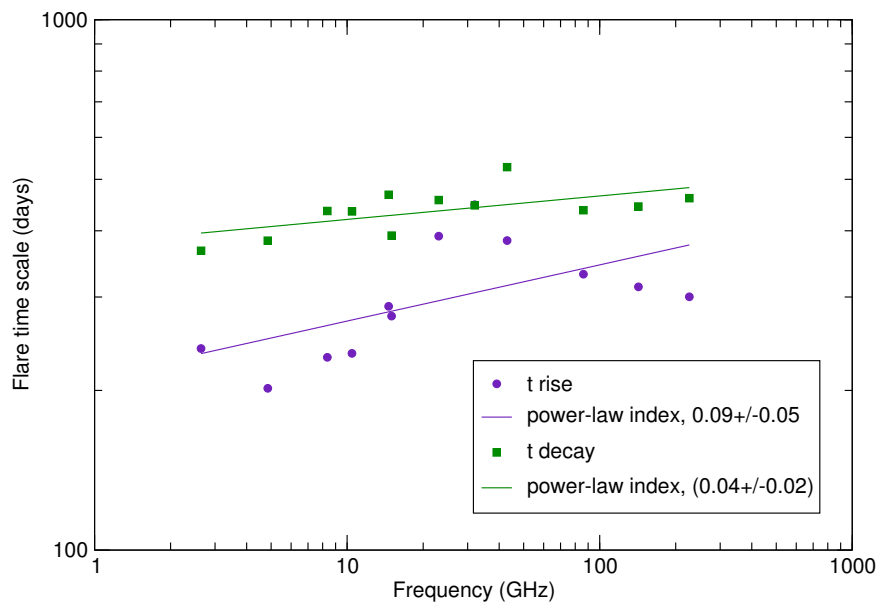


Figure 5.21: Frequency-dependent flare variability time scales, through Gaussian process regression. Purple circles correspond to the rising part of the light curve at each frequency, while filled green squares to the decaying part. Solid lines, color-coded according to the data, indicate the best-fit power-law of the form  $\alpha\nu^b$ . Indices  $b = \{\epsilon_{\text{flare time rise GP}}, \epsilon_{\text{flare time decay GP}}\}$  are shown on the plot.

the set was completed with the monthly-sampled *Fermi*/LAT  $\gamma$ -ray light curve (see Fig. 5.3, 5.4, and 5.5).

The data processing steps were presented in detail in Section 5.2. Those concern the reduction of data from both the main F-GAMMA facilities, namely the Effelsberg 100-m and IRAM 30-m.

A detailed section was devoted to the three independent approaches used in order to quantify the observed flare of PKS 1502+106 in the time domain. Those are: (i) a light curve decomposition into exponential flares (Section 5.4.1), (ii) a Gaussian process (GP) regression algorithm (Section 5.4.2), and to assess the presence of correlated variability, (iii) a discrete cross-correlation function (DCCF; Section 5.4.3). This is among the first times that GP regression is used in the field of blazar variability and it has shown to perform well. It is a viable approach to the problem of “fitting” discrete, unevenly sampled, blazar light curves and extracting relevant parameters.

The flare in PKS 1502+106 is a “clean”, isolated outburst clearly seen across observing frequencies. Our findings include cross-band delays (see Section 5.5 and Fig. 5.15), flare amplitudes (see Section 5.7.3 and Fig. 5.19), and flare time scales (see Section 5.7.3 along with Fig. 5.20 and 5.21). The aforementioned light curve parameters show a characteristic dependence on frequency that can be approximated by a power law.

The flare amplitude follows an increasing trend—up to the frequency of 43 GHz where it peaks—after which a decreasing trend follows (Fig. 5.19). The second attribute is the delay with which the flare peaks. This is characterized by increasing time delay towards lower frequencies (Fig. 5.15). The flare rising time is increasing with frequency and after the peak flux density is reached the flare decays with a time scale that appears discrepant using our two methods (Fig. 5.20 and 5.21).

Through the observed opacity-driven time lags the structure of PKS 1502+106 in terms of synchrotron opacity is deduced—i.e. using a “time-lag core-shift” method (see Table 5.7). The positions of the 10 radio unit-opacity surfaces at all frequencies with respect to the vertex of an assumed-conical jet were deduced, with distances in the range  $\sim 10.0$  to  $\sim 3$  pc. These frequency-dependent core positions allow for the calculation of the equipartition magnetic field values along the jet, at the position of each core,  $B_{\text{core}}$ , and also at a distance of 1 pc from the jet base,  $B_{1\text{ pc}}$  (see Table 5.8). The former, between the frequencies of 2.64 and 86.24 GHz are found to be in the range between  $B_{\text{core } 2.64} \sim 3$  mG and  $B_{\text{core } 86.24} \sim 16$  mG. For the latter, our figures indicate an average value of  $\langle B_{1\text{ pc}} \rangle = 33 \pm 4$  mG.

In combination with the findings of Fuhrmann et al. [2014] the location of the  $\gamma$ -ray emission region is constrained. It is located at approximately 2 pc away from the jet base, well beyond the bulk of BLR material of PKS 1502+106. This yields a contribution of IR torus photons and/or SSC to the production of  $\gamma$  rays in PKS 1502+106

Finally, we compare our findings (slopes of the frequency-dependent light curve parameters) with the expectations of the shock-in-jet model through the analytical simulations of Fromm et al. [2014]. The flare appears to comply with the typical evolution and its overall behavior in the time domain is in accord with the shock-in-jet scenario. We constrain the indices governing the evolution

of physical parameters along the jet  $d$  for the Doppler factor,  $b$  for the magnetic field, and  $s$  for the electron energy distribution (see 5.7.1) in the ranges  $-0.30 \lesssim d \lesssim -0.15$  with most probable value towards the lower end of this range. In any case, from the good constraints on  $d$ , it follows that the jet is most probably accelerating with the Doppler factor increasing as we move along the jet. This is in agreement with the conclusions of the VLBI kinematical analysis. Parameters  $b$  and  $s$ , cannot be adequately constrained since they depend heavily on Doppler factor.

Forthcoming comparison in the frequency domain and extraction of the slopes during the flare evolutionary path in the  $v_{\max}$ - $S_{\max}$  plane, will shed more light on the physical conditions of the shock and its evolution with distance within the jet flow.

When seen in light of the VLBI findings discussed in Chapter 4, the results of this chapter corroborate the scenario that there exists a certain amount of acceleration within the relativistic outflow and that the flare of PKS 1502+106 was induced by a shock, seen at high-frequency VLBI images as component C3 traveling downstream the core at 43/86 GHz maps. This traveling disturbance is associated with the multi-frequency flare seen from radio up to  $\gamma$ -ray energies.



THE VIEWING ANGLE TOWARDS THE RADIO- AND  
GAMMA-RAY-LOUD NARROW-LINE SEYFERT 1 GALAXY  
1H 0323+342

---

## 6.1 INTRODUCTION

*Narrow-line Seyfert 1* galaxies (NLS1) are a distinct sub-class of AGN (see Chapter 1 for a short introduction to AGN classification). Recently, the discovery of a new population of few radio- and  $\gamma$ -ray-loud NLS1 rendered them the third  $\gamma$ -ray emitting AGN class on top of radiogalaxies and blazars [Abdo et al., 2009a]. In the wake of this discovery our understanding of jet launching, physical conditions, and hosts of relativistic jets is put to the test. NLS1 galaxies through their physical characteristics extend the parameter space for the study of extragalactic jets to the lower mass–higher mass accretion rate regime. One of them is even thought of being harbored in a spiral galaxy, adding to the handful of spirals featuring such jets, with 0313–192 being the first [Ledlow et al., 1998, 2001] and J1649+2635 the latest addition [Mao et al., 2015] to this short list of sources.

Classification of NLS1 is based upon their optical emission line spectra. Their spectra feature hydrogen Balmer lines narrower than the rest of the Seyfert 1 class—i.e. their broad emission lines are narrower. Defining criteria for the classification as NLS1 are [Osterbrock and Pogge, 1985; Goodrich, 1989]:

1. An optical spectrum with  $H\beta$  line width  $\text{FWHM}(H\beta) \leq 2000 \text{ km s}^{-1}$ ,
2. low line-intensity ratio of  $[\text{OIII}] \lambda 5007 / (H\beta) < 3$ —i.e. weak forbidden lines, and
3. sometimes presence of strong FeII emission lines.

NLS1 galaxies are usually radio-quiet (we will return to this soon) with SMBH masses in the range  $10^6$ – $10^8 M_{\odot}$ , accretion luminosities  $\sim 0.01$ – $0.49 L_{\text{Edd}}$  and jet powers  $\sim 10^{42.6}$ – $10^{45.6} \text{ erg s}^{-1}$  [Foschini et al., 2015, see also Komossa [2008] and Pogge [2000] for reviews].

### 6.1.1 Radio-loud NLS1 galaxies

Only a small fraction of AGN are radio-loud, with index  $R > 10$  (see Section 1.5 for the definition). The exact causes for this dichotomy are not yet clear but the fact is that only 15–20% of all AGN are radio-loud [see Urry and Padovani, 1995, and references therein].

During early efforts of studying their radio properties, NLS1s appeared to largely belong to the prevalent species of radio-quiet AGN [Ulvestad et al., 1995; Moran, 2000]. There were only a few exceptions to what seemed to be the rule [Remillard et al., 1986; Grupe, 2000; Zhou et al., 2003].

New surveys have increased the number of sources with  $R > 10$  thus giving birth to the new breed of *radio-loud NLS1* (RLNLS1). In a systematic search for

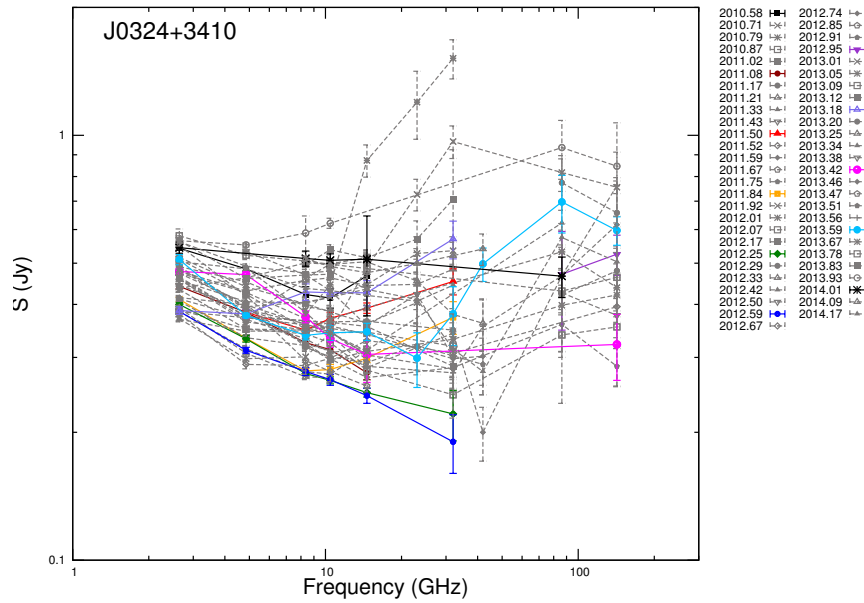


Figure 6.1: Radio SED of 1H 0323+342. Data points are connected with line segments to facilitate visual inspection. For the same reason one spectrum every five is colored. The legend shows the observation date of the quasi-simultaneous SED in the form of fractional year.

strong radio signatures from NLS1s, Komossa et al. [2006] studied a sample of 128 sources concluding that:

- about 7% of NLS1 galaxies are radio loud with  $R > 10$ ,
- only 2.5% exceed a radio-loudness index of  $R > 100$ ,
- the majority of RLNLS1 show compact steep-spectrum (CSS) characteristics both morphologically and spectrally, and
- their black-hole masses are generally higher than their radio-quiet counterparts (RQNLS1s) while RLNLS1 accrete close to or above the Eddington mass accretion limit,  $\dot{M}_{\text{Edd}}$  (see Section 1.7.3).

The entire population of RLNLS1 can be divided into two sub-classes, those resembling steep-spectrum radio sources and those characterized by flat or inverted spectra, intense variability and possibly relativistic Doppler boosting—i.e. blazar-like attributes [Yuan et al., 2008]. In Fig. 6.1 and Fig. 6.2 the radio SED and light curve of 1H 0323+342 are shown, respectively. This source is a good example of a RLNLS1 exhibiting blazar-like behavior.

### 6.1.2 Radio- and $\gamma$ -ray-loud NLS1 galaxies

Detection of J0948+0022 as the first RLNLS1 at MeV/GeV energies by *Fermi*/LAT was a turning point providing more insights into these intriguing objects and clear evidence that they can produce and sustain relativistic jets [Abdo et al., 2009a; Foschini et al., 2010]. In its first year of science operations *Fermi* detected four  $\gamma$ -ray emitting NLS1 [Abdo et al., 2009c] while as of today a total number

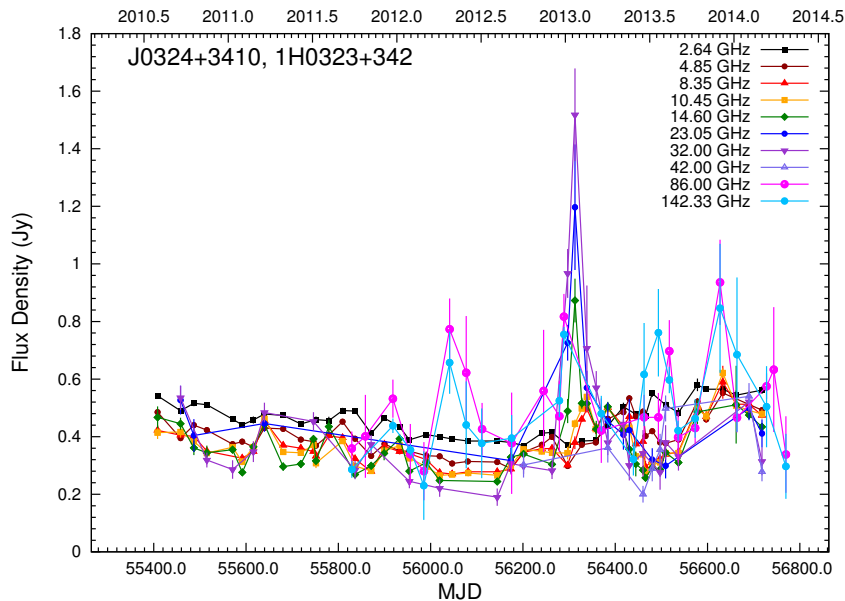


Figure 6.2: Radio light curves of 1H0323+342 at all frequency bands employed by the F-GAMMA monitoring program.

of seven are known to be emitting at MeV/GeV energies (see Table 6.1 and references therein). These sources with their observed spectral energy distributions sufficiently extending towards  $\gamma$ -ray energies have revealed even more dramatically their resemblance to powerful beamed blazars (see Fig. 6.3).

Subsequent multi-wavelength monitoring campaigns undertaken ever since have revealed the complex nature of these objects and lent ground to the scenario that these sources feature relativistic jets viewed at moderate angles to the observer’s line of sight [e.g. [Abdo et al., 2009b](#); [Foschini et al., 2011](#); [Giroletti et al., 2011](#); [Fuhrmann et al., 2011](#); [D’Ammando et al., 2014, 2015](#)].

[Angelakis et al. \[2015\]](#) have presented the most recent systematic study of  $\gamma$ -ray-emitting RLNLS1 galaxies at radio bands between 2.64–143.22 GHz under the auspices of the F-GAMMA monitoring program (see Section 5.2). Based on observations of a sample of four radio- and  $\gamma$ -loud NLS1s spanning a time period of more than five years, they conclude that their phenomenology in the time and frequency domain is consistent with that of blazars, namely spectral evolution and rapid variability. However, reported flux densities and variability amplitudes of individual flaring events appear smaller than those of powerful blazars. Spectral evolution could hint towards the presence of evolving shocks within the flow of an underlying steady-state radio jet. As an example, the F-GAMMA radio light curves of 1H0323+342 seen in Fig. 6.2 and spectra in Fig. 6.1 show intense variability and spectral evolution reminiscent of evolving internal shocks. Additionally, the steep and steady appearance of the spectrum towards lower frequencies is indicative of the presence of a quiescent-state jet which also justifies the estimates of the jet power (see Table 6.1). The mean spectral index between 2.64–8.35 GHz is  $-0.21$  [[Angelakis et al., 2015](#)]; i.e. flat (on average) as expected for blazar-type objects.

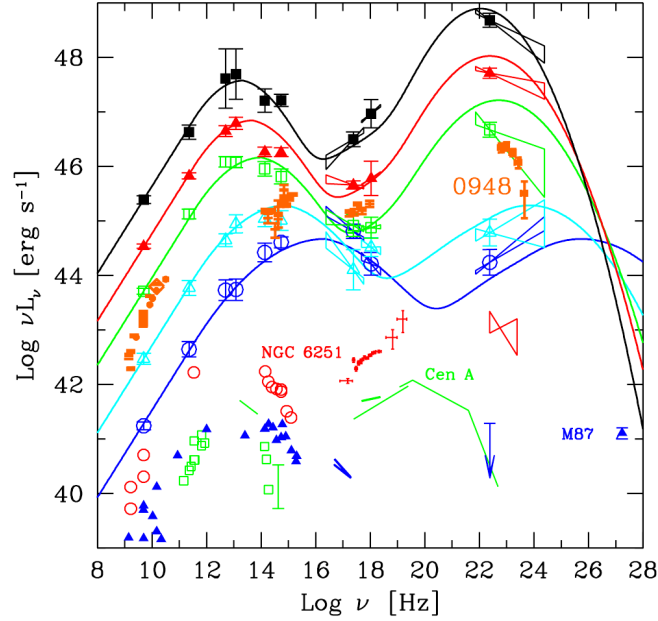


Figure 6.3: Spectral energy distributions of AGN and of the  $\gamma$ -loud RLNLS1 J0948+0022 (orange data points without fit). Blazar SEDs are shown in colored points along with their respective best-fit SED models. Starting from top (black line) to bottom (blue), one moves from FSRQs to BL Lacs along the “blazar sequence”. Also shown for comparison are SEDs of the radio galaxies NGC 6251, Centaurus A, and M87. Image from Foschini et al. [2010].

SOURCE	$z$	$P_{\text{jet,rad}}^{\dagger}$ ( $\text{erg s}^{-1}$ )	$P_{\text{jet,kin}}^{\dagger}$ ( $\text{erg s}^{-1}$ )	$P_{\text{jet,tot}}^{\dagger}$ ( $\text{erg s}^{-1}$ )	$M_{\text{BH}}^{\ddagger}$ ( $\times 10^7 M_{\odot}$ )
J0324+3410	0.061	$1.7 \times 10^{43}$	$3.0 \times 10^{43}$	$4.7 \times 10^{43}$	3.6
J0849+5108	0.584	$6.6 \times 10^{44}$	$2.5 \times 10^{45}$	$3.1 \times 10^{45}$	3.2
J0948+0022	0.585	$7.9 \times 10^{44}$	$3.0 \times 10^{45}$	$3.7 \times 10^{45}$	7.5
J1102+2239	0.453	...	...	...	11.5
J1246+0238	0.363	...	...	...	5.9
J1505+0326	0.409	$5.0 \times 10^{44}$	$1.7 \times 10^{45}$	$5.0 \times 10^{45}$	1.9
J2007–4434	0.240	...	...	...	0.43

Table 6.1: The seven  $\gamma$ -ray-detected RLNLS1 galaxies and their physical characteristics. Columns from left to right: (1) source name under the J2000 designation; (2) redshift; (3) radiative, (4) kinetic, and (5) total jet powers; and finally (6) estimated mass of their SMBH.

References:  $^{\dagger}$ Angelakis et al. [2015];  $^{\ddagger}$ Foschini et al. [2015]

## 6.2 WHY ARE NLS1 GALAXIES INTERESTING AFTER ALL?

In summary, this new and distinct class of  $\gamma$ -ray emitting AGN (besides blazars and radiogalaxies) are interesting for a number of reasons. Among other:

- They extend the study of relativistic jet formation and propagation towards the lower end of the distributions of black hole masses and jet powers (see e.g. Table 6.1).
- They present a population well-suited for discussing and comparing analogies and differences to traditional high-powered blazars.
- Exhibiting small BH masses but high mass accretion rates, close to the Eddington limit, they could corroborate the hypothesis that the FR I–FR II division originates in differences of accretion rate with respect to the Eddington limit and not its absolute values.
- Properties of relativistic jets are intimately connected to the accretion flow fueling them. Parameters such as the magnetic field threading the SMBH, its spin, and accretion rate tune the launching and subsequent acceleration mechanisms, ultimately leading to powerful jets or not. In the extragalactic realm the dichotomy between FR I–FR II objects and their beamed counterparts—BL Lacs and FSRQs, respectively—may originate here. In the case of FR Is a sub-Eddington mass accretion rate could lead to radiatively inefficient accretion flows, thus giving rise to weaker jets. On the other hand, FR IIs could be explained through accretion rates close to the Eddington limit resulting in bright disks and powerful jets [Ghisellini and Celotti, 2001]. As such, through the study of their jets, NLS1s can shed some light on the properties of their accretion flows.
- Finally, the observationally well-documented but not yet confirmed possibility that 1H 0323+342 is hosted by a one-armed spiral or ring-shaped galaxy (see Sect. 6.3 and references therein) questions the usual notion that ellipticals are much more likely to host relativistic jets.

Putative blazar-like characteristics of NLS1 make the determination of the prime unification parameter, the viewing angle towards these accretion-powered systems, an observable of uttermost importance. The present study is among the first to address this issue for NLS1s, using VLBI and single-dish radio monitoring data. In the following, VLBI images at 15 GHz from the MOJAVE monitoring program [Lister et al., 2009] in combination with the findings of Angelakis et al. [2015] from the F-GAMMA monitoring, allow for the calculation of the viewing angle towards a prime radio- and  $\gamma$ -ray-loud NLS1 example, namely 1H 0323+342.

## 6.3 THE SOURCE: 1H 0323+342 (A.K.A. J0324+3410)

At redshift  $z = 0.061$  [Marcha et al., 1996] 1H 0323+342 is the closest of the seven  $\gamma$ -ray emitting RLNLS1 posing a curious case due to the morphological characteristic of its galactic host. Deep imaging using the *Hubble Space Telescope*

(HST) suggests that the host is a one-arm spiral [Zhou et al., 2007], while ground-based observations with the Nordic Optical Telescope (NOT) point towards a ring-like host, possible remnant of a previous galaxy-galaxy merging episode [Antón et al., 2008]. In any case, the unusual non-elliptical morphology of the host challenges the paradigm under which relativistic jets are more prevalent among giant elliptical galaxies [Ho, 2002; Sikora et al., 2007].

The mass of its central black hole is estimated to be  $3.6 \times 10^7 M_{\odot}$  [Foschini et al., 2015] a figure in accordance to the mass estimate from SED modeling of  $10^7 M_{\odot}$  [Abdo et al., 2009c, see Table 6.1].

Estimates of the accretion disk luminosity are also obtained from Abdo et al. [2009c] with  $L_{\text{disk}} = 1.4 \times 10^{45} \text{ erg s}^{-1}$  translating into  $0.9 L_{\text{Edd}}$ , a value not unheard-of for NLS1s. What is remarkable about 1H 0323+342 is its extreme radio loudness with index  $R = 318$  [Foschini, 2011], a signature of its relativistic-jet activity.

Angelakis et al. [2015] discuss also the polarization characteristics of the source both at radio and in the R optical band. At 4.85 GHz they report 7% and at 8.35 GHz, 6% of fractional linear polarization, with electric vector position angles (EVPA) of  $\sim 44^{\circ}$  and  $\sim 36^{\circ}$  at these frequency bands, respectively. These values are significantly higher than average values of radio linear polarization observed in AGN. In the R band it shows a low level of fractional linear polarization that does not exceed  $\sim 3\%$ .

Within the timespan of the F-GAMMA observations the source has undergone significant radio variability at all bands. The variability amplitudes are moderate but the frequency of outbursts seen across observing frequencies is very high. Through the characteristics of these flares, namely their amplitudes and time scales, Angelakis et al. [2015] estimate variability Doppler factors for the source (see Section 6.9.2). A visual inspection of the total-intensity F-GAMMA light curves in Fig. 6.2 is indicative of this fast variability.

Finally, at the highest TeV energies a  $2.5\sigma$  marginal detection using the Whipple 10 m imaging air Cerenkov  $\gamma$ -ray telescope is reported in Falcone et al. [2004].

Due to its proximity 1H 0323+342 is an ideal—and possibly only—candidate for detailed studies of radio- and  $\gamma$ -ray-loud NLS1 galaxies. Exploiting VLBI data at 15 GHz we are able to shed some light onto this intriguing source.

At a redshift  $z = 0.061$  an angular separation of 1 mas corresponds to 1.16 pc and a proper motion of  $1 \text{ mas yr}^{-1}$  translates into an apparent velocity  $\beta_{\text{app}} = 4.01$ , with  $\beta_{\text{app}}$  defined as the apparent velocity in units of the speed of light,  $\beta_{\text{app}} = v_{\text{app}}/c$ . The luminosity distance of 1H 0323+342 is  $D_L$  is 269.9 Mpc.

#### 6.4 VLBI OBSERVATIONS AND DATA REDUCTION

1H 0323+342 was regularly monitored by the Monitoring Of Jets in Active galactic nuclei with VLBA Experiments (MOJAVE<sup>1</sup>) program at 15 GHz [Lister et al., 2009] until their sample revision, with the new sample including only sources of the Second Catalog of Active Galactic Nuclei Detected by the *Fermi*/LAT [2LAC; Ackermann et al., 2011] with a spectral index harder than 2.1. In any case a total number of eight observing epochs are available spanning the time period be-

<sup>1</sup> <http://www.physics.purdue.edu/MOJAVE/>

OBS. DATE	ARRAY	$S_{\text{peak}}$ (Jy beam $^{-1}$ )	RMS (mJy beam $^{-1}$ )	$S_{\text{total}}$ (Jy)	$b_{\text{maj}}$ (mas)	$b_{\text{min}}$ (mas)	PA ( $^{\circ}$ )
2010-10-15	VLBA $_{10}$	0.216	0.35	0.308	0.745	0.432	-3.7
2011-03-05	VLBA $_{10}$	0.344	0.39	0.414	0.707	0.584	-13.2
2011-05-26	VLBA $_{10}$	0.264	0.40	0.342	0.714	0.437	-9.8
2011-07-15	VLBA $_{10}$	0.222	0.40	0.295	0.761	0.450	-8.1
2011-12-29	VLBA $_{10}$	0.314	0.43	0.378	0.710	0.495	2.6
2012-07-12	VLBA $_{10}$	0.191	0.39	0.237	0.822	0.429	-18.5
2012-12-23	VLBA $_{10}$	0.206	0.43	0.205	0.918	0.540	14.7
2013-07-08	VLBA $_{10}$	0.145	0.26	0.220	0.704	0.431	-11.6

Table 6.2: Summary of the 8 observing epochs at 15 GHz of 1H 0323+342 obtained within the MOJAVE monitoring program. Columns from left to right: (1) date of observation; (2) array elements; (3) peak flux density; (4) RMS noise level; (5) total flux density of components in the MODELFIT image; (6) major and (7) minor axes along with the (8) position angle of the restoring beam. All parameters listed in the table correspond to the final, untapered, uniform-weighted MODELFIT image. VLBA $_{10}$  station designations: BR – Brewster; FD – Fort Davis; HN – Hancock; KP – Kitt Peak; LA – Los Alamos; MK – Mauna Kea; NL – North Liberty; OV – Owens Valley; PT – Pie Town; SC – St. Croix.

tween 2010 October 15 until 2013 June 8. A summary of the VLBI observations is presented in Table 6.2.

Data are in the form of fully self-calibrated interferometric visibilities and the necessary steps of imaging and model fitting were performed within the DIFMAP package [Shepherd, 1997; Shepherd et al., 1994]. There, the brightness distribution of the source is modeled by two-dimensional Gaussian functions utilizing a least-squares fitting method. For details on the specifics of the method see Section 3.2.4 where also MODELFIT parameter uncertainties are discussed. MODELFIT results are shown in Table C.1.

## 6.5 PARSEC-SCALE JET MORPHOLOGY

Fig. 6.4 shows the final MODELFIT maps of 1H 0323+342 at 15 GHz. The source is characterized by a one-sided jet that appears remarkably straight laying at a mean position angle of  $\sim 124^{\circ}$  (see Fig. 6.5) and extends out to almost 10 mas from its bright, unresolved core.

It can also be seen in the VLBI maps, that the jet of 1H 0323+342 is not undisrupted all the way until its maximum angular extent. Further downstream from the core, at a distance variable with time, the jet exhibits a gap of emission. On average this gap is visible between 3–6 mas away from the core at the PA of the jet, whereafter the flow becomes visible again.

At our observing frequency the jet can be decomposed into 6 to 9 MODELFIT components with a number of 7 being used more frequently in order to describe its structural dynamics. Based on the parameters of the model and their temporal evolution we are able to positively cross-identify 7 components between all eight observing epochs. Starting from the outermost one—in terms of radial sep-

aration from the core—the letter C is used, followed by a number between 1 and 6 to designate and hereafter refer to them. Apart from traveling components, our findings suggest the presence of a quasi-stationary component, referred to with the letter S, positioned very close to the core at a mean distance of  $\sim 0.3$  mas. Furthermore, at epoch 2013.52 a new component emerges, most probably ejected at some time between the latest two observing epochs; i.e. between 2012.98 and 2013.52 (see Sect. 6.7). We refer to this knot as NC which stands for new component (cf. VLBI maps in Fig. 6.4).

## 6.6 RADIO FLUX DENSITY DECOMPOSITION

As can be seen in Fig. 6.6 the main flaring component at 15 GHz, according to our VLBI findings, appears to be the core with all other jet components within the jet of 1H 0323+342 sharing a low and largely constant flux density level. Comparison between the F-GAMMA filled-aperture light curve at 15 GHz and the VLBI total flux density of all components indicates that VLBI flux densities account for most of the single-dish flux density, a hint that extended structure—for VLBI scales—does not contribute a significant flux density level. It, in fact, hints that the total intensity flares originate in the unresolved 15 GHz core region of the source, since the core flux accounts for most of the observed VLBI flux density and also due to the fact that other components show non-significant temporal flux density variations.

## 6.7 SOURCE KINEMATICS

The kinematical parameters for each knot are obtained through a weighted linear regression fit of their positions relative to the core with respect to time. In Fig. 6.7 each component's radial separation from the core at each observing epoch is shown, along with the linear fits, from the slope of which we deduce their velocity relative to the core. Making use of Eq. 4-1 once more, we obtain the apparent velocities of components in units of speed of light ( $c$ ).

As it is readily seen from the slopes in Fig. 6.7 the jet is characterized by three  $\beta_{\text{app}}$  regimes. In the region closest to the core, containing the quasi-stationary feature, S, and component C6, the apparent velocities are very low in comparison to other superluminal sources. For S it is  $\beta_{\text{app}} \simeq 0.1$ , while for C6 the apparent velocity is  $0.93 c$ .

Further outwards, beyond the first mas where the jet is still visible, but before the area void of radio emission,  $\beta_{\text{app}}$  shows an increasing trend. There, superluminal knots C5 and C4 travel with apparent velocities of  $\sim 4 c$  and  $\sim 7 c$ , respectively. Superluminal knot C4 is the fastest moving component in the relativistic flow of 1H 0323+342.

After the gap of emission when the jet becomes visible again, the flow is again characterized by slower speeds. Components C3, C2 and C1 are used to describe the elongated area of emission extending out to a radial distance between 6–10 mas away from the core. Their speeds are superluminal, only slightly slower than in the jet area before the gap, with  $\beta_{\text{app},C3} \simeq 1.6$ ,  $\beta_{\text{app},C2} \simeq 3$ , and  $\beta_{\text{app},C1} \simeq 4$ .



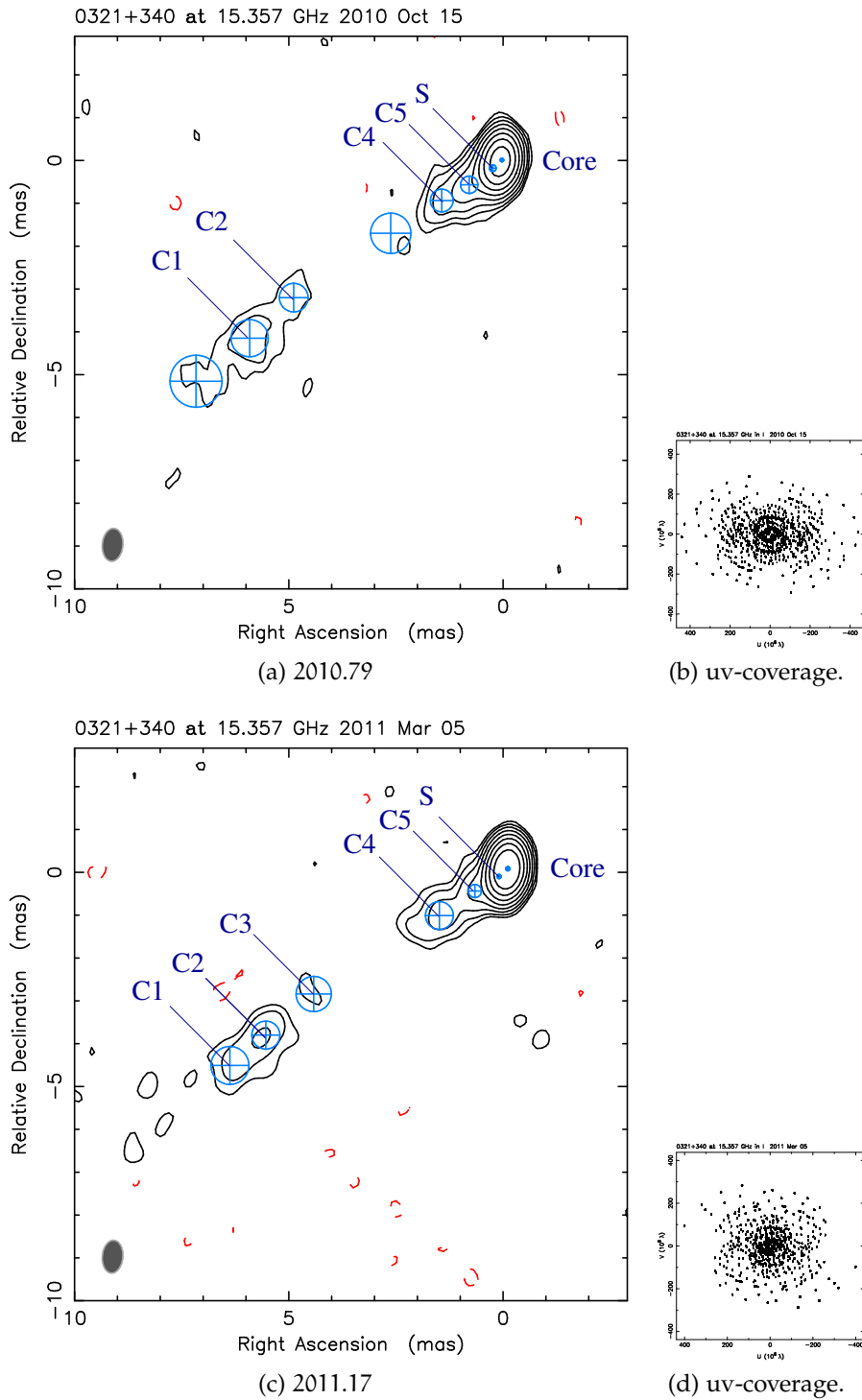


Figure 6.4: Uniform-weighted MODELFIT maps of 1H0323+342 at 15 GHz from the VLBA. Contour levels correspond to  $-0.3\%$ ,  $0.3\%$ ,  $0.6\%$ ,  $1.2\%$ ,  $2.4\%$ ,  $4.8\%$ ,  $9.6\%$ ,  $19.2\%$ , and  $38.4\%$  of the highest peak flux density of  $0.344$  Jy/beam (epoch 2011.17) as a common reference. All maps are convolved with an average beam with major and minor axes of  $0.768$  and  $0.481$  mas, respectively with the major axis at a PA of  $-5^\circ$ . Also shown, is the coverage for the uv-plane associated to the observation.

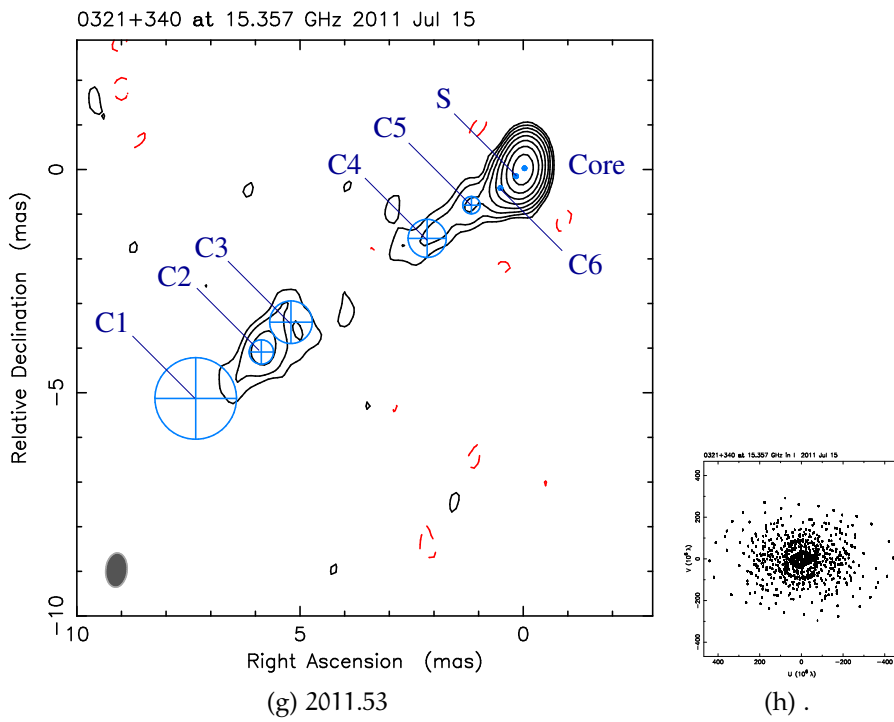
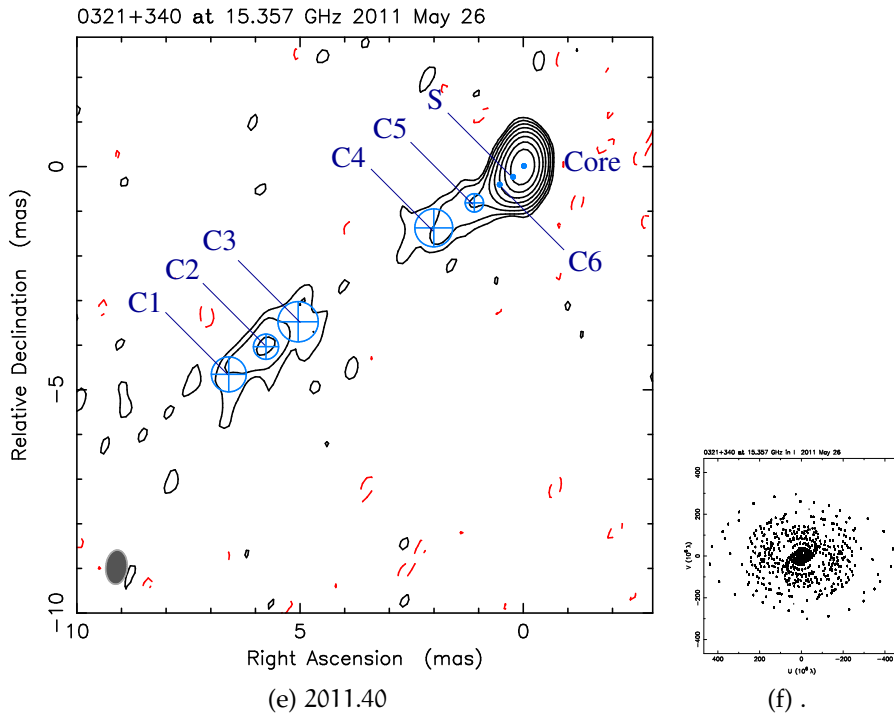


Figure 6.4: continued.

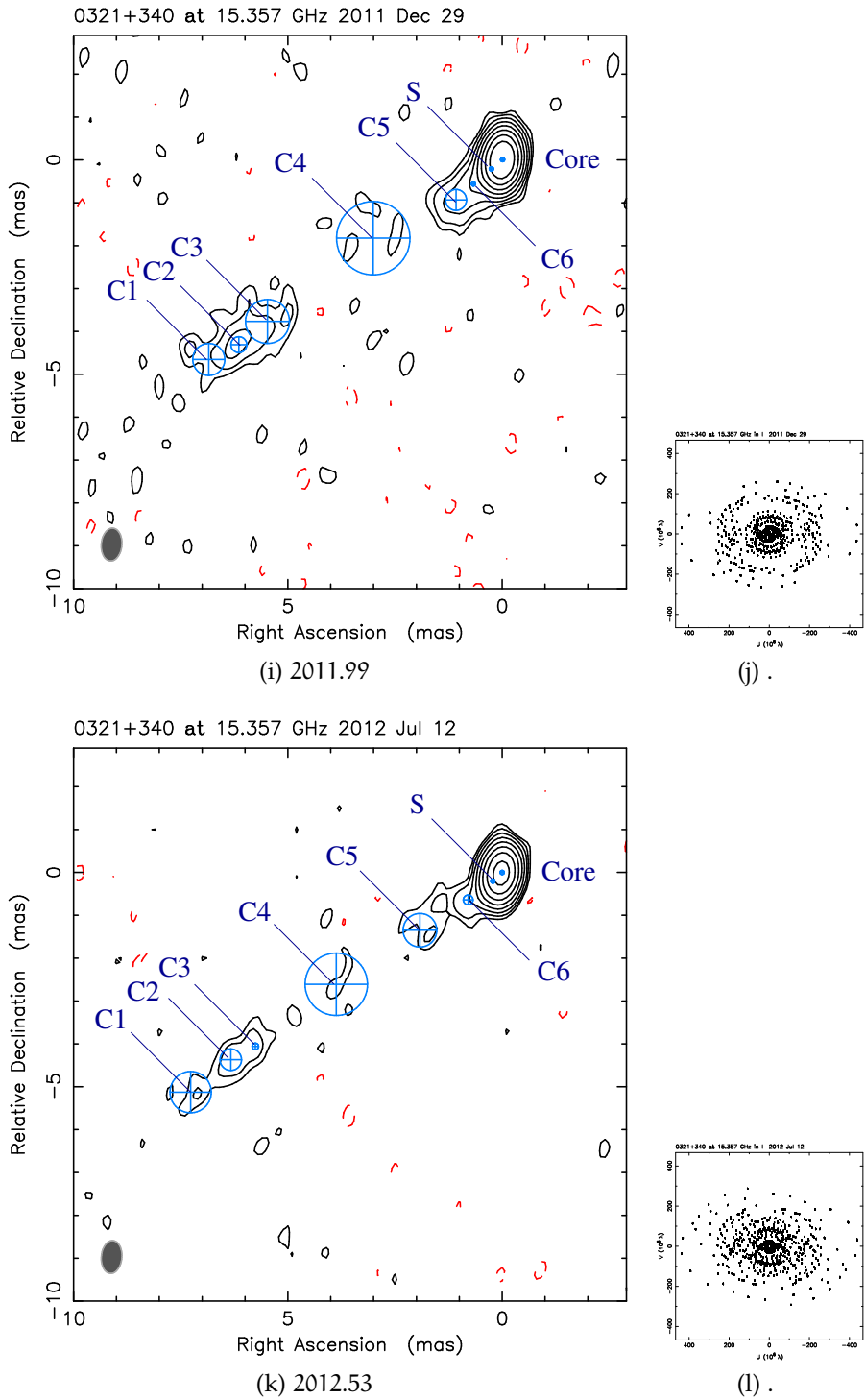


Figure 6.4: continued.

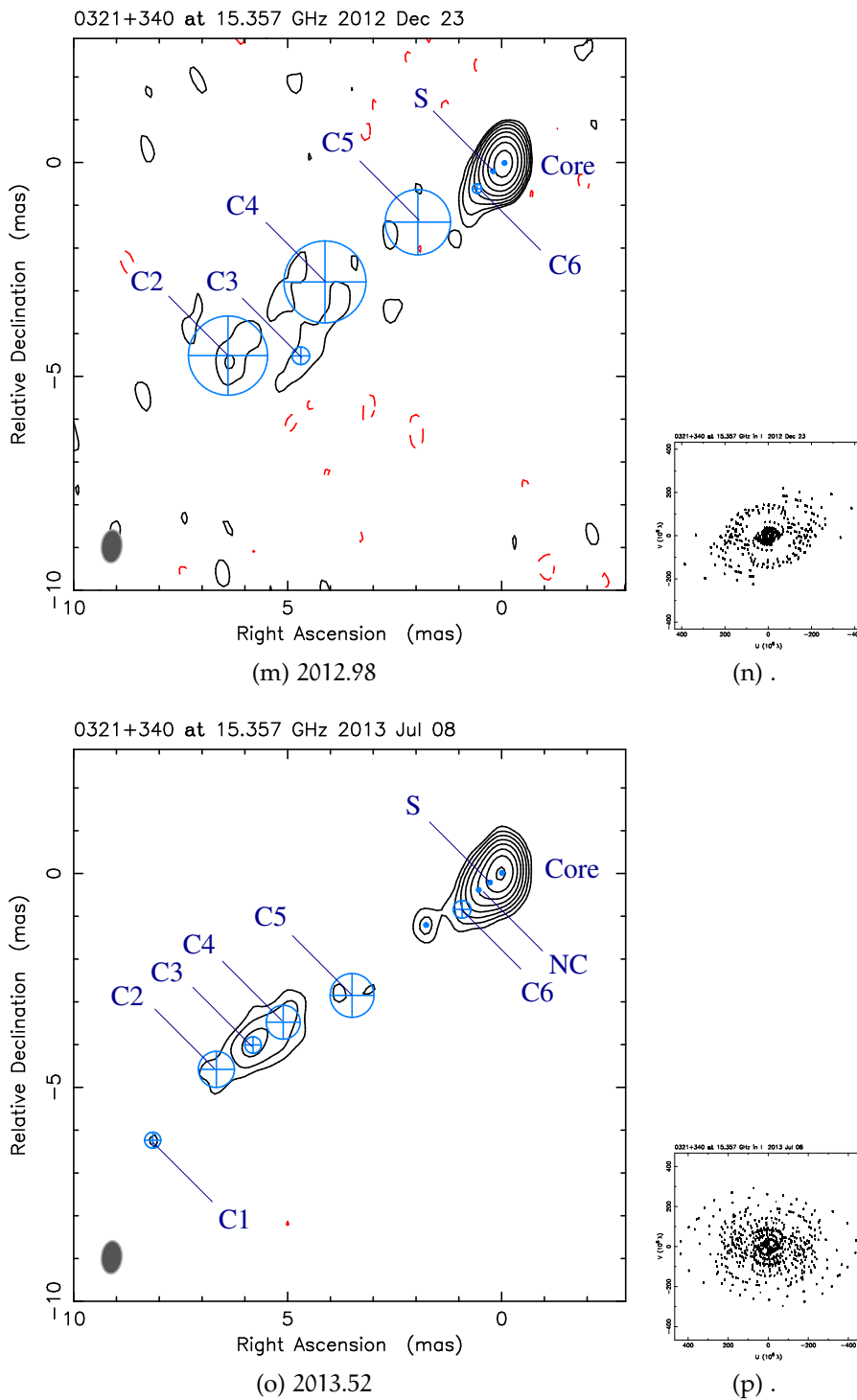


Figure 6.4: continued.

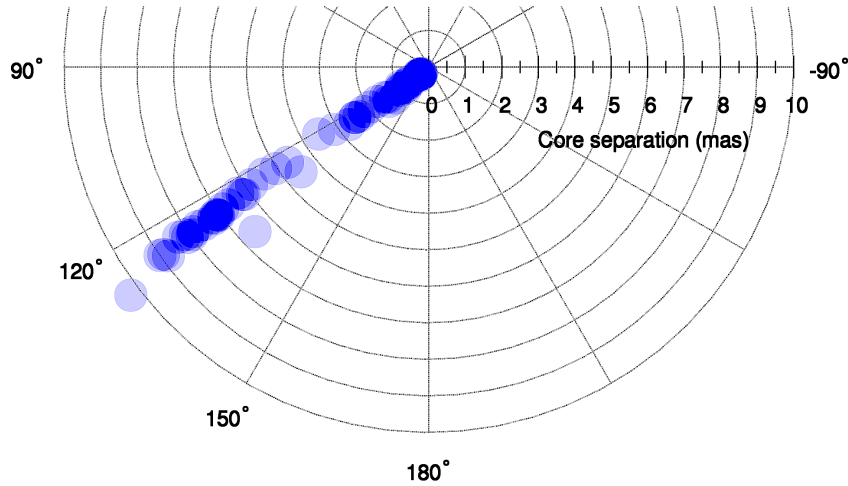


Figure 6.5: Position angle (PA) of all fitted components at all epochs. The jet axis remains strikingly stable at a mean PA of  $\sim 124^\circ$  over  $\sim 3$  yr. Here, only the southernmost region of the plane is shown with  $0^\circ$  to the North (not shown).

Additionally, ejection times of knots are deduced by back-extrapolation to the time of zero separation from the core and are given in the last column of Table 6.3. The source appears very active in this respect showing an ejection of a new VLBI component every  $\sim 2.6$  years on average. Due to the limited time baseline of the single-dish observations, we are unable to establish a one-to-one correspondence between component ejection times and total intensity flares. This becomes clearer from the estimated ejection times of components reported in Table 6.3, none of which appears to have separated from the core within the time baseline of our filled-aperture radio monitoring. The only exception appears to be a new jet component (referred to as NC) only seen to be present in the data of the last epoch (2013.52, see Fig. 6.7). Given the flaring activity preceding its separation from the core, this knot could be tentatively associated with the highest-peaking flare seen in the single-dish data (Fig. 6.2) at epoch  $\sim 2013.1$ . Its integrated flux density at this epoch is  $\sim 19$  mJy (see Table C.1).

Results of the VLBI kinematic study are summarized in Table 6.3.

## 6.8 JET-TO-COUNTER-JET RATIO

Despite the fact that there is no sign of emission from the counter-jet side of the source (see VLBI maps in Fig. 6.4), we have nonetheless tried to constrain its non-observability as much as possible. First, the VLBI map with the best signal-to-noise ratio was selected. Using the CLEAN algorithm [Högbom, 1974] and by utilizing CLEAN windows to constrain the area where the algorithm searches for peaks, we have tried to place delta components at the opposite side of the jet in an effort to “artificially create” a fake counter-jet. Mostly positive and negative components with no significant flux (below the noise level of the map) were fitted in this area of the image—if at all—as expected. Another test was performed using the MODELFIT algorithm this time by attempting to fit the phase-only self-calibrated visibilities with circular Gaussian components. The results were negative in this case too, with no significant components laying on the opposite side of the jet.

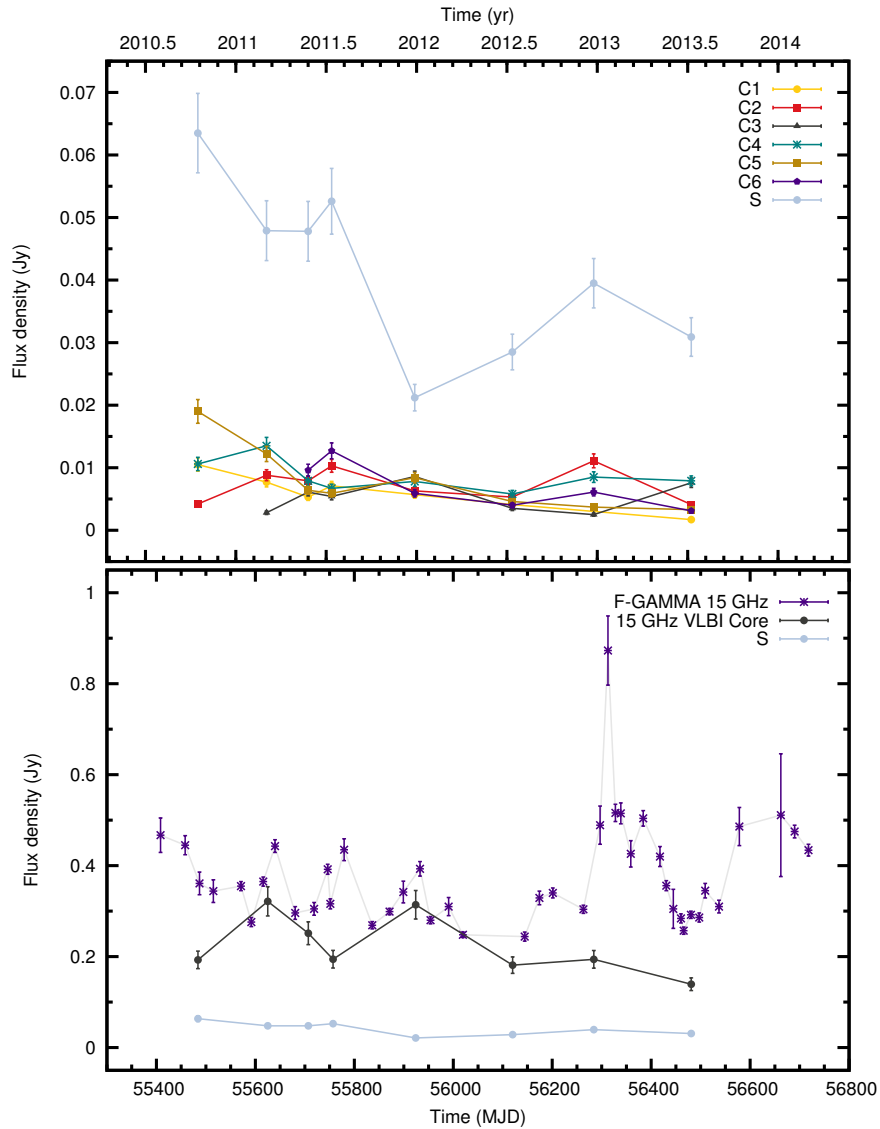


Figure 6.6: Light curves of all VLBI components. Bottom panel also shows the total intensity single-dish light curve at 15 GHz obtained within F-GAMMA. Note the different flux density scales. Light curve of the quasi-stationary component, S, is plotted in both plot for visual comparison of the different flux density scales. Note the fast variability pattern of 1H 0323+342 and the low-frequency of VLBI sampling compared to it.

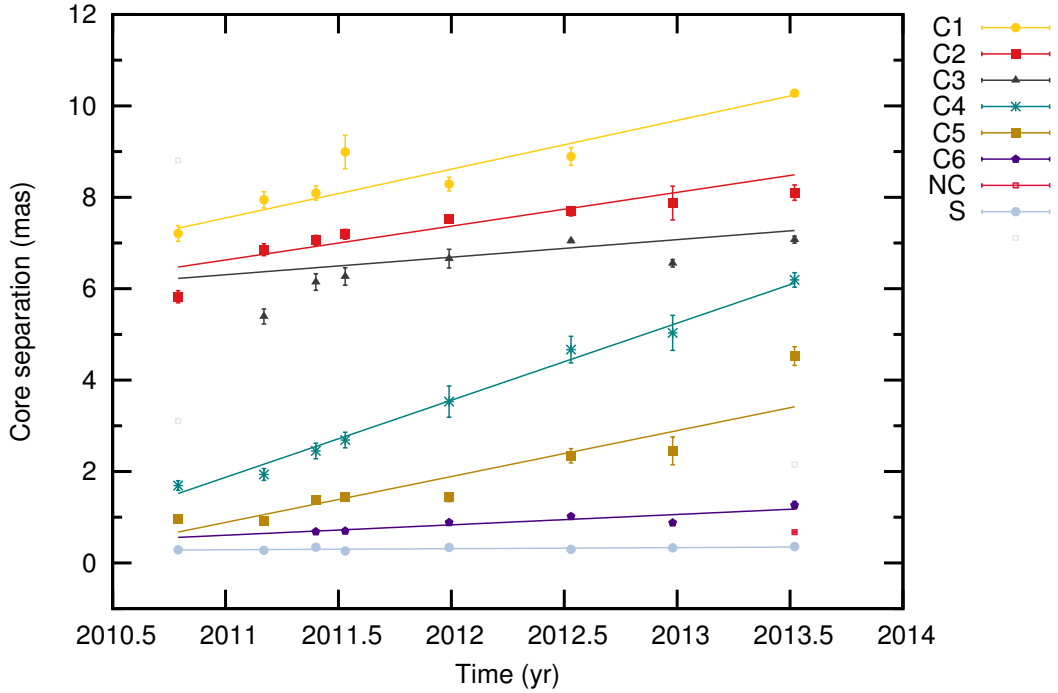


Figure 6.7: Temporal evolution of fitted component separation from the core. Line segments represent the best-fit linear model describing each knot’s kinematical behavior. Apart from robustly identified knots (C#), open squares denote non-robust features. The new component (NC), visible in the latest epoch only, is shown as a red square right after the quasi-stationary feature S.

KNOT	$\mu$ (mas y <sup>-1</sup> )	$\beta_{\text{app}}$ (c)	$t_{\text{ej}}$ (yr)
C1	$1.07 \pm 0.09$	$4.38 \pm 0.35$	$2003.93 \pm 0.71$
C2	$0.74 \pm 0.15$	$3.03 \pm 0.63$	$2002.03 \pm 2.06$
C3	$0.38 \pm 0.26$	$1.58 \pm 1.06$	$1994.58 \pm 12.13$
C4	$1.69 \pm 0.07$	$6.92 \pm 0.29$	$2009.89 \pm 0.08$
C5	$1.00 \pm 0.20$	$4.12 \pm 0.82$	$2010.12 \pm 0.28$
C6	$0.23 \pm 0.06$	$0.93 \pm 0.24$	$2008.33 \pm 0.91$
S	$0.02 \pm 0.01$	$0.10 \pm 0.05$	$1998.68 \pm 7.64$

Table 6.3: Kinematical parameters of all VLBI components of 1H0323+342. Columns from left to right: (1) knot designation; (2) proper motion in mas y<sup>-1</sup>; (3) Apparent velocity in units of c; (4) time of zero core separation—i.e. time of component ejection.

Doppler boosting is responsible for the apparent enhancement of emission in extragalactic jets, while deboosting leads to the opposite effect; that is, suppression of emission from the counter-jet side of such sources. It is almost certain that boosting is responsible for the one-sidedness of—what are believed to be—intrinsically symmetric dipolar outflows, at least most times. Both flavors of the effect are consequences of the theory of special relativity and are closely connected to the viewing angle towards the source.

Estimation of the jet-to-counter-jet ratio,  $R$ , can yield important insights into the conditions of the jet, especially when combining VLBI and single-dish observations as we do in this study.  $R$  represents the ratio of flux densities of the approaching and receding jets and is given by [e.g. [Urry and Padovani, 1995](#)]

$$R = \frac{S_{\text{Jet}}}{S_{\text{cJet}}} = \left( \frac{1 + \beta \cos \theta}{1 - \beta \cos \theta} \right)^{2-\alpha} \quad (6-1)$$

where,  $\beta$  and  $\theta$  are the intrinsic speed and jet angle to the observer's line of sight. Exponent  $(2 - \alpha)$  refers to a continuous jet flow and can change to  $(3 - \alpha)$  for a blobby jet, with  $\alpha$  the spectral index of the optically thin part of the emission (see Section 1.7.2).

In the case of NLS1 galaxy 1H 0323+342 the total flux density of all components in the VLBA images is associated with the jet, while counter-jet emission is not detected—i.e. at the opposite direction of the core and to the North (see Fig 6.4). Under the assumption that Doppler de-boosting is responsible for the suppression of the counter-jet one can obtain a lower limit for the jet-to-counter-jet ratio  $R$ . For that, we use the VLBI map with the best signal-to-noise ratio; that is the highest peak flux density over the lowest rms error, on 2011 March 5. The  $3\sigma$  root mean square noise level in the MODELFIT map ( $\text{rms} = 0.38 \text{ mJy beam}^{-1}$ ) was taken as the upper limit for the counter-jet flux density level, since any counter-jet emission ought to be below this level. Then, through the expression

$$R = \frac{S_{\text{Jet}}}{S_{\text{cJet}}} = \frac{S_{\text{Jet}}}{S_{3\sigma}} \quad (6-2)$$

we estimate that  $R \geq 363.54$ .

### 6.8.1 A first lower limit for the Doppler factor

From the jet-to-counter-jet ratio,  $R$ , and the measured apparent jet speed,  $\beta_{\text{app}}$ , one can already get a lower limit of the Doppler factor  $\delta$  from expression [e.g. [Kadler et al., 2012](#)]

$$R = \left( \frac{1 + \beta \cos \theta}{1 - \beta \cos \theta} \right)^{2-\alpha} = \left( \beta_{\text{app}}^2 + \delta^2 \right)^{2-\alpha} \Rightarrow \delta = \sqrt{R^{\frac{1}{2-\alpha}} - \beta_{\text{app}}^2} \quad (6-3)$$

with  $\alpha$  being the spectral index defined as  $S \propto \nu^\alpha$ . Here we adopt  $\alpha = -0.04$  [[Angelakis et al., 2015](#)]. With the use of the aforementioned value for  $R$  and the measured fastest apparent velocity  $\beta_{\text{app}} = 6.9$ , we obtain an unphysical  $\delta$  ( $\delta \in \mathbb{I}$ , imaginary). This is due to the square root in the last part of Eq. 6-3 and



implies that in order to accommodate for this high measured apparent speed of component C4 a jet/counter-jet ratio  $R_{\text{req}} \geq 2646.0$  is required.  $R_{\text{req}}$  is the lower limit for  $R$  in order for the Doppler factor,  $\delta$ , to be real-valued. This high value of  $R$  is in line with the lesser constrained  $R \geq 363.54$  obtained directly from the map and implies that significant Doppler beaming is at play.

## 6.9 THE VIEWING ANGLE TOWARDS 1H 0323+342

### 6.9.1 Viewing angle using only VLBI data

A first estimate for the viewing angle towards the source can be obtained through the combination of the measured,  $R$ , and required,  $R_{\text{req}}$ , jet-to-counter-jet ratios under the assumption that the intrinsic speed of the component is close to the speed of light, i.e. letting  $\beta \rightarrow 1$ , through the following expression [e.g. [Kadler et al., 2012](#)]

$$\theta \leq \arccos \left( \frac{R^{\frac{1}{2-\alpha}} - 1}{R^{\frac{1}{2-\alpha}} + 1} \right) \beta^{-1}. \quad (6-4)$$

For  $R = 363.54$  one arrives to a viewing angle  $\theta \leq 26^\circ$  but the solution is rejected due to the unphysical Doppler factor it implies (see Section 6.8.1). For  $R_{\text{req}} = 2646.0$  the more stringent constraint limits the viewing angle to  $\theta \leq 16^\circ$ .

In Fig. 6.8 the parameter space for the intrinsic jet velocity,  $\beta$ , and viewing angle,  $\theta$ , as constrained through the jet/counter-jet ratio and the observed  $\beta_{\text{app}}$ . The most rigorous constraints are put by the highest observed  $\beta_{\text{app}} = 6.9$  (red shaded area) and the required jet-to-counter-jet ratio  $R_{\text{req}} = 2646.0$ . The limiting value of  $\theta \leq 16^\circ$  is visible. They also constrain the area of possible intrinsic flow speed to  $\beta \gtrsim 0.96$ , a number that indicates fast relativistic motion of the flow. Gray shaded areas, based on lower values of the two parameters, constrain the intrinsic parameters of the flow to a lesser extend—as expected. For example, the light gray shaded area corresponds to possible combinations of  $\beta$  and  $\theta$  based on the lowest observed  $\beta_{\text{app}} = 0.93$ .

Another way of constraining the viewing angle towards the source is the following. Having a measured value for  $\beta_{\text{app}}$  one can calculate the minimum Lorentz factor in order to have this apparent speed. This is

$$\gamma_{\text{min}} = \sqrt{\beta_{\text{app}}^2 + 1}. \quad (6-5)$$

Then using Eq. 6-5 under the assumption that this is the Lorentz factor characterizing the source, a lower limit for the viewing angle can be estimated through [e.g. [Urry and Padovani, 1995](#)]

$$\theta_{\text{crit}} = \arcsin \left( \frac{1}{\gamma_{\text{min}}} \right). \quad (6-6)$$

In this way and for  $\beta_{\text{app}} = 6.9$ , the minimum Lorentz factor is  $\gamma_{\text{min}} = 6.97$  and  $\theta_{\text{crit}} = 8.2^\circ$ . For a discussion on the limitations of the critical viewing angle see Section 4.5.3.

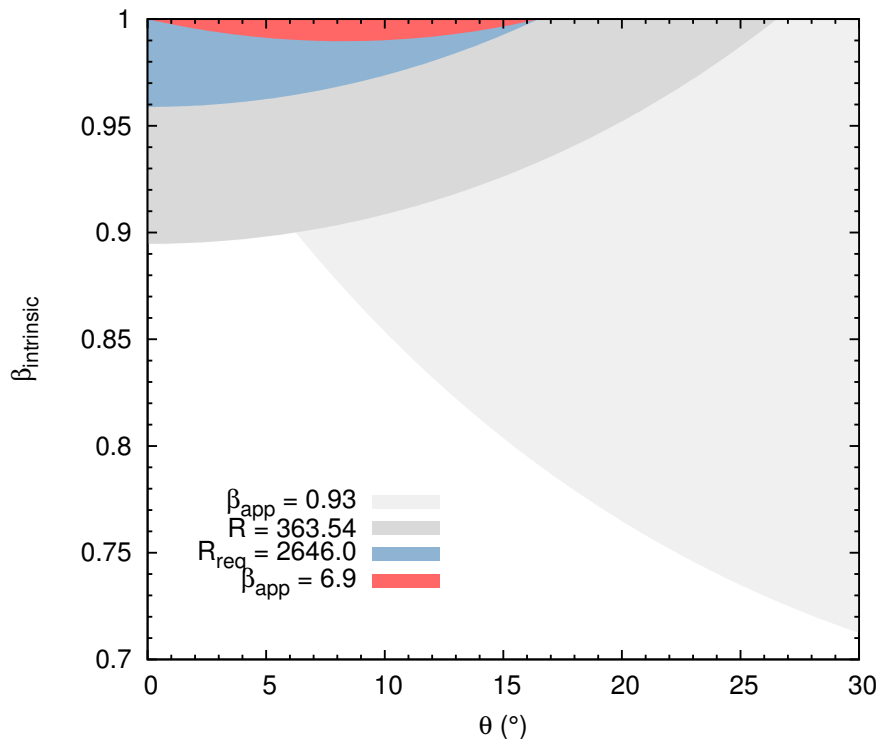


Figure 6.8: Intrinsic speed of components,  $\beta$ , and viewing angle,  $\theta$ , constrained by the observed apparent speed,  $\beta_{\text{app}}$ , and the jet-to-counter-jet ratio,  $R$ . Shown are the regions of valid  $\beta$  and  $\theta$  combinations according to highest and lowest observed  $\beta_{\text{app}}$ , 6.9 and 0.93, respectively. A further constraint is set by  $R$ , measured from the map and required  $R_{\text{req}}$ , in order for the Doppler factor to be real-valued. The most stringent constraints are set by the highest apparent speed and jet-to-counter-jet ratio, limiting the region of possible  $\beta$  and  $\theta$  combinations to the red shaded area.

### 6.9.2 A powerful combination of VLBI and single-dish data

Combination of variability characteristics and VLBI kinematical parameters can yield insights into the physical parameters of jets [see e.g. Section 4.4.1, 4.4.2, and Hovatta et al., 2009]. Ideally, one needs to use the kinematical parameters of the traveling VLBI knot causing the total intensity outburst (if any), however this cannot be done in the case of 1H 0323+342 and the available data. With the underlying assumption that regions exhibiting variability cannot be but causally connected—i.e. the size of the emitting region cannot exceed the light travel time across it ( $\vartheta \leq c\Delta t$ , with  $\Delta t$  the variability time scale), we derive a Lorentz factor estimate from

$$\gamma_{\text{var}} = \frac{\beta_{\text{app}}^2 + \delta_{\text{var}}^2 + 1}{2\delta_{\text{var}}} \quad (6-7)$$

along with a viewing angle towards the source,  $\theta_{\text{var}}$ , given by

$$\theta_{\text{var}} = \arctan \left( \frac{2\beta_{\text{app}}}{\beta_{\text{app}}^2 + \delta_{\text{var}}^2 - 1} \right) \quad (6-8)$$

where  $\delta_{\text{var}}$  is the Doppler factor deduced from observed single-dish variability.

Using a novel flare detection and light curve decomposition method into individual flares, based on the F-GAMMA single-dish light curves, Angelakis et al. [2015] provide estimates of the variability Doppler boosting factor for 1H 0323+342. The latter have been obtained by assuming that the observed flare brightness temperature cannot exceed the brightness temperature limit of  $5 \times 10^{10}$  K set by equipartition arguments [Readhead, 1994] and attributing any excess to Doppler boosting. Using single-dish monitoring data spanning almost five years they report the highest variability Doppler factor observed for the source at 2.64 GHz,  $\delta_{\text{var } 2.64} = 4.3$ . They also deduce a variability Doppler factor at 14.60 GHz, being somewhat lower, namely  $\delta_{\text{var } 14.60} = 3.6$ .

Combining the observed highest apparent velocity seen in the 15 GHz VLBI monitoring data  $\beta_{\text{app}} = 6.9$  and  $\delta_{\text{var}} = 4.3$  from single-dish data, using Eq. 6-7 and 6-8 we obtain for the variability Lorentz factor  $\gamma_{\text{var}} \simeq 7.8$  and viewing angle  $\theta_{\text{var}} \simeq 12^\circ$ . We employ the highest observed  $\beta_{\text{app}}$  because this sets the tightest constraint to the viewing angle, for constant  $\beta$  (see Eq. 4-1). Use of the lower value for the variability Doppler factor at 14.60 GHz leads to a higher Lorentz factor  $\gamma_{\text{var}} \simeq 8.5$  and a comparable value for the viewing angle  $\theta_{\text{var}} \simeq 13^\circ$ .

Results of all calculations are summarized in Table 6.6.

## 6.10 DISCUSSION

A striking morphological feature of 1H 0323+342 is the gap of emission seen at a radial separation between 3 and 6 mas from the core. Its exact nature is largely unknown but nevertheless some hypotheses can be discussed. First, it could be explained through geometrical considerations, meaning that the jet could be starting at a small angle to the line of sight but later, as it propagates, interaction with the ambient medium may cause it to deflect away from our line of sight. Further downstream, as its axis comes again close to our line of sight, the jet

SOURCE	$\nu$ (GHz)	$T_{\text{var}}$ (K)	$\delta_{\text{var}}$
J0324+3410	2.64	$25 \times 10^{11}$	4.3
J0324+3410	14.60	$18 \times 10^{11}$	3.6

Table 6.4: Findings of the single-dish analysis of [Angelakis et al. \[2015\]](#). Columns from left to right: (1) source name under the J2000 designation; (2) observing frequency; (3) variability brightness temperature and (4) variability Doppler factor.

becomes visible and continues its largely straight path. Though not impossible, this scenario would require a very small transversal component of the projected PA, given the very straight morphology of the jet evident both before and after the gap.

Reappearance of the jet after the zone void of radio emission could also be explained as a shock (standing or traveling) indicating the onset of a deceleration zone at  $\sim 6$  mas away from the core. A viable hypothesis is as follows. The jet of 1H 0323+342 starts its expansion in a very straight geometry at a moderate viewing angle. As it accelerates the radiation beaming cone becomes smaller-and-smaller (see Section 1.7.1) and whilst the angle of the jet axis to our line of sight remains relatively constant, the jet becomes invisible because the beaming cone is too narrow. We are able to see the jet again when it decelerates and the cone becomes wider again. This scenario can be checked by modeling the flux density of VLBI components while approaching and emerging from the gap (see Fig. 6.6).

What can readily be seen in Fig 6.7 from the eight epochs we discuss here is that components appear to travel in ballistic trajectories (i.e. no clear sign of acceleration) that are characterized by different speeds. This seems to disfavor the scenario discussed in the previous paragraph. Observed speeds appear to increase with component age in the area before the gap—i.e. older components appear to travel faster. This trend of higher apparent speed with component age continues also after the gap. In essence, in the full length of the jet of 1H 0323+342 there exists a bimodal pattern with apparent speeds increasing, both before and after the radio emission void. To allow for drawing more robust conclusions more data is needed along with a longer time baseline of VLBI monitoring.

Finally, free-free absorption from the disk and/or a molecular torus obscuring the central engine and part of the jet is also possible. This scenario would imply that absorption renders the jet invisible at a de-projected distance ranging between  $\sim 16$ – $32$  pc from the 15 GHz core. These figures although slightly larger than usually quoted AGN tori inner radii, they are well within the range of measured values for such structures [e.g. [Struve and Conway, 2010](#)]. In any case, this possibility calls for spectral information in order to be corroborated.

A first indication that the viewing angle towards 1H 0323+342 should be in a moderate range is the remarkably straight jet. Since the jet appears so aligned, it follows that it should be directed to a not-so-small viewing angle, otherwise PA variations would be greatly enhanced and more pronounced, as in the case

of small viewing angles, due to relativistic aberration effects. While the viewing angle can be loosely constrained through interferometric data only, the powerful combination of VLBI and single-dish methods allows us to accurately estimate it. We thus obtain a good estimate for it, being in the range  $12^\circ$ – $13^\circ$ . This figure is slightly larger than the one obtained through the calculation of the critical viewing angle being  $\theta_{\text{crit}} = 8.2^\circ$ . The values we obtain combining VLBI kinematics and single-dish variability are in accord with the looser constraints using the jet-to-counter-jet ratio.

In Table 6.5 the calculated mean brightness temperature for each component within the relativistic flow of 1H 0323+342 is shown. Our VLBI results are in good agreement with the values reported in Angelakis et al. [2015], obtained through an independent method of single-dish light curve decomposition into individual flares. Should the 15 GHz VLBI data were covering a longer time period, we would be able to identify knot ejections with these individual flares. The rapid variability pattern of the source (see lower panel of Fig. 6.6) is also a deterrent and VLBI monitoring campaigns with better time sampling are required. In any case, the new component (NC) only seen to emerge in our latest epoch in 2013 June 8, may be connected to the high-amplitude, multi-wavelength flare observed in the single-dish, total-intensity data peaking at epoch  $\sim 2013.1$  (see Fig. 6.2).

Finally, the brightness temperatures deduced from single-dish variability and those inferred from VLBI sizes and flux densities of individual components, are in reasonable agreement with each other. Brightness temperature of the core and also the first quasi-stationary feature are high and especially for the core, assuming that it is naturally limited by equipartition, implies a moderate amount of Doppler beaming.

In summary, a VLBI study of the  $\gamma$ - and radio-loud NLS1 galaxy 1H 0323+342 was presented. Using different methods and ultimately combining VLBI and single-dish data we deduced the viewing angle towards the source in the range  $12^\circ$ – $13^\circ$ . The numbers are in accordance with other studies suggesting that radio-loud NLS1s harbor mildly relativistic jets which are roughly estimated to be viewed at a moderate angle to the line of sight ( $10^\circ$ – $15^\circ$ ) [see e.g. Richards and Lister, 2015] in contrast to classical blazars and their ultra-relativistic outflows directed typically at  $1^\circ$ – $5^\circ$  [Hovatta et al., 2009]. This work embodies what is among the first measurements of this important observable—within schemes of unification by orientation—for this new class of intriguing objects.

KNOT	$\langle T_b \rangle$ (K)
C1	$3.6 \times 10^7$
C2	$6.4 \times 10^7$
C3	$5.8 \times 10^7$
C4	$3.8 \times 10^7$
C5	$9.2 \times 10^7$
C6	$9.7 \times 10^8$
S	$2.0 \times 10^{10}$
Core	$1.3 \times 10^{11}$

Table 6.5: Average brightness temperature of components deduced from VLBI. The mean size of components across the 8 observing epochs is used.

MEASURED QUANTITIES	INFERRED PARAMETERS
VLBI data only	
$R = 363.54$	$\delta \in \mathbb{I}$
$\beta \rightarrow 1$	$\theta \leq 26^\circ$
$R_{\text{req}} = 2646.0$	$\delta \in \mathbb{R}$
$\beta \rightarrow 1$	$\theta \leq 16^\circ$
Critical values	
$\beta_{\text{app}} = 6.9$	$\gamma_{\text{min}} = 6.97$
	$\theta_{\text{crit}} = 8.2^\circ$
VLBI and single dish	
$\beta_{\text{app}} = 6.9$	$\gamma_{\text{var}} = 7.8$
$\delta_{\text{var}} = 4.3$	$\theta_{\text{var}} = 12^\circ$
$\beta_{\text{app}} = 6.9$	$\gamma_{\text{var}} = 8.5$
$\delta_{\text{var}} = 3.6$	$\theta_{\text{var}} = 13^\circ$

Table 6.6: Table of inferred physical parameters. The left column contains measured quantities used in each calculation, leading to the values in the right column. The table is divided in three parts that, from top to bottom, contain the results obtained with the use of VLBI data only, the critical values for the Lorentz factor (minimum value) and the viewing angle, and finally, results obtained through the combination of VLBI and filled-aperture monitoring data.





## CONCLUDING REMARKS AND OUTLOOK

---

The focal point of the thesis at hand was the multi-wavelength, VLBI and single-dish study of the intense 2008/2010 outburst seen in the blazar PKS 1502+106. This pronounced broadband flare, seen from radio up to  $\gamma$ -ray energies, triggered the first *Fermi*-GST multi-frequency campaign covering the electromagnetic spectrum in its entirety, both with filled-aperture instruments and with VLBI arrays.

Towards a better understanding of the inner workings of the source during the pronounced flare, multi-epoch, single-dish and VLBI data were reduced and analyzed. F-GAMMA single-dish data, obtained with the Effelsberg 100-m (EB) and IRAM 30-m (PV) telescopes, in combination with high-frequency GMVA observations at 86 and 43 GHz, supplemented by MOJAVE VLBA observations at 15 GHz, evince that PKS 1502+106 is a unique case towards a detailed understanding of flux density outbursts and subsequent structural variability.

The observational evidence discussed in this work enabled the global view of the jet of PKS 1502+106 and its physical characteristics. First, the mm-VLBI monitoring employed, allowed for the connection between superluminal component C<sub>3</sub>, traveling within the ultra-relativistic flow of PKS 1502+106, with the flare. Second, the powerful combination of VLBI and single-dish techniques allows for decisively constraining the  $\gamma$ -ray emission region to  $\sim 2$  pc away from the jet base, well beyond the bulk of BLR material of PKS 1502+106, placed at  $R_{\text{BLR}} \approx 0.1$  pc. Good candidates for IC up-scattering are the photon fields of the outer BLR and/or the IR torus in addition to the SSC process.

More specifically, from the VLBI study at cm and mm wavelengths the physical characteristics and geometry of the bent, parsec-scale jet are revealed at their highest detail. Extreme superluminal speeds, in the range 10–22  $c$ , are observed for all components within the jet. The fastest  $\beta_{\text{app}} \sim 22 c$  constrains the critical aspect angle towards it, to  $\theta_c = 2.6^\circ$ . PKS 1502+106 features an intrinsic jet opening angle  $\phi_{\text{int}} = 1.6^\circ\text{--}2.2^\circ$ .

Doppler and Lorentz factor estimates for individual components were obtained using variability and VLBI kinematical arguments. Doppler factor estimates are strikingly different for knot C<sub>3</sub> at  $r < 0.5$  mas and C<sub>1</sub> at a distance  $r > 1$  mas. Knot C<sub>1</sub> is characterized by a minimum Doppler boosting factor of  $\delta_{\beta_{\text{app}, C_1}} \approx \beta_{\text{app}, C_1} \approx 22.1$  at 15 GHz. Its significant variability at 15 GHz enables the estimation of  $\delta_{\text{var}}$  using causality arguments yielding ( $\delta_{\text{var}} \leq 51.4$ ) and Lorentz factor of ( $\gamma_{\text{var}} \leq 30.5$ ). An additional Doppler factor estimate through the relative strength of equipartition and SSA magnetic fields is in good agreement with the aforementioned figure. Knot C<sub>3</sub> exhibits consistent behavior at both high frequencies with  $\delta_{\text{var}} \leq 12\text{--}15$  and  $\gamma_{\text{var}} \leq 7.1\text{--}9.2$ .

The viewing angle towards the source is constrained to  $\theta \geq 2.9^\circ\text{--}3.4^\circ$  for the inner and  $\theta \geq 0.8^\circ$  for the outer portions of the jet, after about 1 mas.

These differences in apparent speed and viewing angle imply a jet bending after the first mas. The bending results in differential Doppler boosting with

increasing  $\delta$  from  $\sim 12$ – $15$  to  $\sim 50$  as traced by components C3 and C1 at  $<0.5$  mas and  $>1$  mas from the core, respectively. Additionally, this Doppler factor gradient cannot be ascribed to jet bending only. Acceleration within the first mas also takes place in this region, with the Lorentz factor increasing from  $\sim 10$  to  $\sim 22$ .

The decomposition of single-dish radio flux density into distinct VLBI components shows that, during the outburst, the bulk of radio emission originates from the core at all frequencies. At 43 and 86 GHz another component is visible separating from the core and sharing a significant flux density level. Knot C3 appears to be in a decaying flux density phase while separating radially from the core. From the flux density decomposition and its estimated core separation date, coinciding with the flare onset, the conclusion is drawn that C3 is responsible for the radio flare of 2008–2010. Given also the established correlation between radio and  $\gamma$ -ray activity for the source, C3 initiated the high-energy activity as well. From the VLBI data alone, the  $\gamma$ -ray emission region can be constrained to reside at a de-projected distance of  $\leq 10$ – $15$  pc from the jet base.

In Chapter 5, the F-GAMMA single-dish data set was presented along with the reduction procedure and additional data used from other instruments. The dense, long-term F-GAMMA radio light curves between 2.64 and 142.33 GHz, obtained with EB and PV, enabled the detailed study of PKS 1502+106 at scales inaccessible even to mm-VLBI. Three independent methods were employed, namely (i) light curve decomposition into exponential flares, (ii) non-parametric Gaussian process (GP) regression, and (iii) a discrete cross-correlation function analysis. Based on those, the relevant light curve parameters such as the flare amplitude, rise and decay time scales, and cross-band time lags were extracted and their dependence on observing frequency was established. In fact, their frequency-dependencies are well described by power laws. It is among the first (if not the first) times that GP regression is used in the study of AGN light curves. The method performs well, fast, and appears as a good alternative to conventional, parametric fitting methods.

The observed opacity-driven time lags draw a detailed picture of the source in terms of synchrotron opacity. The positions of the 10 radio unit-opacity surfaces at all frequencies with respect to the jet base were deduced, with distances ranging from  $\sim 10.0$  pc for the 2.64 GHz core, down to  $\sim 4$  pc for the unit-opacity surface at 86.24 GHz. These frequency-dependent core positions allow for the calculation of the equipartition magnetic field values along the jet at the position of each core and at a distance of 1 pc from the jet base. Those are found to be  $\langle B_{1\text{pc}} \rangle = 33 \pm 4$  mG and the magnetic field at each respective core in the range  $3 \text{ mG} < B_{\text{core}} < 16 \text{ mG}$  for the frequencies between 2.64 and 86.24 GHz.

The frequency-dependent light curve parameters are subsequently compared with the results of analytical simulations based on the shock-in-jet model. Overall, the 2008–2010 flare of PKS 1502+106 is in good agreement with the typical shock evolutionary path. The related shock physical parameters and their variation with distance are also constrained. The Doppler factor increases with distance. In light of the findings from the cm-/mm-VLBI monitoring, these results suggest a shock origin for the flare of PKS 1502+106. The initiating disturbance is seen at high-frequency VLBI images as component C3 traveling downstream the core at 43/86 GHz maps. This traveling disturbance is associated with the multi-frequency flare seen from radio up to  $\gamma$ -ray energies. The Doppler factor

gradient inferred from the comparison with the analytical model simulations corroborates the scenario of an accelerating relativistic outflow for the jet of PKS 1502+106.

Through the powerful combination of VLBI and single-dish techniques and with the addition of previous findings, the  $\gamma$ -ray emission region can be decisively constrained to reside at a distance of  $\sim 2$  pc away from the jet base and well downstream of the bulk of the BLR material for the source. Consequently, for PKS 1502+106 the  $\gamma$ -ray emission originates in regions much further than a few Schwarzschild radii away from the central engine, thus a number of models can be readily discarded. Additionally, the target photon field for inverse Compton up-scattering has to be sought much further than the accretion disk and the bulk of the BLR material for the source.

The final chapter was devoted to the VLBI study of the radio- and  $\gamma$ -ray-loud narrow-line Seyfert 1 galaxy 1H 0323+342, with additional single-dish add-ons in the form of F-GAMMA monitoring products. This object belongs to a newly emerged class of  $\gamma$ -ray emitting AGN, besides blazars and radio galaxies. Their importance is discussed in detail in Chapter 6, along with their resemblances and differences to powerful blazars. The seven  $\gamma$ -ray-loud RLNLS1 known to date are believed to host mildly relativistic jets.

By re-analyzing archival MOJAVE VLBA data at 15 GHz parsec-scale jet morphology of the source is discussed and a kinematical model is deduced. The jet of 1H 0323+342 shows moderate superluminal motion of jet features in the range  $0.9c$  to  $\sim 7c$  and a quasi-stationary feature. A striking morphological characteristic of the source is a gap of radio emission between 3–6 mas from the core laying at the position angle of the jet. By employing the jet-to-counter-jet ratio a first limit of  $\theta \leq 16^\circ$  to the viewing angle is set. The critical viewing angle, using the apparent speed of the fastest component, is  $\theta_{\text{crit}} = 8.2^\circ$ . Once more, for the NLS1 galaxy 1H 0323+342, the powerful combination of VLBI and single-dish monitoring provides a compelling estimate for its viewing angle. With the use of previous estimates of single-dish, variability Doppler factors and VLBI kinematics presented here, the viewing angle towards the source is constrained to  $12^\circ$ – $13^\circ$  to the line of sight. Compared to typical blazars ( $\theta \sim 1^\circ$ – $5^\circ$ ), the jet of 1H 0323+342 is viewed at a moderate angle to our line of sight.

This work has shown the scientific potential of deep, ultra-high resolution VLBI observations and their intimate connection with single-dish monitoring at multiple frequencies. Combination of the two approaches offers the best possibility for unveiling the intricate processes that give rise to blazar variability and their structural dynamics. VLBI at even higher frequencies and longer baselines has the potential of directly imaging the active regions of blazars where most of the observed variability takes place.

Single source studies, as those presented here, can offer an extremely detailed picture exploiting both VLBI and filled-aperture monitoring. Difficult to achieve core-shift measurements can be obtained through the accurate timing analysis of flares, thus probing regions inaccessible to even the highest-resolution VLBI available today. The still open question of where the  $\gamma$  rays are produced can be touched on a case-by-case basis, thus constraining emission models and the nature of target photon-fields for the production of high energy emission.

The work started here will be continued, exploiting both approaches and different methods within each one. The densely-sampled, multi-frequency light curves of the F-GAMMA program constitute an invaluable collection of data towards these goals. We intend to extensively and systematically exploit it drawing conclusion from its large sample of monitored sources and individual flaring events. Detailed variability studies within the framework of the shock-in-jet and other competing models will constrain the parameter space and discard old, amend existing, and ultimately give rise to new ones.

Specifically for PKS 1502+106, forthcoming comparison in the frequency domain and extraction of the slopes during the flare evolutionary path in the  $\nu_{\max}$ – $S_{\max}$  plane will shed more light on the physical parameters of the jet and their evolution with distance.

Finally, further investigation of the new class of  $\gamma$ -ray active AGN—the  $\gamma$ -RLNLS1s—will provide insights into the properties of active galaxies hosting lower-mass black holes and their massive counterparts. Relativistic jets emanating from their cores can question even basic bits of our understanding of AGN and deserve the community's efforts.

## APPENDICES



# PKS 1502+106: INDIVIDUAL VLBI COMPONENT LIGHT CURVES AT 15, 43, AND 86 GHz

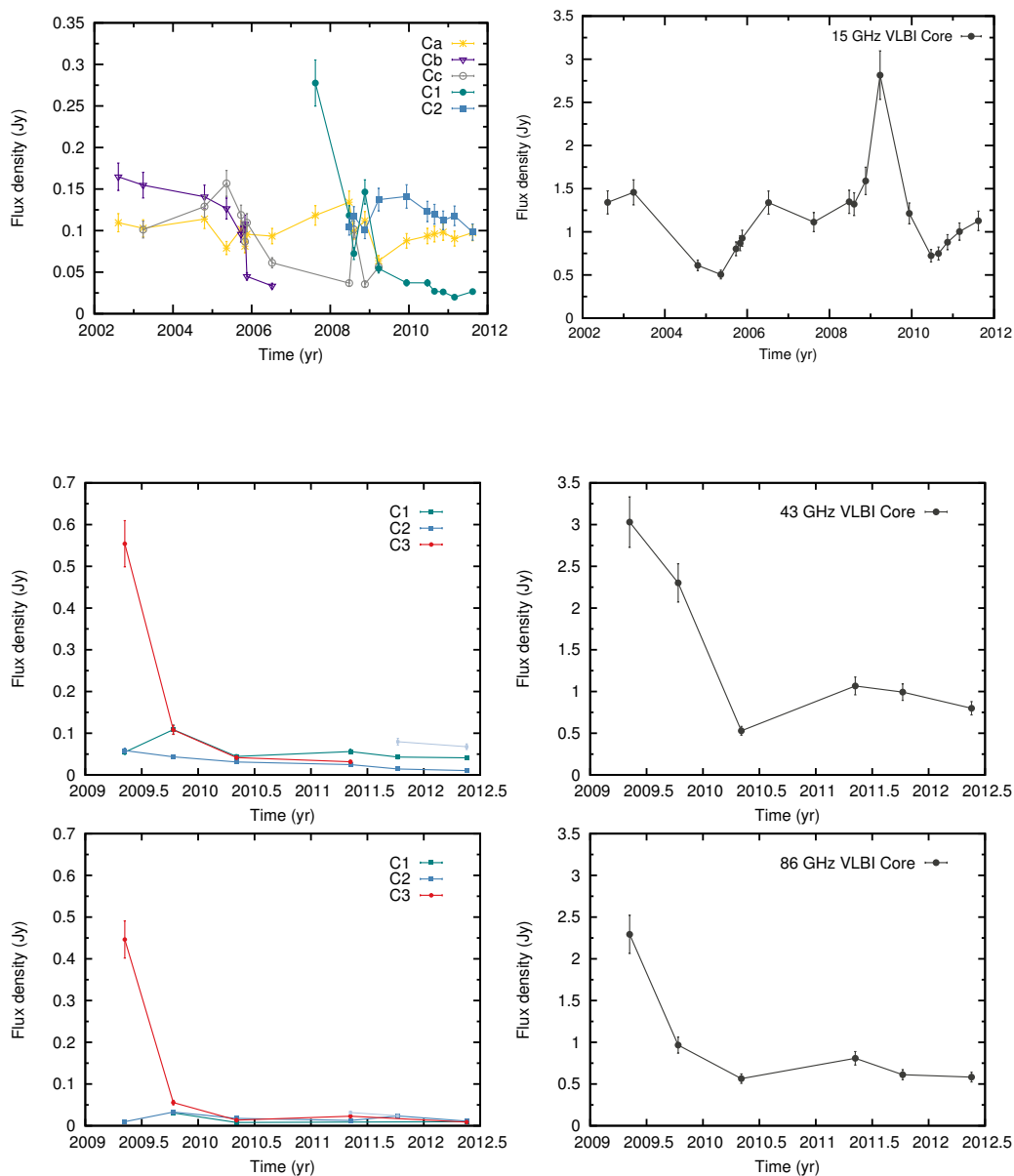


Figure A.1: Light curves of individual components (left panels) and the core (right panels) at 15, 43, and 86 GHz, from top to bottom, respectively. Component C1 at 15 GHz shows significant variability between 2008 and 2010. Component C3 at 43 and 86 GHz is at its decaying flux density phase.





## PKS 1502+106 MODELFIT RESULTS

Table B.1: MODELFIT results 15 GHz. Columns from left to right: (1) observing epoch in fractional year; (2) MJD of the observing epoch; (3) epoch identifier between 1–19; (4) integrated component flux density; (5) radial separation from the core; (6) position angle; (7) component size given as the FWHM of the major axis; (8) component identification label.

Epoch	MJD	Epoch ID	S (Jy)	r (mas)	PA (°)	FWHM (mas)	ID
2009.23	54915.5	13	$0.0382 \pm 0.0038$	$4.61 \pm 0.13$	$103.4 \pm 11.2$	$4.57 \pm 0.46$	...
2002.61	52498.5	1	$0.1095 \pm 0.0110$	$1.98 \pm 0.28$	$122.9 \pm 7.9$	$1.38 \pm 0.14$	Ca
2003.24	52727.5	2	$0.1028 \pm 0.0103$	$2.30 \pm 0.32$	$123.3 \pm 7.9$	$1.60 \pm 0.16$	Ca
2004.80	53296.5	3	$0.1139 \pm 0.0114$	$2.03 \pm 0.36$	$125.7 \pm 10.0$	$1.79 \pm 0.18$	Ca
2005.36	53503.5	4	$0.0790 \pm 0.0079$	$2.65 \pm 0.37$	$122.8 \pm 7.9$	$1.83 \pm 0.18$	Ca
2005.73	53636.5	5	$0.1016 \pm 0.0102$	$2.47 \pm 0.38$	$121.8 \pm 8.8$	$1.91 \pm 0.19$	Ca
2005.83	53672.5	6	$0.0813 \pm 0.0081$	$2.60 \pm 0.31$	$122.1 \pm 6.8$	$1.55 \pm 0.16$	Ca
2005.88	53691.5	7	$0.0956 \pm 0.0096$	$2.27 \pm 0.25$	$121.5 \pm 6.2$	$1.23 \pm 0.12$	Ca
2006.52	53923.5	8	$0.0934 \pm 0.0093$	$2.38 \pm 0.27$	$122.7 \pm 6.5$	$1.36 \pm 0.14$	Ca
2007.62	54328.5	9	$0.1183 \pm 0.0118$	$2.59 \pm 0.33$	$122.7 \pm 7.3$	$1.66 \pm 0.17$	Ca
2008.48	54642.5	10	$0.1342 \pm 0.0134$	$2.46 \pm 0.42$	$123.2 \pm 9.6$	$2.09 \pm 0.21$	Ca
2008.60	54684.5	11	$0.0996 \pm 0.0100$	$2.84 \pm 0.36$	$123.0 \pm 7.2$	$1.78 \pm 0.18$	Ca
2008.88	54789.5	12	$0.1118 \pm 0.0112$	$2.79 \pm 0.42$	$122.6 \pm 8.6$	$2.11 \pm 0.21$	Ca
2009.23	54915.5	13	$0.0637 \pm 0.0064$	$2.93 \pm 0.30$	$124.8 \pm 5.8$	$1.48 \pm 0.15$	Ca
2009.94	55175.5	14	$0.0877 \pm 0.0088$	$2.97 \pm 0.46$	$121.9 \pm 8.8$	$2.30 \pm 0.23$	Ca
2010.47	55366.5	15	$0.0935 \pm 0.0094$	$3.04 \pm 0.53$	$120.9 \pm 10.0$	$2.67 \pm 0.27$	Ca
2010.65	55435.5	16	$0.0959 \pm 0.0096$	$3.00 \pm 0.54$	$120.7 \pm 10.2$	$2.70 \pm 0.27$	Ca
2010.87	55513.5	17	$0.0981 \pm 0.0098$	$3.02 \pm 0.58$	$120.9 \pm 10.9$	$2.91 \pm 0.29$	Ca
2011.16	55619.5	18	$0.0904 \pm 0.0090$	$3.08 \pm 0.58$	$119.8 \pm 10.6$	$2.89 \pm 0.29$	Ca
2011.62	55788.5	19	$0.0975 \pm 0.0098$	$3.22 \pm 0.67$	$118.6 \pm 11.7$	$3.35 \pm 0.33$	Ca
2002.61	52498.5	1	$0.1648 \pm 0.0165$	$0.68 \pm 0.07$	$119.6 \pm 5.5$	$0.32 \pm 0.03$	Cb
2003.24	52727.5	2	$0.1547 \pm 0.0155$	$0.97 \pm 0.11$	$120.8 \pm 6.4$	$0.54 \pm 0.05$	Cb
2004.80	53296.5	3	$0.1407 \pm 0.0141$	$0.84 \pm 0.13$	$117.1 \pm 8.9$	$0.65 \pm 0.07$	Cb
2005.36	53503.5	4	$0.1266 \pm 0.0127$	$1.16 \pm 0.21$	$121.6 \pm 10.1$	$1.03 \pm 0.10$	Cb
2005.73	53636.5	5	$0.0957 \pm 0.0096$	$1.21 \pm 0.19$	$123.9 \pm 9.0$	$0.96 \pm 0.10$	Cb
2005.83	53672.5	6	$0.1079 \pm 0.0108$	$1.19 \pm 0.19$	$121.4 \pm 9.3$	$0.97 \pm 0.10$	Cb
2005.88	53691.5	7	$0.0449 \pm 0.0045$	$1.26 \pm 0.10$	$135.6 \pm 4.4$	$0.49 \pm 0.05$	Cb
2006.52	53923.5	8	$0.0334 \pm 0.0033$	$1.19 \pm 0.14$	$140.5 \pm 6.7$	$0.10 \pm 0.01$	Cb

Table B.1: continued.

Epoch	MJD	Epoch ID	S (Jy)	r (mas)	PA ( $^{\circ}$ )	FWHM (mas)	ID
2003.24	52727.5	2	$0.1012 \pm 0.0101$	$0.37 \pm 0.13$	$122.8 \pm 19.1$	$0.10 \pm 0.01$	Cc
2004.80	53296.5	3	$0.1289 \pm 0.0129$	$0.42 \pm 0.13$	$97.6 \pm 17.4$	$0.10 \pm 0.01$	Cc
2005.36	53503.5	4	$0.1568 \pm 0.0157$	$0.58 \pm 0.10$	$100.6 \pm 9.8$	$0.50 \pm 0.05$	Cc
2005.73	53636.5	5	$0.1188 \pm 0.0119$	$0.64 \pm 0.10$	$100.2 \pm 9.2$	$0.52 \pm 0.05$	Cc
2005.83	53672.5	6	$0.0868 \pm 0.0087$	$0.66 \pm 0.10$	$98.6 \pm 8.2$	$0.48 \pm 0.05$	Cc
2005.88	53691.5	7	$0.1095 \pm 0.0110$	$0.71 \pm 0.12$	$96.5 \pm 9.2$	$0.57 \pm 0.06$	Cc
2006.52	53923.5	8	$0.0613 \pm 0.0061$	$0.82 \pm 0.15$	$90.0 \pm 10.4$	$0.75 \pm 0.07$	Cc
2008.48	54642.5	10	$0.0368 \pm 0.0037$	$1.30 \pm 0.13$	$98.6 \pm 5.8$	$0.10 \pm 0.01$	Cc
2008.60	54684.5	11	$0.1014 \pm 0.0101$	$1.14 \pm 0.14$	$102.7 \pm 7.2$	$0.72 \pm 0.07$	Cc
2008.88	54789.5	12	$0.0356 \pm 0.0036$	$1.47 \pm 0.08$	$102.8 \pm 3.1$	$0.39 \pm 0.04$	Cc
2009.23	54915.5	13	$0.0562 \pm 0.0056$	$1.35 \pm 0.20$	$105.3 \pm 8.3$	$0.98 \pm 0.10$	Cc
2007.62	54328.5	9	$0.2776 \pm 0.0278$	$0.61 \pm 0.08$	$96.8 \pm 7.1$	$0.38 \pm 0.04$	C1
2008.48	54642.5	10	$0.1182 \pm 0.0118$	$0.77 \pm 0.05$	$93.6 \pm 3.4$	$0.23 \pm 0.02$	C1
2008.60	54684.5	11	$0.0724 \pm 0.0072$	$0.76 \pm 0.14$	$91.3 \pm 10.6$	$0.10 \pm 0.01$	C1
2008.88	54789.5	12	$0.1465 \pm 0.0147$	$0.80 \pm 0.06$	$94.9 \pm 4.6$	$0.32 \pm 0.03$	C1
2009.23	54915.5	13	$0.0544 \pm 0.0054$	$0.92 \pm 0.15$	$91.7 \pm 9.2$	$0.10 \pm 0.01$	C1
2009.94	55175.5	14	$0.0372 \pm 0.0037$	$1.26 \pm 0.18$	$97.5 \pm 8.0$	$0.89 \pm 0.09$	C1
2010.47	55366.5	15	$0.0371 \pm 0.0037$	$1.30 \pm 0.15$	$97.2 \pm 6.8$	$0.77 \pm 0.08$	C1
2010.65	55435.5	16	$0.0270 \pm 0.0027$	$1.38 \pm 0.13$	$92.8 \pm 5.3$	$0.64 \pm 0.06$	C1
2010.87	55513.5	17	$0.0262 \pm 0.0026$	$1.47 \pm 0.13$	$96.0 \pm 5.1$	$0.66 \pm 0.07$	C1
2011.16	55619.5	18	$0.0199 \pm 0.0020$	$1.57 \pm 0.09$	$97.8 \pm 3.2$	$0.43 \pm 0.04$	C1
2011.62	55788.5	19	$0.0266 \pm 0.0027$	$1.58 \pm 0.12$	$104.5 \pm 4.2$	$0.59 \pm 0.06$	C1
2008.48	54642.5	10	$0.1050 \pm 0.0105$	$0.32 \pm 0.13$	$89.8 \pm 22.6$	$0.10 \pm 0.01$	C2
2008.60	54684.5	11	$0.1171 \pm 0.0117$	$0.35 \pm 0.14$	$97.6 \pm 21.9$	$0.10 \pm 0.01$	C2
2008.88	54789.5	12	$0.1004 \pm 0.0100$	$0.43 \pm 0.14$	$101.0 \pm 18.6$	$0.10 \pm 0.01$	C2
2009.23	54915.5	13	$0.1373 \pm 0.0137$	$0.58 \pm 0.06$	$99.0 \pm 6.3$	$0.32 \pm 0.03$	C2
2009.94	55175.5	14	$0.1411 \pm 0.0141$	$0.74 \pm 0.09$	$99.5 \pm 6.8$	$0.44 \pm 0.04$	C2
2010.47	55366.5	15	$0.1230 \pm 0.0123$	$0.71 \pm 0.11$	$103.3 \pm 8.7$	$0.54 \pm 0.05$	C2
2010.65	55435.5	16	$0.1196 \pm 0.0120$	$0.74 \pm 0.11$	$103.2 \pm 8.7$	$0.57 \pm 0.06$	C2
2010.87	55513.5	17	$0.1123 \pm 0.0112$	$0.77 \pm 0.11$	$104.7 \pm 8.3$	$0.56 \pm 0.06$	C2
2011.16	55619.5	18	$0.1178 \pm 0.0118$	$0.81 \pm 0.11$	$107.9 \pm 7.9$	$0.56 \pm 0.06$	C2
2011.62	55788.5	19	$0.0982 \pm 0.0098$	$0.82 \pm 0.14$	$113.1 \pm 9.6$	$0.69 \pm 0.07$	C2
2002.61	52498.5	1	$1.3409 \pm 0.1341$	$0.00 \pm 0.02$	$0.0 \pm 0.0$	$0.23 \pm 0.02$	Core
2003.24	52727.5	2	$1.4571 \pm 0.1457$	$0.00 \pm 0.02$	$0.0 \pm 0.0$	$0.22 \pm 0.02$	Core
2004.80	53296.5	3	$0.6113 \pm 0.0611$	$0.00 \pm 0.02$	$0.0 \pm 0.0$	$0.20 \pm 0.02$	Core
2005.36	53503.5	4	$0.5050 \pm 0.0505$	$0.00 \pm 0.12$	$0.0 \pm 0.0$	$0.11 \pm 0.01$	Core
2005.73	53636.5	5	$0.8028 \pm 0.0803$	$0.00 \pm 0.01$	$0.0 \pm 0.0$	$0.12 \pm 0.01$	Core
2005.83	53672.5	6	$0.8678 \pm 0.0868$	$0.00 \pm 0.12$	$0.0 \pm 0.0$	$0.11 \pm 0.01$	Core
2005.88	53691.5	7	$0.9259 \pm 0.0926$	$0.00 \pm 0.15$	$0.0 \pm 0.0$	$0.11 \pm 0.01$	Core

Table B.1: continued.

Epoch	MJD	Epoch ID	S (Jy)	r (mas)	PA (°)	FWHM (mas)	ID
2006.52	53923.5	8	$1.3386 \pm 0.1339$	$0.00 \pm 0.02$	$0.0 \pm 0.0$	$0.23 \pm 0.02$	Core
2007.62	54328.5	9	$1.1127 \pm 0.1113$	$0.00 \pm 0.12$	$0.0 \pm 0.0$	$0.09 \pm 0.01$	Core
2008.48	54642.5	10	$1.3477 \pm 0.1348$	$0.00 \pm 0.12$	$0.0 \pm 0.0$	$0.09 \pm 0.01$	Core
2008.60	54684.5	11	$1.3203 \pm 0.1320$	$0.00 \pm 0.12$	$0.0 \pm 0.0$	$0.08 \pm 0.01$	Core
2008.88	54789.5	12	$1.5894 \pm 0.1589$	$0.00 \pm 0.12$	$0.0 \pm 0.0$	$0.08 \pm 0.01$	Core
2009.23	54915.5	13	$2.8151 \pm 0.2815$	$0.00 \pm 0.13$	$0.0 \pm 0.0$	$0.06 \pm 0.01$	Core
2009.94	55175.5	14	$1.2132 \pm 0.1213$	$0.00 \pm 0.12$	$0.0 \pm 0.0$	$0.09 \pm 0.01$	Core
2010.47	55366.5	15	$0.7228 \pm 0.0723$	$0.00 \pm 0.13$	$0.0 \pm 0.0$	$0.10 \pm 0.01$	Core
2010.65	55435.5	16	$0.7485 \pm 0.0749$	$0.00 \pm 0.12$	$0.0 \pm 0.0$	$0.09 \pm 0.01$	Core
2010.87	55513.5	17	$0.8795 \pm 0.0880$	$0.00 \pm 0.12$	$0.0 \pm 0.0$	$0.09 \pm 0.01$	Core
2011.16	55619.5	18	$1.0025 \pm 0.1003$	$0.00 \pm 0.12$	$0.0 \pm 0.0$	$0.09 \pm 0.01$	Core
2011.62	55788.5	19	$1.1272 \pm 0.1127$	$0.00 \pm 0.13$	$0.0 \pm 0.0$	$0.09 \pm 0.01$	Core

Table B.2: MODELFIT results at 43 GHz. Columns from left to right: (1) observing epoch in fractional year; (2) MJD of the observing epoch; (3) epoch identifier between 1–6; (4) integrated component flux density; (5) radial separation from the core; (6) position angle; (7) component size given as the FWHM of the major axis; (8) component identification label.

Epoch	MJD	Epoch ID	S (Jy)	r (mas)	PA (°)	FWHM (mas)	ID
2009.35	54959.36	1	$0.0546 \pm 0.0055$	$0.93 \pm 0.08$	$93.7 \pm 5.0$	$0.404 \pm 0.040$	C <sub>1</sub>
2009.78	55117.82	2	$0.1087 \pm 0.0109$	$0.87 \pm 0.08$	$99.3 \pm 5.3$	$0.404 \pm 0.040$	C <sub>1</sub>
2010.34	55323.28	3	$0.0444 \pm 0.0044$	$1.08 \pm 0.19$	$97.4 \pm 10.2$	$0.965 \pm 0.096$	C <sub>1</sub>
2011.35	55688.76	4	$0.0561 \pm 0.0056$	$1.20 \pm 0.24$	$106.6 \pm 11.4$	$1.211 \pm 0.121$	C <sub>1</sub>
2011.77	55843.86	5	$0.0429 \pm 0.0043$	$1.20 \pm 0.20$	$102.6 \pm 9.6$	$1.017 \pm 0.102$	C <sub>1</sub>
2012.38	56065.17	6	$0.0411 \pm 0.0041$	$1.35 \pm 0.29$	$96.5 \pm 12.2$	$1.467 \pm 0.147$	C <sub>1</sub>
2009.35	54959.36	1	$0.0585 \pm 0.0059$	$0.57 \pm 0.04$	$100.3 \pm 4.0$	$0.202 \pm 0.020$	C <sub>2</sub>
2009.78	55117.82	2	$0.0435 \pm 0.0044$	$0.49 \pm 0.07$	$98.9 \pm 8.3$	$0.040 \pm 0.004$	C <sub>2</sub>
2010.34	55323.28	3	$0.0311 \pm 0.0031$	$0.74 \pm 0.03$	$100.4 \pm 2.5$	$0.160 \pm 0.016$	C <sub>2</sub>
2011.35	55688.76	4	$0.0249 \pm 0.0025$	$0.78 \pm 0.04$	$108.2 \pm 2.8$	$0.191 \pm 0.019$	C <sub>2</sub>
2011.77	55843.86	5	$0.0143 \pm 0.0014$	$0.71 \pm 0.03$	$107.8 \pm 2.1$	$0.130 \pm 0.013$	C <sub>2</sub>
2012.38	56065.17	6	$0.0105 \pm 0.0011$	$0.65 \pm 0.03$	$120.1 \pm 2.8$	$0.159 \pm 0.016$	C <sub>2</sub>
2009.35	54959.36	1	$0.5541 \pm 0.0554$	$0.08 \pm 0.06$	$130.4 \pm 37.3$	$0.030 \pm 0.003$	C <sub>3</sub>
2009.78	55117.82	2	$0.1080 \pm 0.0108$	$0.14 \pm 0.07$	$125.7 \pm 26.1$	$0.040 \pm 0.004$	C <sub>3</sub>
2010.34	55323.28	3	$0.0417 \pm 0.0042$	$0.22 \pm 0.04$	$114.6 \pm 10.0$	$0.194 \pm 0.019$	C <sub>3</sub>
2011.35	55688.76	4	$0.0316 \pm 0.0032$	$0.18 \pm 0.08$	$60.8 \pm 22.9$	$0.040 \pm 0.004$	C <sub>3</sub>
2011.77	55843.86	5	$0.0797 \pm 0.0080$	$0.14 \pm 0.02$	$70.4 \pm 7.1$	$0.089 \pm 0.009$	...
2012.38	56065.17	6	$0.0677 \pm 0.0068$	$0.13 \pm 0.07$	$70.2 \pm 27.8$	$0.050 \pm 0.005$	...
2009.35	54959.36	1	$3.0298 \pm 0.3030$	$0.00 \pm 0.06$	$0.0 \pm 0.0$	$0.029 \pm 0.003$	Core
2009.78	55117.82	2	$2.3014 \pm 0.2301$	$0.00 \pm 0.07$	$0.0 \pm 0.0$	$0.056 \pm 0.006$	Core
2010.34	55323.28	3	$0.5295 \pm 0.0530$	$0.00 \pm 0.07$	$0.0 \pm 0.0$	$0.054 \pm 0.005$	Core
2011.35	55688.76	4	$1.0665 \pm 0.1067$	$0.00 \pm 0.03$	$0.0 \pm 0.0$	$0.131 \pm 0.013$	Core
2011.77	55843.86	5	$0.9928 \pm 0.0993$	$0.00 \pm 0.01$	$0.0 \pm 0.0$	$0.073 \pm 0.007$	Core
2012.38	56065.17	6	$0.7993 \pm 0.0799$	$0.00 \pm 0.07$	$0.0 \pm 0.0$	$0.040 \pm 0.004$	Core

Table B.3: MODELFIT results at 86 GHz. Columns from left to right: (1) observing epoch in fractional year; (2) MJD of the observing epoch; (3) epoch identifier between 1–6; (4) integrated component flux density; (5) radial separation from the core; (6) position angle; (7) component size given as the FWHM of the major axis; (8) component identification label.

Epoch	MJD	Epoch ID	S (Jy)	r (mas)	PA ( $^{\circ}$ )	FWHM (mas)	ID
2009.35	54959.36	1	$0.0713 \pm 0.0071$	$1.18 \pm 0.16$	$99.1 \pm \dots$	$0.780 \pm 0.078$	...
2010.34	55323.28	3	$0.0105 \pm 0.0011$	$1.39 \pm 0.03$	$99.5 \pm \dots$	$0.135 \pm 0.014$	...
2012.38	56065.54	6	$0.0037 \pm 0.0004$	$1.78 \pm 0.02$	$99.7 \pm \dots$	$0.100 \pm 0.010$	...
2009.78	55117.82	2	$0.0307 \pm 0.0031$	$0.86 \pm 0.01$	$103.2 \pm 0.9$	$0.065 \pm 0.006$	C <sub>1</sub>
2010.34	55323.28	3	$0.0078 \pm 0.0008$	$0.97 \pm 0.03$	$92.6 \pm 1.9$	$0.018 \pm 0.002$	C <sub>1</sub>
2012.38	56065.54	6	$0.0097 \pm 0.0010$	$1.50 \pm 0.01$	$107.3 \pm 0.4$	$0.052 \pm 0.005$	C <sub>1</sub>
2009.35	54959.36	1	$0.0097 \pm 0.0010$	$0.49 \pm 0.03$	$101.9 \pm 2.9$	$0.016 \pm 0.002$	C <sub>2</sub>
2009.78	55117.82	2	$0.0328 \pm 0.0033$	$0.46 \pm 0.01$	$106.0 \pm 1.5$	$0.061 \pm 0.006$	C <sub>2</sub>
2010.34	55323.28	3	$0.0176 \pm 0.0018$	$0.62 \pm 0.05$	$117.3 \pm 5.0$	$0.269 \pm 0.027$	C <sub>2</sub>
2011.35	55688.76	4	$0.0127 \pm 0.0013$	$0.63 \pm 0.07$	$84.4 \pm 6.0$	$0.331 \pm 0.033$	C <sub>2</sub>
2011.77	55843.86	5	$0.0235 \pm 0.0024$	$0.79 \pm 0.04$	$110.2 \pm 3.0$	$0.211 \pm 0.021$	C <sub>2</sub>
2012.38	56065.54	6	$0.0111 \pm 0.0011$	$0.75 \pm 0.04$	$124.0 \pm 3.0$	$0.197 \pm 0.020$	C <sub>2</sub>
2009.35	54959.36	1	$0.4463 \pm 0.0446$	$0.07 \pm 0.03$	$136.5 \pm 20.3$	$0.016 \pm 0.002$	C <sub>3</sub>
2009.78	55117.82	2	$0.0555 \pm 0.0056$	$0.15 \pm 0.02$	$110.0 \pm 7.7$	$0.016 \pm 0.002$	C <sub>3</sub>
2010.34	55323.28	3	$0.0136 \pm 0.0014$	$0.20 \pm 0.03$	$132.1 \pm 9.4$	$0.024 \pm 0.002$	C <sub>3</sub>
2011.35	55688.76	4	$0.0229 \pm 0.0023$	$0.27 \pm 0.03$	$101.3 \pm 6.0$	$0.016 \pm 0.002$	C <sub>3</sub>
2012.38	56065.54	6	$0.0088 \pm 0.0009$	$0.36 \pm 0.03$	$142.0 \pm 4.0$	$0.015 \pm 0.002$	C <sub>3</sub>
2009.35	54959.36	1	$0.0323 \pm 0.0032$	$0.25 \pm 0.03$	$133.6 \pm 5.9$	$0.016 \pm 0.002$	...
2009.78	55117.82	2	$0.0156 \pm 0.0016$	$0.27 \pm 0.02$	$98.8 \pm 4.3$	$0.016 \pm 0.002$	...
2011.35	55688.76	4	$0.0316 \pm 0.0032$	$0.06 \pm 0.01$	$30.1 \pm 5.3$	$0.029 \pm 0.003$	...
2011.77	55843.86	5	$0.0240 \pm 0.0024$	$0.17 \pm 0.02$	$102.5 \pm 7.9$	$0.022 \pm 0.002$	...
2009.35	54959.36	1	$2.2934 \pm 0.2293$	$0.00 \pm 0.01$	$0.0 \pm 0.0$	$0.031 \pm 0.003$	Core
2009.78	55117.82	2	$0.9664 \pm 0.0966$	$0.00 \pm 0.01$	$0.0 \pm 0.0$	$0.029 \pm 0.003$	Core
2010.34	55323.28	3	$0.5644 \pm 0.0564$	$0.00 \pm 0.01$	$0.0 \pm 0.0$	$0.038 \pm 0.004$	Core
2011.35	55688.76	4	$0.8082 \pm 0.0808$	$0.00 \pm 0.03$	$0.0 \pm 0.0$	$0.026 \pm 0.003$	Core
2011.77	55843.86	5	$0.6115 \pm 0.0612$	$0.00 \pm 0.01$	$0.0 \pm 0.0$	$0.036 \pm 0.004$	Core
2012.38	56065.54	6	$0.5826 \pm 0.0583$	$0.00 \pm 0.01$	$0.0 \pm 0.0$	$0.027 \pm 0.003$	Core



## 1H 0323+342 MODELFIT RESULTS

Table C.1: 1H 0323+342 MODELFIT results at 15 GHz. Columns from left to right: (1) observing epoch in fractional year; (2) integrated component flux density; (3) radial separation from the core; (4) position angle; (5) component size given as the FWHM of the major axis; (6) component identification label. C denotes the core, S the quasi-stationary component and C# the rest of the moving features.

EPOCH	S (Jy)	r (mas)	PA ( $^{\circ}$ )	FWHM (mas)	ID
2010.79	$0.1928 \pm 0.0193$	...	...	$0.08 \pm 0.01$	C
2010.79	$0.0635 \pm 0.0064$	$0.29 \pm 0.03$	$131.6 \pm 6.2$	$0.16 \pm 0.02$	S
2010.79	$0.0190 \pm 0.0019$	$0.96 \pm 0.08$	$127.0 \pm 4.8$	$0.41 \pm 0.04$	C5
2010.79	$0.0106 \pm 0.0011$	$1.69 \pm 0.11$	$123.9 \pm 3.6$	$0.53 \pm 0.05$	C4
2010.79	$0.0021 \pm 0.0002$	$3.11 \pm 0.19$	$123.4 \pm 3.5$	$0.94 \pm 0.09$	un
2010.79	$0.0042 \pm 0.0004$	$5.82 \pm 0.13$	$123.5 \pm 1.3$	$0.67 \pm 0.07$	C2
2010.79	$0.0105 \pm 0.0010$	$7.21 \pm 0.17$	$125.2 \pm 1.4$	$0.87 \pm 0.09$	C1
2010.79	$0.0049 \pm 0.0005$	$8.81 \pm 0.24$	$125.9 \pm 1.6$	$1.21 \pm 0.12$	C0
2011.17	$0.3215 \pm 0.0322$	...	...	$0.10 \pm 0.01$	C
2011.17	$0.0479 \pm 0.0048$	$0.28 \pm 0.02$	$131.6 \pm 4.0$	$0.10 \pm 0.01$	S
2011.17	$0.0122 \pm 0.0012$	$0.93 \pm 0.06$	$124.2 \pm 3.8$	$0.31 \pm 0.03$	C5
2011.17	$0.0135 \pm 0.0013$	$1.94 \pm 0.13$	$124.4 \pm 3.8$	$0.65 \pm 0.07$	C4
2011.17	$0.0028 \pm 0.0003$	$5.39 \pm 0.16$	$122.9 \pm 1.7$	$0.82 \pm 0.08$	C3
2011.17	$0.0088 \pm 0.0009$	$6.85 \pm 0.13$	$124.5 \pm 1.1$	$0.66 \pm 0.07$	C2
2011.17	$0.0077 \pm 0.0008$	$7.95 \pm 0.18$	$125.3 \pm 1.3$	$0.89 \pm 0.09$	C1
2011.40	$0.2514 \pm 0.0251$	...	...	$0.10 \pm 0.01$	C
2011.40	$0.0478 \pm 0.0048$	$0.34 \pm 0.02$	$135.1 \pm 3.2$	$0.10 \pm 0.01$	S
2011.40	$0.0096 \pm 0.0010$	$0.68 \pm 0.02$	$127.5 \pm 1.6$	$0.10 \pm 0.01$	C6
2011.40	$0.0064 \pm 0.0006$	$1.38 \pm 0.08$	$126.7 \pm 3.4$	$0.41 \pm 0.04$	C5
2011.40	$0.0079 \pm 0.0008$	$2.45 \pm 0.17$	$124.5 \pm 4.0$	$0.85 \pm 0.08$	C4
2011.40	$0.0061 \pm 0.0006$	$6.15 \pm 0.18$	$124.6 \pm 1.7$	$0.90 \pm 0.09$	C3
2011.40	$0.0079 \pm 0.0008$	$7.06 \pm 0.11$	$125.0 \pm 0.9$	$0.56 \pm 0.06$	C2
2011.40	$0.0053 \pm 0.0005$	$8.09 \pm 0.16$	$125.2 \pm 1.1$	$0.78 \pm 0.08$	C1
2011.53	$0.1943 \pm 0.0194$	...	...	$0.10 \pm 0.01$	C
2011.53	$0.0526 \pm 0.0053$	$0.26 \pm 0.02$	$133.4 \pm 4.2$	$0.10 \pm 0.01$	S
2011.53	$0.0127 \pm 0.0013$	$0.70 \pm 0.02$	$129.4 \pm 1.6$	$0.10 \pm 0.01$	C6
2011.53	$0.0059 \pm 0.0006$	$1.45 \pm 0.08$	$124.8 \pm 3.1$	$0.39 \pm 0.04$	C5
2011.53	$0.0067 \pm 0.0007$	$2.69 \pm 0.17$	$125.8 \pm 3.6$	$0.86 \pm 0.09$	C4

Table C.1: continued.

EPOCH	S (Jy)	r (mas)	PA (°)	FWHM (mas)	ID
2011.53	$0.0054 \pm 0.0005$	$6.27 \pm 0.19$	$123.4 \pm 1.7$	$0.96 \pm 0.10$	C <sub>3</sub>
2011.53	$0.0103 \pm 0.0010$	$7.19 \pm 0.11$	$124.9 \pm 0.9$	$0.55 \pm 0.05$	C <sub>2</sub>
2011.53	$0.0071 \pm 0.0007$	$8.99 \pm 0.37$	$125.0 \pm 2.3$	$1.83 \pm 0.18$	C <sub>1</sub>
2011.99	$0.3140 \pm 0.0314$	...	...	$0.10 \pm 0.01$	C
2011.99	$0.0212 \pm 0.0021$	$0.34 \pm 0.02$	$129.6 \pm 3.2$	$0.10 \pm 0.01$	S
2011.99	$0.0059 \pm 0.0006$	$0.89 \pm 0.02$	$129.7 \pm 1.2$	$0.10 \pm 0.01$	C <sub>6</sub>
2011.99	$0.0084 \pm 0.0008$	$1.44 \pm 0.10$	$130.9 \pm 3.9$	$0.49 \pm 0.05$	C <sub>5</sub>
2011.99	$0.0078 \pm 0.0008$	$3.53 \pm 0.34$	$121.3 \pm 5.5$	$1.71 \pm 0.17$	C <sub>4</sub>
2011.99	$0.0086 \pm 0.0009$	$6.66 \pm 0.21$	$124.5 \pm 1.8$	$1.03 \pm 0.10$	C <sub>3</sub>
2011.99	$0.0063 \pm 0.0006$	$7.52 \pm 0.07$	$125.0 \pm 0.6$	$0.37 \pm 0.04$	C <sub>2</sub>
2011.99	$0.0057 \pm 0.0006$	$8.29 \pm 0.15$	$124.2 \pm 1.0$	$0.75 \pm 0.07$	C <sub>1</sub>
2012.53	$0.1813 \pm 0.0181$	...	...	$0.10 \pm 0.01$	C
2012.53	$0.0285 \pm 0.0028$	$0.30 \pm 0.02$	$132.8 \pm 3.7$	$0.10 \pm 0.01$	S
2012.53	$0.0040 \pm 0.0004$	$1.02 \pm 0.05$	$128.9 \pm 2.5$	$0.23 \pm 0.02$	C <sub>6</sub>
2012.53	$0.0046 \pm 0.0005$	$2.34 \pm 0.16$	$125.1 \pm 3.8$	$0.78 \pm 0.08$	C <sub>5</sub>
2012.53	$0.0058 \pm 0.0006$	$4.67 \pm 0.29$	$124.0 \pm 3.6$	$1.46 \pm 0.15$	C <sub>4</sub>
2012.53	$0.0035 \pm 0.0004$	$7.04 \pm 0.03$	$125.2 \pm 0.2$	$0.15 \pm 0.02$	C <sub>3</sub>
2012.53	$0.0053 \pm 0.0005$	$7.69 \pm 0.10$	$124.6 \pm 0.7$	$0.50 \pm 0.05$	C <sub>2</sub>
2012.53	$0.0041 \pm 0.0004$	$8.89 \pm 0.19$	$125.2 \pm 1.2$	$0.96 \pm 0.10$	C <sub>1</sub>
2012.98	$0.1940 \pm 0.0194$	...	...	$0.10 \pm 0.01$	C
2012.98	$0.0395 \pm 0.0039$	$0.33 \pm 0.02$	$125.5 \pm 3.3$	$0.10 \pm 0.01$	S
2012.98	$0.0061 \pm 0.0006$	$0.88 \pm 0.04$	$133.0 \pm 2.9$	$0.22 \pm 0.02$	C <sub>6</sub>
2012.98	$0.0037 \pm 0.0004$	$2.45 \pm 0.31$	$124.3 \pm 7.1$	$1.53 \pm 0.15$	C <sub>5</sub>
2012.98	$0.0085 \pm 0.0008$	$5.03 \pm 0.38$	$123.5 \pm 4.4$	$1.92 \pm 0.19$	C <sub>4</sub>
2012.98	$0.0025 \pm 0.0002$	$6.56 \pm 0.08$	$133.4 \pm 0.7$	$0.41 \pm 0.04$	C <sub>3</sub>
2012.98	$0.0111 \pm 0.0011$	$7.88 \pm 0.37$	$124.9 \pm 2.7$	$1.85 \pm 0.19$	C <sub>2</sub>
2013.52	$0.1393 \pm 0.0139$	...	...	$0.10 \pm 0.01$	C
2013.52	$0.0309 \pm 0.0031$	$0.36 \pm 0.02$	$128.5 \pm 3.1$	$0.10 \pm 0.01$	S
2013.52	$0.0194 \pm 0.0019$	$0.67 \pm 0.02$	$126.3 \pm 1.6$	$0.10 \pm 0.01$	NC
2013.52	$0.0031 \pm 0.0003$	$1.26 \pm 0.08$	$132.4 \pm 3.7$	$0.41 \pm 0.04$	C <sub>6</sub>
2013.52	$0.0022 \pm 0.0002$	$2.15 \pm 0.02$	$124.5 \pm 0.5$	$0.10 \pm 0.01$	un
2013.52	$0.0033 \pm 0.0003$	$4.53 \pm 0.21$	$129.3 \pm 2.6$	$1.03 \pm 0.10$	C <sub>5</sub>
2013.52	$0.0079 \pm 0.0008$	$6.19 \pm 0.16$	$124.3 \pm 1.5$	$0.79 \pm 0.08$	C <sub>4</sub>
2013.52	$0.0076 \pm 0.0008$	$7.07 \pm 0.08$	$124.7 \pm 0.6$	$0.39 \pm 0.04$	C <sub>3</sub>
2013.52	$0.0041 \pm 0.0004$	$8.10 \pm 0.17$	$124.5 \pm 1.2$	$0.84 \pm 0.08$	C <sub>2</sub>
2013.52	$0.0017 \pm 0.0002$	$10.28 \pm 0.08$	$127.4 \pm 0.4$	$0.38 \pm 0.04$	C <sub>1</sub>



## BIBLIOGRAPHY

---

- A. A. Abdo, M. Ackermann, M. Ajello, M. Axelsson, L. Baldini, J. Ballet, G. Barbiellini, D. Bastieri, M. Battelino, B. M. Baughman, K. Bechtol, R. Bellazzini, E. D. Bloom, E. Bonamente, A. W. Borgland, J. Bregeon, A. Brez, M. Brigida, P. Bruel, G. A. Caliandro, R. A. Cameron, P. A. Caraveo, J. M. Casandjian, E. Cavazzuti, C. Cecchi, A. Chekhtman, C. C. Cheung, J. Chiang, S. Ciprini, R. Claus, J. Cohen-Tanugi, W. Collmar, J. Conrad, L. Costamante, C. D. Dermer, A. de Angelis, F. de Palma, S. W. Digel, E. d. C. e. Silva, P. S. Drell, R. Dubois, D. Dumora, C. Farnier, C. Favuzzi, W. B. Focke, L. Foschini, M. Frailis, L. Fuhrmann, Y. Fukazawa, S. Funk, P. Fusco, F. Gargano, N. Gehrels, S. Germani, B. Giebels, N. Giglietto, F. Giordano, M. Giroletti, T. Glanzman, I. A. Grenier, M.-H. Grondin, J. E. Grove, L. Guillemot, S. Guiriec, Y. Hanabata, A. K. Harding, R. C. Hartman, M. Hayashida, E. Hays, R. E. Hughes, G. Jóhannesson, A. S. Johnson, R. P. Johnson, W. N. Johnson, T. Kamae, H. Katagiri, J. Kataoka, M. Kerr, J. Knödseder, F. Kuehn, M. Kuss, J. Lande, L. Latronico, M. Lemoine-Goumard, F. Longo, F. Loparco, B. Lott, M. N. Lovellette, P. Lubrano, G. M. Madejski, A. Makeev, W. Max-Moerbeck, M. N. Mazziotta, W. McConville, J. E. McEnery, C. Meurer, P. F. Michelson, W. Mitthumsiri, T. Mizuno, C. Monte, M. E. Monzani, A. Morselli, I. V. Moskalenko, S. Murgia, P. L. Nolan, J. P. Norris, E. Nuss, T. Ohsugi, N. Omodei, E. Orlando, J. F. Ormes, D. Paneque, J. H. Panetta, D. Parent, V. Pavlidou, T. J. Pearson, M. Pepe, M. Pesce-Rollins, F. Piron, T. A. Porter, S. Rainò, R. Rando, M. Razzano, A. Readhead, A. Reimer, O. Reimer, T. Reposeur, J. L. Richards, S. Ritz, A. Y. Rodriguez, R. W. Romani, F. Ryde, H. F.-W. Sadrozinski, R. Sambruna, D. Sanchez, A. Sander, P. M. S. Parkinson, J. D. Scargle, T. L. Schalk, C. Sgrò, D. A. Smith, G. Spandre, P. Spinelli, J.-L. Starck, M. Stevenson, M. S. Strickman, D. J. Suson, G. Tagliaferri, H. Takahashi, T. Tanaka, J. G. Thayer, D. J. Thompson, L. Tibaldo, O. Tibolla, D. F. Torres, G. Tosti, A. Tramacere, Y. Uchiyama, T. L. Usher, N. Vilchez, V. Vitale, A. P. Waite, B. L. Winer, K. S. Wood, T. Ylinen, J. A. Zensus, M. Ziegler, Fermi/LAT Collaboration, G. Ghisellini, L. Maraschi, F. Tavecchio, and E. Angelakis. Fermi/Large Area Telescope Discovery of Gamma-Ray Emission from a Relativistic Jet in the Narrow-Line Quasar PMN J0948+0022. *ApJ*, 699:976–984, July 2009a. doi: 10.1088/0004-637X/699/2/976.
- A. A. Abdo, M. Ackermann, M. Ajello, M. Axelsson, L. Baldini, J. Ballet, G. Barbiellini, D. Bastieri, B. M. Baughman, K. Bechtol, and et al. Multiwavelength Monitoring of the Enigmatic Narrow-Line Seyfert 1 PMN J0948+0022 in 2009 March–July. *ApJ*, 707:727–737, December 2009b. doi: 10.1088/0004-637X/707/1/727.
- A. A. Abdo, M. Ackermann, M. Ajello, L. Baldini, J. Ballet, G. Barbiellini, D. Bastieri, K. Bechtol, R. Bellazzini, B. Berenji, E. D. Bloom, E. Bonamente, A. W. Borgland, J. Bregeon, A. Brez, M. Brigida, P. Bruel, T. H. Burnett, G. A. Caliandro, R. A. Cameron, P. A. Caraveo, J. M. Casandjian, C. Cecchi, Ö. Çelik, A. Chekhtman, C. C. Cheung, J. Chiang, S. Ciprini, R. Claus, J. Cohen-Tanugi, J. Conrad, S. Cutini, C. D. Dermer, F. de Palma, E. d. C. e. Silva, P. S. Drell, R. Dubois, D. Dumora, C. Farnier, C. Favuzzi, S. J. Fegan, W. B. Focke, L. Foschini, M. Frailis, Y. Fukazawa, P. Fusco, F. Gargano, N. Gehrels, S. Germani, B. Giebels, N. Giglietto, F. Giordano, M. Giroletti, T. Glanzman, G. Godfrey, I. A. Grenier, J. E. Grove, L. Guillemot, S. Guiriec, M. Hayashida, E. Hays, D. Horan, R. E. Hughes, G. Jóhannesson, A. S. Johnson, W. N. Johnson, M. Kadler, T. Kamae, H. Katagiri, J. Kataoka, M. Kerr, J. Knödseder, M. Kuss, J. Lande, L. Latronico, F. Longo, F. Loparco, B. Lott, M. N. Lovellette, P. Lubrano, A. Makeev, M. N. Mazziotta, W. McConville, J. E. McEnery, C. Meurer, P. F. Michelson, W. Mitthumsiri, T. Mizuno, C. Monte, M. E. Monzani, A. Morselli, I. V. Moskalenko, S. Murgia, P. L. Nolan, J. P. Norris, E. Nuss, T. Ohsugi, N. Omodei, E. Orlando, J. F. Ormes, V. Pelassa, M. Pepe, M. Persic, M. Pesce-Rollins, F. Piron, T. A. Porter, S. Rainò, R. Rando, M. Razzano, L. S. Rochester, A. Y. Rodriguez, F. Ryde, H. F.-W. Sadrozinski, R. Sambruna, A. Sander, P. M. Saz Parkinson, J. D. Scargle, C. Sgrò, P. D. Smith, G. Spandre, P. Spinelli, M. S. Strickman, D. J. Suson, G. Tagliaferri, H. Takahashi, T. Takahashi, T. Tanaka, J. B. Thayer, J. G. Thayer, D. J. Thompson, L. Tibaldo, O. Tibolla, D. F. Torres, G. Tosti, A. Tramacere, Y. Uchiyama, T. L. Usher, V. Vasileiou, N. Vilchez, V. Vitale, A. P. Waite, P. Wang, B. L. Winer, K. S. Wood, T. Ylinen,

- M. Ziegler, Fermi/LAT Collaboration, G. Ghisellini, L. Maraschi, and F. Tavecchio. Radio-Loud Narrow-Line Seyfert 1 as a New Class of Gamma-Ray Active Galactic Nuclei. *ApJ*, 707: L142–L147, December 2009c. doi: 10.1088/0004-637X/707/2/L142.
- A. A. Abdo, M. Ackermann, M. Ajello, W. B. Atwood, M. Axelsson, L. Baldini, J. Ballet, G. Barbiellini, D. Bastieri, B. M. Baughman, and et al. PKS 1502+106: A New and Distant Gamma-ray Blazar in Outburst Discovered by the Fermi Large Area Telescope. *ApJ*, 710:810–827, February 2010. doi: 10.1088/0004-637X/710/1/810.
- A. A. Abdo, M. Ackermann, M. Ajello, L. Baldini, J. Ballet, G. Barbiellini, D. Bastieri, K. Bechtol, R. Bellazzini, B. Berenji, and et al. Multi-wavelength Observations of the Flaring Gamma-ray Blazar 3C 66A in 2008 October. *ApJ*, 726:43, January 2011. doi: 10.1088/0004-637X/726/1/43.
- M. Ackermann, M. Ajello, A. Allafort, E. Antolini, W. B. Atwood, M. Axelsson, L. Baldini, J. Ballet, G. Barbiellini, D. Bastieri, K. Bechtol, R. Bellazzini, B. Berenji, R. D. Blandford, E. D. Bloom, E. Bonamente, A. W. Borgland, E. Bottacini, A. Bouvier, J. Bregeon, M. Brigida, P. Bruel, R. Buehler, T. H. Burnett, S. Buson, G. A. Caliandro, R. A. Cameron, P. A. Caraveo, J. M. Casandjian, E. Cavazzuti, C. Cecchi, E. Charles, C. C. Cheung, J. Chiang, S. Ciprini, R. Claus, J. Cohen-Tanugi, J. Conrad, L. Costamante, S. Cutini, A. de Angelis, F. de Palma, C. D. Dermer, S. W. Digel, E. d. C. e. Silva, P. S. Drell, R. Dubois, L. Escande, C. Favuzzi, S. J. Fegan, E. C. Ferrara, J. Finke, W. B. Focke, P. Fortin, M. Frailis, Y. Fukazawa, S. Funk, P. Fusco, F. Gargano, D. Gasparrini, N. Gehrels, S. Germani, B. Giebels, N. Giglietto, P. Giommi, F. Giordano, M. Giroletti, T. Glanzman, G. Godfrey, I. A. Grenier, J. E. Grove, S. Guiriec, M. Gustafsson, D. Hadasch, M. Hayashida, E. Hays, S. E. Healey, D. Horan, X. Hou, R. E. Hughes, G. Iafate, G. Jóhannesson, A. S. Johnson, W. N. Johnson, T. Kamae, H. Katagiri, J. Kataoka, J. Knödseder, M. Kuss, J. Lande, S. Larsson, L. Latronico, F. Longo, F. Loparco, B. Lott, M. N. Lovellette, P. Lubrano, G. M. Madejski, M. N. Mazziotta, W. McConville, J. E. McEnery, P. F. Michelson, W. Mitthumsiri, T. Mizuno, A. A. Moiseev, C. Monte, M. E. Monzani, E. Moretti, A. Morselli, I. V. Moskalenko, S. Murgia, T. Nakamori, M. Naumann-Godo, P. L. Nolan, J. P. Norris, E. Nuss, M. Ohno, T. Ohsugi, A. Okumura, N. Omodei, M. Orienti, E. Orlando, J. F. Ormes, M. Ozaki, D. Paneque, D. Parent, M. Pesce-Rollins, M. Pierbattista, S. Piranomonte, F. Piron, G. Pivato, T. A. Porter, S. Rainò, R. Rando, M. Razzano, S. Razzaque, A. Reimer, O. Reimer, S. Ritz, L. S. Rochester, R. W. Romani, M. Roth, D. A. Sanchez, C. Sbarra, J. D. Scargle, T. L. Schalk, C. Sgrò, M. S. Shaw, E. J. Siskind, G. Spandre, P. Spinelli, A. W. Strong, D. J. Suson, H. Tajima, H. Takahashi, T. Takahashi, T. Tanaka, J. G. Thayer, J. B. Thayer, D. J. Thompson, L. Tibaldo, M. Tinivella, D. F. Torres, G. Tosti, E. Troja, Y. Uchiyama, J. Vandenbroucke, V. Vasileiou, G. Vianello, V. Vitale, A. P. Waite, E. Wallace, P. Wang, B. L. Winer, D. L. Wood, K. S. Wood, and S. Zimmer. The Second Catalog of Active Galactic Nuclei Detected by the Fermi Large Area Telescope. *ApJ*, 743:171, December 2011. doi: 10.1088/0004-637X/743/2/171.
- J. K. Adelman-McCarthy, M. A. Agüeros, S. S. Allam, C. Allende Prieto, K. S. J. Anderson, S. F. Anderson, J. Annis, N. A. Bahcall, C. A. L. Bailer-Jones, I. K. Baldry, J. C. Barentine, B. A. Bassett, A. C. Becker, T. C. Beers, E. F. Bell, A. A. Berlind, M. Bernardi, M. R. Blanton, J. J. Bochanski, W. N. Boroski, J. Brinchmann, J. Brinkmann, R. J. Brunner, T. Budavári, S. Carliles, M. A. Carr, F. J. Castander, D. Cinabro, R. J. Cool, K. R. Covey, I. Csabai, C. E. Cunha, J. R. A. Davenport, B. Dilday, M. Doi, D. J. Eisenstein, M. L. Evans, X. Fan, D. P. Finkbeiner, S. D. Friedman, J. A. Frieman, M. Fukugita, B. T. Gänsicke, E. Gates, B. Gillespie, K. Glazebrook, J. Gray, E. K. Grebel, J. E. Gunn, V. K. Gurbani, P. B. Hall, P. Harding, M. Harvanek, S. L. Hawley, J. Hayes, T. M. Heckman, J. S. Hendry, R. B. Hindsley, C. M. Hirata, C. J. Hogan, D. W. Hogg, J. B. Hyde, S.-i. Ichikawa, Ž. Ivezić, S. Jester, J. A. Johnson, A. M. Jorgensen, M. Jurić, S. M. Kent, R. Kessler, S. J. Kleinman, G. R. Knapp, R. G. Kron, J. Krzesinski, N. Kuropatkin, D. Q. Lamb, H. Lampeitl, S. Lebedeva, Y. S. Lee, R. F. Leger, S. Lépine, M. Lima, H. Lin, D. C. Long, C. P. Loomis, J. Loveday, R. H. Lupton, O. Malanushenko, V. Malanushenko, R. Mandelbaum, B. Margon, J. P. Marriner, D. Martínez-Delgado, T. Matsubara, P. M. McGehee, T. A. McKay, A. Meiksin, H. L. Morrison, J. A. Munn, R. Nakajima, E. H. Neilsen, Jr., H. J. Newberg, R. C. Nichol, T. Nicinski, M. Nieto-Santisteban, A. Nitta, S. Okamura, R. Owen, H. Oyaizu, N. Padmanabhan, K. Pan, C. Park, J. Peoples, Jr., J. R. Pier, A. C. Pope, N. Purger, M. J. Rad-dick, P. Re Fiorentin, G. T. Richards, M. W. Richmond, A. G. Riess, H.-W. Rix, C. M. Rockosi,

- M. Sako, D. J. Schlegel, D. P. Schneider, M. R. Schreiber, A. D. Schwobe, U. Seljak, B. Sesar, E. Sheldon, K. Shimasaku, T. Sivarani, J. A. Smith, S. A. Snedden, M. Steinmetz, M. A. Strauss, M. SubbaRao, Y. Suto, A. S. Szalay, I. Szapudi, P. Szkody, M. Tegmark, A. R. Thakar, C. A. Tremonti, D. L. Tucker, A. Uomoto, D. E. Vanden Berk, J. Vandenberg, S. Vidrih, M. S. Vogeley, W. Voges, N. P. Vogt, Y. Wadadekar, D. H. Weinberg, A. A. West, S. D. M. White, B. C. Wilhite, B. Yanny, D. R. Yocum, D. G. York, I. Zehavi, and D. B. Zucker. The Sixth Data Release of the Sloan Digital Sky Survey. *ApJS*, 175:297–313, April 2008. doi: 10.1086/524984.
- F. Agterberg. *Geomathematics: Theoretical Foundations, Applications and Future Developments*. Quantitative geology and geostatistics. Springer, 2014. ISBN 9783319068749. URL <http://books.google.de/books?id=MjkkqBAAAQBAJ>.
- I. Agudo, S. G. Jorstad, A. P. Marscher, V. M. Larionov, J. L. Gómez, A. Lähteenmäki, M. Gurwell, P. S. Smith, H. Wiesemeyer, C. Thum, J. Heidt, D. A. Blinov, F. D. D’Arcangelo, V. A. Hagen-Thorn, D. A. Morozova, E. Nieppola, M. Roca-Sogorb, G. D. Schmidt, B. Taylor, M. Tornikoski, and I. S. Troitsky. Location of  $\gamma$ -ray Flare Emission in the Jet of the BL Lacertae Object OJ287 More than 14 pc from the Central Engine. *ApJ*, 726:L13, January 2011. doi: 10.1088/2041-8205/726/1/L13.
- W. Alef. Introduction to phase-reference mapping. In M. Felli and R. E. Spencer, editors, *NATO Advanced Science Institutes (ASI) Series C*, volume 283 of *NATO Advanced Science Institutes (ASI) Series C*, pages 261–274, 1989.
- W. Alef and R. W. Porcas. VLBI fringe-fitting with antenna-based residuals. *A&A*, 168:365–368, November 1986.
- T. An, X. Y. Hong, T. Venturi, D. R. Jiang, and W. H. Wang. Extreme superluminal motion in the curved Jet of PKS 1502+106. *A&A*, 421:839–846, July 2004. doi: 10.1051/0004-6361:20035816.
- E. Angelakis, L. Fuhrmann, I. Nestoras, J. A. Zensus, N. Marchili, V. Pavlidou, and T. P. Krichbaum. The F-GAMMA program: multi-wavelength AGN studies in the Fermi-GST era. *ArXiv e-prints*, June 2010.
- E. Angelakis, L. Fuhrmann, N. Marchili, L. Foschini, I. Myserlis, V. Karamanavis, S. Komossa, D. Blinov, T. P. Krichbaum, A. Sievers, H. Ungerechts, and J. A. Zensus. Radio jet emission from GeV-emitting narrow-line Seyfert 1 galaxies. *A&A*, 575:A55, March 2015. doi: 10.1051/0004-6361/201425081.
- S. Antón, I. W. A. Browne, and M. J. Marchã. The colour of the narrow line Sy1-blazar 0324+3410. *A&A*, 490:583–587, November 2008. doi: 10.1051/0004-6361:20078926.
- R. R. J. Antonucci and J. S. Miller. Spectropolarimetry and the nature of NGC 1068. *ApJ*, 297: 621–632, October 1985. doi: 10.1086/163559.
- T. G. Arshakian, J. León-Tavares, M. Böttcher, J. Torrealba, V. H. Chavushyan, M. L. Lister, E. Ros, and J. A. Zensus. Radio-optical-gamma-ray properties of MOJAVE AGN detected by Fermi/LAT. *A&A*, 537:A32, January 2012. doi: 10.1051/0004-6361/201117140.
- K. Asada, M. Inoue, Y. Uchida, S. Kameno, K. Fujisawa, S. Iguchi, and M. Mutoh. A Helical Magnetic Field in the Jet of 3C 273. *PASJ*, 54:L39–L43, June 2002. doi: 10.1093/pasj/54.3.L39.
- W. B. Atwood, A. A. Abdo, M. Ackermann, W. Althouse, B. Anderson, M. Axelsson, L. Baldini, J. Ballet, D. L. Band, G. Barbiellini, and et al. The Large Area Telescope on the Fermi Gamma-Ray Space Telescope Mission. *ApJ*, 697:1071–1102, June 2009. doi: 10.1088/0004-637X/697/2/1071.
- U. Bach, T. P. Krichbaum, E. Ros, S. Britzen, W. W. Tian, A. Kraus, A. Witzel, and J. A. Zensus. Kinematic study of the blazar S5 0716+714. *A&A*, 433:815–825, April 2005. doi: 10.1051/0004-6361:20040388.

- U. Bach, M. Villata, C. M. Raiteri, I. Agudo, H. D. Aller, M. F. Aller, G. Denn, J. L. Gómez, S. Jorstad, A. Marscher, R. L. Mutel, and H. Teräsranta. Structure and flux variability in the VLBI jet of BL Lacertae during the WEBT campaigns (1995-2004). *A&A*, 456:105–115, September 2006. doi: 10.1051/0004-6361:20065235.
- P. D. Barthel. Unified Schemes of FR2 Radio Galaxies and Quasars. In G. V. Bicknell, M. A. Dopita, and P. J. Quinn, editors, *The Physics of Active Galaxies*, volume 54 of *Astronomical Society of the Pacific Conference Series*, page 175, 1994.
- A. S. Bennett. The revised 3C catalogue of radio sources. *MmRAS*, 68:163, 1962.
- R. D. Blandford. Black Holes and Relativistic Jets. *Progress of Theoretical Physics Supplement*, 143: 182–201, 2001. doi: 10.1143/PTPS.143.182.
- R. D. Blandford and A. Königl. Relativistic jets as compact radio sources. *ApJ*, 232:34–48, August 1979. doi: 10.1086/157262.
- R. D. Blandford and A. Levinson. Pair cascades in extragalactic jets. 1: Gamma rays. *ApJ*, 441: 79–95, March 1995. doi: 10.1086/175338.
- R. D. Blandford and D. G. Payne. Hydromagnetic flows from accretion discs and the production of radio jets. *MNRAS*, 199:883–903, June 1982.
- R. D. Blandford and R. L. Znajek. Electromagnetic extraction of energy from Kerr black holes. *MNRAS*, 179:433–456, May 1977.
- M. Boettcher. Models for the Spectral Energy Distributions and Variability of Blazars. *ArXiv e-prints: 1006.5048*, June 2010.
- S. Bogovalov and K. Tsiganos. Shock formation at the magnetic collimation of relativistic jets. *MNRAS*, 357:918–928, March 2005. doi: 10.1111/j.1365-2966.2005.08671.x.
- M. Camenzind and M. Krockenberger. The lighthouse effect of relativistic jets in blazars - A geometric origin of intraday variability. *A&A*, 255:59–62, February 1992.
- W. W. Campbell and J. H. Moore. The spectrographic velocities of the bright-line nebulae. *Publications of Lick Observatory*, 13:75–186, 1918.
- S. Ciprini. GLAST LAT detection of a possible new gamma-ray flaring blazar: PKS 1502+106. *The Astronomer's Telegram*, 1650:1, August 2008.
- B. G. Clark. Coherence in Radio Astronomy. In G. B. Taylor, C. L. Carilli, and R. A. Perley, editors, *Synthesis Imaging in Radio Astronomy II*, volume 180 of *Astronomical Society of the Pacific Conference Series*, page 1, 1999.
- M. H. Cohen, W. Cannon, G. H. Purcell, D. B. Shaffer, J. J. Broderick, K. I. Kellermann, and D. L. Jauncey. The Small-Scale Structure of Radio Galaxies and Quasi-Stellar Sources at 3.8 Centimeters. *ApJ*, 170:207, December 1971. doi: 10.1086/151204.
- M. H. Cohen, R. P. Linfield, A. T. Moffet, G. A. Seielstad, K. I. Kellermann, D. B. Shaffer, I. I. K. Pauliny-Toth, E. Preuss, A. Witzel, and J. D. Romney. Radio sources with superluminal velocities. *Nature*, 268:405–409, August 1977. doi: 10.1038/268405a0.
- N. J. Cooper, M. L. Lister, and M. D. Kochanzyk. MOJAVE: Monitoring of Jets in Active Galactic Nuclei with VLBA Experiments. III. Deep VLA Images at 1.4 GHz. *ApJS*, 171:376–388, August 2007. doi: 10.1086/518654.
- T. J. Cornwell and P. N. Wilkinson. A new method for making maps with unstable radio interferometers. *MNRAS*, 196:1067–1086, September 1981.
- W. D. Cotton. Fringe Fitting. In J. A. Zensus, P. J. Diamond, and P. J. Napier, editors, *Very Long Baseline Interferometry and the VLBA*, volume 82 of *Astronomical Society of the Pacific Conference Series*, page 189, 1995.

- S. M. Croke, S. P. O'Sullivan, and D. C. Gabuzda. The parsec-scale distributions of intensity, linear polarization and Faraday rotation in the core and jet of Mrk501 at 8.4-1.6 GHz. *MNRAS*, 402:259–270, February 2010. doi: 10.1111/j.1365-2966.2009.15923.x.
- R. A. Daly and A. P. Marscher. The gasdynamics of compact relativistic jets. *ApJ*, 334:539–551, November 1988. doi: 10.1086/166858.
- F. D'Ammando, J. Larsson, M. Orienti, C. M. Raiteri, E. Angelakis, A. Carramiñana, L. Carrasco, A. J. Drake, L. Fuhrmann, M. Giroletti, T. Hovatta, W. Max-Moerbeck, A. Porras, A. C. S. Readhead, E. Recillas, and J. L. Richards. Multiwavelength observations of the  $\gamma$ -ray-emitting narrow-line Seyfert 1 PMN J0948+0022 in 2011. *MNRAS*, 438:3521–3534, March 2014. doi: 10.1093/mnras/stt2464.
- F. D'Ammando, M. Orienti, J. Finke, C. M. Raiteri, T. Hovatta, J. Larsson, W. Max-Moerbeck, J. Perkins, A. C. S. Readhead, J. L. Richards, M. Beilicke, W. Benbow, K. Berger, R. Bird, V. Bugaev, J. V. Cardenzana, M. Cerruti, X. Chen, L. Ciupik, H. J. Dickinson, J. D. Eisch, M. Errando, A. Falcone, J. P. Finley, H. Fleischhack, P. Fortin, L. Fortson, A. Furniss, L. Gerard, G. H. Gillanders, S. T. Griffiths, J. Grube, G. Gyuk, N. Håkansson, J. Holder, T. B. Humensky, P. Kar, M. Kertzman, Y. Khassen, D. Kieda, F. Krennrich, S. Kumar, M. J. Lang, G. Maier, A. McCann, K. Meagher, P. Moriarty, R. Mukherjee, D. Nieto, A. O. de Bhróithe, R. A. Ong, A. N. Otte, M. Pohl, A. Popkow, H. Prokoph, E. Pueschel, J. Quinn, K. Ragan, P. T. Reynolds, G. T. Richards, E. Roache, J. Rousselle, M. Santander, G. H. Sembroski, A. W. Smith, D. Staszak, I. Tezhinsky, J. V. Tucci, J. Tyler, A. Varlotta, V. V. Vassiliev, S. P. Wakely, A. Weinstein, R. Welsing, D. A. Williams, and B. Zitzer. The most powerful flaring activity from the NLSy1 PMN J0948+0022. *MNRAS*, 446:2456–2467, January 2015. doi: 10.1093/mnras/stu2251.
- C. D. Dermer, K. Murase, and H. Takami. Variable Gamma-Ray Emission Induced by Ultra-high Energy Neutral Beams: Application to 4C +21.35. *ApJ*, 755:147, August 2012. doi: 10.1088/0004-637X/755/2/147.
- D. Downes. Radio Astronomy Techniques. In I. Appenzeller, H. J. Habing, and P. Lena, editors, *Evolution of Galaxies: Astronomical Observations*, volume 333 of *Lecture Notes in Physics*, Berlin Springer Verlag, page 351, 1989. doi: 10.1007/3-540-51315-9\_8.
- R. A. Edelson and J. H. Krolik. The discrete correlation function - A new method for analyzing unevenly sampled variability data. *ApJ*, 333:646–659, October 1988. doi: 10.1086/166773.
- H. Falcke, E. Körding, and S. Markoff. A scheme to unify low-power accreting black holes. Jet-dominated accretion flows and the radio/X-ray correlation. *A&A*, 414:895–903, February 2004. doi: 10.1051/0004-6361:20031683.
- A. D. Falcone, I. H. Bond, P. J. Boyle, S. M. Bradbury, J. H. Buckley, D. Carter-Lewis, O. Celik, W. Cui, M. Daniel, M. D'Vali, I. de la Calle Perez, C. Duke, D. J. Fegan, S. J. Fegan, J. P. Finley, L. F. Fortson, J. Gaidos, S. Gammell, K. Gibbs, G. H. Gillanders, J. Grube, J. Hall, T. A. Hall, D. Hanna, A. M. Hillas, J. Holder, D. Horan, A. Jarvis, G. E. Kenny, M. Kertzman, D. Kieda, J. Kildea, J. Knapp, K. Kosack, H. Krawczynski, F. Krennrich, M. J. Lang, S. LeBohec, E. Linton, J. Lloyd-Evans, A. Milovanovic, P. Moriarty, D. Muller, T. Nagai, S. Nolan, R. Ong, R. Palladini, D. Petry, F. Pizlo, B. Power-Mooney, J. Quinn, M. Quinn, K. Ragan, P. Rebillot, P. T. Reynolds, H. J. Rose, M. Schroedter, G. Sembroski, S. P. Swordy, A. Syson, K. Tyler, V. V. Vassiliev, S. P. Wakely, G. Walker, T. C. Weekes, and J. Zweerink. A Search for TeV Gamma-Ray Emission from High-peaked Flat-Spectrum Radio Quasars Using the Whipple Air Cerenkov Telescope. *ApJ*, 613:710–715, October 2004. doi: 10.1086/423128.
- B. L. Fanaroff and J. M. Riley. The morphology of extragalactic radio sources of high and low luminosity. *MNRAS*, 167:31P–36P, May 1974.
- E. A. Fath. The Spectra of Some Spiral Nebulae and Globular Star Clusters. *Popular Astronomy*, 17:504–508, October 1909.
- L. Ferrarese and H. Ford. Supermassive Black Holes in Galactic Nuclei: Past, Present and Future Research. *Space Sci. Rev.*, 116:523–624, February 2005. doi: 10.1007/s11214-005-3947-6.

- A. L. Fey, A. W. Clegg, and R. L. Fiedler. VLBI Observations of Eight Extreme Scattering Event Sources: Milliarcsecond-Scale Structure. *ApJ*, 468:543, September 1996. doi: 10.1086/177713.
- L. Foschini. Evidence of powerful relativistic jets in narrow-line Seyfert 1 galaxies. In *Narrow-Line Seyfert 1 Galaxies and their Place in the Universe*, page 24, 2011.
- L. Foschini, Fermi/Lat Collaboration, G. Ghisellini, L. Maraschi, F. Tavecchio, and E. Angelakis. Fermi/LAT Discovery of Gamma-Ray Emission from a Relativistic Jet in the Narrow-Line Seyfert 1 Quasar PMN J0948+0022. In L. Maraschi, G. Ghisellini, R. Della Ceca, and F. Tavecchio, editors, *Accretion and Ejection in AGN: a Global View*, volume 427 of *Astronomical Society of the Pacific Conference Series*, pages 243–248, October 2010.
- L. Foschini, G. Ghisellini, Y. Y. Kovalev, M. L. Lister, F. D’Ammando, D. J. Thompson, A. Tramacere, E. Angelakis, D. Donato, A. Falcone, L. Fuhrmann, M. Hauser, Y. A. Kovalev, K. Mannheim, L. Maraschi, W. Max-Moerbeck, I. Nestoras, V. Pavlidou, T. J. Pearson, A. B. Pushkarev, A. C. S. Readhead, J. L. Richards, M. A. Stevenson, G. Tagliaferri, O. Tibolla, F. Tavecchio, and S. Wagner. The first gamma-ray outburst of a narrow-line Seyfert 1 galaxy: the case of PMN J0948+0022 in 2010 July. *MNRAS*, 413:1671–1677, May 2011. doi: 10.1111/j.1365-2966.2011.18240.x.
- L. Foschini, M. Berton, A. Caccianiga, S. Ciroi, V. Cracco, B. M. Peterson, E. Angelakis, V. Braito, L. Fuhrmann, L. Gallo, D. Grupe, E. Järvelä, S. Kaufmann, S. Komossa, Y. Y. Kovalev, A. Lähteenmäki, M. M. Lisakov, M. L. Lister, S. Mathur, J. L. Richards, P. Romano, A. Sievers, G. Tagliaferri, J. Tammi, O. Tibolla, M. Tornikoski, S. Vercellone, G. La Mura, L. Maraschi, and P. Rafanelli. Properties of flat-spectrum radio-loud narrow-line Seyfert 1 galaxies. *A&A*, 575:A13, March 2015. doi: 10.1051/0004-6361/201424972.
- C. M. Fromm, M. Perucho, E. Ros, T. Savolainen, A. P. Lobanov, J. A. Zensus, M. F. Aller, H. D. Aller, M. A. Gurwell, and A. Lähteenmäki. Catching the radio flare in CTA 102. I. Light curve analysis. *A&A*, 531:A95, July 2011. doi: 10.1051/0004-6361/201116857.
- C. M. Fromm, E. Ros, M. Perucho, T. Savolainen, P. Mimica, M. Kadler, A. P. Lobanov, M. L. Lister, Y. Y. Kovalev, and J. A. Zensus. Catching the radio flare in CTA 102. II. VLBI kinematic analysis. *A&A*, 551:A32, March 2013a. doi: 10.1051/0004-6361/201219913.
- C. M. Fromm, E. Ros, M. Perucho, T. Savolainen, P. Mimica, M. Kadler, A. P. Lobanov, and J. A. Zensus. Catching the radio flare in CTA 102. III. Core-shift and spectral analysis. *A&A*, 557:A105, September 2013b. doi: 10.1051/0004-6361/201321784.
- C. M. Fromm, L. Fuhrmann, and M. Perucho. Multi-frequency properties of synthetic blazar radio light curves within the shock-in-jet scenario. *ArXiv e-prints: 1412.7194*, December 2014.
- L. Fuhrmann, J. A. Zensus, T. P. Krichbaum, E. Angelakis, and A. C. S. Readhead. Simultaneous Radio to (Sub-) mm-Monitoring of Variability and Spectral Shape Evolution of potential GLAST Blazars. In S. Ritz, P. Michelson, and C. A. Meegan, editors, *The First GLAST Symposium*, volume 921 of *American Institute of Physics Conference Series*, pages 249–251, July 2007. doi: 10.1063/1.2757314.
- L. Fuhrmann, T. P. Krichbaum, A. Witzel, A. Kraus, S. Britzen, S. Bernhart, C. M. V. Impellizzeri, I. Agudo, J. Klare, B. W. Sohn, E. Angelakis, U. Bach, K. É. Gabányi, E. Körding, A. Pagels, J. A. Zensus, S. J. Wagner, L. Ostorero, H. Ungerechts, M. Grewing, M. Tornikoski, A. J. Apponi, B. Vila-Vilaró, L. M. Ziurys, and R. G. Strom. Testing the inverse-Compton catastrophe scenario in the intra-day variable blazar S5 0716+71. III. Rapid and correlated flux density variability from radio to sub-mm bands. *A&A*, 490:1019–1037, November 2008. doi: 10.1051/0004-6361:20078893.
- L. Fuhrmann, E. Angelakis, I. Nestoras, T. P. Krichbaum, N. Marchili, R. Schmidt, J. A. Zensus, H. Unberegts, A. Sievers, D. Riquelme, L. Foschini, G. Ghisellini, G. Ghirlanda, G. Tagliaferri, F. Tavecchio, L. Maraschi, M. Giroletti, G. Calderone, M. Colpi, and R. Decarli. Gamma-ray NLSy1s and ‘classical’ blazars: are they different at radio cm/mm bands? In *Narrow-Line Seyfert 1 Galaxies and their Place in the Universe*, page 26, 2011.

- L. Fuhrmann, S. Larsson, J. Chiang, E. Angelakis, J. A. Zensus, I. Nestoras, T. P. Krichbaum, H. Ungerechts, A. Sievers, V. Pavlidou, A. C. S. Readhead, W. Max-Moerbeck, and T. J. Pearson. Detection of significant cm to sub-mm band radio and  $\gamma$ -ray correlated variability in Fermi bright blazars. *MNRAS*, 441:1899–1909, July 2014. doi: 10.1093/mnras/stu540.
- D. C. Gabuzda. The nature of compact parsec-scale knots in AGN: clues from their polarisation properties. *New A Rev.*, 47:599–603, October 2003. doi: 10.1016/S1387-6473(03)00102-7.
- D. C. Gabuzda, É. Murray, and P. Cronin. Helical magnetic fields associated with the relativistic jets of four BL Lac objects. *MNRAS*, 351:L89–L93, July 2004. doi: 10.1111/j.1365-2966.2004.08037.x.
- C. M. Gaskell and B. M. Peterson. The accuracy of cross-correlation estimates of quasar emission-line region sizes. *ApJS*, 65:1–11, September 1987. doi: 10.1086/191216.
- C. M. Gaskell and L. S. Sparke. Line variations in quasars and Seyfert galaxies. *ApJ*, 305:175–186, June 1986. doi: 10.1086/164238.
- M. Georganopoulos, J. G. Kirk, and A. Mastichiadis. The Beaming Pattern and Spectrum of Radiation from Inverse Compton Scattering in Blazars. *ApJ*, 561:111–117, November 2001. doi: 10.1086/323225.
- I. M. George, K. Nandra, T. J. Turner, and A. Celotti. The X-ray spectrum of the highly polarized quasar PKS 1502+106. *ApJ*, 436:L59–L62, November 1994. doi: 10.1086/187632.
- G. Ghisellini and A. Celotti. The dividing line between FR I and FR II radio-galaxies. *A&A*, 379:L1–L4, November 2001. doi: 10.1051/0004-6361:20011338.
- D. Giannios. Reconnection-driven plasmoids in blazars: fast flares on a slow envelope. *MNRAS*, 431:355–363, May 2013. doi: 10.1093/mnras/stt167.
- V. L. Ginzburg and S. I. Syrovatskii. Cosmic Magnetobremstrahlung (synchrotron Radiation). *ARA&A*, 3:297, 1965. doi: 10.1146/annurev.aa.03.090165.001501.
- M. Giroletti, Z. Paragi, H. Bignall, A. Doi, L. Foschini, K. É. Gabányi, C. Reynolds, J. Blanchard, R. M. Campbell, F. Colomer, X. Hong, M. Kadler, M. Kino, H. J. van Langevelde, H. Nagai, C. Phillips, M. Sekido, A. Szomoru, and A. K. Tzioumis. Global e-VLBI observations of the gamma-ray narrow line Seyfert 1 PMN J0948+0022. *A&A*, 528:L11, April 2011. doi: 10.1051/0004-6361/201116639.
- J. L. Gómez, J. M. A. Martí, A. P. Marscher, J. M. A. Ibanez, and J. M. Marcaide. Parsec-Scale Synchrotron Emission from Hydrodynamic Relativistic Jets in Active Galactic Nuclei. *ApJ*, 449:L19, August 1995. doi: 10.1086/309623.
- R. W. Goodrich. Spectropolarimetry and variability of Seyfert 1.8 and 1.9 galaxies. *ApJ*, 340:190–202, May 1989. doi: 10.1086/167384.
- E. W. Greisen. The Astronomical Image Processing System. In G. Longo and G. Sedmak, editors, *Acquisition, Processing and Archiving of Astronomical Images*, pages 125–142, 1990.
- D. Grupe. Statistical properties of narrow-line Seyfert 1 galaxies. *New A Rev.*, 44:455–460, September 2000. doi: 10.1016/S1387-6473(00)00080-4.
- J. Gubbay, A. J. Legg, D. S. Robertson, A. T. Moffet, R. D. Ekers, and B. Seidel. Variations of Small Quasar Components at 2,300 MHz. *Nature*, 224:1094–1095, December 1969. doi: 10.1038/2241094bo.
- M. A. Gurwell, A. B. Peck, S. R. Hostler, M. R. Darrah, and C. A. Katz. Monitoring Phase Calibrators at Submillimeter Wavelengths. In A. J. Baker, J. Glenn, A. I. Harris, J. G. Mangum, and M. S. Yun, editors, *From Z-Machines to ALMA: (Sub)Millimeter Spectroscopy of Galaxies*, volume 375 of *Astronomical Society of the Pacific Conference Series*, page 234, October 2007.

- C. R. Gwinn, Y. Y. Kovalev, M. D. Johnson, and V. A. Soglasnov. Discovery of Substructure in the Scatter-broadened Image of Sgr A\*. *ApJ*, 794:L14, October 2014. doi: 10.1088/2041-8205/794/1/L14.
- K. Hada, A. Doi, M. Kino, H. Nagai, Y. Hagiwara, and N. Kawaguchi. An origin of the radio jet in M87 at the location of the central black hole. *Nature*, 477:185–187, September 2011. doi: 10.1038/nature10387.
- P. E. Hardee. 3D structures on relativistic jets. *New A Rev.*, 46:427–432, May 2002. doi: 10.1016/S1387-6473(02)00155-0.
- P. E. Hardee. Stability Properties of Strongly Magnetized Spine-Sheath Relativistic Jets. *ApJ*, 664: 26–46, July 2007. doi: 10.1086/518409.
- R. C. Hartman, D. L. Bertsch, C. E. Fichtel, S. D. Hunter, D. J. Thompson, G. Kanbach, H. A. Mayer-Hasselwander, C. von Montigny, K. Pinkau, D. A. Kniffen, Y. C. Lin, P. F. Michelson, P. L. Nolan, J. R. Mattox, B. G. Piner, E. Schneid, P. Sreekumar, and B. L. Dingus. Unidentified High Energy Gamma Ray Sources Detected by EGRET at High Galactic Latitudes. In *American Astronomical Society Meeting Abstracts*, volume 24 of *Bulletin of the American Astronomical Society*, page 1155, September 1992.
- C. Hazard. Lunar Occultation of a Radio Source. *Nature*, 191:58, July 1961. doi: 10.1038/191058a0.
- C. Hazard. The method of lunar occultations and its application to a survey of the radio sources 3C 212. *MNRAS*, 124:343, 1962.
- C. Hazard, M. B. Mackey, and A. J. Shimmins. Investigation of the Radio Source 3C 273 By The Method of Lunar Occultations. *Nature*, 197:1037–1039, March 1963. doi: 10.1038/1971037a0.
- H. Hirabayashi, H. Hirose, H. Kobayashi, Y. Murata, P. G. Edwards, E. B. Fomalont, K. Fujisawa, T. Ichikawa, T. Kii, J. E. J. Lovell, G. A. Moellenbrock, R. Okayasu, M. Inoue, N. Kawaguchi, S. Kameno, K. M. Shibata, Y. Asaki, T. Bushimata, S. Enome, S. Horiuchi, T. Miyaji, T. Umemoto, V. Migenes, K. Wajima, J. Nakajima, M. Morimoto, J. Ellis, D. L. Meier, D. W. Murphy, R. A. Preston, J. G. Smith, S. J. Tingay, D. L. Traub, R. D. Wietfeldt, J. M. Benson, M. J. Claussen, C. Flatters, J. D. Romney, J. S. Ulvestad, L. R. D’Addario, G. I. Langston, A. H. Minter, B. R. Carlson, P. E. Dewdney, D. L. Jauncey, J. E. Reynolds, A. R. Taylor, P. M. McCulloch, W. H. Cannon, L. I. Gurvits, A. J. Mioduszewski, R. T. Schilizzi, and R. S. Booth. Overview and Initial Results of the Very Long Baseline Interferometry Space Observatory Programme. *Science*, 281:1825, September 1998. doi: 10.1126/science.281.5384.1825.
- K. Hirotani. Kinetic Luminosity and Composition of Active Galactic Nuclei Jets. *ApJ*, 619:73–85, January 2005. doi: 10.1086/426497.
- L. C. Ho. On the Relationship between Radio Emission and Black Hole Mass in Galactic Nuclei. *ApJ*, 564:120–132, January 2002. doi: 10.1086/324399.
- J. A. Högbom. Aperture Synthesis with a Non-Regular Distribution of Interferometer Baselines. *A&AS*, 15:417, June 1974.
- D. C. Homan, M. L. Lister, Y. Y. Kovalev, A. B. Pushkarev, T. Savolainen, K. I. Kellermann, J. L. Richards, and E. Ros. MOJAVE. XII. Acceleration and Collimation of Blazar Jets on Parsec Scales. *ApJ*, 798:134, January 2015. doi: 10.1088/0004-637X/798/2/134.
- T. Hovatta, E. Valtaoja, M. Tornikoski, and A. Lähteenmäki. Doppler factors, Lorentz factors and viewing angles for quasars, BL Lacertae objects and radio galaxies. *A&A*, 494:527–537, February 2009. doi: 10.1051/0004-6361:200811150.
- T. Hovatta, M. L. Lister, M. F. Aller, H. D. Aller, D. C. Homan, Y. Y. Kovalev, A. B. Pushkarev, and T. Savolainen. MOJAVE: Monitoring of Jets in Active Galactic Nuclei with VLBA Experiments. VIII. Faraday Rotation in Parsec-scale AGN Jets. *AJ*, 144:105, October 2012. doi: 10.1088/0004-6256/144/4/105.



- Željko Ivezić, Andrew J. Connolly, Jacob T. VanderPlas, and Alexander Gray. *Statistics, Data Mining, and Machine Learning in Astronomy*. Princeton Series in Modern Observational Astronomy. Princeton University Press, student edition edition, 2014. URL <http://www.jstor.org/stable/j.ctt4cgbdj>.
- W. Jaffe, H. C. Ford, L. Ferrarese, F. van den Bosch, and R. W. O'Connell. A large nuclear accretion disk in the active galaxy NGC4261. *Nature*, 364:213–215, July 1993. doi: 10.1038/364213a0.
- W. Jaffe, H. Ford, L. Ferrarese, F. van den Bosch, and R. W. O'Connell. The Nuclear Disk of NGC 4261: Hubble Space Telescope Images and Ground-based Spectra. *ApJ*, 460:214, March 1996. doi: 10.1086/176963.
- K. G. Jansky. Radio Waves from Outside the Solar System. *Nature*, 132:66, July 1933. doi: 10.1038/132066a0.
- S. G. Jorstad, A. P. Marscher, M. L. Lister, A. M. Stirling, T. V. Cawthorne, W. K. Gear, J. L. Gómez, J. A. Stevens, P. S. Smith, J. R. Forster, and E. I. Robson. Polarimetric Observations of 15 Active Galactic Nuclei at High Frequencies: Jet Kinematics from Bimonthly Monitoring with the Very Long Baseline Array. *AJ*, 130:1418–1465, October 2005. doi: 10.1086/444593.
- W. Junor, J. A. Biretta, and M. Livio. Formation of the radio jet in M87 at 100 Schwarzschild radii from the central black hole. *Nature*, 401:891–892, October 1999. doi: 10.1038/44780.
- M. Kadler, D. Eisenacher, E. Ros, K. Mannheim, D. Elsässer, and U. Bach. The blazar-like radio structure of the TeV source IC 310. *A&A*, 538:L1, February 2012. doi: 10.1051/0004-6361/201118212.
- C. R. Kaiser. The flat synchrotron spectra of partially self-absorbed jets revisited. *MNRAS*, 367: 1083–1094, April 2006. doi: 10.1111/j.1365-2966.2006.10030.x.
- K. I. Kellermann and I. I. K. Pauliny-Toth. The Spectra of Opaque Radio Sources. *ApJ*, 155:L71, February 1969. doi: 10.1086/180305.
- K. I. Kellermann, R. Sramek, M. Schmidt, D. B. Shaffer, and R. Green. VLA observations of objects in the Palomar Bright Quasar Survey. *AJ*, 98:1195–1207, October 1989. doi: 10.1086/115207.
- É. Y. Khachikyan and D. W. Weedman. A spectroscopic study of luminous galactic nuclei. *Astrophysics*, 7:231–240, July 1971. doi: 10.1007/BF01001021.
- J. G. Kirk and A. Mastichiadis. X-ray flares from runaway pair production in active galactic nuclei. *Nature*, 360:135–137, November 1992. doi: 10.1038/360135a0.
- Wayne H. Knox, Miguel Alonso, and Emil Wolf. Spatial coherence from ducks. *Physics Today*, *AIP Publishing*, 63(3):11, 2010. doi: 10.1063/1.3366225. URL <http://dx.doi.org/10.1063/1.3366225>.
- S. S. Komissarov. Blandford-Znajek Mechanism versus Penrose Process. *Journal of Korean Physical Society*, 54:2503, June 2009. doi: 10.3938/jkps.54.2503.
- S. Komossa. Narrow-line Seyfert 1 Galaxies. In *Revista Mexicana de Astronomía y Astrofísica Conference Series*, volume 32 of *Revista Mexicana de Astronomía y Astrofísica Conference Series*, pages 86–92, April 2008.
- S. Komossa, W. Voges, D. Xu, S. Mathur, H.-M. Adorf, G. Lemson, W. J. Duschl, and D. Grupe. Radio-loud Narrow-Line Type 1 Quasars. *AJ*, 132:531–545, August 2006. doi: 10.1086/505043.
- A. Königl. Relativistic jets as X-ray and gamma-ray sources. *ApJ*, 243:700–709, February 1981. doi: 10.1086/158638.

- Y. Y. Kovalev, A. P. Lobanov, A. B. Pushkarev, and J. A. Zensus. Opacity in compact extragalactic radio sources and its effect on astrophysical and astrometric studies. *A&A*, 483:759–768, June 2008. doi: 10.1051/0004-6361:20078679.
- N. A. Kudryavtseva, D. C. Gabuzda, M. F. Aller, and H. D. Aller. A new method for estimating frequency-dependent core shifts in active galactic nucleus jets. *MNRAS*, 415:1631–1637, August 2011. doi: 10.1111/j.1365-2966.2011.18808.x.
- A. M. Kutkin, K. V. Sokolovsky, M. M. Lisakov, Y. Y. Kovalev, T. Savolainen, P. A. Voytsik, A. P. Lobanov, H. D. Aller, M. F. Aller, A. Lahteenmaki, M. Tornikoski, A. E. Volvach, and L. N. Volvach. The core shift effect in the blazar 3C 454.3. *MNRAS*, 437:3396–3404, February 2014. doi: 10.1093/mnras/stt2133.
- M. L. Kutner and B. L. Ulich. Recommendations for calibration of millimeter-wavelength spectral line data. *ApJ*, 250:341–348, November 1981. doi: 10.1086/159380.
- A. Lähteenmäki and E. Valtaoja. Total Flux Density Variations in Extragalactic Radio Sources. III. Doppler Boosting Factors, Lorentz Factors, and Viewing Angles for Active Galactic Nuclei. *ApJ*, 521:493–501, August 1999. doi: 10.1086/307587.
- A. Lähteenmäki, E. Valtaoja, and K. Wiik. Total Flux Density Variations in Extragalactic Radio Sources. II. Determining the Limiting Brightness Temperature for Synchrotron Sources. *ApJ*, 511:112–117, January 1999. doi: 10.1086/306649.
- S. Larsson. Statistical Analysis of Multiwavelength Light curves. *ArXiv e-prints*, July 2012.
- S. Larsson, L. Fuhrmann, A. Weiss, E. Angelakis, T. P. Krichbaum, I. Nestoras, J. A. Zensus, M. Axelsson, D. Nilsson, F. Ryde, L. Hjalmsdotter, J. Larsson, A. Lundgren, F. Mac-Auliffe, R. Parra, and G. Siringo. APEX sub-mm monitoring of gamma-ray blazars. *ArXiv e-prints*, June 2012.
- M. J. Ledlow, F. N. Owen, and W. C. Keel. An Unusual Radio Galaxy in Abell 428: A Large, Powerful FR I Source in a Disk-dominated Host. *ApJ*, 495:227–238, March 1998. doi: 10.1086/305251.
- M. J. Ledlow, F. N. Owen, M. S. Yun, and J. M. Hill. A Large-Scale Jet and FR I Radio Source in a Spiral Galaxy: The Host Properties and External Environment. *ApJ*, 552:120–132, May 2001. doi: 10.1086/320458.
- S.-S. Lee. Intrinsic Brightness Temperature of Compact Radio Sources at 86GHz. *Journal of Korean Astronomical Society*, 46:243–251, December 2013. doi: 10.5303/JKAS.2013.46.6.243.
- J. León-Tavares, V. Chavushyan, V. Patiño-Álvarez, E. Valtaoja, T. G. Arshakian, L. Č. Popović, M. Tornikoski, A. Lobanov, A. Carramiñana, L. Carrasco, and A. Lähteenmäki. Flare-like Variability of the Mg II  $\lambda 2800$  Emission Line in the  $\Gamma$ -Ray Blazar 3C 454.3. *ApJ*, 763:L36, February 2013. doi: 10.1088/2041-8205/763/2/L36.
- M. L. Lister, M. H. Cohen, D. C. Homan, M. Kadler, K. I. Kellermann, Y. Y. Kovalev, E. Ros, T. Savolainen, and J. A. Zensus. MOJAVE: Monitoring of Jets in Active Galactic Nuclei with VLBA Experiments. VI. Kinematics Analysis of a Complete Sample of Blazar Jets. *AJ*, 138:1874–1892, December 2009. doi: 10.1088/0004-6256/138/6/1874.
- M. L. Lister, M. F. Aller, H. D. Aller, D. C. Homan, K. I. Kellermann, Y. Y. Kovalev, A. B. Pushkarev, J. L. Richards, E. Ros, and T. Savolainen. MOJAVE. X. Parsec-scale Jet Orientation Variations and Superluminal Motion in Active Galactic Nuclei. *AJ*, 146:120, November 2013. doi: 10.1088/0004-6256/146/5/120.
- A. Lobanov. Physical properties of blazar jets from VLBI observations. *ArXiv e-prints*, October 2010.
- A. P. Lobanov. *Physics of the Parsec-Scale Structures in the Quasar 3C 345*. PhD thesis, New Mexico Institute of Mining and Technology, Socorro, NM, US, (1996), 1996.

- A. P. Lobanov. Ultracompact jets in active galactic nuclei. *A&A*, 330:79–89, February 1998.
- A. P. Lobanov. Resolution limits in astronomical images. *arXiv:astro-ph/0503225*, March 2005.
- A. P. Lobanov and J. A. Zensus. A Cosmic Double Helix in the Archetypical Quasar 3C273. *Science*, 294:128–131, October 2001. doi: 10.1126/science.1063239.
- K. Mannheim. The proton blazar. *A&A*, 269:67–76, March 1993.
- M. Y. Mao, F. Owen, R. Duffin, B. Keel, M. Lacy, E. Momjian, G. Morrison, T. Mroczkowski, S. Neff, R. P. Norris, H. Schmitt, V. Toy, and S. Veilleux. J1649+2635: a grand-design spiral with a large double-lobed radio source. *MNRAS*, 446:4176–4185, February 2015. doi: 10.1093/mnras/stu2302.
- D. Maoz and H. Netzer. Evaluation of the cross-correlation method and the size of AGN emission-line regions. *MNRAS*, 236:21–29, January 1989.
- J. M. Marcaide and I. I. Shapiro. VLBI study of 1038 + 528 A and B - Discovery of wavelength dependence of peak brightness location. *ApJ*, 276:56–59, January 1984. doi: 10.1086/161592.
- M. J. M. Marcha, I. W. A. Browne, C. D. Impey, and P. S. Smith. Optical spectroscopy and polarization of a new sample of optically bright flat radio spectrum sources. *MNRAS*, 281: 425–448, July 1996.
- A. P. Marscher. Accurate formula for the self-Compton X-ray flux density from a uniform, spherical, compact radio source. *ApJ*, 264:296, January 1983. doi: 10.1086/160597.
- A. P. Marscher. Probes of the Inner Jets of Blazars. *Proceedings of the National Academy of Science*, 92:11439–11441, December 1995. doi: 10.1073/pnas.92.25.11439.
- A. P. Marscher. The Inner Jets of Blazars. In P. E. Hardee, A. H. Bridle, and J. A. Zensus, editors, *Energy Transport in Radio Galaxies and Quasars*, volume 100 of *Astronomical Society of the Pacific Conference Series*, page 45, 1996.
- A. P. Marscher. The Core of a Blazar Jet. In T. A. Rector and D. S. De Young, editors, *Extragalactic Jets: Theory and Observation from Radio to Gamma Ray*, volume 386 of *Astronomical Society of the Pacific Conference Series*, page 437, June 2008.
- A. P. Marscher. Turbulent, Extreme Multi-zone Model for Simulating Flux and Polarization Variability in Blazars. *ApJ*, 780:87, January 2014. doi: 10.1088/0004-637X/780/1/87.
- A. P. Marscher and W. K. Gear. Models for high-frequency radio outbursts in extragalactic sources, with application to the early 1983 millimeter-to-infrared flare of 3C 273. *ApJ*, 298: 114–127, November 1985. doi: 10.1086/163592.
- I. Martí-Vidal, T. P. Krichbaum, A. Marscher, W. Alef, A. Bertarini, U. Bach, F. K. Schinzel, H. Rottmann, J. M. Anderson, J. A. Zensus, M. Bremer, S. Sanchez, M. Lindqvist, and A. Mu-junen. On the calibration of full-polarization 86 GHz global VLBI observations. *A&A*, 542: A107, June 2012. doi: 10.1051/0004-6361/201218958.
- T. A. Matthews and A. R. Sandage. Optical Identification of 3C 48, 3C 196, and 3C 286 with Stellar Objects. *ApJ*, 138:30, July 1963. doi: 10.1086/147615.
- R. Mauersberger, M. Guélin, J. Martín-Pintado, C. Thum, J. Cernicharo, H. Hein, and S. Navarro. Line calibrators at  $\lambda = 1.3, 2, \text{ and } 3$  MM. *A&AS*, 79:217–261, August 1989.
- W. Max-Moerbeck, T. Hovatta, J. L. Richards, O. G. King, T. J. Pearson, A. C. S. Readhead, R. Reeves, M. C. Shepherd, M. A. Stevenson, E. Angelakis, L. Fuhrmann, K. J. B. Grainge, V. Pavlidou, R. W. Romani, and J. A. Zensus. Time correlation between the radio and gamma-ray activity in blazars and the production site of the gamma-ray emission. *MNRAS*, 445: 428–436, November 2014. doi: 10.1093/mnras/stu1749.

- J. C. McKinney and R. D. Blandford. Stability of relativistic jets from rotating, accreting black holes via fully three-dimensional magnetohydrodynamic simulations. *MNRAS*, 394:L126–L130, March 2009. doi: 10.1111/j.1745-3933.2009.00625.x.
- J. C. McKinney, A. Tchekhovskoy, and R. D. Blandford. General relativistic magnetohydrodynamic simulations of magnetically choked accretion flows around black holes. *MNRAS*, 423: 3083–3117, July 2012. doi: 10.1111/j.1365-2966.2012.21074.x.
- D. L. Meier. The theory and simulation of relativistic jet formation: towards a unified model for micro- and macroquasars. *New A Rev.*, 47:667–672, October 2003. doi: 10.1016/S1387-6473(03)00120-9.
- D. L. Meier, S. Koide, and Y. Uchida. Magnetohydrodynamic Production of Relativistic Jets. *Science*, 291:84–92, January 2001. doi: 10.1126/science.291.5501.84.
- A. Merloni, S. Heinz, and T. di Matteo. A Fundamental Plane of black hole activity. *MNRAS*, 345:1057–1076, November 2003. doi: 10.1046/j.1365-2966.2003.07017.x.
- A. A. Michelson. Note on the Definition, the Resolving Power and the Accuracy of Telescopes and microscopes. *PASP*, 2:115–117, May 1890. doi: 10.1086/120110.
- A. A. Michelson. Measurement of Jupiter’s Satellites by Interference. *Nature*, 45:160–161, December 1891. doi: 10.1038/045160a0.
- A. A. Michelson. On the Application of Interference Methods to Astronomical Measurements. *ApJ*, 51:257, June 1920. doi: 10.1086/142550.
- A. A. Michelson and F. G. Pease. Measurement of the diameter of alpha Orionis with the interferometer. *ApJ*, 53:249–259, May 1921. doi: 10.1086/142603.
- E. C. Moran. Radio properties of NLS1s. *New A Rev.*, 44:527–529, September 2000. doi: 10.1016/S1387-6473(00)00092-0.
- A. L. Moser and P. M. Bellan. Magnetic reconnection from a multiscale instability cascade. *Nature*, 482:379–381, February 2012. doi: 10.1038/nature10827.
- I. Nestoras, et al., and . F-GAMMA program: Multi-frequency study of Active Galactic Nuclei in the Fermi-GST era III. The first 5 years of IRAM 30-m monitoring. *A&A*, in prep.
- D. E. Osterbrock and R. W. Pogge. The spectra of narrow-line Seyfert 1 galaxies. *ApJ*, 297: 166–176, October 1985. doi: 10.1086/163513.
- A. G. Pacholczyk. *Radio astrophysics. Nonthermal processes in galactic and extragalactic sources.* 1970.
- F. Pedregosa, G. Varoquaux, A. Gramfort, V. Michel, B. Thirion, O. Grisel, M. Blondel, P. Prettenhofer, R. Weiss, V. Dubourg, J. Vanderplas, A. Passos, D. Cournapeau, M. Brucher, M. Perrot, and E. Duchesnay. Scikit-learn: Machine learning in Python. *Journal of Machine Learning Research*, 12:2825–2830, 2011.
- A. A. Penzias and C. A. Burrus. Millimeter-Wavelength Radio-Astronomy Techniques. *ARA&A*, 11:51, 1973. doi: 10.1146/annurev.aa.11.090173.000411.
- M. Perucho, J. M. Martí, and M. Hanasz. Stability of hydrodynamical relativistic planar jets. II. Long-term nonlinear evolution. *A&A*, 427:431–444, November 2004. doi: 10.1051/0004-6361:20040350.
- B. M. Peterson. *An Introduction to Active Galactic Nuclei.* February 1997.
- B. M. Peterson, I. Wanders, K. Horne, S. Collier, T. Alexander, S. Kaspi, and D. Maoz. On Uncertainties in Cross-Correlation Lags and the Reality of Wavelength-dependent Continuum Lags in Active Galactic Nuclei. *PASP*, 110:660–670, June 1998. doi: 10.1086/316177.

- E. Pian, P. Ubertini, A. Bazzano, V. Beckmann, D. Eckert, G. Ghisellini, T. Pursimo, G. Tagliaferri, F. Tavecchio, M. Türler, S. Bianchi, V. Bianchin, R. Hudec, L. Maraschi, C. M. Raiteri, S. Soldi, A. Treves, and M. Villata. INTEGRAL observations of the GeV blazar PKS 1502+106 and the hard X-ray bright Seyfert galaxy Mkn 841. *A&A*, 526:A125, February 2011. doi: 10.1051/0004-6361/201015414.
- R. W. Pogge. Narrow-line Seyfert 1s: 15 years later. *New A Rev.*, 44:381–385, September 2000. doi: 10.1016/S1387-6473(00)00065-8.
- R. Porcas. Superluminal motions - Astronomers still puzzled. *Nature*, 302:753, April 1983. doi: 10.1038/302753a0.
- R.W. Porcas. Observing blazars with vlbi. In Franco Mantovani and Andrzej Kus, editors, *The Role of VLBI in Astrophysics, Astrometry and Geodesy*, volume 135 of *NATO Science Series II: Mathematics, Physics and Chemistry*, pages 93–106. Springer Netherlands, 2005. ISBN 978-1-4020-1875-6. doi: 10.1007/1-4020-2406-1\_5. URL [http://dx.doi.org/10.1007/1-4020-2406-1\\_5](http://dx.doi.org/10.1007/1-4020-2406-1_5).
- A. B. Pushkarev, Y. Y. Kovalev, M. L. Lister, and T. Savolainen. Jet opening angles and gamma-ray brightness of AGN. *A&A*, 507:L33–L36, November 2009. doi: 10.1051/0004-6361/200913422.
- A. B. Pushkarev, T. Hovatta, Y. Y. Kovalev, M. L. Lister, A. P. Lobanov, T. Savolainen, and J. A. Zensus. MOJAVE: Monitoring of Jets in Active galactic nuclei with VLBA Experiments. IX. Nuclear opacity. *A&A*, 545:A113, September 2012. doi: 10.1051/0004-6361/201219173.
- B. Rani, T. P. Krichbaum, L. Fuhrmann, M. Böttcher, B. Lott, H. D. Aller, M. F. Aller, E. Angelakis, U. Bach, D. Bastieri, A. D. Falcone, Y. Fukazawa, K. E. Gabanyi, A. C. Gupta, M. Gurwell, R. Itoh, K. S. Kawabata, M. Krips, A. A. Lähteenmäki, X. Liu, N. Marchili, W. Max-Moerbeck, I. Nestoras, E. Nieppola, G. Quintana-Lacaci, A. C. S. Readhead, J. L. Richards, M. Sasada, A. Sievers, K. Sokolovsky, M. Stroh, J. Tammi, M. Tornikoski, M. Uemura, H. Ungerechts, T. Urano, and J. A. Zensus. Radio to gamma-ray variability study of blazar S5 0716+714. *A&A*, 552:A11, April 2013. doi: 10.1051/0004-6361/201321058.
- Carl Edward Rasmussen and Christopher K. I. Williams. *Gaussian Processes for Machine Learning (Adaptive Computation and Machine Learning)*. The MIT Press, 2005. ISBN 026218253X.
- A. C. S. Readhead. Equipartition brightness temperature and the inverse Compton catastrophe. *ApJ*, 426:51–59, May 1994. doi: 10.1086/174038.
- M. J. Rees. Appearance of Relativistically Expanding Radio Sources. *Nature*, 211:468–470, July 1966. doi: 10.1038/211468a0.
- R. A. Remillard, H. V. Bradt, D. A. H. Buckley, W. Roberts, D. A. Schwartz, I. R. Tuohy, and K. Wood. The discovery of eight bright active galactic nuclei observed with the HEAO 1 scanning modulation collimator. *ApJ*, 301:742–752, February 1986. doi: 10.1086/163940.
- J. L. Richards and M. L. Lister. Kiloparsec-Scale Jets in Three Radio-Loud Narrow-Line Seyfert 1 Galaxies. *ApJ*, 800:L8, February 2015. doi: 10.1088/2041-8205/800/1/L8.
- J. L. Richards, W. Max-Moerbeck, V. Pavlidou, O. G. King, T. J. Pearson, A. C. S. Readhead, R. Reeves, M. C. Shepherd, M. A. Stevenson, L. C. Weintraub, L. Fuhrmann, E. Angelakis, J. A. Zensus, S. E. Healey, R. W. Romani, M. S. Shaw, K. Grainge, M. Birkinshaw, K. Lancaster, D. M. Worrall, G. B. Taylor, G. Cotter, and R. Bustos. Blazars in the Fermi Era: The OVRO 40 m Telescope Monitoring Program. *ApJS*, 194:29, June 2011. doi: 10.1088/0067-0049/194/2/29.
- S. Ritz. Overview of the GLAST Mission and Opportunities. In S. Ritz, P. Michelson, and C. A. Meegan, editors, *The First GLAST Symposium*, volume 921 of *American Institute of Physics Conference Series*, pages 3–7, July 2007. doi: 10.1063/1.2757255.
- S. Roberts, M. Osborne, M. Ebden, S. Reece, N. Gibson, and S. Aigrain. Gaussian processes for time-series modelling. *Philosophical Transactions of the Royal Society of London A: Mathematical, Physical and Engineering Sciences*, 371(1984), 2012. ISSN 1364-503X. doi: 10.1098/rsta.2011.0550.

- M. Ryle and A. Hewish. The synthesis of large radio telescopes. *MNRAS*, 120:220, 1960.
- T. Savolainen, K. Wiik, E. Valtaoja, S. G. Jorstad, and A. P. Marscher. Connections between millimetre continuum variations and VLBI structure in 27 AGN. *A&A*, 394:851–861, November 2002. doi: 10.1051/0004-6361:20021236.
- P. A. G. Scheuer and A. C. S. Readhead. Superluminally expanding radio sources and the radio-quiet QSOs. *Nature*, 277:182–185, January 1979. doi: 10.1038/277182a0.
- M. Schmidt. 3C 273 : A Star-Like Object with Large Red-Shift. *Nature*, 197:1040, March 1963. doi: 10.1038/1971040a0.
- M. Schmidt. Optical Spectra and Redshifts of 31 Radio Galaxies. *ApJ*, 141:1, January 1965. doi: 10.1086/148085.
- F. R. Schwab and W. D. Cotton. Global fringe search techniques for VLBI. *AJ*, 88:688–694, May 1983. doi: 10.1086/113360.
- M. A. Scott and A. C. S. Readhead. The low-frequency structure of powerful radio sources and limits to departures from equipartition. *MNRAS*, 180:539–550, September 1977.
- C. K. Seyfert. Nuclear Emission in Spiral Nebulae. *ApJ*, 97:28, January 1943. doi: 10.1086/144488.
- M. C. Shepherd. Difmap: an Interactive Program for Synthesis Imaging. In G. Hunt and H. Payne, editors, *Astronomical Data Analysis Software and Systems VI*, volume 125 of *Astronomical Society of the Pacific Conference Series*, page 77, 1997.
- M. C. Shepherd, T. J. Pearson, and G. B. Taylor. DIFMAP: an interactive program for synthesis imaging. In *Bulletin of the American Astronomical Society*, volume 26 of *Bulletin of the American Astronomical Society*, pages 987–989, May 1994.
- M. Sikora, Ł. Stawarz, and J.-P. Lasota. Radio Loudness of Active Galactic Nuclei: Observational Facts and Theoretical Implications. *ApJ*, 658:815–828, April 2007. doi: 10.1086/511972.
- G. Siringo, E. Kreysa, A. Kovács, F. Schuller, A. Weiß, W. Esch, H.-P. Gemünd, N. Jethava, G. Lundershausen, A. Colin, R. Güsten, K. M. Menten, A. Beelen, F. Bertoldi, J. W. Beeman, and E. E. Haller. The Large APEX BOlometer CAmera LABOCA. *A&A*, 497:945–962, April 2009. doi: 10.1051/0004-6361/200811454.
- V. M. Slipher. The spectrum and velocity of the nebula N.G.C. 1068 ( M 77). *Lowell Observatory Bulletin*, 3:59–62, 1917.
- A. Sokolov and A. P. Marscher. External Compton Radiation from Rapid Nonthermal Flares in Blazars. *ApJ*, 629:52–60, August 2005. doi: 10.1086/431321.
- K. V. Sokolovsky, Y. Y. Kovalev, A. B. Pushkarev, P. Mimica, and M. Perucho. VLBI-selected sample of compact symmetric object candidates and frequency-dependent position of hotspots. *A&A*, 535:A24, November 2011. doi: 10.1051/0004-6361/201015772.
- M. Spada, G. Ghisellini, D. Lazzati, and A. Celotti. Internal shocks in the jets of radio-loud quasars. *MNRAS*, 325:1559–1570, August 2001. doi: 10.1046/j.1365-8711.2001.04557.x.
- H. C. Spruit. Theory of Magnetically Powered Jets. In T. Belloni, editor, *Lecture Notes in Physics, Berlin Springer Verlag*, volume 794 of *Lecture Notes in Physics, Berlin Springer Verlag*, page 233, March 2010. doi: 10.1007/978-3-540-76937-8\_9.
- C. Struve and J. E. Conway. An H I absorbing circumnuclear disk in Cygnus A. *A&A*, 513:A10, April 2010. doi: 10.1051/0004-6361/200913572.
- F. Tavecchio and G. Ghisellini. “Flat” broad line region and gamma-ray absorption in blazars. *ArXiv e-prints*, September 2012.

- A. Tchekhovskoy, J. C. McKinney, and R. Narayan. Efficiency of Magnetic to Kinetic Energy Conversion in a Monopole Magnetosphere. *ApJ*, 699:1789–1808, July 2009. doi: 10.1088/0004-637X/699/2/1789.
- H. Terasranta, M. Tornikoski, A. Mujunen, K. Karlamaa, T. Valtonen, N. Henelius, S. Urpo, M. Lainela, T. Pursimo, K. Nilsson, S. Wiren, A. Lahteenmaeki, M. Korpi, R. Rekola, P. Heinaemaeki, M. Hanski, P. Nurmi, K. Kokkonen, P. Keinaenen, O. Joutsamo, J. Oksanen, H. Pietilae, E. Valtaoja, M. Valtonen, and P. Koenoenen. Fifteen years monitoring of extragalactic radio sources at 22, 37 and 87 GHz. *A&AS*, 132:305–331, November 1998. doi: 10.1051/aas:1998297.
- E. Thiébaud. Image reconstruction with optical interferometers. *New A Rev.*, 53:312–328, November 2009. doi: 10.1016/j.newar.2010.07.011.
- M. Türler, T. J.-L. Courvoisier, and S. Paltani. Modelling 20 years of synchrotron flaring in the jet of 3C 273. *A&A*, 361:850–862, September 2000.
- M.-H. Ulrich, L. Maraschi, and C. M. Urry. Variability of Active Galactic Nuclei. *ARA&A*, 35:445–502, 1997. doi: 10.1146/annurev.astro.35.1.445.
- J. S. Ulvestad, R. R. J. Antonucci, and R. W. Goodrich. Radio properties of narrow-lined Seyfert 1 galaxies. *AJ*, 109:81–86, January 1995. doi: 10.1086/117258.
- H. Ungerechts, C. Kramer, B. Lefloch, S. Leon, F. Masset, R. Moreno, G. Paubert, D. Reynaud, A. Sievers, and W. Wild. Millimeter Continuum Monitoring of Extragalactic Radio Sources with the IRAM 30m Telescope. In J. A. Zensus, G. B. Taylor, and J. M. Wrobel, editors, *IAU Colloq. 164: Radio Emission from Galactic and Extragalactic Compact Sources*, volume 144 of *Astronomical Society of the Pacific Conference Series*, page 149, 1998.
- C. M. Urry. Multiwavelength properties of blazars. *Astroparticle Physics*, 11:159–167, June 1999. doi: 10.1016/S0927-6505(99)00043-2.
- C. M. Urry and P. Padovani. Unification of BL Lac Objects and FR 1 Radio Galaxies. In G. V. Bicknell, M. A. Dopita, and P. J. Quinn, editors, *The Physics of Active Galaxies*, volume 54 of *Astronomical Society of the Pacific Conference Series*, page 215, 1994.
- C. M. Urry and P. Padovani. Unified Schemes for Radio-Loud Active Galactic Nuclei. *PASP*, 107:803, September 1995. doi: 10.1086/133630.
- E. Valtaoja and H. Teräsranta. Gamma radiation from radio shocks in AGN jets. *A&A*, 297:L13–L16, May 1995.
- E. Valtaoja, H. Terasranta, S. Urpo, N. S. Nesterov, M. Lainela, and M. Valtonen. Five Years Monitoring of Extragalactic Radio Sources - Part Three - Generalized Shock Models and the Dependence of Variability on Frequency. *A&A*, 254:71, February 1992.
- E. Valtaoja, A. Lähteenmäki, H. Teräsranta, and M. Lainela. Total Flux Density Variations in Extragalactic Radio Sources. I. Decomposition of Variations into Exponential Flares. *ApJS*, 120:95–99, January 1999. doi: 10.1086/313170.
- P.H van Cittert. Die wahrscheinliche schwingungsverteilung in einer von einer lichtquelle direkt oder mittels einer linse beleuchteten ebene. *Physica*, 1:201 – 210, 1934. ISSN 0031-8914. doi: [http://dx.doi.org/10.1016/S0031-8914\(34\)90026-4](http://dx.doi.org/10.1016/S0031-8914(34)90026-4). URL <http://www.sciencedirect.com/science/article/pii/S0031891434900264>.
- H. van der Laan. A Model for Variable Extragalactic Radio Sources. *Nature*, 211:1131, September 1966. doi: 10.1038/2111131a0.
- Alan R. Whitney, Irwin I. Shapiro, Alan E. E. Rogers, Douglas S. Robertson, Curtis A. Knight, Thomas A. Clark, Richard M. Goldstein, Gerard E. Marandino, and Nancy R. Vandenberg. Quasars revisited: Rapid time variations observed via very-long-baseline interferometry. *Science*, 173(3993):225–230, 1971. doi: 10.1126/science.173.3993.225. URL <http://www.sciencemag.org/content/173/3993/225.abstract>.

- Helmut Wiesemeyer and Axel Nothnagel. Very long baseline interferometry. pages 1509–1515, 2014. doi: [10.1007/978-90-481-8702-7\\_99](https://doi.org/10.1007/978-90-481-8702-7_99). URL [http://dx.doi.org/10.1007/978-90-481-8702-7\\_99](http://dx.doi.org/10.1007/978-90-481-8702-7_99).
- C. K. I. Williams and C. E. Rasmussen. Gaussian Processes for Regression. In D. S. Touretzky, M. C. Mozer, and M. E. Hasselmo, editors, *Advances in Neural Information Processing Systems 8*, MIT Press, 1996.
- T. Young. The Bakerian Lecture: On the Theory of Light and Colours. *Royal Society of London Philosophical Transactions Series I*, 92:12–48, 1802.
- W. Yuan, H. Y. Zhou, S. Komossa, X. B. Dong, T. G. Wang, H. L. Lu, and J. M. Bai. A Population of Radio-Loud Narrow-Line Seyfert 1 Galaxies with Blazar-Like Properties? *ApJ*, 685:801–827, October 2008. doi: [10.1086/591046](https://doi.org/10.1086/591046).
- J. A. Zensus. Parsec-Scale Jets in Extragalactic Radio Sources. *ARA&A*, 35:607–636, 1997. doi: [10.1146/annurev.astro.35.1.607](https://doi.org/10.1146/annurev.astro.35.1.607).
- J. A. Zensus, M. H. Cohen, and S. C. Unwin. The Parsec-scale jet in quasar 3C 345. *ApJ*, 443:35–53, April 1995a. doi: [10.1086/175501](https://doi.org/10.1086/175501).
- J. A. Zensus, P. J. Diamond, and P. J. Napier, editors. *Very Long Baseline Interferometry and the VLBA*, volume 82 of *Astronomical Society of the Pacific Conference Series*, 1995b.
- F. Zernike. The concept of degree of coherence and its application to optical problems. *Physica*, 5(8):785 – 795, 1938. ISSN 0031-8914. doi: [http://dx.doi.org/10.1016/S0031-8914\(38\)80203-2](http://dx.doi.org/10.1016/S0031-8914(38)80203-2). URL <http://www.sciencedirect.com/science/article/pii/S0031891438802032>.
- H. Zhou, T. Wang, W. Yuan, H. Shan, S. Komossa, H. Lu, Y. Liu, D. Xu, J. M. Bai, and D. R. Jiang. A Narrow-Line Seyfert 1-Blazar Composite Nucleus in 2MASX J0324+3410. *ApJ*, 658:L13–L16, March 2007. doi: [10.1086/513604](https://doi.org/10.1086/513604).
- H.-Y. Zhou, T.-G. Wang, X.-B. Dong, Y.-Y. Zhou, and C. Li. SDSS J094857.3+002225: A Very Radio Loud, Narrow-Line Quasar with Relativistic Jets? *ApJ*, 584:147–152, February 2003. doi: [10.1086/345523](https://doi.org/10.1086/345523).



## ERKLÄRUNG

---

Ich versichere, dass ich die von mir vorgelegte Dissertation selbständig angefertigt, die benutzten Quellen und Hilfsmittel vollständig angegeben und die Stellen der Arbeit, einschließlich Tabellen, Karten und Abbildungen, die anderen Werken im Wortlaut oder dem Sinn nach entnommen sind, in jedem Einzelfall als Entlehnung kenntlich gemacht habe; dass diese Dissertation noch keiner anderen Fakultät oder Universität zur Prüfung vorgelegen hat; dass sie, abgesehen von unten angegebenen Teilpublikationen – noch nicht veröffentlicht worden ist sowie, dass ich eine solche Veröffentlichung vor Abschluss des Promotionsverfahrens nicht vornehmen werde. Die Bestimmungen der Promotionsordnung sind mir bekannt. Die von mir vorgelegte Dissertation ist von Prof. Dr. J. Anton Zensus und Prof. Dr. Andreas Eckart betreut worden.

Köln, den 16.03.2015



1. Localizing the  $\gamma$  rays from blazar PKS 1502+106. **V. Karamanavis**, L. Fuhrmann, T. P. Krichbaum, E. Angelakis, J. Hodgson, I. Myserlis, I. Nestoras, J. A. Zensus, H. Ungerechts and A. Sievers. To appear in proceedings of 12th European VLBI Network Symposium and Users Meeting, 7–10 October 2014.
2. Radio jet emission from GeV-emitting narrow-line Seyfert 1 galaxies. E. Angelakis, L. Fuhrmann, N. Marchili, L. Foschini, I. Myserlis, **V. Karamanavis**, S. Komossa, D. Blinov, T. P. Krichbaum, A. Sievers, H. Ungerechts, and J. A. Zensus. *A&A*, 575:A55, March 2015.
3. What powers the radio-loud narrow-line Seyfert 1 galaxy RX J2314.9+2243? A view onto its central engine from radio to X-rays. S. Komossa, D. Xu, L. Fuhrmann, D. Grupe, S. Yao, Z. Fan, I. Myserlis, E. Angelakis, **V. Karamanavis**, W. Yuan, and J. A. Zensus. *A&A*, 574:A121, February 2015.
4. VizieR Online Data Catalog: RXJ2314.9+2243 from radio to X-rays (Komossa+, 2015). S. Komossa, D. Xu, L. Fuhrmann, D. Grupe, S. Yao, Z. Fan, I. Myserlis, E. Angelakis, **V. Karamanavis**, W. Yuan, and J. A. Zensus. *VizieR Online Data Catalog*, 357:49121, November 2014.
5. A multi-wavelength study of the radio-loud Narrow-line Seyfert 1 galaxy RXJ23149+2. D. Xu, S. Komossa, L. Fuhrmann, D. Grupe, E. Angelakis, I. Myserlis, **V. Karamanavis**, and A. Zensus. A multi-wavelength study of the radio-loud Narrow-line Seyfert 1 galaxy RXJ23149+2. In *The X-ray Universe 2014*, page 336, July 2014.
6. Multi-frequency linear and circular radio polarization monitoring of jet emission elements in *Fermi* blazars. I. Myserlis, E. Angelakis, L. Fuhrmann, V. Pavlidou, I. Nestoras, **V. Karamanavis**, A. Kraus, and J. A. Zensus. *ArXiv e-prints*:1401.2072, January 2014.
7. The Gamma-ray Activity of the high-z Quasar 0836+71. S. Jorstad, A. Marscher, V. Larionov, J. L. Gómez, I. Agudo, E. Angelakis, C. Casadio, M. Gurwell, T. Hovatta, M. Joshi, L. Fuhrmann, **V. Karamanavis**, A. Lähteenmäki, S. Molina, D. Morozova, I. Myserlis, I. Troitsky, H. Ungerechts, and J. A. Zensus. The Gamma-ray Activity of the high-z Quasar 0836+71. In *European Physical Journal Web of Conferences*, volume 61 of *European Physical Journal Web of Conferences*, page 4003, December 2013.
8. An Exceptional Radio Flare in Markarian 421. J. L. Richards, T. Hovatta, M. L. Lister, A. C. S. Readhead, W. Max-Moerbeck, T. Savolainen, E. Angelakis, L. Fuhrmann, M. F. Aller, H. D. Aller, I. Myserlis, and **V. Karamanavis**. In *European Physical Journal Web of Conferences*, volume 61 of *European Physical Journal Web of Conferences*, page 4010, December 2013.
9. Multifrequency studies of the narrow-line Seyfert 1 galaxy SBS 0846+513. F. D'Ammando, M. Orienti, J. Finke, C. M. Raiteri, E. Angelakis, L. Fuhrmann, M. Giroletti, T. Hovatta, **V. Karamanavis**, W. Max-Moerbeck, I. Myserlis, A. C. S. Readhead, and J. L. Richards. *MNRAS*, 436:191â201, November 2013.

10. Zooming towards the Event Horizon - mm-VLBI today and tomorrow. T. P. Krichbaum, A. Roy, J. Wagner, H. Rottmann, J. A. Hodgson, A. Bertarini, W. Alef, J. A. Zensus, A. P. Marscher, S. G. Jorstad, R. Freund, D. Marrone, P. Strittmatter, L. Ziurys, R. Blundell, J. Weintroub, K. Young, V. Fish, S. Doeleman, M. Bremer, S. Sanchez, L. Fuhrmann, E. Angelakis, and **V. Karamanavis**. ArXiv e-prints: 1305.2811, May 2013.
11. Properties of the radio jet emission of four gamma-ray Narrow Line Seyfert 1 galaxies. E. Angelakis, L. Fuhrmann, I. Myserlis, I. Nestoras, **V. Karamanavis**, T. P. Krichbaum, J. A. Zensus, N. Marchili, L. Foschini, H. Ungerechts, and A. Sievers. ArXiv e-prints: 1304.1706, April 2013.
12. Recent radio activity of the Fermi blazar 4C +38.41. I. Myserlis, E. Angelakis, L. Fuhrmann, **V. Karamanavis**, I. Nestoras, T. P. Krichbaum, J. A. Zensus, H. Ungerechts, and A. Sievers. *The Astronomer's Telegram*, 4448:1, October 2012.
13. Recent radio activity of the Fermi blazar CTA 102. I. Myserlis, E. Angelakis, L. Fuhrmann, **V. Karamanavis**, I. Nestoras, T. P. Krichbaum, J. A. Zensus, H. Ungerechts, and A. Sievers. *The Astronomer's Telegram*, 4449:1, October 2012.
14. Recent radio activity of the Fermi blazar S5 0716+714. I. Myserlis, E. Angelakis, L. Fuhrmann, **V. Karamanavis**, I. Nestoras, T. P. Krichbaum, J. A. Zensus, H. Ungerechts, and A. Sievers. *The Astronomer's Telegram*, 4447:1, October 2012.
15. Follow-up radio observations of Nova Mon 2012 at 10–142 GHz. L. Fuhrmann, J. L. Richards, U. Bach, T. Hovatta, M. Bremer, I. Nestoras, **V. Karamanavis**, K. Moolley, I. Myserlis, A. C. S. Readhead, C. C. Cheung, T. Pearson, and E. Angelakis. *The Astronomer's Telegram*, 4376:1, September 2012.
16. Gamma-ray blazar BL Lacertae: the highest recorded cm/mm radio flux over the past 30 years. **V. Karamanavis**, I. Myserlis, L. Fuhrmann, E. Angelakis, I. Nestoras, T. P. Krichbaum, J. A. Zensus, H. Ungerechts, A. Sievers, and D. Riquelme. *The Astronomer's Telegram*, 4349:1, August 2012.
17. Survey for variable stars and exoplanet transits from Holomon Astronomical Station. P. Ioannidis, **V. Karamanavis**, C. Avdellidou, D. Mislis, J. Antoniadis, and J. Seiradakis. Survey for variable stars and exoplanet transits from Holomon Astronomical Station. In I. Papadakis and A. Anastasiadis, editors, 10th Hellenic Astronomical Conference, page 28, January 2012.
18. A wide-field survey for variable stars. **V. Karamanavis**. Diploma thesis, Aristotle University of Thessaloniki, April 2011.
19. ThReT: A New Survey for Extrasolar Planetary Transits at Mt. Holomon, Greece. J. Antoniadis, **V. Karamanavis**, D. Mislis, A. Nitsos, and J. H. Seiradakis. ThReT: A New Survey for Extrasolar Planetary Transits at Mt. Holomon Greece. In K. Tsinganos, D. Hatzidimitriou, and T. Matsakos, editors, 9th International Conference of the Hellenic Astronomical Society, volume 424 of Astronomical Society of the Pacific Conference Series, page 218, July 2010.
20. Post-common envelope binaries from SDSS - III. Seven new orbital periods. A. Rebassa-Mansergas, B. T. Gänsicke, M. R. Schreiber, J. Southworth, A. D. Schwobe, A. Nebot Gomez-Moran, A. Aungwerojwit, P. Rodríguez-Gil, **V. Karamanavis**, M. Krumpke, E. Tremou, R. Schwarz, A. Staude, and J. Vogel. *MNRAS*, 390:1635–1646, November 2008.

## LEBENS LAUF

---

### PERSÖNLICHE DATEN

Vasileios (Vassilis) Karamanavis

Geburtsdatum: 31. März 1987  
Geburtsort: Thessaloniki, Griechenland  
Staatsangehörigkeit: Griechisch

### ANSCHRIFT

Max-Planck-Institut für Radioastronomie  
Auf dem Hügel 69  
53121 Bonn  
Deutschland  
email: vkaraman@mpifr-bonn.mpg.de

### AUSBILDUNG

- 2012–2015 Doktorand an der Universität zu Köln und dem  
Max-Planck-Institut für Radioastronomie in Bonn  
Stipendium der International Max Planck Research School for  
Astronomy and Astrophysics  
wiss. Betreuer Dr. Lars Fuhrmann und  
Prof. Dr. J. Anton Zensus  
Titel: *"Zooming into  $\gamma$ -ray loud galactic nuclei:  
broadband emission and structure dynamics of the blazar  
PKS 1502+106 and the narrow-line Seyfert 1 1H 0323+342"*
- 2004–2011 Diplomstudent an der Aristotle University of Thessaloniki,  
Diplom Physik  
wiss. Betreuer Prof. Dr. John H. Seiradakis  
Titel: *"A wide-field survey for variable stars"*
- 1998–2004 Allgemeine Hochschulreife am 9. Gymnasium und Hochschule,  
Thessaloniki